

Technical Report Documentation Page

1. Report No. FHWA/TX-06/0-4177-3		2. Government Accession No.		3. Recipient's Catalog No.	
4. Title and Subtitle EVALUATION OF CRUSHED CONCRETE AND RECYCLED ASPHALT PAVEMENT AS BACKFILL FOR MECHANICALLY STABILIZED EARTH WALLS				5. Report Date March 2006	
				6. Performing Organization Code	
7. Author(s) Ellen M. Rathje, Alan F. Rauch, David Trejo, Kevin J. Folliard, Chirayus Viyanant, Michael Esfellar, Abhishek Jain, and Moses Ogalla				8. Performing Organization Report No. 0-4177-3	
9. Performing Organization Name and Address Center for Transportation Research The University of Texas at Austin 3208 Red River, Suite 200 Austin, TX 78705-2650				10. Work Unit No. (TRAIIS)	
				11. Contract or Grant No. 0-4177	
12. Sponsoring Agency Name and Address Texas Department of Transportation Research and Technology Implementation Office P.O. Box 5080 Austin, TX 78763-5080				13. Type of Report and Period Covered Final Report, 09/01/2001-12/31/2003	
				14. Sponsoring Agency Code	
15. Supplementary Notes Project performed in cooperation with the Texas Department of Transportation and the Federal Highway Administration.					
16. Abstract This report presents the results from an experimental program aimed at evaluating the use of the crushed concrete (CC) and recycled asphalt pavement (RAP) for use in mechanically stabilized earth (MSE) walls. Various properties of RAP and CC (strength, hydraulic conductivity, pull out resistance, creep potential, corrosivity) were investigated. CC was judged as an adequate backfill for MSE walls, although its marginal hydraulic conductivity requires additional drainage to be provided behind walls. RAP displayed a significant potential for deviatoric creep, making this material unsuitable as select backfill for MSE walls.					
17. Key Words Recycled asphalt, crushed concrete, MSE walls			18. Distribution Statement No restrictions. This document is available to the public through the National Technical Information Service, Springfield, Virginia 22161; www.ntis.gov.		
19. Security Classif. (of report) Unclassified	20. Security Classif. (of this page) Unclassified	21. No. of pages 182		22. Price	





## **Evaluation of Crushed Concrete and Recycled Asphalt Pavement as Backfill for Mechanically Stabilized Earth Walls**

Ellen M. Rathje  
Alan F. Rauch  
David Trejo  
Kevin J. Folliard  
Chirayus Viyanant  
Michael Esfellar  
Abhishek Jain  
Moses Ogalla

---

CTR Technical Report:	0-4177-3
Report Date:	March 2006
Project:	0-4177
Project Title:	<i>Use of Recycled Asphalt Pavement and Crushed Concrete as Backfill for Mechanically Stabilized Earth Retaining Walls</i>
Sponsoring Agency:	Texas Department of Transportation
Performing Agency:	Center for Transportation Research at The University of Texas at Austin

Project performed in cooperation with the Texas Department of Transportation and the Federal Highway Administration.

Center for Transportation Research  
The University of Texas at Austin  
3208 Red River  
Austin, TX 78705

[www.utexas.edu/research/ctr](http://www.utexas.edu/research/ctr)

Copyright (c) 2006  
Center for Transportation Research  
The University of Texas at Austin

All rights reserved  
Printed in the United States of America

## **Disclaimers**

**Author's Disclaimer:** The contents of this report reflect the views of the authors, who are responsible for the facts and the accuracy of the data presented herein. The contents do not necessarily reflect the official view or policies of the Federal Highway Administration or the Texas Department of Transportation (TxDOT). This report does not constitute a standard, specification, or regulation.

**Patent Disclaimer:** There was no invention or discovery conceived or first actually reduced to practice in the course of or under this contract, including any art, method, process, machine manufacture, design or composition of matter, or any new useful improvement thereof, or any variety of plant, which is or may be patentable under the patent laws of the United States of America or any foreign country.

Notice: The United States Government and the State of Texas do not endorse products or manufacturers. If trade or manufacturers' names appear herein, it is solely because they are considered essential to the object of this report.

### **Engineering Disclaimer**

NOT INTENDED FOR CONSTRUCTION, BIDDING, OR PERMIT PURPOSES.

## **Acknowledgments**

The support and assistance of the personnel at the Texas Department of Transportation (TxDOT) are gratefully acknowledged. These personnel include the project coordinator Mark McClelland (BRG), the project director Marcus Galvan (BRG), and the project monitoring committee, which includes John Delphia (BRY), Harold Albers (CST), and Mario Garza (CRP).

## Table of Contents

1. Introduction.....	1
1.1 Background.....	1
2. Potential Use of Crushed Concrete and Recycled Asphalt Pavement for MSE Walls.....	3
2.1 Introduction.....	3
2.2 Previous Uses of Crushed Concrete and Recycled Asphalt Pavement.....	3
2.2.1 Crushed Concrete.....	3
2.2.2 Recycled Asphalt Pavement.....	6
2.3 Mechanically Stabilized Earth Walls.....	9
2.3.2 MSE Wall Design.....	10
2.3.3 Critical Backfill Properties.....	12
2.4 MSE Wall Backfill Specifications.....	15
2.4.1 Gradation.....	15
2.4.2 Compaction.....	15
2.4.3 Hydraulic Conductivity.....	17
2.4.4 Shear Strength.....	17
2.4.5 Creep Potential.....	18
2.4.6 Corrosivity.....	18
2.5 Summary.....	19
3. Selection of Test Materials and Initial Characterization.....	21
3.1 Selection of Test Materials.....	21
3.2 Index Properties.....	21
3.3 Laboratory Compaction.....	26
3.4 Summary.....	29
4. Geotechnical Properties of CC and RAP.....	31
4.1 Introduction.....	31
4.2 Test Equipment.....	31
4.3 Shear Strength.....	34
4.3.1 Consolidated-Drained Triaxial Tests.....	35
4.3.2 Large-Scale Drained Direct Shear Tests.....	40
4.3.3 Integration of Shear Strength Results.....	45
4.4 Hydraulic Conductivity.....	48
4.5 Collapse Potential.....	50
4.6 Field Compaction.....	53
4.6.1 Methods for Field Compaction Control.....	54
4.6.2 Field Testing Program and Results.....	56
4.7 Durability of CC.....	62
4.7.1 Expansion Caused by Alkali-Silica Reaction.....	62
4.7.2 Expansion Caused by Sulfate Attack.....	66
4.8 Summary.....	68
5. Evaluation of Pullout Resistance for CC and RAP.....	71
5.1 Introduction.....	71
5.2 Experimental Materials and Test Equipment.....	71
5.3 Quantification of Pullout Resistance.....	76
5.4 Results from Pullout Testing.....	78

5.5 Summary.....	86
6. Evaluation of Creep Potential of RAP.....	87
6.1 Introduction.....	87
6.2 Theoretical Background.....	87
6.3 Experimental Program.....	89
6.4 Creep Test Results.....	90
6.4.1 Creep Tests at $\sigma'_3 = 20$ psi.....	91
6.4.2 Creep Tests at $\sigma'_3 = 40$ psi.....	92
6.4.3 Creep Tests at $\bar{D} = 0.80$ .....	94
6.4.4 Creep Rupture.....	96
6.4.5 Discussion.....	98
6.5 Summary.....	98
7. Corrosion Experimental Program.....	99
7.1 Introduction.....	99
7.2 Research Objectives and Significance.....	99
7.3 Experimental Program.....	99
7.3.1 Material Characterization.....	99
7.3.2 Corrosion Testing.....	100
7.4 Materials Characterization.....	100
7.4.1 Backfill Materials.....	101
Pore Solution pH.....	103
Resistivity.....	103
Soluble Salts.....	103
7.4.2 MSE Reinforcement.....	104
Size.....	104
Chemical Composition.....	105
Galvanization Coating Weight.....	106
7.5 Corrosion Testing Methods.....	107
7.5.1 Short-term Corrosion Testing Program.....	107
Experimental Design.....	107
Experimental Setup.....	109
7.5.2 Long-term Corrosion Testing Program.....	113
Experimental Design.....	113
Experimental Setup.....	114
Preparation of the Backfill Forms.....	114
7.6 Summary.....	116
8. Results from Corrosion Testing.....	117
8.1 Introduction.....	117
8.2 Short-term Testing Results.....	117
8.2.1 Pore Solution.....	117
8.2.2 Mass Loss and Corrosion Rates.....	123
8.2.3 Electrochemical Test Results.....	127
8.2.4 Summary.....	129
8.3 Long-term Testing Results.....	130
8.3.1 Potential Readings.....	130
8.3.2 Backfill Material Characteristics.....	133

8.3.3 Mass Loss and Corrosion Rates.....	138
8.3.4 LTT Electrochemical Test Results.....	139
8.4 Comparison of Short-term and Longer-term Test Results.....	143
8.5 Summary.....	143
9. Corrosion Service Life Model .....	145
9.1 Introduction.....	145
9.2 Methodology and Assumptions .....	145
9.3 Service Life Prediction of MSE Walls in Environments with No Chlorides .....	145
9.4 Service Life Prediction of MSE Walls in Environments Containing Chloride Ions .....	151
9.5 Service Life Model Comparison.....	151
9.6 Comparison of Service Life Times of MSE Walls Backfilled with CFM, CC and RAP..	153
9.7 Summary.....	154
10. Conclusions and Recommendations .....	155
10.1 Introduction.....	155
10.2 Geotechnical Evaluation.....	155
10.2.1 Crushed Concrete (CC).....	155
10.2.2 Recycled Asphalt Pavement (RAP).....	156
10.3 Corrosion Evaluation .....	157
10.4 Specification Recommendations.....	158
References .....	159



## List of Figures

Figure 2.1	Sample of Crushed Concrete (CC) .....	4
Figure 2.2	Sample of Recycled Asphalt Pavement (RAP).....	7
Figure 2.3	Schematic view of a reinforced earth wall (after Schlosser and Delage 1988) .....	9
Figure 2.4	Stress transfer mechanisms mobilized on reinforcement (after Morris and Delphia 1999) .....	10
Figure 2.5	External stability mechanisms of failure (Elias and Christopher 1996) .....	11
Figure 2.6	Internal failure due to (a) tensile failure and (b) pullout failure .....	11
Figure 3.1	Grain Size Distribution of the CC Stockpile .....	22
Figure 3.2	Grain Size Distribution of the RAP Stockpile .....	23
Figure 3.3	Grain Size Distribution of the CFM Stockpile .....	24
Figure 3.4	Proposed reference gradation for testing program.....	25
Figure 3.5	Compaction curve for CC based on Tex-113-E test method .....	27
Figure 3.6	Compaction curve for RAP based on the Tex-113-E test method.....	27
Figure 3.7	Compaction curve for CFM based on the Tex-113-E test method .....	28
Figure 4.1	Triaxial cell and loading components .....	32
Figure 4.2	Large-scale (20 in x20 in) direct shear machine.....	33
Figure 4.3	Cross section of the large-scale direct shear machine .....	33
Figure 4.4	Grain size distribution of reference gradation and triaxial test specimens .....	35
Figure 4.5	Consolidated-drained triaxial test results for CC specimens .....	37
Figure 4.6	Consolidated-drained triaxial test results for RAP specimens.....	38
Figure 4.7	Consolidated-drained triaxial test results for CFM specimens .....	39
Figure 4.8	Results from large-scale direct shear tests on CC.....	42
Figure 4.9	Results from large-scale direct shear tests on CFM.....	43
Figure 4.10	Best-fit Coulomb envelopes for large-scale drained direct shear tests on CC and CFM specimens .....	44
Figure 4.11	Large-scale, load-controlled direct shear tests on RAP specimens .....	45
Figure 4.12	Final shear strength envelope for CC.....	47
Figure 4.13	Final shear strength envelope for CFM .....	47
Figure 4.14	Compression curves from collapse potential tests.....	51
Figure 4.15	Collapse indexes of test materials at different normal stresses.....	52
Figure 4.16	Nuclear gauge setup: (a) direct transmission method and (b) backscatter method (from Troxler 2001) .....	55
Figure 4.17	Comparison of moist densities measured by rubber balloon and nuclear gauge methods in all three material stockpiles.....	57
Figure 4.18	Comparison of moist densities measured by rubber balloon and test pit methods .....	59
Figure 4.19	Comparison of moist densities measured by test pit and nuclear gauge.....	60
Figure 4.20	Figure 4-20 Comparison of the moisture contents measured with the nuclear gauge and oven drying .....	61
Figure 4.21	Test Apparatus for Compacted CC Expansion Samples.....	63
Figure 4.22	Laboratory CC ASR Expansion Samples. Samples 1,2,3 in Water; samples 4,5,6 in 1N-NaOH Solution (Concrete had Previously Experienced ASR Attack).....	64

Figure 4.23	Laboratory CC ASR Expansion Samples. Samples 7, 8, 9 in Water; Samples 10, 11, 12 in 1N-NaOH Solution (Concrete had not Experienced ASR Attack).....	64
Figure 4.24	Commercial CC ASR Expansion. Samples placed in 1N-NaOH Solution. ....	65
Figure 4.25	Laboratory CC Sulfate Expansion Results. Samples 1,2,3 in Water; Samples 4,5,6 in 5% Sulfate Solution (Samples from concrete that had Previously Experience Sulfate Attack). ....	67
Figure 4.26	Commercial CC Sulfate Expansion Results. Samples placed in 5% Sulfate Solution. ....	68
Figure 5.1	Gradation of Ottawa Sand (OS).....	72
Figure 5.2	Metallic ribbed strip reinforcement with sheathed telltales.....	72
Figure 5.3	Schematic of ribbed metallic strip reinforcement.....	73
Figure 5.4	(a) Vertical cross-sectional view of pullout apparatus, (b) Plan view of pullout apparatus.....	74
Figure 5.5	Photographs of pullout apparatus.....	75
Figure 5.6	Reinforced earth design $\mu^*$ values for smooth and ribbed metallic strips (from Christopher et al. 1990) .....	78
Figure 5.7	Pullout of ribbed metallic strips in Ottawa Sand .....	79
Figure 5.8	Results from three pullout tests on ribbed metallic strip in CFM.....	81
Figure 5.9	Theoretical and measured friction factors for Conventional Fill Material .....	81
Figure 5.10	Results from three pullout tests on ribbed metallic strip in CC.....	83
Figure 5.11	Theoretical and measured friction factors for Crushed Concrete .....	84
Figure 5.12	Results from five pullout tests on ribbed metallic strip in RAP .....	85
Figure 5.13	Comparison of friction factors in Recycled Asphalt Pavement.....	86
Figure 6.1	Time-dependent creep deformation under a constant stress level. ....	88
Figure 6.2	Effect of m values on predicted creep strains (Mitchell 1993).....	89
Figure 6.3	Deviator stress level versus time for creep test specimens at $\sigma'_3 = 20$ psi .....	90
Figure 6.4	Axial strain vs. time for RAP specimens tested at $\sigma'_3 = 20$ psi.....	91
Figure 6.5	Axial strain rate vs. time for RAP specimens tested at $\sigma'_3 = 20$ psi.....	92
Figure 6.6	Axial strain vs. time for RAP specimens tested at $\sigma'_3 = 40$ psi.....	93
Figure 6.7	Axial strain rate vs. time for RAP specimens tested at $\sigma'_3 = 40$ psi.....	94
Figure 6.8	Figure 6-8 Axial strain vs. log(time) for tests performed at different $\sigma'_3$ .....	95
Figure 6.9	Axial strain rate vs. time for tests performed at different $\sigma'_3$ .....	96
Figure 6.10	Time to creep rupture at different shear stress levels ( $\sigma_d / \sigma_{df}$ ) for RAP and Haney clay (Vaid and Campanella 1977) .....	97
Figure 7.1	Side view of a galvanized earth reinforcing strip showing ribs.....	105
Figure 7.2	Micrograph of the galvanized coating on a galvanized-steel strip. ....	107
Figure 7.3	Typical steel sample following preparation for STT. ....	110
Figure 7.4	Corrosion cell system and components used for the STT.....	111
Figure 7.5	Drainage collection from the backfill materials for the STT.....	112
Figure 7.6	Purging of corrosion cells with oxygen during the STT.....	113
Figure 7.7	Perspective view of form for backfill materials used during LTT.....	115
Figure 7.8	Section View of LTT Sample for Performing Corrosion Testing. ....	115
Figure 8.1	Pore solution pH versus the number of drainages through the backfill materials.....	118
Figure 8.2	Pore solution resistivity for NCL drainages versus the number of drainages through the backfill materials. ....	119

Figure 8.3	Pore solution resistivity for CL drainages versus the number of drainages through the backfill materials. ....	119
Figure 8.4	Pore solution chloride concentration for CL drainages versus the number of drainages through the backfill materials. ....	120
Figure 8.5	Pore solution chloride concentration for NCL drainages versus the number of drainages through the backfill materials. ....	121
Figure 8.6	Pore solution sulfate concentration for CL drainages versus the number of drainages through the backfill materials. ....	122
Figure 8.7	Pore solution sulfate concentration for NCL drainages versus the number of drainages through the backfill materials. ....	122
Figure 8.8	Boxplots of corrosion rates calculated from mass loss data for all STT CL groups. ....	124
Figure 8.9	Boxplots of corrosion rates calculated from mass loss data for all STT NCL groups. ....	125
Figure 8.10	Boxplots of corrosion rates calculated from mass loss data for all STT G groups. ....	126
Figure 8.11	Boxplots of corrosion rates calculated from mass loss data for all STT S groups. ....	127
Figure 8.12	Box-plot of Stern-Geary coefficients derived from cyclic polarization testing plots for all the STT G samples. ....	128
Figure 8.13	Box-plot of Stern-Geary coefficients derived from cyclic polarization testing plots for all the STT S Samples. ....	128
Figure 8.14	Corrosion rates calculated from mass loss (ordinate) versus the $R_p$ corrosion rates for the CL LTT samples. ....	129
Figure 8.15	Distribution Plot of Average Cu-Cu <sub>2</sub> SO <sub>4</sub> Potential Readings for LTT G Samples. ....	130
Figure 8.16	Distribution plot of average potential readings for LTT S samples. ....	131
Figure 8.17	Average potential readings versus time plot of for LTT G samples. ....	132
Figure 8.18	Average Cu-Cu <sub>2</sub> SO <sub>4</sub> potential readings versus time plot of for LTT S samples. ....	133
Figure 8.19	Boxplots of LTT sample densities. ....	134
Figure 8.20	Boxplots of LTT pH values. ....	135
Figure 8.21	Boxplots of resistivity values from the LTT Samples. ....	136
Figure 8.22	Boxplots of chloride concentration for each LTT group. ....	137
Figure 8.23	Boxplots of sulfate concentrations for each LTT group. ....	137
Figure 8.24	Boxplot of corrosion rates calculated from mass loss data for all LTT samples. ....	139
Figure 8.25	Corrosion rates calculated from mass loss versus the estimated corrosion rate calculated from $R_p$ measurements for the LTT samples exposed to chloride solution. ....	140
Figure 8.26	Corrosion rates calculated from mass loss versus the corrosion rate determined from average $R_p$ measurements for the NCL LTT samples. ....	141
Figure 8.27	Box-plot of Stern-Geary constants derived from cyclic polarization testing plots for all the LTT G samples. ....	142
Figure 8.28	Box-plot of Stern-Geary coefficients derived from cyclic polarization testing plots for all the LTT S samples. ....	142

Figure 8.29	Comparison of corrosion rates from STT and LTT. ....	143
Figure 9.1	Estimated service life times for galvanized MSE strips embedded in CFM, CC, and RAP using average corrosion rates. ....	147
Figure 9.2	Texas locations where deicing/anti-icing chemicals are used (non-hatched area). ....	147
Figure 9.3	Estimated service life times for galvanized MSE strips embedded in CFM, CC, and RAP using the 90 <sup>th</sup> percentile of the corrosion rates. ....	148
Figure 9.4	Estimated service life times for galvanized MSE reinforcing strips embedded in CFM, CC, and RAP using the 70 <sup>th</sup> percentile of the corrosion rates. ....	148
Figure 9.5	Estimated service life times for plain-steel MSE reinforcing strips embedded in CFM, CC, and RAP using the average corrosion rates. ....	149
Figure 9.6	Estimated service life times for plain-steel MSE reinforcing strips embedded in CFM, CC, and RAP using the 70 <sup>th</sup> percentile of the corrosion rates. ....	150
Figure 9.7	Estimated service life times for plain-steel MSE reinforcing strips embedded in CFM, CC, and RAP using the 90 <sup>th</sup> percentile of the corrosion rates. ....	150
Figure 9.8	Estimated service life times for plain-steel MSE reinforcing strips embedded in CFM, CC, and RAP using the 90 <sup>th</sup> percentile of the corrosion rates. ....	152
Figure 9.9	Correlation between CalTrans 643 and mean results determined in this research. ....	153

## List of Tables

Table 2.1	TxDOT projects using CC as backfill material (after TxDOT 1999a).....	5
Table 2.2	TxDOT experience with RAP backfill (after TxDOT 1999b).....	8
Table 2.3	Select backfill gradation limits by TxDOT (2004) and FHWA (2004).....	16
Table 3.1	Specific Gravity of Test Materials.....	25
Table 4.1	Comparison of drained shear strength parameters of the tested materials.....	40
Table 4.2	Drained shear strength parameters of the test materials .....	48
Table 4.3	Summary of hydraulic conductivity results .....	49
Table 4.4	ASTM classification of collapse index .....	53
Table 4.5	Table 4-5 Ratio of moist densities measured by nuclear gauge ( $\gamma_{m,NG}$ ) and rubber balloon method ( $\gamma_{m,BAL}$ ).....	58
Table 4.6	Ratio of moisture contents measured by nuclear gauge ( $w_{NG}$ ) and oven drying ( $w_{oven}$ ).....	61
Table 5.1	Test conditions in different types of pullout boxes.....	79
Table 5.2	Pullout test results from medium-size box on metallic ribbed strips in CFM .....	80
Table 5.3	Pullout test results from medium-size box on ribbed metallic strips in CC .....	82
Table 5.4	Pullout test results from medium-size box on metallic ribbed strips in RAP.....	85
Table 7.1	Chemical Analysis of Plain-steel Earth Reinforcing Strip Specimen.....	105
Table 7.2	Chemical composition of the galvanized coating on reinforcing strips.....	106
Table 7.3	Sample identifications based on the controlled variables for STT. ....	108
Table 7.4	Testing program for decanted backfill material pore solutions. ....	109
Table 7.5	Testing program for the samples while in the corrosion cells. ....	109
Table 7.6	Sample identifications based on the controlled variables for LTT samples. ....	113
Table 9.1	Estimated service life (years) of MSE walls in the various backfill materials with plain-steel and galvanized strips exposed to solutions without chloride ions.....	151
Table 9.2	Estimated service life (years) of MSE walls in the various backfill materials with plain-steel and galvanized strips exposed to solutions containing chloride ions.....	151
Table 9.3	Table 9-3 Percent change in service life when compared with CFM in same backfill and exposure condition.....	154



# 1. Introduction

## 1.1 Background

Mechanically stabilized earth (MSE) walls have been used throughout the United States since the 1970s (Mitchell and Christopher 1990). The popularity of MSE systems is based on their low cost, aesthetic appeal, simple construction, and reliability (Mitchell and Christopher 1990). To ensure long-term integrity of MSE walls, conventional backfills consisting predominantly of granular soils have been recommended and used. This limitation on material type can significantly increase the cost of construction on some projects because of the cost of transporting select material to the construction site when local select fill is not available.

The Texas Department of Transportation (TxDOT) is a leader in the construction of MSE walls. However, many areas of Texas do not have backfill materials that meet the current TxDOT material specifications for MSE walls. In these cases, contractors must transport select backfill material from other parts of the state. These transportation costs can be significant and may make the construction of MSE walls impractical. At the same time, contractors often must dispose of crushed concrete and asphalt from demolished pavements. Again, contractors must pay transportation costs, as well as disposal fees, to discard these materials. One solution is to recycle these materials, often called recycled asphalt pavement (RAP) and crushed concrete (CC), and use them as alternative backfill. Throughout the U.S., substantial amounts of RAP and CC are being produced, and it is estimated that more than 73 million tons of RAP and 95 million tons of CC are being processed each year (Kelly 1998). If RAP and CC were used as backfill for MSE walls, transportation and disposal costs for these materials could be greatly reduced, translating into significant savings for TxDOT and other state departments of transportation.

Before RAP and CC can be used as backfill in MSE walls, the suitability of these materials must be evaluated. This evaluation encompasses traditional geotechnical tests, reinforcement pullout tests, creep tests, and corrosion/durability tests. This report presents the results from a laboratory investigation that characterized RAP and CC backfills, including the geotechnical and corrosion performance of these materials.

This report consists of four major sections: Section 1 consists of three chapters (including this Introduction) addressing background information and selection of the test materials; Section 2 (Chapters 4 through 6) focuses on the geotechnical evaluation of RAP and CC; Section 3 (Chapters 7 through 9) includes the results from the corrosion evaluation of RAP and CC; and Section 4 (Chapter 10) presents the findings and recommendations from this research.



## **2. Potential Use of Crushed Concrete and Recycled Asphalt Pavement for MSE Walls**

### **2.1 Introduction**

This chapter introduces crushed concrete (CC) and recycled asphalt pavement (RAP) materials, and discusses previous field applications reported in the literature. A general background on MSE walls and a broad overview of the current MSE wall design criteria are presented. Critical backfill properties and current MSE wall backfill material specifications from TxDOT and FHWA are reviewed, and the potential issues related to corrosivity are discussed.

### **2.2 Previous Uses of Crushed Concrete and Recycled Asphalt Pavement**

#### **2.2.1 Crushed Concrete**

Crushed Concrete (CC) is generated through the demolition of portland cement concrete elements from roads, airport runways, and concrete structures. CC is generally removed by a backhoe or payloader and loaded into dump trucks for removal from the original site. In cases where CC is secured from demolished pavements, soil and small quantities of bituminous concrete are expected in the excavated materials. Usually, the reclaimed concrete materials are hauled to a central processing plant where crushing, screening, and ferrous metal recovery are performed before stockpiling. However, on-site recycling and processing can alternatively be performed with a mobile plant.

At the central processing plant, reclaimed CC is subjected to primary and secondary crushers. The primary crusher breaks the reinforcing elements from the concrete debris and breaks down the rubble to particle sizes of about 3 to 4 in. Removal of reinforcing steel by an electromagnetic separator occurs while conveying the materials to the secondary crusher. The secondary crusher further breaks down the particle sizes to the desired gradation. Stockpiling of crushed concrete is usually done through the separation of coarse and fine particles to avoid inadvertent commingling of materials. Figure 2-1 shows a bulk sample of CC that was produced by a commercial producer in Dallas, Texas.

CC has been used successfully in highway construction since the 1940s (Halm 1980). Laboratory research on recycled concrete was first carried out in Europe and the USSR shortly after World War II (Halm 1980), because the considerable amount of CC produced by bombing and shelling during the war was used in rebuilding urban areas. In the U.S., the majority of CC is generated through the demolition of portland cement concrete elements in roads and buildings, with an estimate of 150 million tons of annual CC production in the year 2000. The primary application of CC in the U.S. is as an aggregate substitute in pavement construction. This practice has become so common that CC aggregate is considered by many agencies as conventional aggregate. Using CC as a backfill material has apparently gained only minor interest compared to other applications. However, it is reportedly one of the first waste materials considered for backfill applications (FHWA 2000).



*Figure 2.1 Sample of Crushed Concrete (CC)*

There have been several studies on CC to evaluate its performance for different engineering applications. Significant attention has focused on the suitability of CC as an aggregate substitute for structural concrete in buildings or paving structures. As a result, the laboratory investigations in most of the previous research have concentrated primarily on the material characteristics of CC for such applications. This previous research has indicated that concrete made with CC aggregate has comparable performance to concrete made with virgin aggregate (e.g., Cuttell et al. 1997).

FHWA (2000) indicates that CC is more angular in shape, has a lower specific gravity, and has higher water absorption than comparatively sized virgin aggregate. The specific gravity of CC ranges from 2.0 to 2.5, while the water absorption varies from 2 percent to 8 percent, depending on the size of the CC particles. The low value of specific gravity is attributed to the presence of mortar from the original concrete structure. Fine CC particles have a lower specific gravity than coarse CC particles because more mortar is found in the finer fraction of the material.

Other research has focused on the shear strength of CC for geotechnical purposes. O'Mahony and Milligan (1991) reported peak friction angles of between 40 and 50 degrees for CC, measured from direct shear tests. Tests were performed at normal stresses between 40 and 200 kPa (5.9 to 29.4 psi), and a slight reduction in friction angle was observed with increasing normal stress.

The pH of a CC-water mixture often exceeds 11. The high alkalinity of CC can cause corrosion of aluminum or galvanized steel that are in direct contact with CC and in the presence of moisture (FHWA 2000). Moreover, CC may be contaminated with chloride ions, because of the application of deicing salts, or with sulfates, because of immediate contact with sulfate-rich soils. The presence of sulfate is also linked to CC obtained from buildings, which is likely to contain calcium sulfates from plaster or gypsum wallboard (Buck 1973). Chloride ions are associated with the corrosion of steel, while sulfate reactions lead to expansive disintegration of cement paste (FHWA 2000).

TxDOT has had some previous experience with CC. The first TxDOT project that used CC as aggregate in new pavement was in the Houston district (TxDOT 1999a). There was no virgin aggregate used in this project, meaning that both coarse and fine aggregates were from recycled concrete, and the performance evaluation on this pavement was reported as good. TxDOT has reported three projects that used CC as backfill material. Table 2-1 summarizes the key findings from these projects reported to TxDOT. It should be noted that the results of these projects were reported as good and excellent.

*Table 2.1 TxDOT projects using CC as backfill material (after TxDOT 1999a)*

<b>TxDOT District</b>	<b>Location</b>	<b>Results</b>	<b>Year</b>	<b>Specification</b>	<b>Comments</b>
Corpus Christi	Various	Excellent	1977	TxDOT Material Spec. No.132	Used for embankment and erosion protection
Lufkin	District wide	Excellent	1982	—	—
Beaumont	SH 82, SH 87	Good	1994	None	Used for embankment to control erosion

A major concern when using CC as a backfill material in MSE walls is the potential corrosion of metallic reinforcements. This concern is drawn from the hypothesis that the high pH of a CC-water mixture will increase the rate of steel corrosion. Popova et al. (1998) studied the corrosive behavior of crushed concrete for potential use as a backfill material in MSE walls. For a galvanized steel rod embedded in fill material, the rates of corrosion at the beginning of the test were the same for both CC and typical granular soil fill (approximately 0.8 mils/year). However, the rate of corrosion increased with time for the CC material (~ 3 mils/year at 400 days), while it decreased for the case of granular soil fill (0.2 mils/year at 400 days).

An unresolved issue for a CC backfill is the potential precipitation of tufa (calcium carbonate, CaCO<sub>3</sub>) contained in the CC leachate. This problem first surfaced when significant CC fines were observed to clog filter fabric-wrapped subsurface drains in CC pavement sub-bases (Barksdale et al. 1992; Mack et al. 1993). A suggested series of chemical reactions between portlandite [Ca(OH)<sub>2</sub>] in CC and other chemical reactants that lead to tufa formation is shown below.

Carbon dioxide (CO<sub>2</sub>) from the atmosphere and automobile exhaust reacts with rainwater, forming carbonic acid (H<sub>2</sub>CO<sub>3</sub>)



Carbonic acid (H<sub>2</sub>CO<sub>3</sub>) reacts with portlandite [calcium hydroxide, Ca(OH)<sub>2</sub>] in CC forming calcium bicarbonate [Ca(HCO<sub>3</sub>)<sub>2</sub>].



At the drainage outlet, water from this enriched solution of calcium bicarbonate [Ca(HCO<sub>3</sub>)<sub>2</sub>] evaporates in warm temperatures, and carbon dioxide (CO<sub>2</sub>) escapes into the atmosphere. This condition leads to the precipitation of calcium carbonate (CaCO<sub>3</sub>) and the formation of tufa.



Warmer temperatures in the summer months increase the rate of deposition of tufa, whereas cold temperatures in the winter months cause the carbon dioxide to remain in solution. The preceding chemical reactions clearly indicate that the concentration of water, carbon dioxide, temperature, and humidity are the major contributing factors that control tufa precipitation.

To control the tufa precipitation, washing of CC aggregates is required by some agencies to remove the dust that typically contains free lime and portlandite. This processing step is a safety measure to reduce tufa formation potential. FHWA recommends using suitable CC that does not contain significant quantities of unhydrated cement or free lime for embankment or fill applications. Also, leachate testing may be required to obtain the tufa precipitation potential of CC for embankment and MSE wall applications.

### **2.2.2 Recycled Asphalt Pavement**

Recycled Asphalt Pavement (RAP) is derived from demolished asphalt pavement, and thus its inherent properties are a function of parent hot-mix asphalt. Hot-mix asphalt is a blend of aggregate and asphalt cement binder, with the asphalt cement derived from the distillation of crude oil. The properties (e.g., viscosity, ductility) of the asphalt cement are a function of the type of virgin crude oil and the distillation process (Roberts et al. 1996). AASHTO MP1a-04 provides standard specifications for asphalt cement binders that are based on achieving specific properties at specific temperatures. Thus, the selected asphalt cement performance grade is typically determined by the range of temperatures expected in a region (Roberts et al. 1996). After selection of the asphalt binder, asphalt mix design involves selection of the aggregate, asphalt content, and required in situ density. Typical mix proportions generally range from 3 percent to 7 percent asphalt cement and 97 percent to 93 percent aggregate (Roberts et al. 1996).

RAP is generated by milling or full-depth removal of asphalt pavement. Milling involves removal of the pavement surface using a milling machine, which can remove up to 2 in. of pavement in a single pass. Full-depth removal is usually achieved with a pneumatic pavement breaker or a rhino horn on a bulldozer. The broken materials are transferred to a central facility for a series of recycling processes including crushing, screening, conveying, and stacking.

Asphalt pavement can also be pulverized in place and incorporated into granular or stabilized base courses using a self-propelled pulverizing machine (FHWA 2000). In-place recycling eliminates the cost of transporting material to and from the processing facility. Figure 2.2 illustrates a bulk sample of RAP that was taken from a TxDOT stockpile in Corpus Christi, Texas.

It should be noted that the creep properties of RAP, as well as its other properties, will be influenced by the properties of the parent hot mix asphalt. Most importantly, the asphalt content and asphalt cement performance grade will affect the creep response of RAP, with ageing and aggregate type also having an impact.

Over the past several years, there has been increased use of RAP and CC in highway construction throughout the U.S. However, utilizing RAP and CC as a backfill material has probably gained the least interest compared to other highway applications. RAP and CC are most frequently used as an aggregate substitute for pavement construction and good performance has been reported (TxDOT 1999a, b).



*Figure 2.2 Sample of Recycled Asphalt Pavement (RAP)*

The recycling of asphalt pavements is not a new concept and can be dated back as far as 1915 (FHWA 2004). In the U.S., a large increase in the price of asphalt brought about through the oil crisis of the mid-1970s made the recycling of asphalt pavements an attractive option for reducing highway construction costs (Ahmad 1991; 1992). It is estimated that as much as 36 million tons per year, or 80 percent of the annual excess asphalt, is being used either as a portion of recycled hot mix asphalt, in cold mixes, or as aggregate in granular or stabilized base materials (FHWA 2004). Estakhri and Button (1992) indicated that TxDOT has successfully used untreated RAP in many highway applications. These applications include paving driveway and country road approaches, paving mailbox and litter barrel turnouts, and repairing pavement edges.

TxDOT (1999b) reported that more than 90 percent of RAP construction projects in Texas used RAP for paving purposes. The other 10 percent used RAP as the backfill material for embankment construction. More details on these embankment projects are shown in Table 2-2. The long-term performance of these embankments has been satisfactory, with no collapse or noticeable distress observed.

FHWA (2000) indicates that at least five states (i.e., Connecticut, California, Illinois, Louisiana, and Tennessee) have used RAP directly as a backfill material, while some other states have used RAP as an additive in embankment construction. The performance of RAP in these applications was generally considered satisfactory to good (FHWA 2000). When used as an embankment or fill material, the undersized portion of RAP (smaller than 2 in.) was sometimes blended with soil and/or finely graded aggregates. RAP with larger particles was usually used as an embankment base. The required construction procedures for a RAP embankment (i.e., including material storage, field compaction, quality control, design considerations) are generally the same as the procedures used for conventional embankments. However, FHWA (2000) provides a few specific recommendations regarding construction procedures for RAP embankments as follows:

1. Random sampling and testing of the RAP stockpile must be performed because different sources of RAP can have different properties.
2. Additional attention must take place during compaction to ensure that no poorly compacted zones are created in the fill, leading to long-term differential settlement.
3. Some jurisdictions may require a minimum separation distance between water sources and fill materials containing RAP to avoid submersion of RAP in water, because water leaching from RAP may be a potential environmental concern.

*Table 2.2 TxDOT experience with RAP backfill (after TxDOT 1999b)*

<b>TxDOT District</b>	<b>Location</b>	<b>Result</b>	<b>Year</b>	<b>TxDOT Specification</b>	<b>Comments</b>
Beaumont	Liberty	Good	1987	N/A	
Beaumont	Jasper	Excellent	1987	N/A	
El Paso	El Paso	Unknown	1993	TxDOT Material Spec. No.132	Used as a stabilizer for shoulder surface
Austin	Travis County	Unknown	1995	N/A	
Bryan	SH-21 at Brazos River	Excellent	1996	TxDOT Material Spec. No.132	Mixed soils with sized RAP

## 2.3 Mechanically Stabilized Earth Walls

An MSE wall is defined as a vertical or near vertical earth retaining structure consisting of three major components: a facing panel, earth reinforcement, and reinforced select backfill (Figure 2-3). Such walls are similar to a reinforced earth system, but with the addition of facing components for aesthetic purposes. MSE walls function through interaction between the soil and earth reinforcement. After the vertical stress is introduced to the backfill (e.g., soil self weight), an inherent horizontal pressure is mobilized, resulting from the stress transfer between soil particles. The soil itself does not have the tensile strength to resist such lateral pressure, but embedded reinforcement can provide efficient soil stabilization.

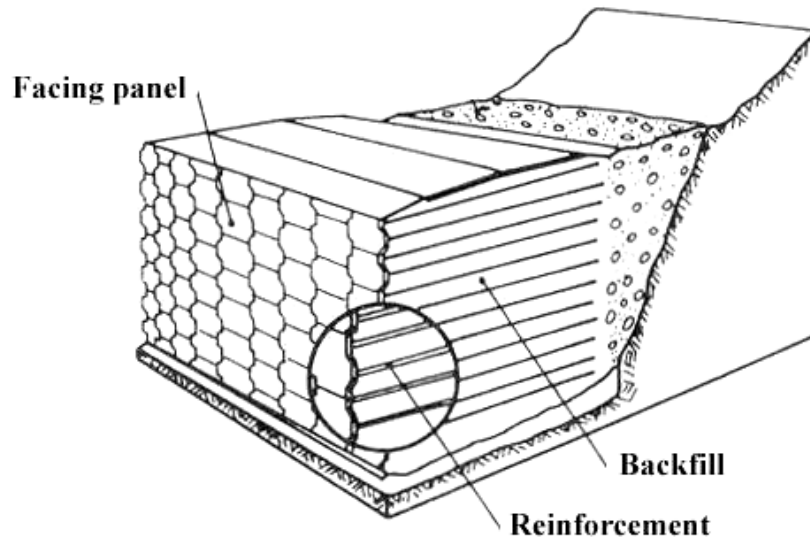


*Figure 2.3 Schematic view of a reinforced earth wall (after Schlosser and Delage 1988)*

The primary function of the reinforcement is to resist the lateral pressure in the soil, and thus improve the mechanical properties of the backfill. Currently, reinforcement is classified as either metallic (typically mild steel) or nonmetallic (generally polymer). Also, reinforcements can be categorized based on their extensibility. Inextensible reinforcement displays deformation at failure much less than the deformability of the soil, whereas extensible reinforcement displays comparable deformation at failure to soil.

There are two types of stress transfer mechanisms between the reinforcement and soil. First, frictional resistance develops where there is a relative shear displacement and corresponding shear stress between the soil and reinforcement surface (Elias and Christopher 1996). Second, passive resistance develops through bearing-type stresses on transverse reinforcement surfaces normal to the direction of relative movement (Elias and Christopher 1996). Figure 2-4 illustrates both stress transfer mechanisms. One of the most commonly used reinforcements in Texas is galvanized ribbed steel strip, which has a combination of the two stress transfer mechanisms.

The cost of the select backfill material dominates the total cost of MSE wall construction. Elias and Christopher (1996) indicate that utilizing locally available soil can significantly reduce the total cost of construction by 20 to 60 percent compared to conventional walls. The major function of the select backfill is to provide the weight, compression resistance, and shearing

strength to ensure the stability of the retaining wall (Morris and Delphia 1999). In terms of physical properties, the select backfill should be well-graded, free draining, and have high frictional strength. Cohesive backfills are typically undesirable because of their low strength, creep potential, and poor drainage characteristics.

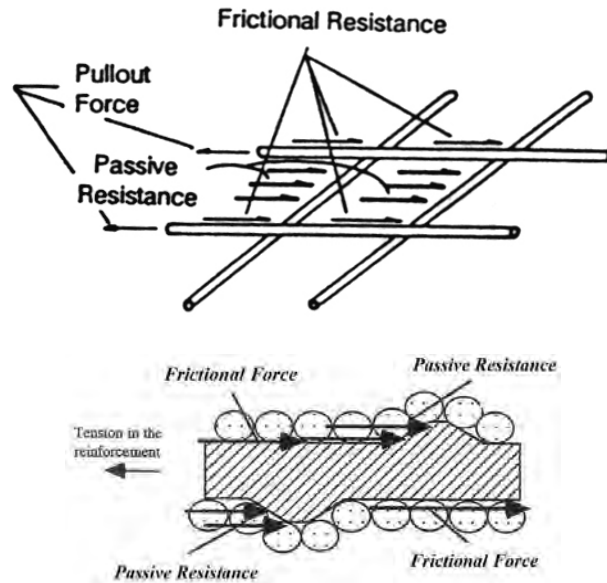


Figure 2.4 Stress transfer mechanisms mobilized on reinforcement (after Morris and Delphia 1999)

### 2.3.2 MSE Wall Design

This section briefly presents the MSE wall design methodology based on FHWA (1996) construction guidelines. The guidelines are for walls with near-vertical faces and identical reinforcement length. The current design procedures consist of determining the geometric and reinforcement requirements to prevent internal and external failure using limit equilibrium methods of analysis.

The external stability of an MSE wall involves the geometry of the entire wall system and failures that occur outside of the reinforced zone. There are four potential failure mechanisms associated with external stability: (1) sliding, (2) overturning, (3) bearing capacity, and (4) deep-seated stability, as shown in Figure 2-5. After the preliminary dimensions of the entire wall system are chosen, external stability checks are performed using standard procedures. The external stability of each failure mode is represented in terms of a factor of safety (FS).

Evaluation of internal stability involves the interaction between the reinforcing elements and the select backfill. The mechanism of stress transfer depends on the type of reinforcement system, extensible or inextensible. Two internal failure modes are taken into account in design: tensile failure and pullout failure (Figure 2-6). Required information for an internal stability check include: (1) determination of the maximum developed tensile forces and their locations along a critical slip surface, and (2) evaluation of the tensile resistance and pullout capacity of the reinforcement.

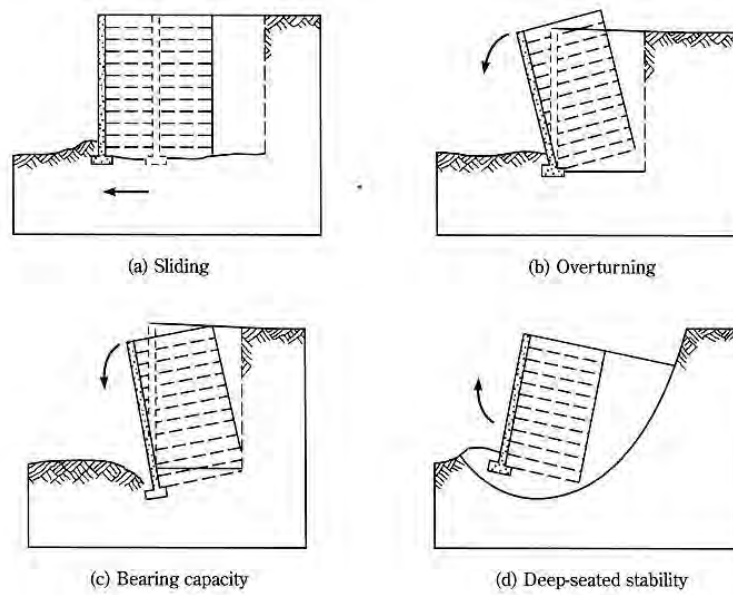


Figure 2.5 External stability mechanisms of failure (Elias and Christopher 1996)

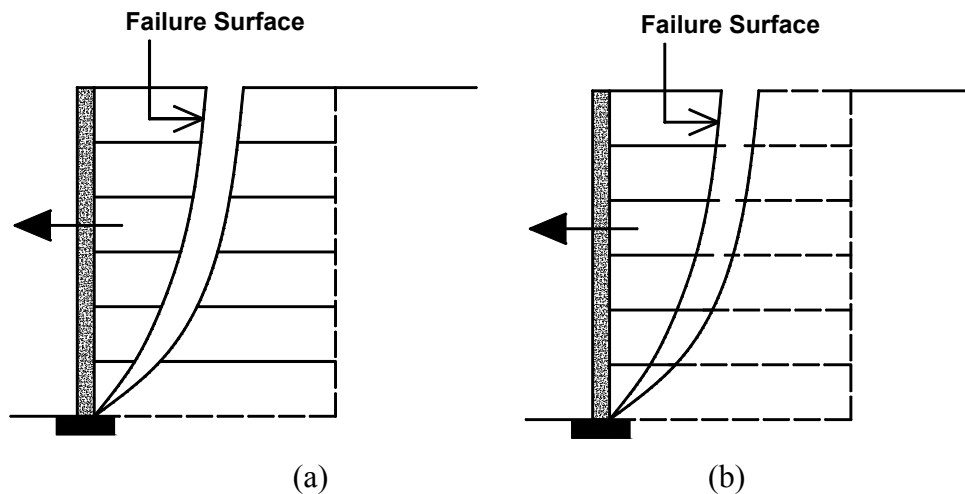


Figure 2.6 Internal failure due to (a) tensile failure and (b) pullout failure

Tension failure occurs when the tensile force in the reinforcement becomes so large that the reinforcement elongates excessively or ruptures (Elias and Christopher 1996). The analytical check for tensile failure involves determining the maximum developed tensile force ( $T_{max}$ ) and comparing it with the allowable tension ( $T_a$ ) in the reinforcement. The allowable tension ( $T_a$ ) is generally provided from either the manufacturer's specification or from laboratory testing. The maximum developed tensile force in each layer is obtained by multiplying the lateral earth pressure coefficient, which is a modified value of the active earth pressure coefficient ( $K_a$ ), by the vertical stress at that depth and the contributing area for each reinforcing element. After the

value of  $T_{max}$  is calculated, a factor of safety against tensile failure is determined by comparing it with  $T_a$ . In general, stronger backfill materials exhibit smaller active earth pressures and induce smaller values of  $T_{max}$ .

Pullout stability evaluation involves calculating the length of reinforcement in the resisting zone beyond the potential internal failure surface required to resist the maximum tensile force in the reinforcement ( $T_{max}$ ). A factor of safety of 1.5 is typically used for pullout assessment. Earlier practice assumed that the pullout resistance is developed behind the Coulomb failure plane. However, field measurements and theoretical analyses have shown that the potential failure surface is coincident with the locations of the maximum tensile forces ( $T_{max}$ ) in the reinforcements (Anderson et. al. 1995). The locations of the maximum tensile forces depend on the extensibility of the reinforcement. And again, a backfill material with high shear strength tends to produce a stronger interactive bond with the embedded reinforcement, resulting in a higher pullout capacity and shorter required reinforcement.

### 2.3.3 Critical Backfill Properties

The backfill is a key element in achieving satisfactory performance of MSE walls. An ideal select backfill material should exhibit high drained shear strength parameters ( $c'$  and  $\phi'$ ) and have good drainage properties. To avoid excessive surface deformations, the select backfill should also exhibit low compressibility over time. Using high quality backfill leads to shorter required reinforcement lengths, which logically lowers the total cost of an MSE wall. Free-draining backfill prevents water from accumulating behind the wall. Water accumulation increases the lateral pressure on the facing system and may cause excessive deformation leading to total wall failure. These properties are major factors when selecting a backfill material. Critical engineering characteristics of a candidate backfill material are discussed below.

*Shear strength* – The select backfill material should exhibit high shear strength to ensure stability within the backfill and to achieve an adequate interaction with the reinforcement (Morris and Delphia 1999). The forces developed in MSE wall reinforcement are related to the horizontal earth pressures acting on the wall at different depths. This horizontal earth pressure is calculated using the shear strength parameters of the backfill. For a general case, when a free-draining material is used, effective shear strength parameters ( $c'$  and  $\phi'$ ) are used to calculate the wall stability.

*Pullout Resistance* – The pullout resistance between the select backfill and reinforcement is needed for the design of the reinforcement length. This parameter is generally acquired from pullout capacity tests or through models that relate the characteristics of the backfill and reinforcement to the pullout capacity. Well-graded materials with high angularity tend to provide larger values of pullout resistance. Also, the moisture content and fines content of the backfill affect the pullout resistance of the reinforcement.

*Compaction Characteristics* – During construction, the select backfill must be well compacted to ensure adequate shear strength, adequate pullout capacity, and minimal compression during and after MSE wall construction. Compaction is typically characterized by the maximum dry unit weight. For a given compaction energy, the maximum dry unit weight is affected by the particle shape, grain size distribution, and water content during compaction. Materials with low

angularity and a wide range of grain sizes (well-graded) tend to exhibit larger values of maximum dry unit weight. Backfill materials compacted at low water contents have internal capillary stresses that resist the compaction of the material, resulting in smaller dry unit weights (Morris and Delphia 1999). Particle breakdown during compaction is another key factor to backfill drainage properties. The additional fines from this breakdown mechanism may reduce the hydraulic conductivity and change the shear strength properties of the backfill.

*Compressibility of compacted material* – Poor compaction or the presence of excessive fines in the select backfill may result in long-term total and differential settlement. These settlements can create problems with the performance of overlying pavements on top of the backfill and may also cause significant damage to the reinforcement and the facing system. When such settlements occur, the reinforcements are forced downward, creating an undesirable vertical stress and deformation on the facing system.

When granular backfill is compacted at a low dry unit weight and water content, it may undergo significant settlement upon wetting. This deformation mechanism is called collapse. A collapsible soil may withstand relatively large applied vertical stress with small settlement while at a low water content but exhibit considerable settlement after wetting, with no additional increase in vertical stress. For typical MSE wall construction, additional water causing undesired wetting to the compacted backfill can come from heavy rainfall or ineffective drainage. Potential problems associated with collapse settlement of an MSE wall backfill may include damage to structures or pavements constructed on the backfill, cracking and slope failure within the backfill itself, as well as excessive distress to the underground utilities. Also, this collapse settlement of the MSE wall backfill can damage the horizontally-aligned reinforcement and break or lose its resisting hinge connector at the back of the facing panel.

*Hydraulic conductivity* – Backfill materials for all types of retaining walls must be free draining so that water pressures do not build up behind the wall. Specifications typically limit the percentage of fines in the backfill to achieve adequate hydraulic conductivity. For MSE walls, backfill materials that are not free draining also increase the corrosion potential for the metallic reinforcements. Therefore, backfill materials with high water absorption potential, such as clay or silt, are generally not considered acceptable for MSE walls.

*Time-dependent (creep) effects* – For MSE walls, creep deformations will interfere with the development of forces in the reinforcement and may potentially lead to wall failure through excessive deformation or full collapse. Creep behavior is temperature dependent and is typically enhanced at higher temperatures. For long-term stability purposes, a backfill material should not be susceptible to creep. For a given material, a creep testing program can be used to define the relationship between the material creep strength and such factors as time to failure, steady-state or minimum creep rate, strain at failure, and temperature. These relationships assist engineers in selecting the appropriate material properties to use in design for a given loading condition.

*Corrosivity* – Corrosion is a major concern for MSE walls incorporating metallic reinforcement. Accelerated or unanticipated corrosion of the reinforcements could cause sudden and catastrophic failure of MSE structures, generally along the locations of the maximum tensile stresses in the reinforcements (Elias and Christopher 1996, see Figure 2-6). A backfill material

should not contain highly deleterious materials that would attack the reinforcement or cause some distresses to the material itself. Typically, resistivity and pH are used as indicators to reflect the corrosion potential of a backfill material. However, many other parameters have been identified as affecting corrosion.

Resistivity indicates how a material allows an electrical current to pass through and how effective it is as an electrolyte. A low resistivity value is indicative of high potential for corrosion because it promotes more electrical activity in the medium. Furthermore, highly acidic (low pH) or highly alkaline (high pH) materials have been reported to be corrosive because of the presence of ions in the pore water, which are believed to cause a voltage difference between metal surfaces and induce current. Resistivity is also influenced by the presence of soluble salts in the material. High concentrations of soluble salts affect the electrochemical reaction at metal surfaces and decrease the resistivity of the material. The type of ion is also important to the corrosion process. Two major chemical ions that have been identified with high corrosivity potential are chlorides and sulfates, and specifications have limited the presence of these two chemicals in backfill.

The appropriateness of CC and RAP for MSE wall applications depends on the corrosion activity of the reinforcement in these materials and the impact on the service-life and life-cycle cost. Service-life prediction methods specifically for MSE walls are just being developed, and the particular influence of using recycled materials as backfill instead of conventional fill materials has not been thoroughly investigated. A determination of the effect of CC and RAP on the corrosion activity of the MSE reinforcement and the service life of MSE walls will enable state highway agencies to make better decisions as to the appropriateness of using these materials instead of conventional materials for these walls.

There are several current challenges with using recycled materials as backfill for MSE walls. Defining the overall cost advantages of MSE walls backfilled with recycled materials is a difficult challenge. Using readily available materials (i.e., these recycled materials) for backfill can substantially reduce the transportation and materials costs. However, if these materials have a negative impact on the corrosion of the MSE wall reinforcement, the service life can be significantly reduced, making it uneconomical to use these materials.

As noted, models to predict the service life of MSE walls are limited because of the limited amount of historical data available on these systems. Frondistou (1985) reported that MSE walls have been in the United States for only 29 years. It is important that the service life of an MSE wall be predicted based on the type of backfill material, reinforcing strip type, environment, and other conditions. The challenge in predicting the service life of MSE walls is complicated further when recycled backfill materials are used. This is the case because these materials are more difficult to classify than conventional aggregates, making their properties more difficult to estimate. In addition, CC and RAP are made of an agglomeration of several different materials. At times, more than one type of aggregate is used in concrete and asphalt mixtures. The challenge of estimating service life is also difficult because there is a limited amount of infrastructure built using recycled materials and studies on the performance of systems containing these materials are limited. Specifically, using recycled materials can improve the

economy of these systems, assuming similar long-term performance can be obtained. The influence of using recycled materials on the corrosivity and service life needs to be investigated.

## **2.4 MSE Wall Backfill Specifications**

This section presents current specifications for all key geotechnical properties of select backfill materials as required in TxDOT (2004) and FHWA (2004) design guidelines. All of the specifications presented were developed for traditional select backfill materials. This section also includes other possible concerns regarding the use of RAP or CC as select backfill in MSE walls.

### **2.4.1 Gradation**

An important geotechnical aspect commonly used to classify different backfill materials is particle gradation. Gradation is an important factor that affects backfill performance, including stability, drainage, and frost susceptibility. Because specifications for recycled materials have not yet been standardized, the gradation requirement for traditional select backfill proposed by TxDOT and FHWA can be used as an initial guideline. The select backfill should be free from organic and deleterious materials, with the material gradation determined through a traditional sieve test. TxDOT and FHWA have relatively similar requirements on select backfill gradation, the major difference being the allowable maximum particle size.

TxDOT has categorized select backfill materials into four types (from Type A to D) based on the material gradation (Table 2-3). Each TxDOT select backfill type is designated for a different wall type, unless the plans show otherwise. Although Type A has the most stringent gradation requirement, it is a fairly new requirement and, thus, rarely specified. FHWA has only one backfill specification with a maximum particle size of 4 in. In cases where nonmetallic or epoxy-coated metallic reinforcement are used, both FHWA and TxDOT limit the maximum particle size of the backfill to 0.75 in. to ensure minimal abrasion to the reinforcement.

### **2.4.2 Compaction**

It is important to evaluate the compaction characteristics of RAP and CC because these recycled materials may not yield similar moisture-dry density curves with those achieved for traditional backfills. Also, crushing of the grains during compaction is a concern. A sieve analysis before and after compaction is required to evaluate the possible increase in fines content because of compaction. The following sections describe the compaction tests currently designated by FHWA and TxDOT.

The TxDOT specifications express the required compaction of select backfill materials for retaining structures in terms of percent of maximum dry density determined in accordance with the Tex-114-E compaction method. Tex-114-E is similar to the standard Proctor compaction test in terms of compaction energy (12,600 ft-lb/ft<sup>3</sup>), although the dimensions of the mold are different. The TxDOT specifications require that the backfill be compacted at 95 percent of maximum dry density determined from Tex-114-E for the top 3 ft. of the backfill, while 90 percent relative density is required for the underlying layers. The Tex-114-E test method limits the maximum particle size to  $\frac{7}{8}$  in., which is significantly smaller than the maximum particle size allowed in the backfill and significantly smaller than the maximum particle size typically found in RAP and CC material. As a result, Tex-114-E recommends that test method Tex-113-E

be used for materials containing particles larger than  $\frac{7}{8}$  in. The Tex-113-E specification uses a larger mold, and a larger hammer and drop height, resulting in a larger compaction energy (22,900 ft-lb/ft<sup>3</sup>).

Table 2.3 Select backfill gradation limits by TxDOT (2004) and FHWA (2004)

Classification		Sieve Size	% Passing	Recommended for
TxDOT (2004) Item 423	Type A	3 in.	100	permanent walls
		$\frac{1}{2}$ in.	0 – 50	
		No. 40	0 – 15	
	Type B	3 in.	100	permanent walls (default)
		No. 40	0 – 60	
		No. 200	0 – 15	
	Type C	3 in.	100	temporary walls
		No. 200	0 – 30	
	Type D	3 in.	100	walls in inundation areas
		$\frac{3}{8}$ in.	0 – 15	
FHWA (2004)		4 in.	100	—
		No. 40	0 – 60	
		No. 200	0 – 15	

Morris and Delphia (1999) recently studied the backfill specifications for MSE walls. They recommend using a vibrating hammer in reference to British Standard 1377 (1990) as a standard laboratory compaction test because test method Tex-113-E tends to give low values of maximum dry density, especially for coarse materials. However, to achieve a larger dry density, the subsection on “Materials Difficult to Compact” in Tex-113-E proposes a higher compaction effort with 100 blows per layer, which results in a compaction energy of 91,700 ft-lb/ft<sup>3</sup>. In a recent study at The University of Texas at Austin (Marx 2001), it was indicated that this modification to the Tex-113-E method produced the largest dry density among all compaction tests.

For field compaction, FHWA (2004) indicates that compaction of RAP and CC can be accomplished with similar methods and equipment as used with conventional backfill materials. It is reported that granular materials containing RAP appear to compact better if incorporated with minimal water (Senior et al. 1994), while compaction of CC usually requires additional

water to facilitate particle arrangement. Also, because of the high angularity of CC materials, equipment with higher compaction energy is required to achieve the specified level of relative compaction. Finally, when compacting gravel-sized particles (such as RAP and CC), caution is needed to ensure that no large voids are formed within the fill that could contribute to future long-term differential settlement.

### **2.4.3 Hydraulic Conductivity**

Select backfill materials must be free draining to ensure that pore water pressures do not develop behind the retaining structure. Also, the rate of corrosion of metallic reinforcement is primarily dependent on the moisture content in the backfill. Fine-grained particles present in the backfill impede the drainage of water behind the retaining structure, resulting in large forces on the wall and a higher rate of reinforcement corrosion. Therefore, fine-grained materials are not typically used as select backfill materials, and the ideal select backfill for an MSE wall is a granular material with little or no plastic fines.

In general, the hydraulic conductivity of an MSE wall select backfill is not explicitly measured because the specification on material gradation generally results in a large hydraulic conductivity. FHWA and TxDOT permit up to 15 percent fines (passing through sieve No. 200) in select backfill, assuming that these limits on gradation will result in a free-draining material. However, it is still unknown how water will interact with RAP and CC backfill. Additionally, crushing of coarse-sized particles may occur during compaction of these recycled aggregates, which can potentially lead to a substantial decrease in hydraulic conductivity owing to an increase in fines.

CC is expected to have higher water absorption than conventional select fill because of the presence of mortar and debris. Moreover, unhydrated cement in CC may react with seepage water to cause a significant reduction in the hydraulic conductivity of the backfill. Therefore, the hydraulic conductivity may vary with time after compaction is completed. TxDOT specifies the constant head test in accordance with ASTM D2434 to measure the hydraulic conductivity of granular materials.

### **2.4.4 Shear Strength**

The shear strength parameters of the select backfill are critical properties in the design phase because they govern the internal stability of the wall. FHWA and TxDOT specifications on material gradation and compaction should yield a high friction-angle backfill. Past laboratory tests on RAP and CC have shown high internal friction angles with little or no cohesion observed. Shear strength of RAP should be comparable to a similarly graded natural aggregate, whereas the shear strength of CC was reportedly similar to that of crushed limestone aggregates (Petrarca and Galdiero 1984). Hence, RAP and CC should have an adequate shearing resistance for the backfill system.

TxDOT specifications do not specify a minimum internal friction angle for select backfill materials. However, the TxDOT standard sheets for retaining walls, RW (MSE), RW (CB), and RW (TEW), assume zero cohesion and a friction angle of 34 degrees for permanent retaining walls and zero cohesion and a friction angle of 30 degrees for temporary retaining walls. The shear strength of the candidate select backfill material should be measured according to test

method Tex-117-E, “Triaxial compression tests for disturbed soils and base materials.” This test measures the shearing resistance, water absorption, and potential expansion of the soil. Each specimen is subjected to absorption measurement prior to a triaxial compression test. At the end of the test, shear strength parameters are reported in terms of cohesion and internal friction angle, along with absorption and expansion characteristics of the materials.

Unlike the TxDOT specification, the FHWA design manual specifies that the internal friction of select backfill materials, measured by the standard direct shear test (AASHTO T-236), must be greater than or equal to  $34^\circ$  for the particles smaller than the No. 10 sieve (2.0 mm). The test specimen is compacted at 95 percent of AASHTO T-99 (essentially standard Proctor) and sheared in a consolidated-drained condition at different normal pressures.

#### **2.4.5 Creep Potential**

When using select backfill and metallic reinforcement, creep is not a concern and not considered in design. Creep of polymeric reinforcement is considered when using select backfill and polymeric reinforcement in an MSE wall. However, when RAP is used as select backfill, the select backfill itself may be susceptible to creep behavior, owing to the viscosity of the asphalt cement in the material. It is possible that excessive creep deformations will occur in the RAP backfill or at the RAP-reinforcement interface under sustained loads below failure. Such creep behavior in RAP is likely to be temperature dependent, with higher severity expected at higher temperatures, because the asphalt stiffness is temperature dependent.

Because TxDOT and FHWA do not anticipate creep of the select backfill itself, creep testing of soil is not discussed in their material specifications or design manuals. However, the creep potential of the select backfill can be studied by conducting classic creep tests with a conventional triaxial test setup.

An additional concern regarding creep characteristics is the creep pullout behavior. This type of creep mechanism is usually associated with creep deformations in polymeric reinforcing elements. Sawicki (1999) indicated that the creep of an MSE wall tends to take place in the active zone, in which the soil is in the plastic state and the reinforcement is in the visco-elastic condition. For a conventional select backfill, this plastic flow in the active zone is controlled by visco-elastic deformations of the reinforcement. However, in a case of reinforced RAP backfill, RAP itself is believed to be a creep-susceptible material. Thus, it is possible that excessive deformation may occur because of the additional contribution of creep from the RAP backfill.

#### **2.4.6 Corrosivity**

As previously noted, the corrosion potential of MSE wall backfill materials is typically characterized in terms of the resistivity and pH of the backfill. TxDOT requires that the resistivity of the backfill be greater than 3000 ohm-cm and that the pH fall between 5.5 and 10. These values are similar to those proposed by FHWA. TxDOT also allows materials with a resistivity between 1500 and 3000 ohm-cm to be used if the chloride content is less than 100 ppm and the sulfate content is less than 200 ppm.

## **2.5 Summary**

This chapter presented a summary of crushed concrete (CC) and recycled asphalt pavement (RAP) materials and described their current applications. An overview of MSE walls was provided and the current MSE wall design methodology was presented. The properties of select fill that are critical to achieve adequate MSE wall performance and current MSE wall backfill specifications were reviewed.



### **3. Selection of Test Materials and Initial Characterization**

#### **3.1 Selection of Test Materials**

There are many producers of CC and RAP in Texas; therefore, it was important to study the variability of CC and RAP obtained from various producers before selecting the source or sources of test materials for subsequent studies. A state-wide survey was distributed in October 2000 to potential CC and RAP providers willing to cooperate in this study (Ogalla 2002). Sixteen companies and eighteen of twenty-five TxDOT districts responded to the survey and completed the questionnaire. Based on the survey results, Southern Crushed Concrete and Big City Crushed Concrete were identified as the two largest commercial producers of CC in Texas, with a combined production of 3 million tons per year. Additionally, the survey showed that TxDOT districts typically produce RAP, but most do not produce or utilize CC. The Corpus Christi district was one of the largest producers of RAP in TxDOT, producing between 60,000 and 120,000 tons per year.

Southern Crushed Concrete, Big City Crushed Concrete, and the Corpus Christi TxDOT district showed interest in the research and were willing to provide samples for initial testing and screening. Each entity was asked to periodically sample their products over a period of 2 months and ship these samples to the research facilities for initial characterization. The purpose of these screening tests was to determine the variation in properties and characteristics of material sampled from different producers at different times.

The characterization tests were performed in early 2001 and the results are reported by Ogalla (2002). Ogalla (2002) reported that the materials from different sources and different times all passed the TxDOT Type B backfill gradation requirement and had very similar index properties. Big City Crushed Concrete and the Corpus Christi district were selected as the final sources of CC and RAP, respectively, because they showed great willingness and cooperation in providing information and samples for the research.

After the initial characterization was completed, it was decided that a conventional MSE wall backfill material (conventional fill material, CFM) should be included in the subsequent testing program for comparison purposes. Texas Crushed Stone, a local supplier located in Georgetown, Texas, was chosen as a supplier of CFM. The material obtained from Texas Crushed Stone is a crushed, quarried limestone.

Approximately 20 tons of CC and RAP were delivered in May 2001 and 10 tons of CFM was received in August 2001. The bulk materials were separately stockpiled at the Pickle Research Center in Austin, Texas, and at the Riverside Campus of Texas A&M University. Each stockpile material was placed on a sheet of heavy-duty geotextile fabric. These stockpiles were the only sources of the test materials for the succeeding experimental program.

#### **3.2 Index Properties**

The gradation, Atterberg Limits, and specific gravity are the index properties that were considered. The index properties were evaluated for CC, RAP, and CFM. Additionally, the

asphalt content of the RAP was estimated with the nuclear gauge (ASTM 4125) and found to be about 3.5 percent. This represents a value on the lower end of the typical range.

The grain size distribution was evaluated through a typical dry sieving method (ASTM D422) in which sieves ranging in size from 3 in. to sieve No. 200 (0.075 mm) were used. Test samples were taken at different locations of the material stockpiles to determine if there is any significant variation in gradation owing to different sampling locations.

Figure 3-1 illustrates the grain size distribution of CC samples taken from four different locations of the stockpile. The grain size distribution of CC is relatively uniform over the stockpile. Less than 5 percent of the material is larger than 1.57 in. (40 mm), and there are no particles larger than 3 in. Approximately 10 percent of the material passed the No.40 sieve (0.425 mm), but no fines passed the No. 200 sieve (0.075 mm). The USCS classification for this material is poorly-graded gravel (GP). Based on these measured gradations, the bulk CC satisfies both TxDOT Type B and FHWA backfill material gradation requirements for MSE walls.

Figure 3-2 shows the grain size distribution of RAP samples taken from four different locations of the RAP stockpile. It can be seen from Figure 3-2 that grain size distribution of the RAP is very uniform over the stockpile. Again, less than 5 percent of the material is larger than 1.57 in. (40 mm) and no particles are larger than 3 in. Only 2 percent of the material passes the No. 40 sieve (0.425 mm) and there are no fines passing the No. 200 sieve (0.075 mm). The USCS

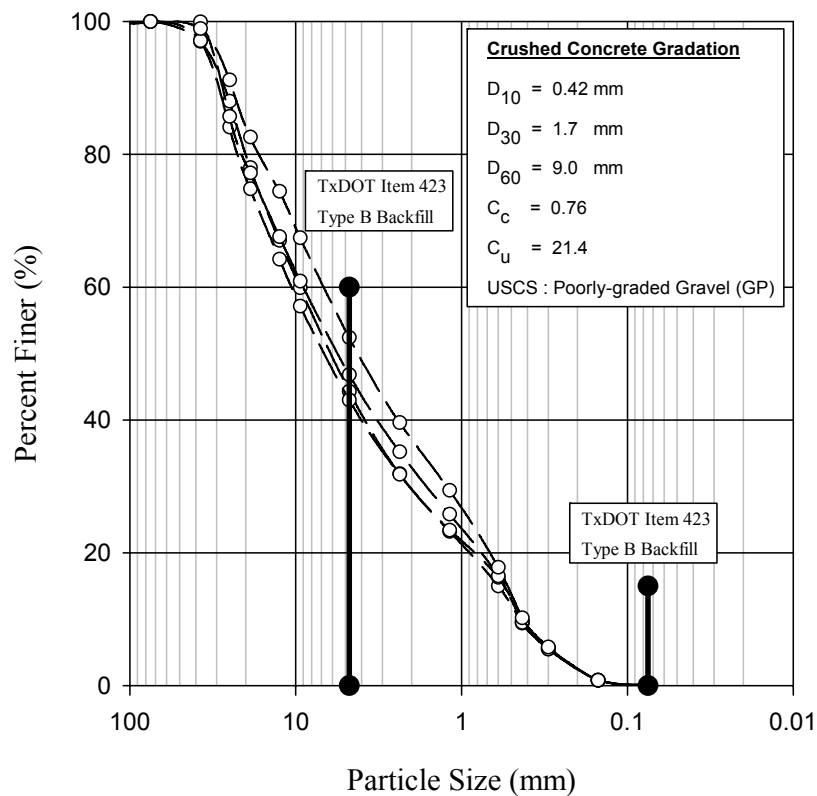


Figure 3.1 Grain Size Distribution of the CC Stockpile

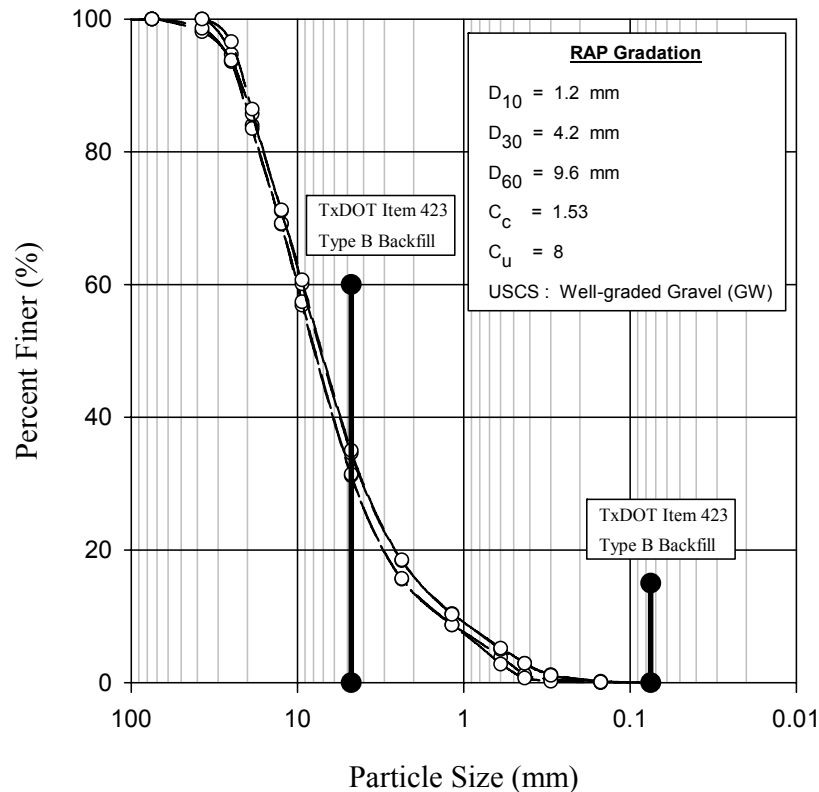


Figure 3.2 Grain Size Distribution of the RAP Stockpile

classification is well-graded gravel (GW). Based on this gradation information, RAP satisfies both TxDOT Type B and FHWA backfill material gradation requirements for MSE walls.

The gradation results from four samples of CFM are shown in Figure 3-3. The results show that the grain size distribution of the CFM is fairly uniform over the stockpile. Less than 5 percent of the CFM is larger than 1.57 in (40 mm) and no particles are larger than 3 in. However, approximately 28 percent of the CFM passes the No.40 sieve (0.425 mm) and, on average, more than 10 percent passes the No. 200 sieve (0.075 mm). Thus, the CFM contains significantly more fines than CC and RAP. The USCS classification of this material is poorly-graded gravel (GP). Based on these measured gradations, the CFM satisfies both the TxDOT Type B and the FHWA backfill gradation requirements for MSE walls.

Because of the different gradations of the stockpiled materials, a single reference gradation was proposed (Figure 3-4). Test specimens for subsequent investigations were mixed to match this reference gradation. Using a single reference gradation will eliminate the effect of grain size distribution on test results, thereby allowing tests to concentrate on the effects of the composition of the different materials. Figure 3-4 shows the proposed reference gradation, as well as the average gradations of the material stockpiles. Key grain-size limitations of the reference gradation include limiting the maximum particle size to 2 in (50 mm), limiting the material



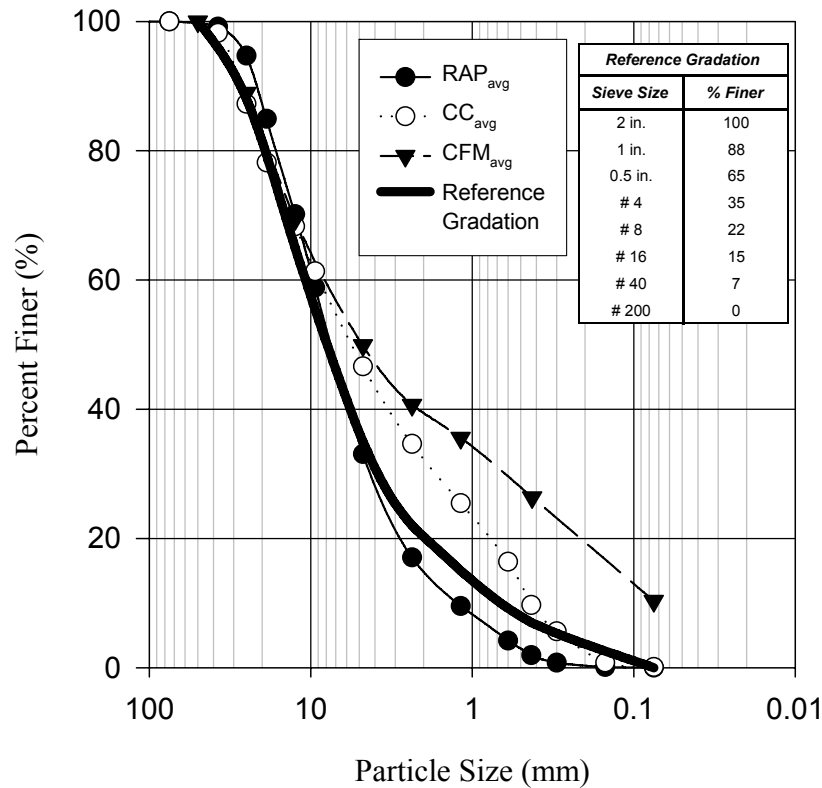


Figure 3.4 Proposed reference gradation for testing program

Table 3-1 shows the specific gravity of the test materials obtained from this approach. It is observed that for each material, the large and small particles have very similar values of specific gravity. While CC and CFM display values of specific gravity that are similar to those expected for granular soils, the specific gravity of RAP is significantly smaller. The lower value of specific gravity for RAP is most likely owing to the bitumen coating around particles that creates a larger impermeable volume of solids and, thus, results in a smaller calculated specific gravity.

Table 3.1 Specific Gravity of Test Materials

Specific Gravity	Material		
	RAP	CC	CFM
> No. 4 sieve*	2.36	2.62	2.64
< No. 4 sieve**	2.28	2.62	2.69
$(G_s)_{avg}$	2.33	2.62	2.66

Note: \* Apparent specific gravity of coarse materials from ASTM C127

\*\* Specific gravity of fine materials from ASTM D854

### 3.3 Laboratory Compaction

Compaction curves (moisture content - dry unit weight relationships) for all three test materials were measured in accordance with the Tex-113-E test method. In this test, soil is compacted in a compaction mold (6-in. diameter by 8-in. height) using a 10 lb hammer with a sector face dropped from a height of 18 in. Compaction is performed in 4 layers, with 50 blows of the hammer applied to each layer. With this compaction procedure, each sample receives a compaction energy of 22,900 ft-lb/ft<sup>3</sup>.

For each test material, a representative sample was taken from the stockpile for compaction testing. The air-dried sample was sieved out to separate different particle sizes, oven-dried at the appropriate drying temperature, and then remixed again to match the reference gradation for the compaction tests. The resulting compaction curves for CC, RAP, and CFM samples are shown in Figures 3-5, 3-6, and 3-7. The zero air voids (ZAV) curve, representing 100 percent saturation for the specific gravity of each material, is shown on each plot.

The compaction curve for CC (Figure 3-5) indicates that the dry unit weight increases as water content increases from 0 to 12 percent. The dry unit weight remains relatively constant when the water content is greater than 12 percent; as these specimens represent conditions close to full saturation. CC specimens could not be constructed at water contents greater than about 14 percent because excess water drained out of the compaction mold. The CC compaction curve does not exhibit a distinct peak, which is typical for gravelly soils because their density is not significantly sensitive to water content (Lambe and Whitman 1979). A water content of 10 percent and a corresponding dry unit weight of 119 lb/ft<sup>3</sup> were used for future testing, which corresponds to approximately 70 percent saturation. This value of water content was chosen because it represents a value that is easy to handle in the laboratory, while still yielding a high dry unit weight.

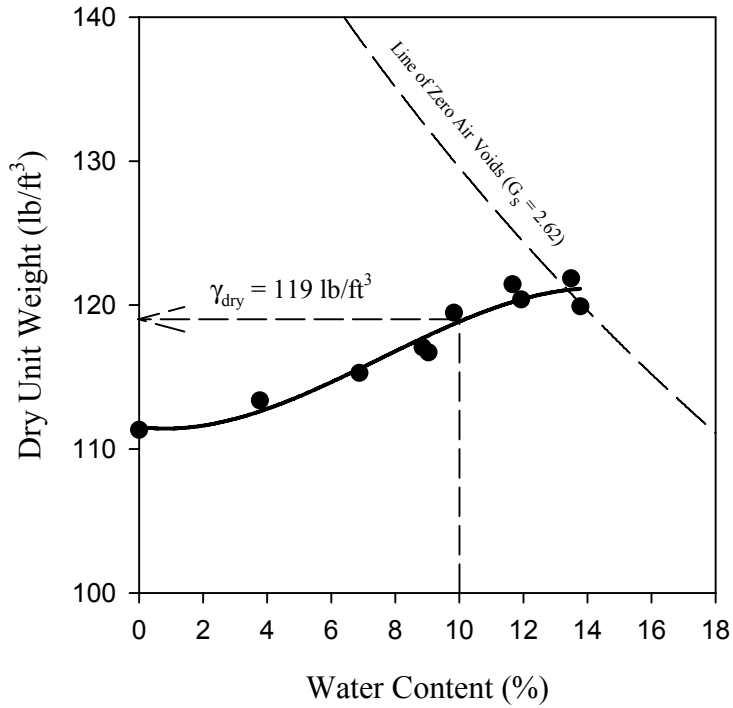


Figure 3.5 Compaction curve for CC based on Tex-113-E test method

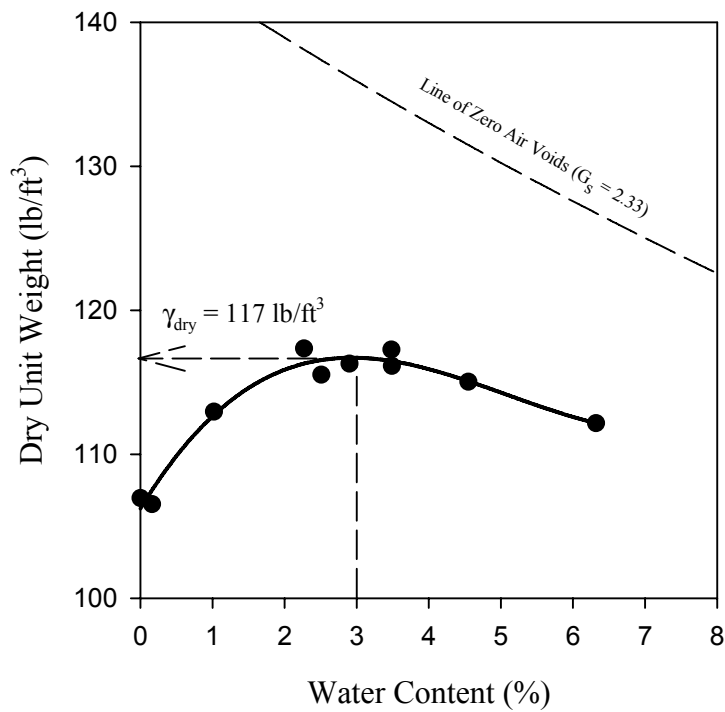


Figure 3.6 Compaction curve for RAP based on the Tex-113-E test method

The RAP compaction curve (Figure 3-6) indicates a slight peak in dry unit weight at 3 percent water content. Compaction specimens could not be constructed at water contents greater than 7 percent because the water quickly escaped from the base of the mold before compaction was complete. This response is indicative of a very freely draining material. The inability of the RAP to maintain larger water contents is also the result of the bitumen coating on the particles not allowing water to adsorb to the soil particles. Based on the compaction curve, a water content of 3 percent and a corresponding dry unit weight of 117 lb/ft<sup>3</sup> were used for future testing.

The compaction curve for CFM (Figure 3-7) is similar to the compaction curve for CC (Figure 3-5). The dry unit weight increases with increasing water content until a water content of about 11 percent is reached. All of the compaction tests at 11 percent water content resulted in dry densities that fell close to the zero air voids curve, indicating 100 percent saturation. Based on this compaction curve, a water content of 10 percent and a corresponding dry unit weight of 125 lb/ft<sup>3</sup> were used for future testing. This water content corresponds to about 80 percent saturation.

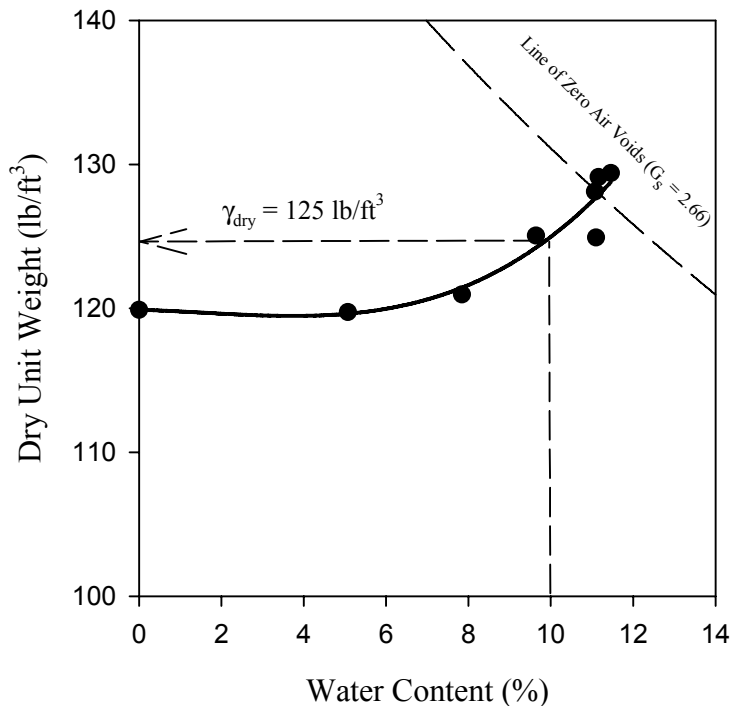


Figure 3.7 Compaction curve for CFM based on the Tex-113-E test method

Fines content (particles passing sieve No. 200) is a major factor in assessing the quality of backfill material. With crushed and recycled materials, additional fines may be created during compaction when larger particles in the material are broken. The potential degradation of CC, RAP, and CFM was evaluated by simple impact compaction. Though impact compaction may not completely mimic the true compaction mechanism that occurs in the field, this compaction provides insight regarding the potential for material breakdown upon compaction.

Five samples of each test material were mixed to match the reference gradation, which contains no fines, and the recommended water content. The samples were subjected to impact compaction following the Tex-113-E test method, and after compaction the gradation was measured via sieve analysis. After compaction the CC and RAP specimens contained 1.6 percent and 0.6 percent fines, respectively. These values are quite low and indicate minor material breakdown. The CFM contained 3.6 percent fines after compaction, which is larger than CC and RAP but is still minimal. These findings suggest that CC and RAP are not likely to produce significant amounts of fines during field compaction.

### **3.4 Summary**

This chapter described the selection of test materials for this study and their initial characterization. Samples of RAP and CC from various producers in Texas indicated that there is not significant variability among producers and that the commercial products met the TxDOT Type B gradation specifications. Thus, a single producer of CC and a single producer of RAP were selected. A crushed limestone supplier was also selected to provide a conventional fill material. A reference gradation was selected to which each material would be matched for subsequent testing.

The specific gravity (Gs) and compaction characteristics of each material were evaluated. The Gs of CC was 2.62, which is similar to the value for granular soils. The Gs of RAP was 2.33, which is significantly lower than for soils. The lower value was attributed to the bitumen coating that creates a larger impermeable volume of solids. The laboratory compaction curves for each material were developed using the Tex-113-E test method. CC displayed a compaction curve similar to CFM, where the curve was relatively flat and reached a maximum close to saturation (10 to 12 percent water content). The compaction curve for RAP displayed a peak at a very low water content (~ 3 percent), and specimens were difficult to construct at water contents larger than 5 percent owing to loss of water. Again, this response is attributed to the bitumen coating, which does not allow adsorption of water to the solid particles. Gradations measured after compaction indicated that neither CC nor RAP should experience particle breakdown during field compaction.



## 4. Geotechnical Properties of CC and RAP

### 4.1 Introduction

The shear strength, hydraulic conductivity, and collapse potential are important backfill properties that relate to its suitability for MSE wall applications. Additionally, field compaction control and the durability of the backfill material also impact its suitability for MSE walls. This chapter discusses the test equipment and experimental program used for the assessment of these important properties. Laboratory testing programs were designed to evaluate the shear strength, hydraulic conductivity, collapse potential, and durability of the test materials, while a field testing program was used to assess field compaction control. The shear strength of the three test materials (RAP, CC, and CFM) was characterized in terms of the effective stress shear strength parameters (i.e.,  $c'$  and  $\phi'$ ), as determined by triaxial and direct-shear tests. Hydraulic conductivity measurements were performed using the falling head-rising tail method in a flexible wall triaxial setup. The collapse potential upon wetting was evaluated through large-scale, one-dimensional constrained compression tests. A collapse index ( $I_c$ ) was defined for each material and compared. Field compaction testing was performed to assess the accuracy of the nuclear gauge in these recycled materials. Finally, durability testing included an assessment of the potential for expansion in CC owing to alkali-silica reaction and sulfate attack.

### 4.2 Test Equipment

This section describes the triaxial testing system and the large-scale direct shear apparatus that were used in this study to evaluate the shear strength, hydraulic conductivity, and collapsible potential of the test materials.

An electro-hydraulic triaxial test system (Figure 4-1) built by GCTS of Tempe, Arizona, was used for three different types of experiments: consolidated-drained triaxial tests, flexible-wall hydraulic conductivity tests, and creep tests (discussed in Chapter 6). The GCTS system is a closed-loop, digitally-controlled servo-hydraulic system with a computer interface that connects the system analog signals to the computer board for data acquisition. The load frame consists of two vertical stainless steel columns with a crosshead to support a double-acting diaphragm hydraulic cylinder of 7000-lb capacity. A 5000-lb external load cell with 0.04 percent accuracy is mounted at the bottom of the piston rod for measurement of the piston load during triaxial tests. The triaxial cell is constructed of three stainless steel columns with an external acrylic cell wall that can take up to 145 psi cell pressure. The triaxial system can accommodate cylindrical specimens of up to 4 in. in diameter and 8 in. high with pressure lines for top and bottom specimen drainage.

A large-scale direct shear device was designed with the specific intent to test large specimens containing particles up to 2 in. at applied normal stresses as high as 30 psi. This normal pressure represents roughly 40 ft of in situ overburden pressure. The general criterion for a direct shear specimen is that the width of the specimen must be at least 10 times larger than the maximum particle size diameter (ASTM D3080), and that the width to thickness ratio of the box should be 2:1. Given that test materials in this study contain particles up to 2 in., a square shear box with an

inside width of 20 in. was selected. The direct shear machine was designed to accommodate a maximum anticipated horizontal shear force of approximately 17,000 lb, which was estimated from the expected shear resistance of the test materials subjected to 30 psi normal stress. Figure 4-2 is a photograph of a complete setup of the large-scale direct shear machine during testing, and Figure 4-3 shows a cross-section of the setup.

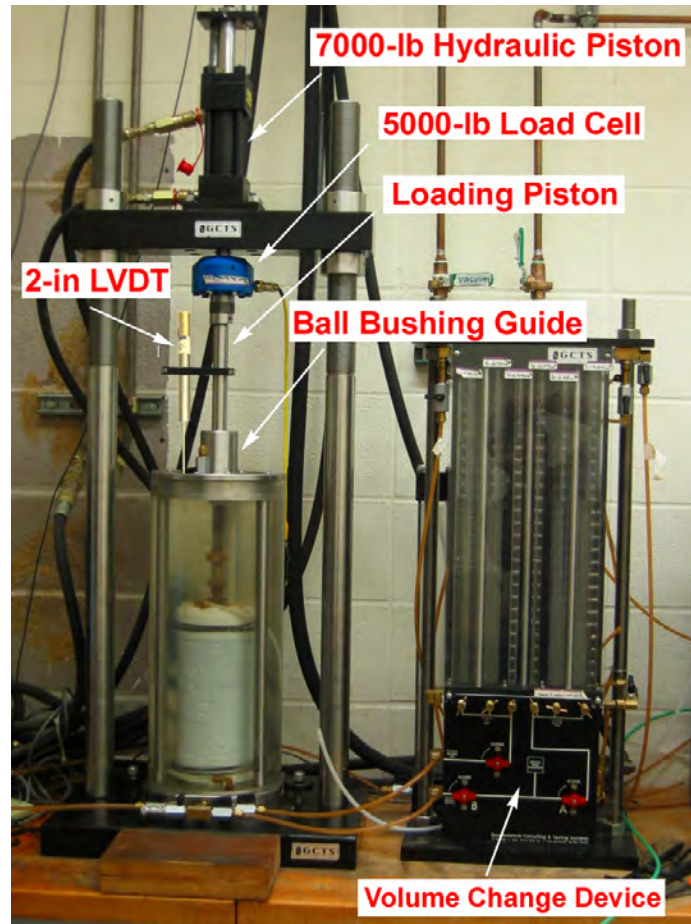


Figure 4.1 Triaxial cell and loading components

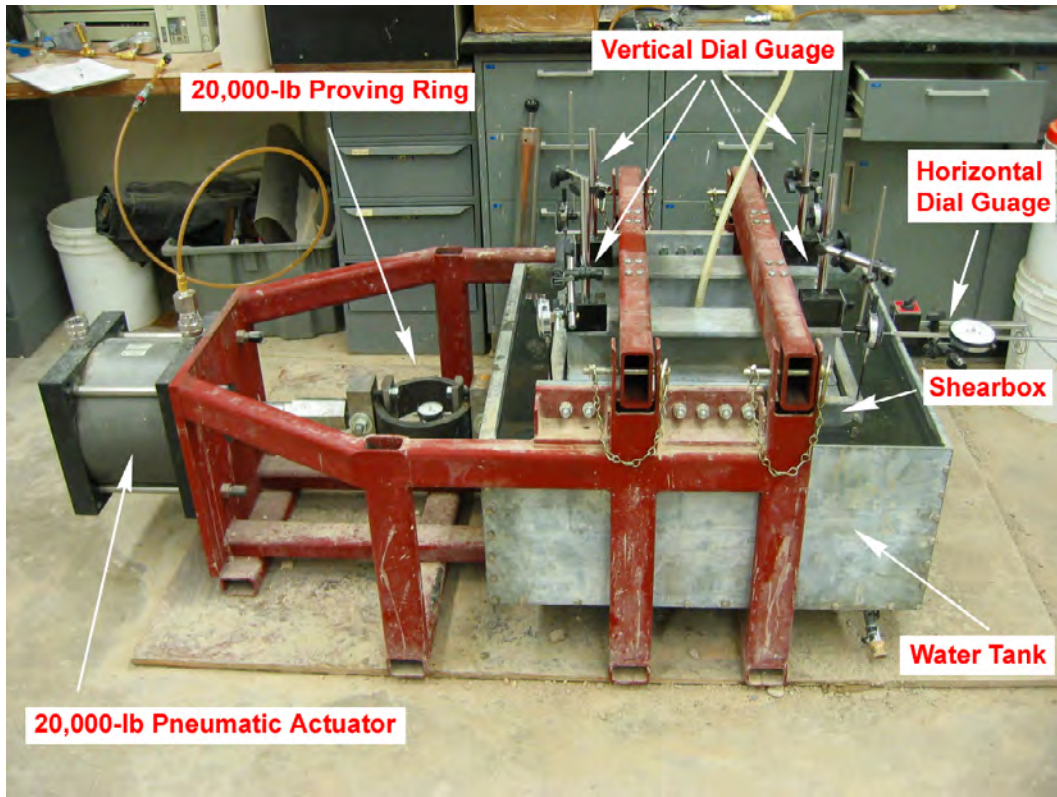


Figure 4.2 Large-scale (20 in. x 20 in.) direct shear machine

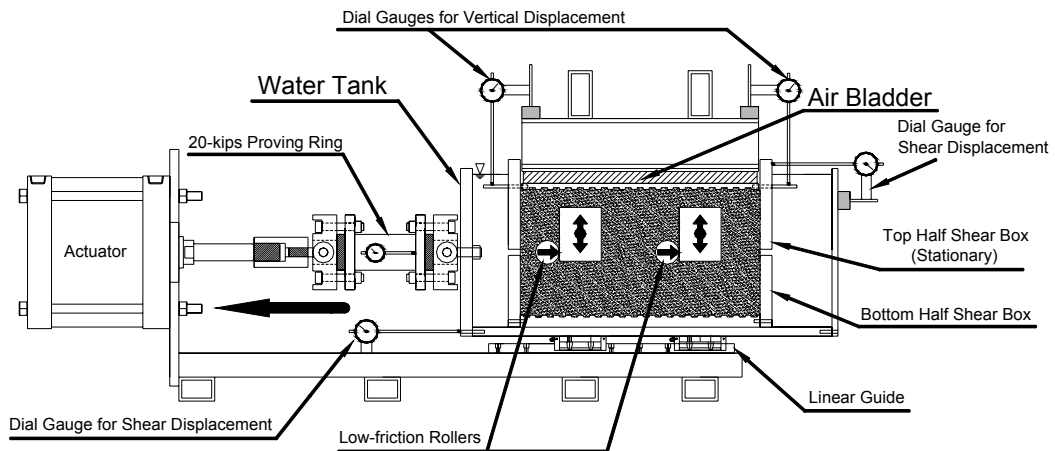


Figure 4.3 Cross section of the large-scale direct shear machine

The shear box is situated inside a water tank, which is filled with water during the test to eliminate any capillary stresses developed within the test specimens that may affect the measured shear strength. The water tank is rigidly attached to the lower half of the shear box, and both move laterally during shearing. The upper half of the shear box is held stationary in the horizontal direction by plates that react against four low-friction rollers, but these rollers also allow the top of the box to move freely in the vertical direction (Figure 4-3). These rollers allow for dilation and contraction of the specimen and also minimize rocking. During shearing, the lower half of the shear box and the surrounding water-filled tank are pulled horizontally by a pneumatic actuator (12-in. diameter, 5-in. stroke) and ride on two linear bearings. Normal stresses are applied to the top of the test specimen using an air-pressurized rubber bladder, which receives a constant air pressure supply from the house pressure line. The horizontal pneumatic actuator is operated with pressures up to 250 psi delivered from pressurized, bottled air and can deliver over 27,000 lb of horizontal shear force.

The direct shear machine is used to conduct stress-controlled direct shear tests, where the shear force is applied in increments by progressively increasing air pressure to the actuator. The shear force is increased when no additional shear displacement owing to the preceding load is observed. Operation of the direct shear machine with pneumatic pressure regulators allows for simple, accurate control for tests of this type. The vertical and horizontal displacements of the specimen are monitored by a system of six dial gauges, two for horizontal displacement (one measuring relative displacement between the top and bottom boxes and the other measuring absolute displacement of the bottom box), and four for vertical displacement (at each corner of the test specimen). All data from the tests were recorded manually using a high resolution pressure gauge for the normal stress, a 20-kip proving ring for the applied shear force, and the set of dial gauges for the shear and vertical displacements.

In addition to the measurement of drained shear strength, the direct shear machine was also used to assess the potential for post-construction settlement in these backfill materials upon wetting (i.e., collapse potential). Vertical compression of the specimens was measured during application of the normal stress and then during subsequent submergence in water. The large scale of these test specimens provided a unique opportunity to assess this behavior in the laboratory using a representative sample gradation containing all particle sizes.

### **4.3 Shear Strength**

The shear strength parameters of MSE wall backfill are critical properties in the design phase because they impact the internal stability of the wall. Generally, MSE wall backfill should have moderately high frictional strength to ensure stability within the backfill itself and to achieve the required interaction with the reinforcement. High shear strength materials typically are well-graded and angular, with minimal fines. Based on visual inspection and the measured gradations, CC and RAP should exhibit high shear strength parameters because of their significant angularity and the absence of fines.

The ASTM standard for triaxial testing (ASTM D4767) states that triaxial specimens have a diameter at least 6 times larger than the largest particles contained in the test specimen. Given a maximum sample diameter of 4 in. for the triaxial setup, any particles larger than approximately 0.67 in. must be removed before forming the test specimens. However, removal of larger

particles may yield unrealistically high strength because these larger particles may be fractured and therefore weaker than the smaller particles. Thus, large-scale direct shear tests measuring 20 in. by 20 in. in plan section were also performed, as this specimen size could accommodate all particle sizes in the reference gradation.

### 4.3.1 Consolidated-Drained Triaxial Tests

A series of fourteen consolidated-drained, strain-controlled triaxial compression tests were completed on compacted specimens of RAP, CC, and CFM. Four tests at four different effective confining pressures (i.e., 20, 30, 40, and 50 psi) were performed on CC and CFM specimens. The RAP specimens were tested at the same effective confining pressures, as well as two additional tests performed at 5 and 10 psi effective confining pressures, to investigate the potential curvature of the RAP failure envelope at low confining pressures.

A consistent reference gradation was selected in Chapter 3 for the preparation of test specimens. However, the 4-in. specimen diameter for the UT Austin triaxial apparatus requires that all particles larger than 0.67 in. be removed. This scalping was accomplished by using only material that passed the 0.63 in. sieve, the closest available sieve size to 0.67 in., which resulted in the specimen gradation illustrated in Figure 4-4.

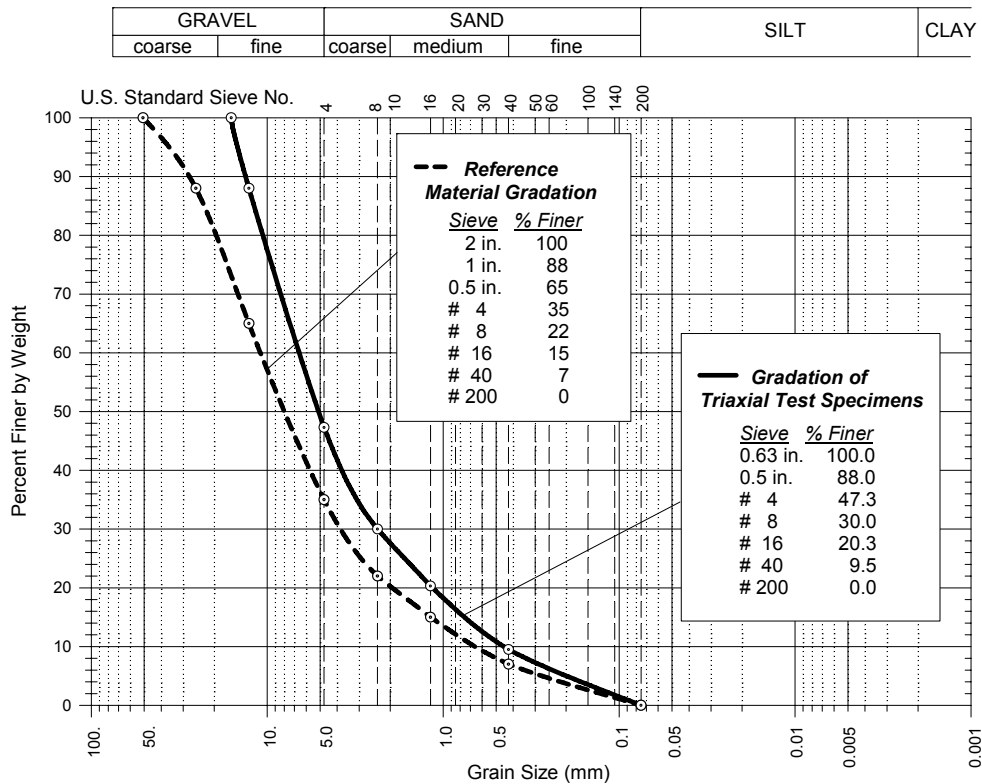


Figure 4.4 Grain size distribution of reference gradation and triaxial test specimens

Results from the consolidated-drained triaxial compression tests performed on specimens of CC, RAP, and CFM are plotted in terms of principal stress difference ( $\sigma_d = \sigma_1 - \sigma_3$ ) versus axial strain

( $\epsilon_a$ ) and volumetric strain ( $\epsilon_v$ ) versus axial strain ( $\epsilon_a$ ) in Figures 4-5, 4-6, and 4-7, respectively. The principal stress difference was computed by dividing the applied piston load by the corresponding cross-sectional area of the specimen, assuming a right circular cylinder area correction. Failure was defined as the maximum principal stress difference (i.e.,  $[\sigma_1 - \sigma_3]_{\max}$ ). Strain-controlled tests were performed to capture any strain-softening behavior after the peak load was applied. The values of major and minor principal stresses at failure (i.e.,  $\sigma'_{1f}$  and  $\sigma'_{3f}$ ) were used for plotting the Mohr circles of stress at failure under drained conditions, after which a best-fit Mohr-Coulomb strength envelope was drawn for each test material.

Figure 4-5 shows that all of the CC tests exhibited strain-softening behavior, reaching a maximum principal stress difference at less than 6 percent axial strain and then declining to a residual value. The CC specimens experienced between 3 percent and 4 percent expansion at the end of testing. All CC specimens displayed a distinct failure plane through the specimen. The effective cohesion and effective friction angle based on these four tests are 22 psi and  $41^\circ$ , respectively.

During the preparation of one CC test specimen, some visual evidence was noted that suggests unhydrated cement paste may be present in the crushed concrete. Subsequently, several samples of uncompacted, wet CC were dried overnight in an oven. Upon removal from the oven, the material had a distinct, hardened crust. The individual aggregate grains were noticeably conglomerated, forming larger chunks of cemented material that were visibly different from the original material. It is possible that bonding occurred owing to rehydration of cement paste in the CC. If true, then the strength of compacted CC may increase somewhat with time following compaction. Only freshly compacted material was evaluated in this study, so this effect is minimal in the test data presented. The cohesion intercept found for CC may be attributed to cementation because of rehydration of the cement paste or the linear extrapolation of the failure envelope from larger confining pressures. The direct shear test program includes a number of drained shear tests performed at low confining pressures, which can further identify whether the CC strength envelope is curved or is a straight line with cohesion.

Tests on RAP were performed at effective confining pressures ranging from 5 to 50 psi (Figure 4-6). All tests exhibited strain-hardening behavior, with the deviator stress continuing to rise or remaining essentially steady throughout the duration of the test. Final volumetric strains ranged from dilative, for tests run at low confining pressures, to contractive for tests performed at higher confining pressures. The contractive response is in contrast to the purely dilative response observed in the tests on CFM and CC. In addition, no RAP specimens displayed a distinct failure plane during shear. Rather, the specimens compressed vertically and exhibited a slight radial bulge near the center as the axial load was applied. These responses are typical for a loose material in drained shear, although it is somewhat unexpected that compacted specimens would exhibit contractive behavior at these confining pressures.

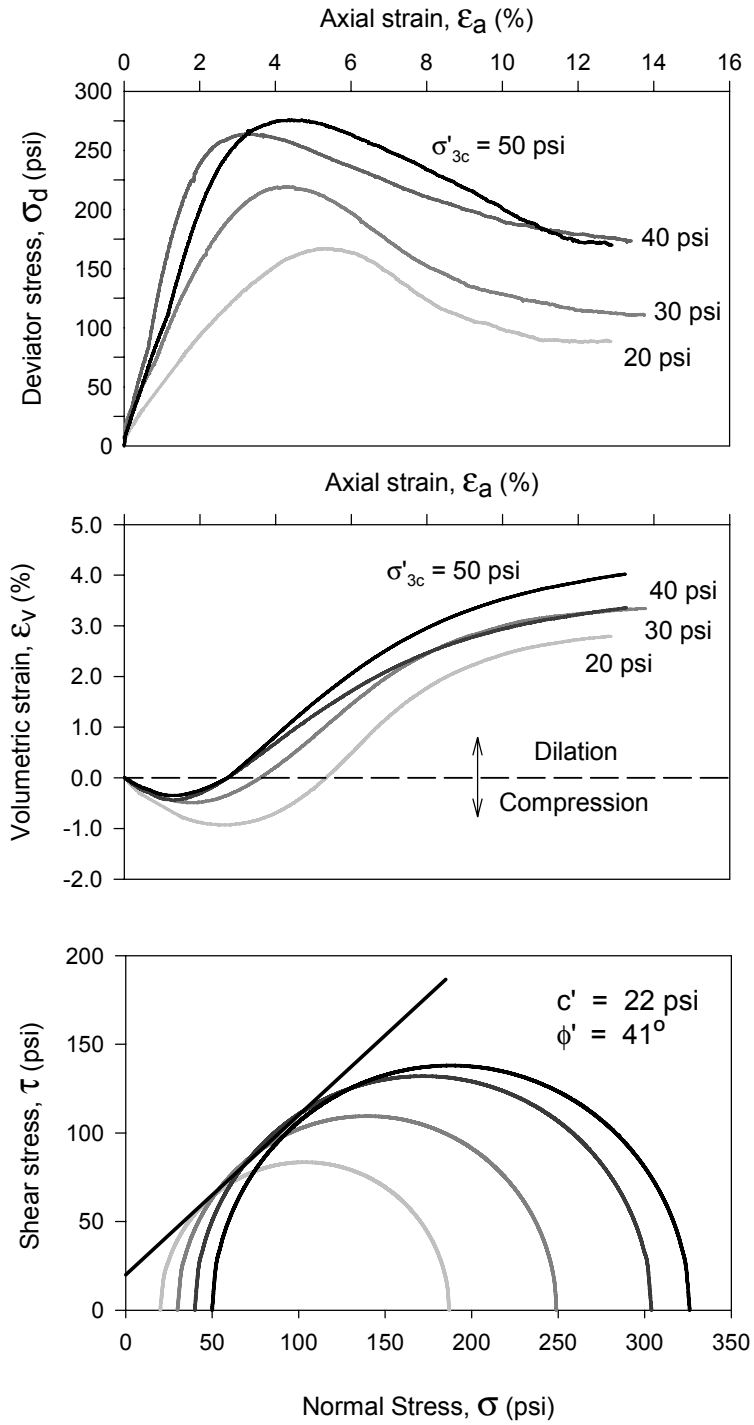


Figure 4.5 Consolidated-drained triaxial test results for CC specimens

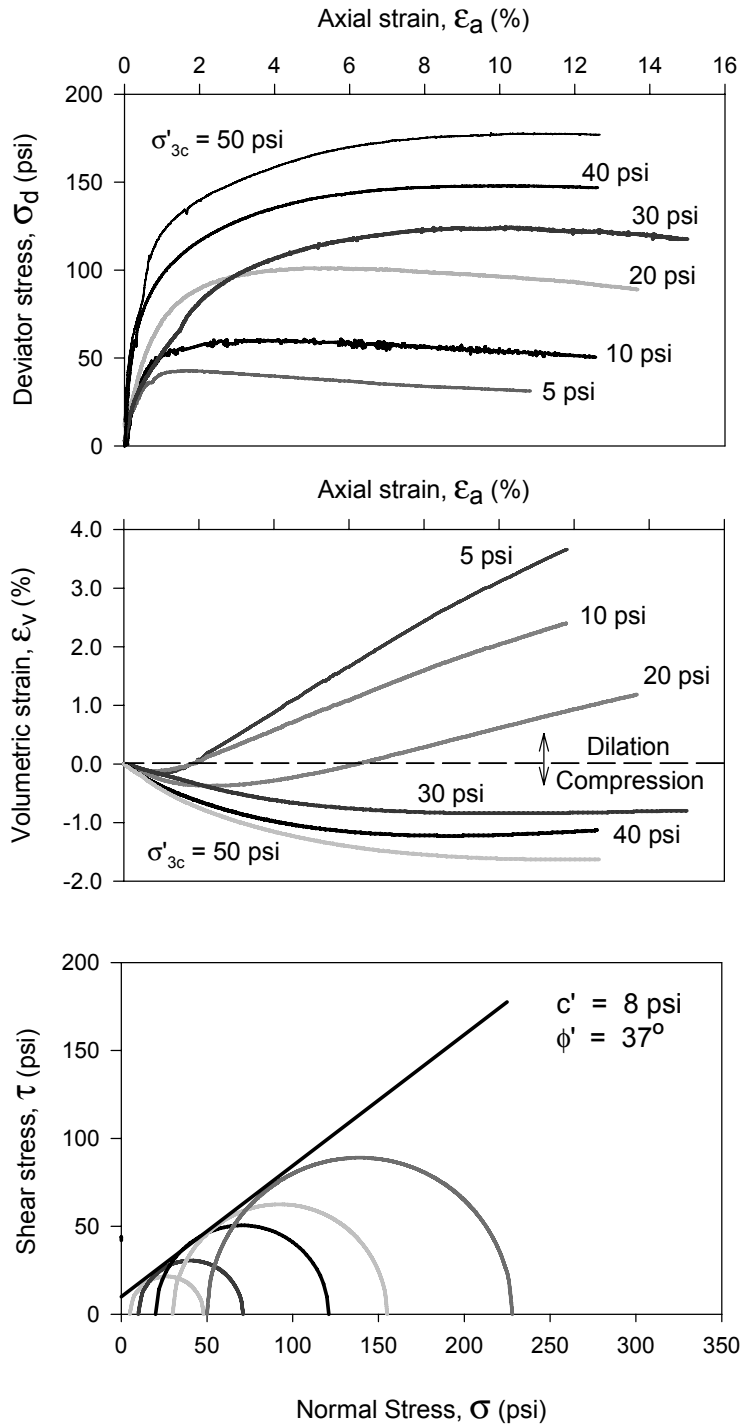


Figure 4.6 Consolidated-drained triaxial test results for RAP specimens

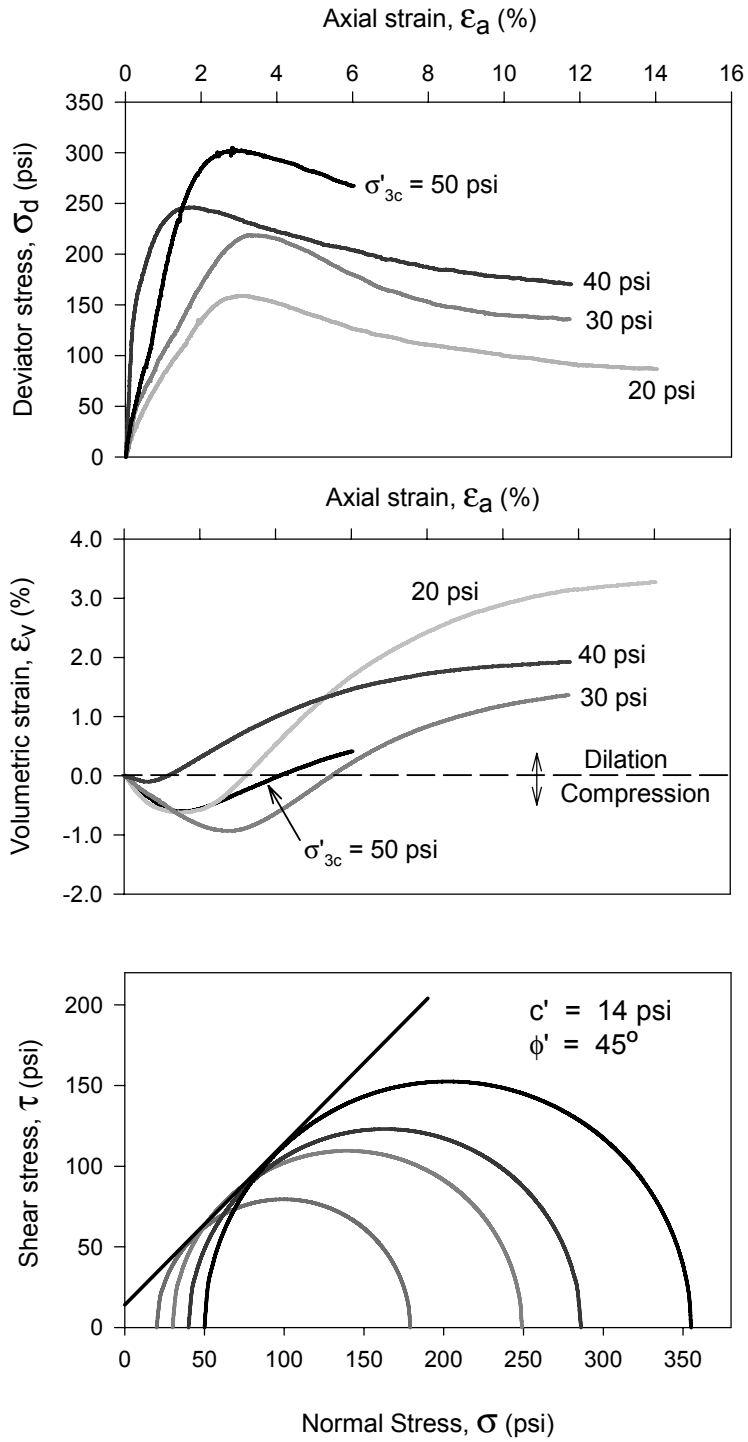


Figure 4.7 Consolidated-drained triaxial test results for CFM specimens

The effective stress friction angle for RAP based on these five tests is 37°, with an effective cohesion intercept of 8 psi. The observed cohesion is likely a result of the residual bitumen bonding the particles together. Although the measured shear strength of RAP was lower than that for CC, RAP appears to exhibit marginal to adequate strength properties for use as MSE wall backfill material. The lower friction angle for RAP, compared with that of CC, may result from more rounded aggregate particles or from reduced interparticle friction because of the residual bitumen in the RAP. Additional investigations were performed in this study to assess the stability of this material, particularly to determine whether RAP is susceptible to creep failure at large to moderate shear stress levels.

Figure 4-7 shows that all of the CFM specimens exhibited strain-softening behavior, reaching a maximum principal stress difference at less than 4 percent axial strain and then declining to a residual value. It should be noted that the CFM specimen sheared at 50 psi effective confining pressure was stopped prematurely because of excessive membrane puncture at large strains. Several additional tests with various corrective measures were performed at this same confining pressure, but all resulted in similar puncture owing to the high angularity of the material. Each specimen that reached full failure experienced between 1 percent and 3 percent shear-induced volumetric dilation at the end of testing. Additionally, all of the CFM specimens displayed a distinct failure plane through the specimen during shear. The strain softening behavior and the distinct failure plane after shear are typical responses of a dense material in drained shear. The effective cohesion ( $c'$ ) and effective friction angle ( $\phi'$ ) based on these four tests are 14 psi and 45°, respectively. The cohesion intercept found for CFM is speculated as a result of either re-cementation of the limestone material or the linear extrapolation of the failure envelope from larger confining pressures.

Table 4-1 summarizes the drained strength parameters for all three test materials. It is clear that CC has comparatively similar strength characteristics to CFM, particularly at the confining pressures representing the heights of typical MSE walls. RAP has distinctively lower shear strength characteristics than CC and CFM, but still maintains adequate strength for typical MSE backfill applications.

*Table 4.1 Comparison of drained shear strength parameters of the tested materials*

<b>Drained Strength Parameter</b>	<b>RAP</b>	<b>CC</b>	<b>CFM</b>
Cohesion ( $c'$ ), psi	8	22	14
Internal friction angle ( $\phi'$ ), degree	37°	41°	45°

### **4.3.2 Large-Scale Drained Direct Shear Tests**

A series of eleven drained, force-controlled direct shear tests were performed on compacted specimens of CC and CFM with initial applied normal stresses ranging from 5 to 28 psi. Two

tests were performed on RAP at normal stresses of 10 and 20 psi, but creep problems were encountered. The results from the three tests series are discussed below.

Figure 4-8 and Figure 4-9 show plots of shear stress versus relative horizontal displacement, and vertical displacement versus relative horizontal displacement for the CC and CFM specimens. An area correction that utilizes the actual specimen shearing surface to calculate the shear and normal stresses was applied. Also, calculation of the final effective normal stress at failure included the summation of the extra loads from the top half of the compacted specimen, air bladder, top bearing plate, and grid plate, minus the estimated water pressure at the shear zone.

The results from the drained, large-scale direct shear tests on CC and CFM specimens show that both materials have very similar responses when sheared. The CC and CFM specimens all exhibited a dilative response, which is typical for dense materials. The degree of expansion depends heavily on the applied normal stress, with less dilatancy occurring at large normal stresses, in general.

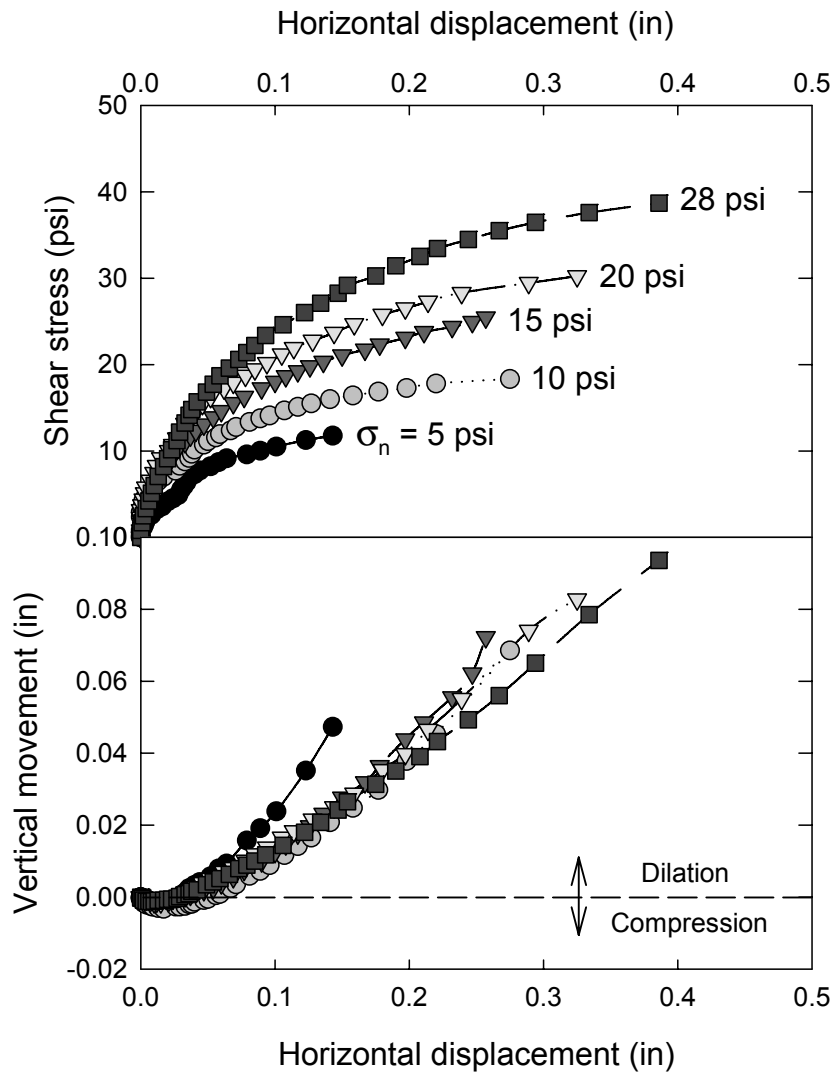


Figure 4.8 Results from large-scale direct shear tests on CC

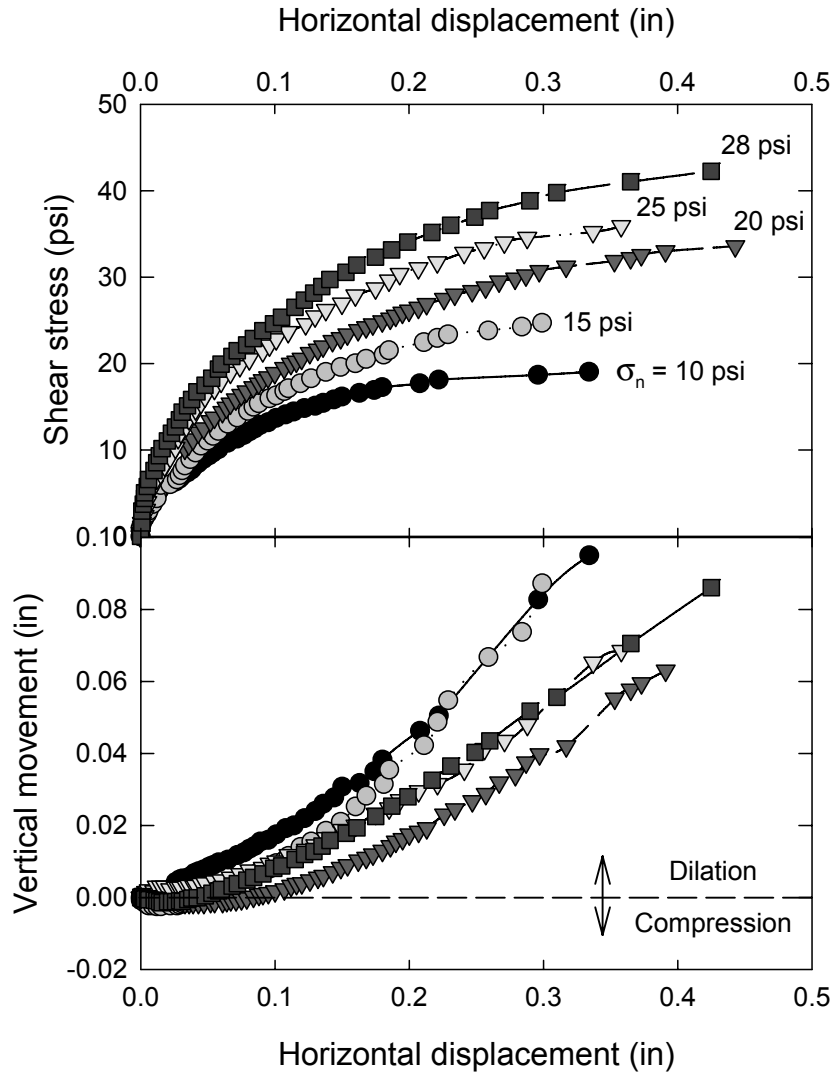


Figure 4.9 Results from large-scale direct shear tests on CFM

The shear stresses and the corresponding corrected normal stresses at failure for the large-scale direct shear test specimens are plotted in Figure 4-10 to determine the best-fit Mohr-Coulomb shear strength parameters for CC and CFM. The data resulted in very similar values of  $c'$  and  $\phi'$  for the two materials ( $c' = 6$  psi and  $\phi' = 49^\circ$  for CC,  $c' = 6$  psi and  $\phi' = 51^\circ$  for CFM). The non-zero values of cohesion for both materials in the direct shear tests were also observed in the triaxial test results and are believed to be the result of re-cementation of the material after compaction.

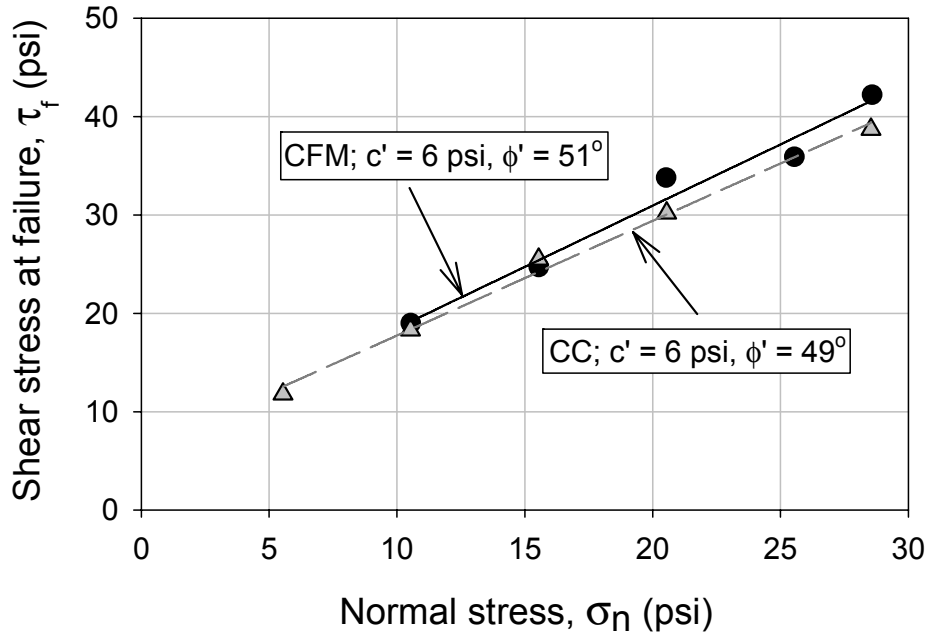


Figure 4.10 Best-fit Coulomb envelopes for large-scale drained direct shear tests on CC and CFM specimens

The direct shear test results for RAP are shown in Figure 4-11. The test at 10 psi initial normal stress was completed with minor creep observed during shearing, although the test took nearly 6 hours to reach the failure point. The test took so long to complete because additional load increments were not placed until deformation from the previous load increment stopped, and the deformations continued for a significant period of time after load application. The test indicated a shear stress at failure of approximately 12 psi, with an area-corrected normal stress of 10.5 psi. Based on this normal stress and the previously measured values of  $c' = 10$  psi and  $\phi' = 36^\circ$  from the triaxial tests, the predicted shear stress at failure is about 17.6 psi. This value is much larger than the measured value, indicating that the specimen may have experienced creep rupture rather than shear failure.

The test at 20 psi normal stress began to creep noticeably after about 0.085 in. of horizontal shear displacement. At this point, the deformation readings from the next two load increments were recorded while creep was taking place and no definite cessation of creep was observed in any of these last few load increments. The last obtainable data was taken at a horizontal shear displacement of about 0.21 in. after about 4 hours of testing. The next load increment was applied, and at this point the deformations appeared to be taken over completely by creep deformation, which eventually led the specimen to complete failure. At no point in time during this last load increment was the proving ring steady enough for accurate reading. The last data point for the 20 psi test indicated a shear stress at failure of about 12 psi, while the previously measured Mohr-Coulomb shear strength parameters would predict a value of 24.9 psi. This comparison supports the conclusion that the specimen experienced creep rupture rather than shear failure.

As a result of this excessive creep behavior of RAP during shear, it was decided to terminate the direct shear test program on RAP and study its creep behavior more thoroughly using triaxial creep tests (Chapter 6).

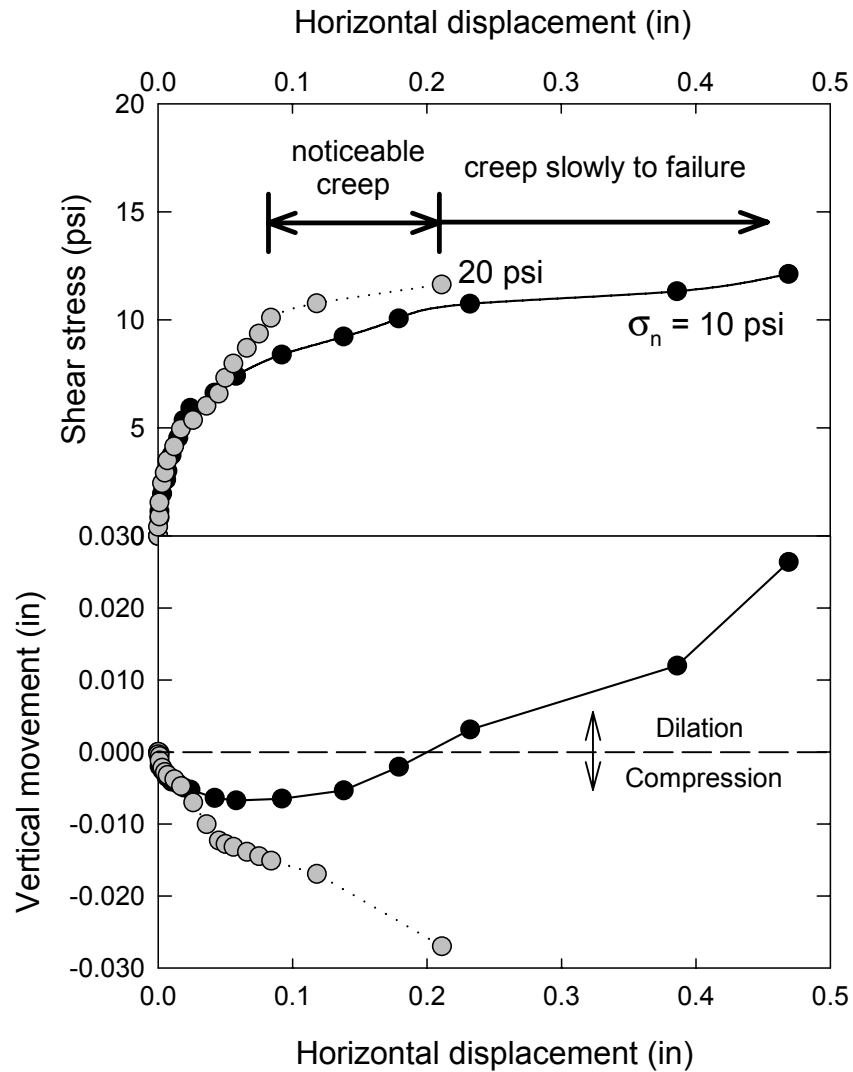


Figure 4.11 Large-scale, load-controlled direct shear tests on RAP specimens

### 4.3.3 Integration of Shear Strength Results

Results from the consolidated-drained triaxial tests and large-scale direct shear tests performed on CC and CFM specimens were combined to develop a better understanding of the strength of these two materials. The direct shear tests included the entire material gradation and were performed at lower normal stresses than the triaxial tests. Final Mohr-Coulomb failure envelopes were obtained by performing regression analysis on the combined data. Because no accurate direct shear data were collected for RAP because of its excessive creep behavior, only the triaxial data are considered for RAP.

Results from the direct shear tests are plotted directly on the shear stress-normal stress coordinate system because this test measures directly the stresses on the shear plane at failure. The triaxial test measures the major and minor principal stresses at failure (i.e.  $\sigma'_{1f}$  and  $\sigma'_{3f}$ ), which allows one to draw a complete Mohr's circle, but these stresses do not represent the stresses on the failure plane of the test specimen at failure. To combine these two datasets for further analysis, it is necessary to identify a single point for each complete Mohr's circle that represents the shear and normal stresses on the failure plane at failure. Ideally, this point can be identified mathematically using basic algebra, if each Mohr's circle is tangent to the failure envelope. That was not the case here, so the failure stresses were identified as the point on each individual Mohr's circle closest to the average shear strength envelope.

Figures 4-12 and 4-13 display the combined triaxial and direct shear data for CC and CFM, respectively. The best-fit Mohr-Coulomb failure envelopes derived from the combined data are also shown. The resulting coefficients of determination ( $R^2$ ) for the combined best-fit envelopes are greater than 0.99 for both CFM and CC, indicating that the data obtained from both test methods are in good agreement. The agreement between the testing devices further suggests that removal of large particles ( $> 0.63$  in.) for the triaxial testing did not result in an overprediction of the overall shear strength of the material. Thus, it is concluded that 4-in. diameter (or larger) triaxial testing can be used to accurately measure the strength of CC.

Again, the best-fit strength envelopes for CC and CFM reaffirm that these two materials display similar shear strength characteristics. Both materials have the same drained internal friction angle (i.e.  $\phi' = 46^\circ$ ) and both exhibited dilative behavior in all tests when sheared under drained condition. CFM has a slightly larger effective cohesion ( $c'$ ), which may be the result of a greater degree of re-cementation of the compacted CFM. However, whether the cohesion is true is uncertain because the data at the lowest normal stresses start to curve towards the origin, which is more noticeable in the case of CC (Figure 4-12).

Unlike CC and CFM, the RAP triaxial specimens all exhibited strain-hardening behavior when sheared. Also, the volumetric response during shear was dependent on the effective confining stress. The direct shear tests on RAP could not be performed accurately because of its excessive creep response during the load-controlled test. Thus, it was decided to further evaluate the creep behavior of RAP using triaxial creep tests (Chapter 6).

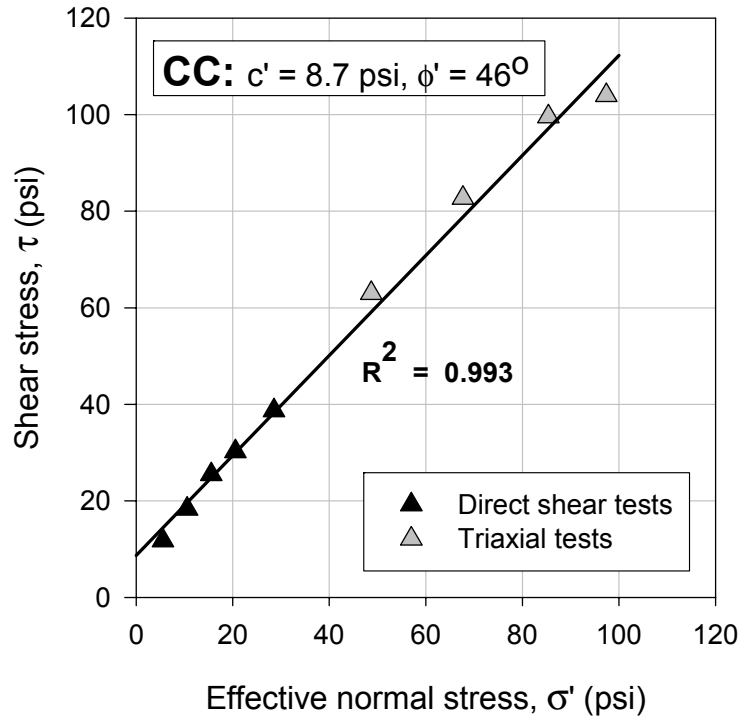


Figure 4.12 Final shear strength envelope for CC

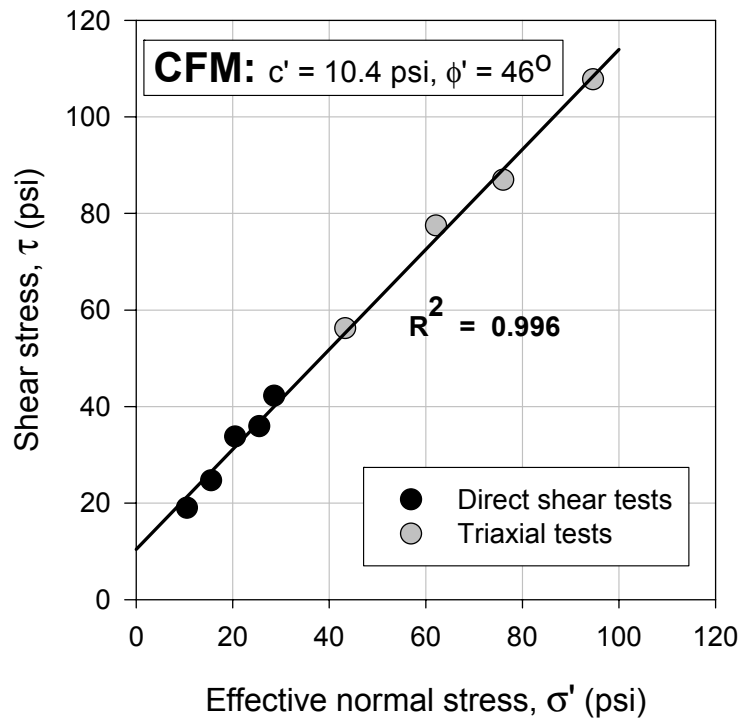


Figure 4.13 Final shear strength envelope for CFM

Table 4-2 summarizes the recommended drained shear strength parameters of all three materials based on the tests performed in this study. CC and CFM exhibited very large friction angles ( $\phi' = 46^\circ$ ), making them ideal materials for MSE wall backfill. The significant volumetric dilation of CC and CFM during drained shear also encourages the use of these materials because the dilatancy effect increases the soil-reinforcement interface friction (Guilloux et al. 1979). RAP, on the other hand, displays a smaller friction angle ( $\phi' = 37^\circ$ ). RAP also displays significant creep behavior that may make it less attractive as MSE wall backfill.

*Table 4.2 Drained shear strength parameters of the test materials*

<b>Drained strength parameter</b>	<b>RAP</b>	<b>CC</b>	<b>CFM</b>
Cohesion (c'), psi	8	9	10
Internal friction angle, ( $\phi'$ ) degree	37	46	46

Although the FHWA MSE wall specifications do not explicitly specify a minimum friction angle for an MSE wall candidate backfill, Elias and Christopher (1996) reported that a lower bound frictional angle of  $34^\circ$  is consistent with materials that have been successfully used in MSE walls. In addition, Palossy et al. (1993) indicated that several European countries including France, Great Britain, Germany, and Hungary have designated a minimum angle of internal friction ( $\phi_{\min}$ ) of  $25^\circ$  for MSE wall backfills. Palossy et al. (1993) also reported that two Hungarian retaining walls were structurally safe using backfill material containing significant amounts of silt and fine sand that marginally satisfied the  $\phi_{\min}$  criterion. Unfortunately, details on the long term performance of these two walls were not mentioned in the study. Nonetheless, CC and RAP meet these minimum friction angle requirements.

#### **4.4 Hydraulic Conductivity**

Hydraulic conductivity ( $k$ ) expresses how well water flows through a particular soil. Current standards for backfill materials do not specify minimum values of hydraulic conductivity, but rather rely on the specified grain-size distribution to produce acceptable values of hydraulic conductivity. The current grain-size specifications require a significant amount of coarse-grained particles to ensure adequate drainage. Nevertheless, this section compares laboratory-measured values of hydraulic conductivity for CC, RAP, and CFM.

A total of fifteen laboratory hydraulic conductivity tests were conducted on the test materials using the falling head-rising tail flexible wall method in accordance with ASTM D5084 “Standard Test Methods for Measurement of Hydraulic Conductivity of Saturated Porous Materials Using a Flexible Wall Permeameter.” Each material was tested at five different effective confining pressures (i.e., 5 to 50 psi), and five measurements of hydraulic conductivity were made on each specimen at each effective confining pressure. All tests were performed on specimens that were subsequently used for the consolidated-drained triaxial tests. Hydraulic conductivity testing was performed after backpressure saturation to the desired B value and after primary consolidation to the target effective confining pressure.

The hydraulic conductivity was calculated from the test data using the following expression (ASTM D 5084):

$$k = \frac{a_{in} \cdot a_{out} \cdot L}{(a_{in} + a_{out}) \cdot A \cdot \Delta t} \ln \left[ \frac{h_1}{h_2} \right] \quad (4.1)$$

where:

- $k$  = hydraulic conductivity, cm/s
- $a_{in}$  = cross-sectional area of influent reservoir, cm<sup>2</sup>
- $a_{out}$  = cross-sectional area of effluent reservoir, cm<sup>2</sup>
- $L$  = length of specimen, cm
- $A$  = cross-sectional area of specimen, cm<sup>2</sup>
- $\Delta t$  = elapsed time between determination of  $h_1$  and  $h_2$ , s
- $h_1$  = difference in hydraulic head across the specimen at time  $t_1$ , cm
- $h_2$  = difference in hydraulic head across the specimen at time  $t_2$ , cm

Because the test specimens have a relatively large value of  $k$ , a correction for the head loss from the porous stones and filter paper was used, although the correction was not significant. Table 4-3 lists the corrected  $k$  values of the test materials averaged from five measurements at each effective confining pressure.

In general, RAP has comparable  $k$  values with CFM. The  $k$  values of the CC specimens, however, are at least one order of magnitude smaller than those for RAP and CFM measured at the same  $\sigma'_c$ . Because the grain-size distributions of all of the test specimens are identical, it is believed that re-cementation of the CC particles may have impeded the water flow and resulted in the smaller  $k$  values. A hydraulic conductivity of  $10^{-4}$  cm/s has been proposed as an approximate boundary between free-draining and poorly-draining materials under low gradients (Casagrande and Fadum 1940). Based on this criterion, CC would be classified marginally as poorly draining, while RAP and CFM would be designated as free draining.

*Table 4.3 Summary of hydraulic conductivity results*

Effective Confining Pressure, $\sigma'_c$ (psi)	Hydraulic Conductivity, $k$ ( x $10^{-4}$ cm/s)		
	RAP	CC	CFM
5	38.4	1.6	13.8
20	25.7	0.84	21.8
30	27.7	0.18	6.4
40	12.7	0.12	4.5
50	5.5	0.11	6.0

## 4.5 Collapse Potential

When a granular backfill is compacted at a low dry density and water content, it can undergo significant settlement upon wetting. This deformation mechanism upon wetting is broadly called collapse. ASTM D5333, “Standard Test Method for Measurement of Collapse Potential of Soils,” defines a collapsible soil as a soil that can withstand relatively large applied vertical stress with small settlement while at a low water content, but exhibits considerable settlement after wetting with no additional increase in vertical stress. Therefore, a large applied vertical stress alone is not solely responsible for collapse.

The study of collapsible soils has been reported in the literature (e.g., Lutenecker and Saber, 1988; Lawton et al., 1992; Houston et al., 1993). Many of these studies concluded that the most critical factors controlling the collapse potential of a given compacted soil are the as-compacted degree of saturation, the as-compacted dry density, and the total overburden pressure, with the collapse potential decreasing with increasing dry density and as-compacted water content. Two additional important observations reported by Lawton et al. (1992) are that there is a critical value of vertical stress and a critical value of degree of saturation, above which negligible collapse occurs.

The experimental study on collapse potential was conducted in accordance with ASTM D 5333, which simply involves one-dimensional deformation measurement of a laterally confined material upon wetting. These tests were performed on the direct shear test specimens prior to performing the direct shear tests. After each specimen was compacted to its full height inside the direct shear box and all the vertical dial gauges were in place, a seating pressure of 1.5 psi was applied to the top of the specimen. Normal stress increments were applied to the specimen until the target normal stress was reached. Each stress increment was maintained on the specimen until no additional vertical movement was observed. After the target normal stress was reached, water was slowly introduced into the water tank from the bottom to avoid trapping of air bubbles inside the specimen, and water was added until the specimen was fully inundated. Vertical movement of the specimen was recorded throughout this entire process. Readings were taken until no significant additional change in vertical movement was observed.

Collapse measurements were conducted on five specimens of CFM and CC, at applied normal stresses ranging from 1.5 psi to 28 psi. Because direct shear tests on RAP were only performed at 10 psi and 20 psi because of creep issues, only two collapse measurements were obtained for RAP. Figure 4-14 illustrates the measured vertical deformation versus applied normal stress for the CC and RAP specimens obtained from this study. The initial deformation was offset to zero at the 1.5 psi seating pressure to remove any compression from specimen surface irregularity and machine compliance. The curves illustrate the compression during consolidation to the desired normal stress and then the additional deformation after soaking. The data in Figure 4-14 reveal that deformations upon wetting for CC are minimal, but are larger for RAP.

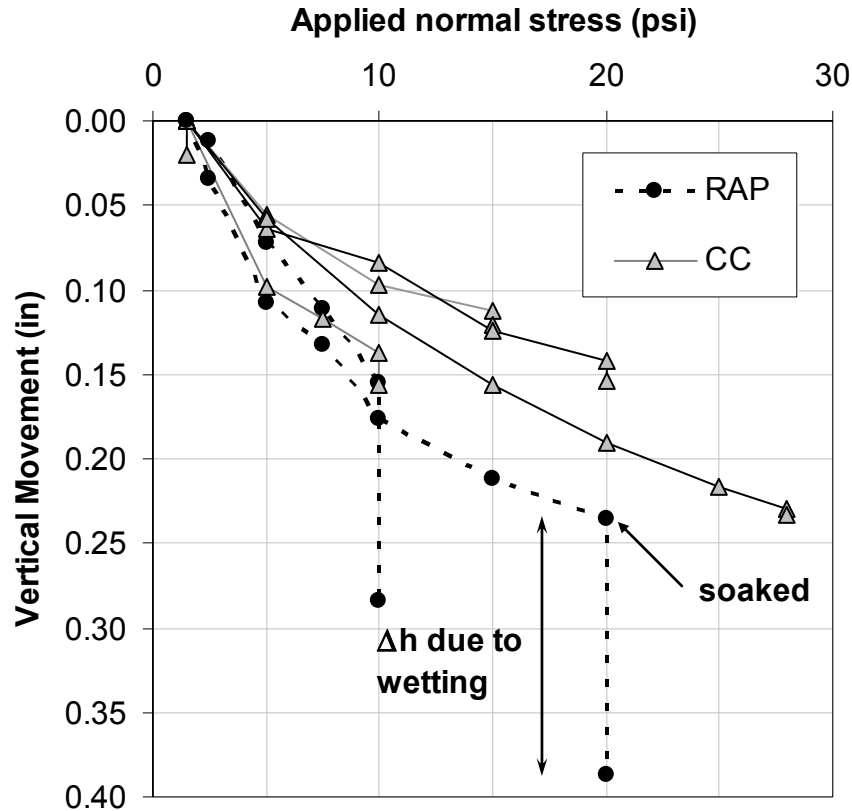


Figure 4.14 Compression curves from collapse potential tests

ASTM D 5333 defines a parameter called the collapse index ( $I_c$ ) to quantify the collapse potential of a soil for the specific vertical stress of interest. This index property is simply the vertical strain, as a percentage, due to wetting and, thus can be directly used to estimate field settlement upon wetting of the same soil under the same vertical stress. The collapse index is defined as:

$$I_c (\%) = \frac{\Delta h}{h_o} \cdot 100 \quad (4.2)$$

where:

- $\Delta h$  = change in specimen height due to wetting (in)
- $h_o$  = initial specimen height prior to wetting (in)

The compression owing to wetting for each test specimen was used to calculate the collapse index. Figure 4-15 displays the resulting collapse indices of the test materials at different applied normal stresses. For CC and CFM,  $I_c$  is very small (0.05 percent to 0.2 percent) and there is no observable trend with normal stress. The  $I_c$  values for RAP are larger (~1.5 percent) and appear to increase slightly with increasing normal stress. The ASTM classification for soil collapse potential based on the laboratory-measured  $I_c$  value is shown in Table 4-4. Based on this classification, CC and CFM both have “none” to “slight” collapse potential. The  $I_c$  values for

RAP were larger than for CC and CFM, but RAP still classifies as “slight” collapse potential, although at the upper end of the range.

The more significant collapse deformation of RAP is most likely because of its initial low degree of saturation (approximately 30 percent) as compared to CC and CFM (approximately 70 percent and 80 percent, respectively). The RAP specimens were not constructed at larger water contents/saturation values because they could not hold additional water owing to the bitumen coating. RAP particles also are less angular than CC and CFM, and thus may collapse more easily. Finally, the collapse potential for CC and CFM may be so small because of the perceived re-cementation of the particles. Cementation of the particles would inhibit deformation of the particles and minimize its collapse potential.

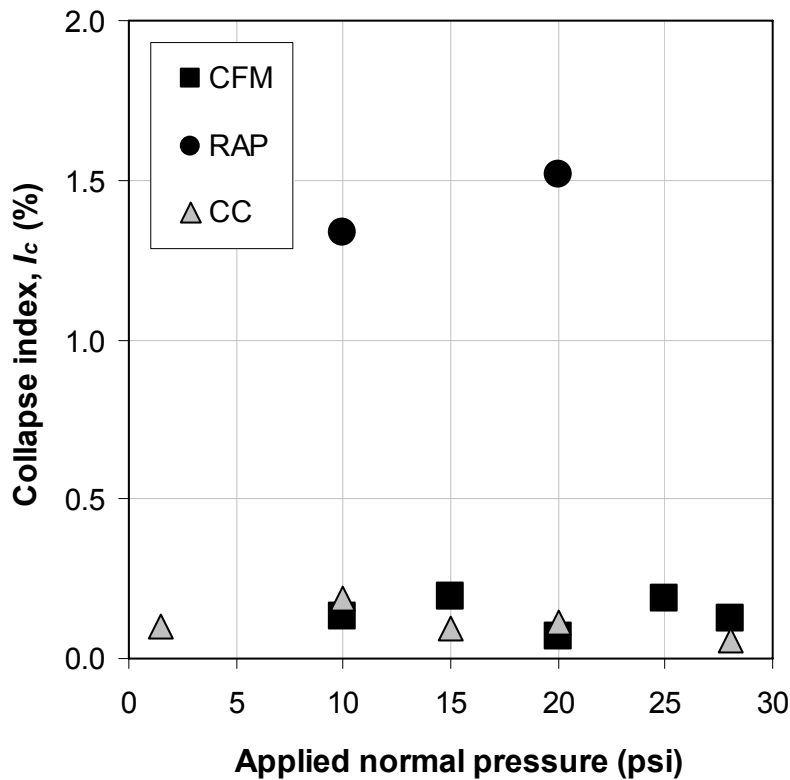


Figure 4.15 Collapse indexes of test materials at different normal stresses

Table 4.4 ASTM classification of collapse index

Degree of Collapse	Collapse Index, $I_c$ (%)
None	0
Slight	0.1 to 2.0
Moderate	2.1 to 6.0
Moderately severe	6.1 to 10.0
Severe	> 10

#### 4.6 Field Compaction

Control of backfill compaction during construction of an MSE wall is critical for proper wall performance. The compacted dry density and water content of a backfill affect its shear strength, hydraulic conductivity, and compressibility, as well as the pullout capacity of the reinforcing elements in the fill. For granular materials, the dry density is the most important compaction condition; a large dry density yields a stronger, less compressible material. For backfill materials with significant fines, water content and dry density are important, with relatively small variations in as-compacted water content adversely affecting backfill shear strength, drainage, compressibility, and reinforcement pullout capacity. Moreover, backfills that are too wet during MSE wall construction can make it difficult to maintain acceptable facing alignment, while materials that are compacted too dry may experience excessive settlement upon subsequent wetting (Elias and Christopher 1996).

Because the compacted dry density, and to a lesser extent moisture content, are critical to the performance of an MSE wall, field compaction control is performed on a regular basis during backfill construction. Nuclear gauges are widely used to measure in-place density and moisture content because the test results can be obtained rapidly. An experimental investigation was conducted to evaluate if the elemental composition of CC and RAP affects the accuracy of the nuclear gauge.

Sand cone, rubber balloon (volumeter), and test pit methods have long been used to measure the in-place density of compacted material. These conventional methods require the manual excavation of a small test hole and are somewhat time consuming. Water contents are obtained by drying the excavated material in an oven, a step that normally takes 12 to 24 hours and significantly delays the final test results. Nuclear gauges, introduced in the 1950's, provide a more rapid means of measuring in-place density and water content. The following sections describe testing procedures for the sand cone, rubber balloon, test pit, and nuclear gauge tests. The advantages and disadvantages of each method are also discussed.

#### 4.6.1 Methods for Field Compaction Control

The sand cone test method (ASTM D1556) is generally accepted as an accurate means of measuring in-place soil density (Mamlouk 1988). The test is performed by first excavating a hole in the test material. The excavated material is weighed and stored in a container for later moisture content determination. A dry uniform reference sand with a known density is then poured into the hole. The weight of the sand placed in the hole is measured and, knowing the density of the reference sand, the volume of the hole can be determined. The moist density is calculated from the weight of excavated material and the volume, while the dry density is computed from the measured moist density and water content.

The sand cone method takes a substantial amount of time, and the water content must be determined by oven drying. Further, the sand cone method is limited to soils that are stiff enough for an excavated hole to remain open without significant deformation or volume change during the test. This test works best in unsaturated soils where water will not seep into the excavated hole. One further drawback is the inevitable commingling of the reference sand with the test material after the test is completed.

The rubber balloon method (ASTM D2167) is similar to the sand cone method. However, instead of pouring a reference sand into the excavated hole, the volume of the hole is measured with a water-filled balloon under a calibrated operating pressure. The volume of the water required to fill the hole, and thus the hole volume, is determined from a graduated cylinder. With the volume of the hole and weight of excavated material known, the in-place density of the test material can be calculated.

One of the major problems associated with the rubber balloon method is the deformation of the excavated hole during the application of the operating pressure. Expansion of the hole is more pronounced when the testing materials are relatively soft or deformable. Inaccurate results can also be attributed to the presence of rocks or coarse particles that make the sides of the hole irregular; rough sides make it difficult for the balloon to fill the entire hole. Moreover, the test can be difficult to perform in materials containing sharp particles that may puncture the rubber balloon. Again, water contents must be determined by oven drying.

The test pit method (ASTM D5030) is based on the same principle as the rubber balloon test, but the excavated hole is significantly larger. In general, a test pit is performed by excavating the test location and replacing the existing soil with a known amount of water. This step determines the volume of the excavation. Knowing the excavation volume and the weight of the soil excavated, the in-place moist density can be calculated. This method typically is used for materials that contain particles larger than 3 in. The test pit method is reasonably simple and straightforward, but it is more time consuming (approximately 30 minutes per test) than the rubber balloon method because of the larger excavation required.

Over the last 50 years, the nuclear gauge test (ASTM D 2922 and ASTM D 2950) has become a popular tool for measuring the in-place soil density and water content. The test method is rapid (less than 5 minutes per measurement) and allows repetitive measurements to be made at a single test location. A nuclear gauge provides simultaneous, independent measurements of the moist density and water content of the compacted material. For density measurements, the device

employs a small gamma radiation source and one or more gamma photon detectors. The moisture content determination involves a fast neutron source and a thermal neutron detector. There are two modes of operation for the nuclear gauge, routinely referred to as “direct transmission” and “backscatter.”

In direct transmission, a rod containing a cesium-137 source is lowered to a predetermined depth (Figure 4-16). Gamma photons emitted by the source travel through the material to the detector, which is located at the base of the nuclear gauge. The density measured by this mode is representative of the material density in the path between the source and the detector (Regimand and Gilbert 1999).

For the backscatter mode, the cesium-137 source is placed on the surface of the test material (Figure 4-16). The gamma photons are introduced into the material and must be reflected to reach the detector (Troxler 2001). Because the measured photons are reflected, the average energy of the photons detected by this method is usually lower than the average energy of the photons detected by the direct transmission method. The density measured in the backscatter method is representative of the average density of the material near the surface.

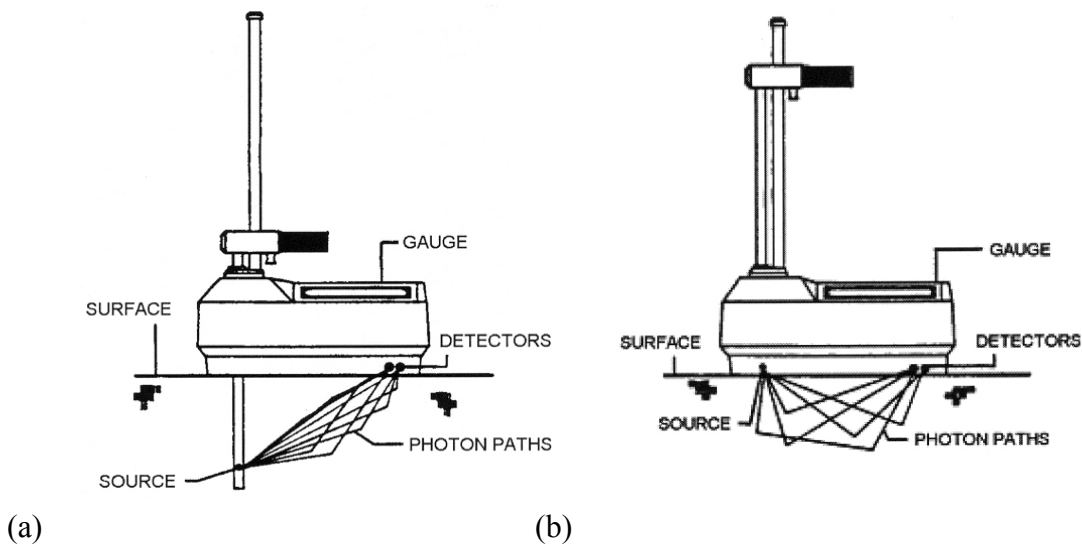


*Figure 4.16 Nuclear gauge setup: (a) direct transmission method and (b) backscatter method (from Troxler 2001)*

The nuclear gauge measures density indirectly by counting the emitted gamma photons that reach the detector. The number of gamma photons reaching the detectors is inversely proportional to the material density (more collisions in higher density materials mean fewer gamma photons reach the detectors). The number of detected gamma photons is usually referred to as the “count ratio”. A calibration chart that relates count ratio to material density is used to determine the material density during testing.

The chemical composition of the material being tested may affect the measured densities, because elements with high atomic numbers will absorb more photons (Nagi and Whiting 1999).

Consequently, a calibration developed from one type of material may not yield an accurate result if it is used to measure density in a different type of material. Accordingly, a calibration curve should be developed for the particular material to be tested (Kennedy et al. 1989; Nagi and Whiting 1999).

To measure water content, the nuclear gauge emits neutrons into the test material. These neutrons are uncharged and collide with the nuclei of other atoms, which reduces the velocity of the neutrons to a minimum. Neutrons traveling at this minimum velocity are called "thermalized" neutrons. Hydrogen nuclei are most efficient in thermalizing neutrons, so the number of thermalized neutrons is proportional to the mass of hydrogen in the material (Nagi and Whiting 1999; Troxler 2001). Thus, by counting the thermalized neutrons that reach the detector, one obtains a measure of the number of hydrogen atoms in the material, which is related to water content. It is important to note that the nuclear gauge relates water content to the number hydrogen atoms present, not to the number of water molecules (Nagi and Whiting 1999). This will cause errors when measuring the water content of materials that contain significant sources of hydrogen other than water.

#### **4.6.2 Field Testing Program and Results**

Testing was performed on the three material stockpiles located at the Pickle Research Center at UT Austin. A front-end loader was used to level off the top of each stockpile while maintaining a minimum height of about 2 ft within the stockpile. The same front-end loader was driven back and forth on the stockpiles to introduce some degree of compaction in the material. The surfaces of the stockpiles at each test location were then leveled using a straight edge. Before testing, water was introduced to vary the water content at each test location.

The experimental program was designed to compare moist densities measured with the nuclear gauge to moist densities obtained from the rubber balloon method. For these tests, the rubber balloon method was selected over the sand cone method to avoid mixing sand into the stockpiled material. Moisture contents obtained with the nuclear gauge were compared to water contents measured by oven drying.

Before testing, calibration of the nuclear gauge was performed according to ASTM D2922. The moist density and water content were then measured at each test location with the nuclear gauge. For this experiment, the direct transmission mode was used because it yields more accurate results (Troxler 2001). Before performing each test, a scraper plate and rod guide were used to prepare the test location and drive a hole for the instrument rod. The radioactive source on the instrument was then advanced in the hole to a depth of 6 in.

Immediately after the nuclear gauge was removed from the test location, a rubber balloon test was performed. A 4-in. diameter hole was excavated to a depth of about 5 in., with the center of the 4-in. diameter hole lying directly between the previous locations of the radioactive source detector. The excavated materials were weighed and stored in containers for moisture content determination through oven drying. The volume of the excavated hole was then measured using a rubber balloon apparatus, with a pre-calibrated operating pressure of 4 psi.

The moist densities for CC, RAP, and CFM as measured by the nuclear gauge and rubber balloon method are compared in Figure 4-17. This figure shows that the moist density measured by the nuclear gauge was consistently larger than the moist density measured by the rubber balloon method for all materials. For each material, the nuclear gauge shows a relatively small variation in the measured densities with all values within  $\pm 5$  percent of each other, suggesting that all three stockpiles had a fairly uniform density. The moist densities measured by the rubber balloon method scatter significantly and were smaller than those measured by the nuclear gauge. This observation is consistent across all of the materials.

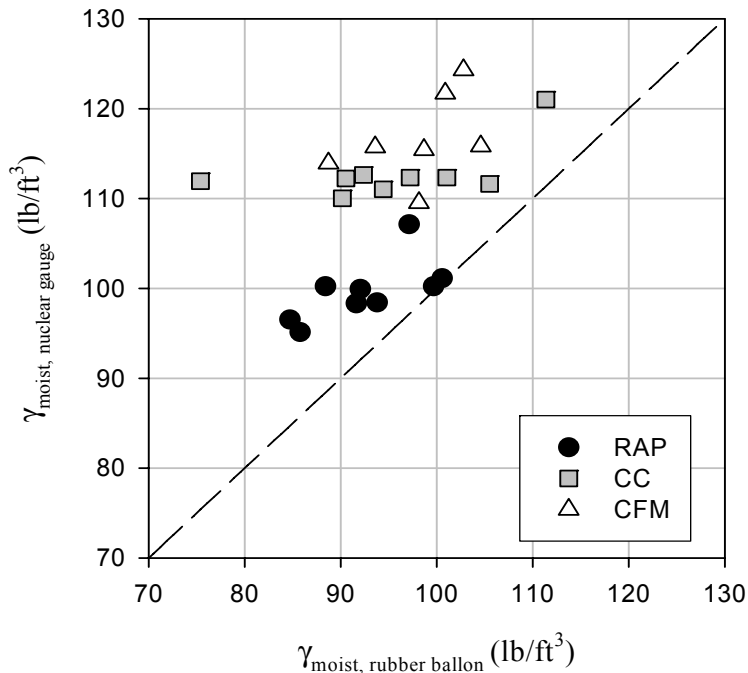


Figure 4.17 Comparison of moist densities measured by rubber balloon and nuclear gauge methods in all three material stockpiles

A comparison of these data can be made in terms of the ratios between the values measured from the nuclear gauge ( $\gamma_{m,NG}$ ) and the values obtained from the rubber balloon method ( $\gamma_{m,BAL}$ ). Table 4-5 shows the average ratio and standard deviation of the ratios for each material tested, as well as the minimum and maximum ratios. On average, the nuclear gauge reports moist densities nearly 20 percent higher than the rubber balloon method for CFM and CC. For RAP, the nuclear gauge is about 10 percent higher. The scatter in the data is most significant for the CC. These values are larger than other studies that found that the nuclear gauge only slightly overpredicted density (Kennedy et al. 1989; Sanders et al. 1994).

The discrepancies in the test data may be attributed to several factors. For the nuclear gauge measurements, it is possible that the soil used to calibrate the nuclear gauge was significantly different from the materials used in this study, making the calibration less accurate. As mentioned previously, calibration of the nuclear gauge with one material may not be appropriate for other materials. For this reason, a calibration curve should be developed for the particular materials on site to ensure accurate results. This is most critical when the test material contains

high atomic number elements that can affect the gauge count (Nagi and Whiting 1999), especially CC and CFM, where calcium ions ( $\text{Ca}^{2+}$ ) are plentiful.

*Table 4.5 Ratio of moist densities measured by nuclear gauge ( $\gamma_{m,NG}$ ) and rubber balloon method ( $\gamma_{m,BAL}$ )*

<b>Ratio</b>		<b>RAP</b>	<b>CC</b>	<b>CFM</b>
$\frac{\gamma_{m,NG}}{\gamma_{m,BAL}}$	Average	1.08	1.19	1.19
	Std. Dev.	0.05	0.13	0.06
	Min to Max	1.01 to 1.14	1.06 to 1.48	1.11 to 1.28

Additionally, the presence of large-sized particles may have affected the nuclear gauge measurements and contributed to the observed differences. When the test material contains large particles or large voids, irregularities may occur in the source-detector path and cause higher or lower measured densities, respectively. To minimize this problem, multiple nuclear gauge tests should be performed at adjacent locations to get an average result (ASTM D2922). However, the nuclear gauge data in Figure 4-16 exhibit relatively limited scatter, especially in the RAP and CC, indicating that the large particles did not impact the results.

In terms of the rubber balloon measurements, the excavated hole may have expanded under the applied operating pressure during the rubber balloon test. However, the field material was stiff and most likely did not deform significantly under the balloon pressure. Large particles also affect the rubber balloon test results if the excavated hole is too small to adequately sample all particle sizes. ASTM D2167 specifies larger excavation volumes for materials containing larger particle sizes. For the maximum particle size of the test materials (2 in.), ASTM D2167 recommends a minimum excavation volume of 2840 cm<sup>3</sup>. Unfortunately, the rubber balloon apparatus used in this study could accommodate volumes only up to 1420 cm<sup>3</sup>, not large enough for the particle size distribution of the test materials. This may have adversely affected the densities measured by the rubber balloon method.

The effect of large particle sizes on the rubber balloon densities was evaluated by comparing moist densities measured using the test pit method with moist densities measured by the rubber balloon method. Nine additional test locations on newly recompacted stockpiles of RAP and CC were selected for this comparison study. At each test location, a rubber balloon measurement was first performed, followed promptly by a test pit measurement at the same location. Moist densities measured from both methods are compared in Figure 4-18. The comparison plot shows that seven out of nine rubber balloon test results were lower than the densities measured by the test pit method by an average of 10 percent. This suggests that the undersized holes excavated for the rubber balloon test did not adequately sample all the particle sizes. Also, the results do not suggest that the type of test material would affect the discrepancies.

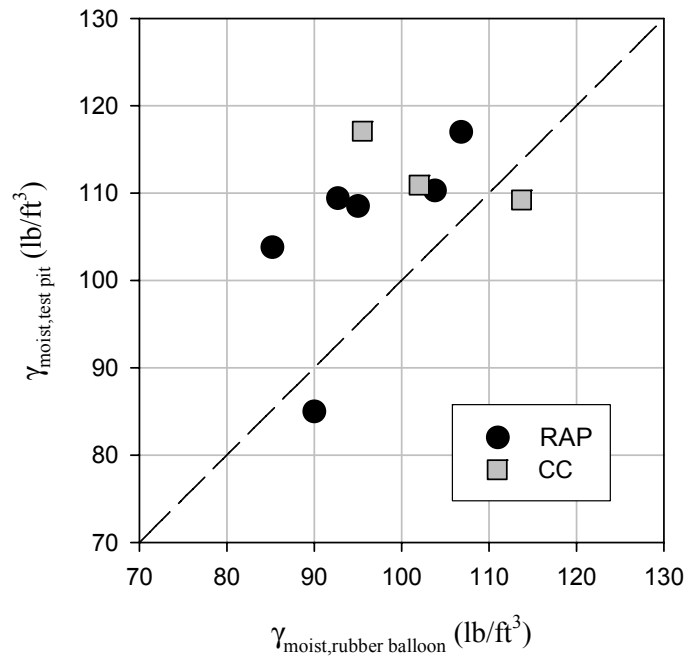


Figure 4.18 Comparison of moist densities measured by rubber balloon and test pit methods

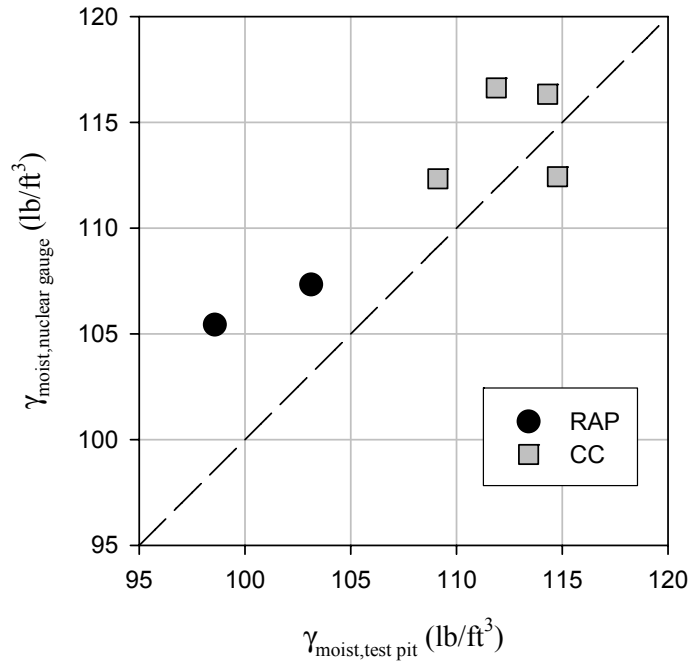


Figure 4.19 Comparison of moist densities measured by test pit and nuclear gauge

Based on this result, it was apparent that a comparison between nuclear gauge and test pit measurements was required. Additional measurements were performed on the CC and RAP stockpiles using the test pit and nuclear gauge methods. At each test location, a nuclear gauge measurement was immediately followed by a test pit measurement. Moist densities measured from these two techniques are compared in Figure 4-19. Here, overprediction by the nuclear gauge (average of 3 percent higher) was less than indicated by the rubber balloon and nuclear gauge comparisons. Hence, it is apparent that the inadequate size of the rubber balloon excavation was the key contributing factor for the inaccurate results found earlier. Assuming all the test pit measurements were accurate, this last set of test results suggests that the nuclear gauge can be a competent density-measuring device for RAP and CC backfill.

Water contents measured by the nuclear gauge and oven drying for the RAP, CC, and CFM are compared in Figure 4-20. The ratios of water contents measured by the two methods for each material are given in Table 4-6. The nuclear gauge gives acceptable results for the CFM when compared to the oven-dried values, with an average ratio of 0.99. Moisture contents measured by the nuclear gauge for CC are somewhat higher (about 20 percent higher, on average) than the values measured by oven drying. For RAP, the nuclear gauge water contents are considerably higher. On average, the nuclear gauge reports that water contents in the RAP are three times larger than those obtained from oven drying.

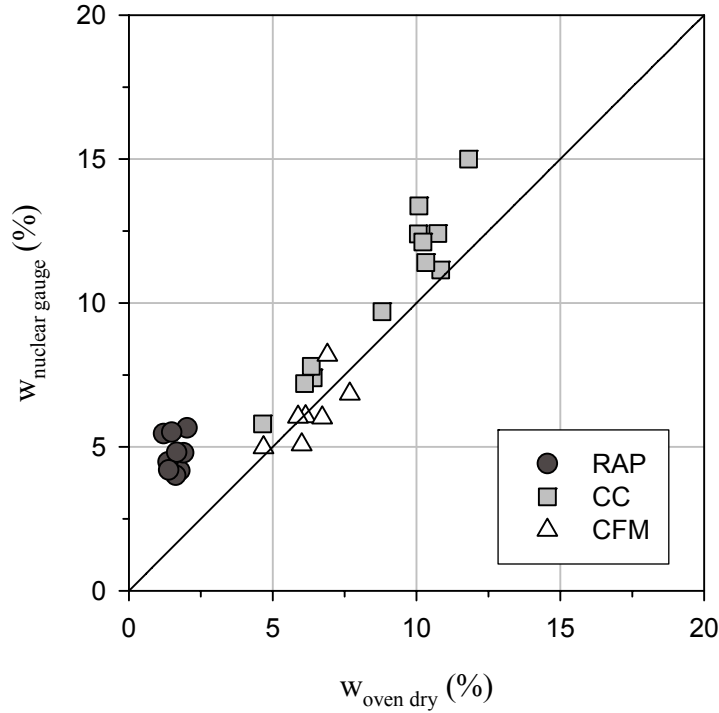


Figure 4.20 Comparison of the moisture contents measured with the nuclear gauge and oven drying

Table 4.6 Ratio of moisture contents measured by nuclear gauge ( $w_{NG}$ ) and oven drying ( $w_{oven}$ )

Ratio		RAP	CC	CFM
$\frac{w_{NG}}{w_{oven}}$	Average	3.07	1.19	0.99
	Std. Dev.	0.69	0.10	0.12
	Min. to Max.	2.36 to 4.51	1.03 to 1.33	0.84 to 1.19

The overestimation of the moisture content in the CC and RAP is a result of the nuclear gauge’s measuring the amount of hydrogen atoms in the material, not the amount of water. The slightly larger measured water contents in CC may be the result of additional hydrogen atoms in the admixtures, modifiers, and cement paste (Nagi and Whiting 1999). For RAP, there are two potential sources of hydrogen other than free water in the mix, the asphalt cement binder and the aggregate minerals (Black 1995). The asphalt cement binder, a petroleum product comprised of a

mixture of hydrocarbon molecules, is the main source of excess hydrogen atoms in RAP. Therefore, these excess hydrogen atoms from the asphalt cement binder lead to an overestimation of water content for RAP as measured by the nuclear gauge.

## **4.7 Durability of CC**

Deleterious materials and harmful impurities in CC may affect the durability of CC backfill. Recycled CC from structures that have suffered from alkali-silica reaction (ASR) and sulfate attack may still be susceptible to expansion after compaction. Because only limited work has focused on assessing the durability of CC when used as a backfill for MSE walls, research was needed to evaluate the potential issues related to using CC, which previously showed poor durability in its originally intended use. To investigate the effects of these attacks on the performance of compacted backfill, concrete was produced in the laboratory and used for accelerated expansion tests. Results from laboratory-produced concrete were then compared with tests performed on CC from commercial producers.

### **4.7.1 Expansion Caused by Alkali-Silica Reaction**

Three essential components are necessary for ASR-induced damage in concrete: (1) reactive silica (from aggregates), (2) sufficient alkalies (mainly from portland cement), and (3) sufficient moisture. The reaction occurs between the hydroxyl ( $\text{OH}^-$ ) ions in the pore solution and certain siliceous components of the aggregates. The presence of high concentrations of sodium and potassium alkalies in the pore solution results in an equally high concentration of  $\text{OH}^-$  ions. It is this high  $\text{OH}^-$  concentration, and thus high pH, that leads to the initial breakdown of reactive silica components in the aggregates. The alkalies ultimately contribute to the formation of expansive ASR gel, which absorbs water and leads to cracking.

To measure expansion caused by ASR attack, compacted CC samples were placed in both water and 1N-NaOH (alkaline) solution. All of the samples were then stored in a 38 °C (100.4 °F) reaction-accelerating control chamber and allowed to expand, with the expansion measured over time for 70 to 100 days. The test apparatus used to measure expansion of compacted CC is shown in Figure 4-21. Bulk CC samples from the commercial producers were tested, as well as CC crushed from laboratory concrete, which used a particularly reactive silica aggregate from El Paso, Texas. During curing, some of the laboratory concrete specimens were subjected to the ASTM C 1293 accelerated ASR prism expansion test at an elevated temperature of 140 °C (284 °F), while some of the prisms were cured under traditional moist cure conditions. The objective was to test expansion of the compacted CC, recycled from a possible worst-case concrete mixture.



*Figure 4.21 Test Apparatus for Compacted CC Expansion Samples*

Figure 4-22 shows expansion results for the laboratory CC samples that had been subjected to ASR attack; half of the samples were placed in water (samples 1, 2, and 3) and half in 1N-NaOH solution (samples 4, 5, and 6). Likewise, Figure 4-23 shows laboratory CC samples that had *not* been subjected to ASR attack; half of the samples were placed in water (sample 7, 8, and 9) and half in 1N-NaOH solution (sample 10, 11, and 12). Placing the samples in water allowed for comparing the results with samples placed in the alkaline solution.

A limit of 0.04 percent expansion was used to indicate potential for ASR problems in concrete prisms. Although this expansion limit is reasonable for concrete, it is significantly low for compacted CC because there is no concern for structural cracking. Only excessive movements of the ground surface or facing panels are of concern in MSE walls. Because no limits have been established to characterize potential ASR problems in compacted crushed concrete, the 0.04 percent expansion has been used for discussions in ensuing sections.

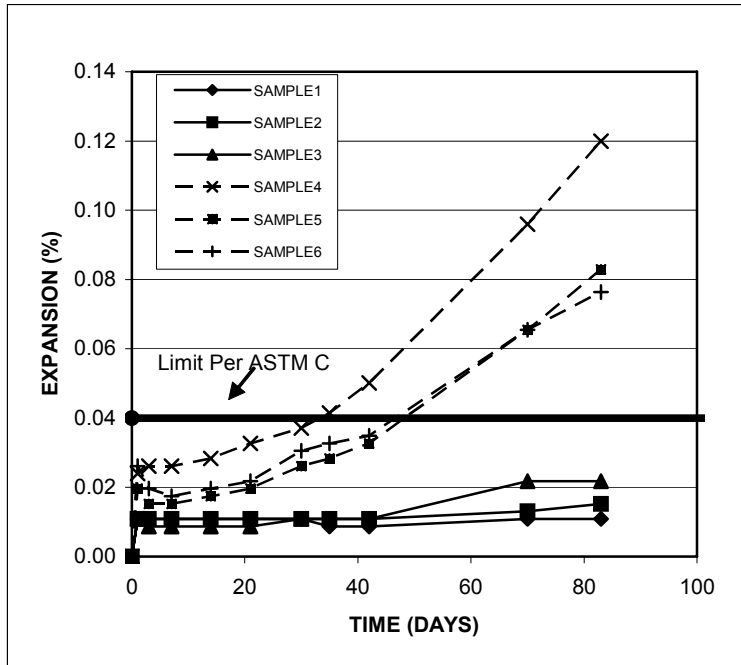


Figure 4.22 Laboratory CC ASR Expansion Samples. Samples 1,2,3 in Water; samples 4,5,6 in 1N-NaOH Solution (Concrete had Previously Experienced ASR Attack)

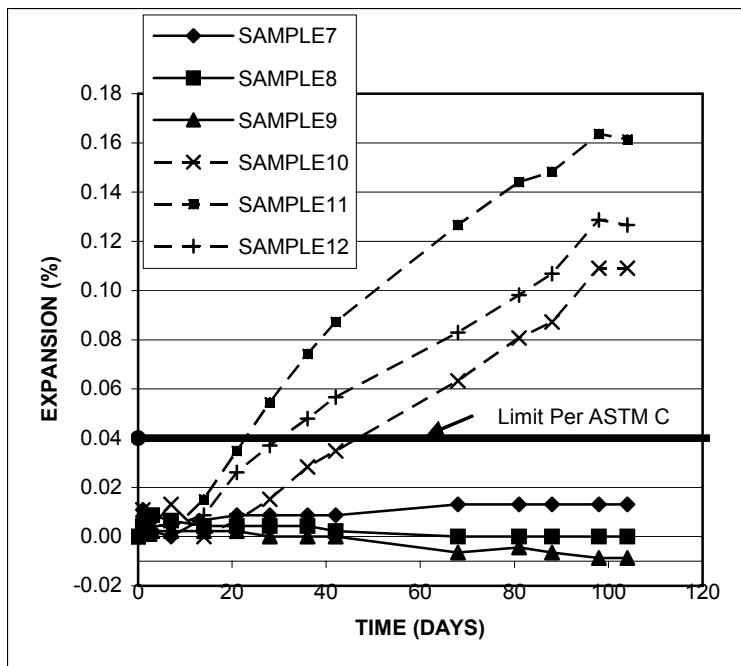


Figure 4.23 Laboratory CC ASR Expansion Samples. Samples 7, 8, 9 in Water; Samples 10, 11, 12 in 1N-NaOH Solution (Concrete had not Experienced ASR Attack)

The ASR samples stored in water (samples 1, 2, and 3, Figure 4-22) did not experience any expansion and were below the 0.04 percent limit. The apparent explanation for this is that the alkalis in the CC were leached into the water, thus minimizing the effects of alkali aggregate reaction. In contrast, samples 4, 5, and 6, which were stored in alkaline solution, continued to expand and reached an average maximum of 0.095 percent at approximately 80 days.

The non-ASR samples stored in water (samples 7, 8, and 9, Figure 4-23) did not expand and behaved in a similar manner to samples 1, 2, and 3 (Figure 4-22). Again, lack of expansion in compacted samples stored in water likely results from leaching of alkalis in the compacted CC. Samples 10, 11, and 12, stored in alkaline solution, experienced an expansion much higher than the 0.04 percent limit, with an average maximum expansion of 0.132 percent observed after 104 days (Figure 4-23).

These results indicate that CC developed from concrete with reactive aggregate can expand by as much as 0.1 percent when a significant alkaline solution is present. However, the expansion is minimal when the CC is placed in a water solution.

Expansion data on compacted CC samples from the commercial producer are given in Figure 4-24. This figure shows that the CC stored in alkaline solution expanded less than 0.01 percent, and in some cases compressed. These results suggest the absence of reactive aggregates in the commercial CC used in this study.

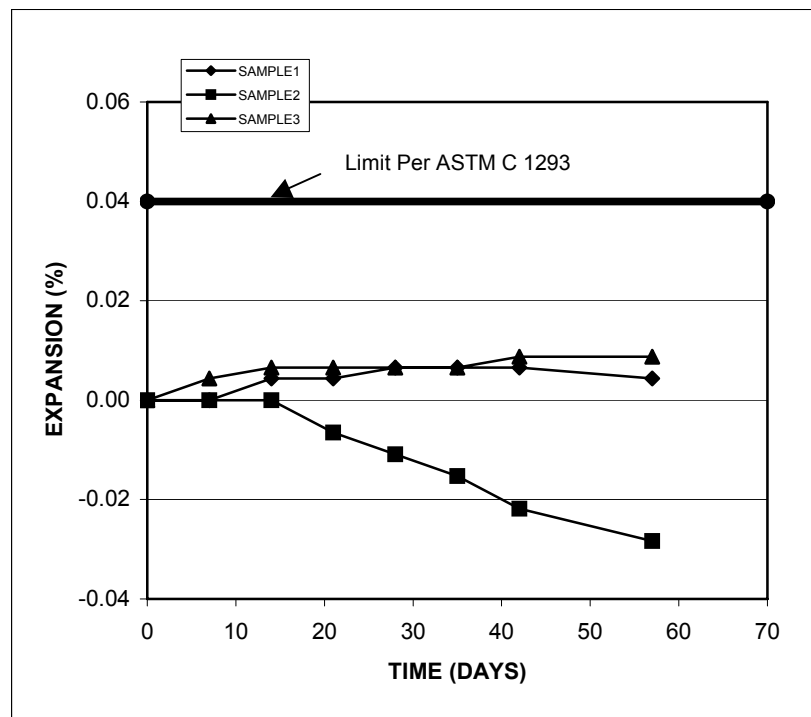


Figure 4.24 Commercial CC ASR Expansion. Samples placed in 1N-NaOH Solution.

#### 4.7.2 Expansion Caused by Sulfate Attack

In the case of sulfate attack, portland cement concrete is attacked by solutions containing sulfate, such as some natural water or polluted groundwater. Attack can lead to strength loss, expansion, spalling of surface layers, and ultimately disintegration.  $\text{Na}_2\text{SO}_4$  and  $\text{MgSO}_4$  in the attacking solution will react with the cement paste, resulting in the formation of ettringite and gypsum. Of concern to MSE facing walls is the expansion that may result because of absorption of water by the ettringite.

CC from laboratory concrete that had been exposed to sulfate attack was tested, as well as the bulk CC from the commercial source. The samples were tested in the same expansion chamber, as previously discussed, and the samples were soaked in either a water solution or a 5 percent sulfate solution.

Figure 4-25 shows expansion results of laboratory CC samples that were constructed from concrete that had previously experienced sulfate attack. Half of the samples were placed in water (samples 1, 2, and 3) and half in a sulfate solution (samples 4, 5, and 6). The samples stored in water show an average expansion of 3.9 percent at 69 days. For those stored in sulfate solution, the average expansion was 2.9 percent at 69 days. The large expansions observed for the two cases result from the large quantity of gypsum added to the concrete, resulting in a total of 9.0 percent  $\text{SO}_3$  by mass of cement and gypsum. These results show that concrete that has previously experienced sulfate attack will continue to expand after crushing and compaction, even when exposed only to water.

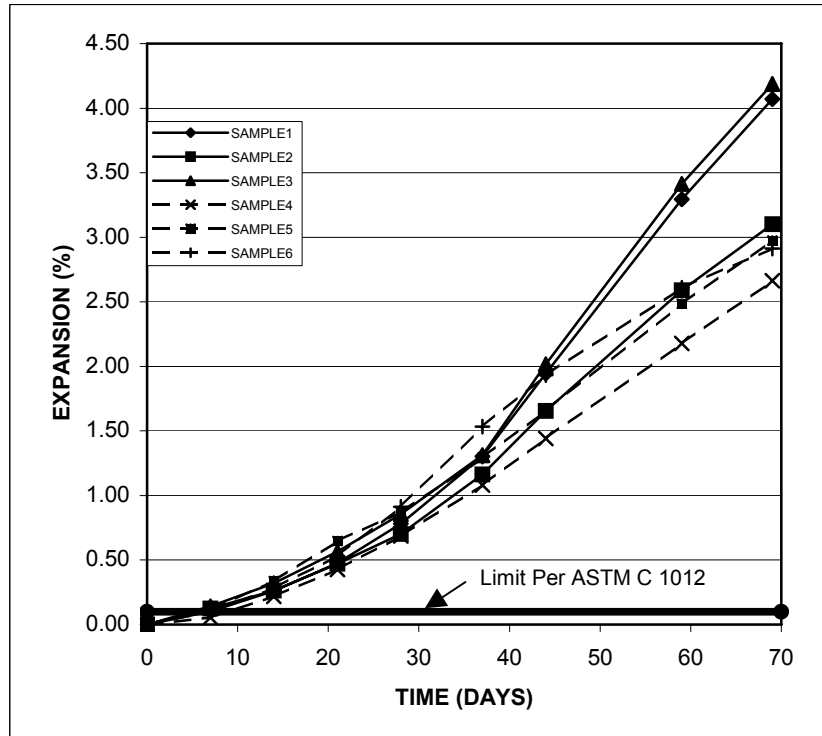


Figure 4.25 Laboratory CC Sulfate Expansion Results. Samples 1,2,3 in Water; Samples 4,5,6 in 5% Sulfate Solution (Samples from concrete that had Previously Experience Sulfate Attack).

Expansion of the compacted CC samples from the commercial producer, stored at 38 °C (100.4 °F) in a 5 percent sulfate solution, is plotted in Figure 4-26. It was observed that the compacted CC, stored in 5 percent sulfate solution, expanded to levels between 0.1 percent and 0.3 percent after 57 days of exposure, which is significantly less than experienced in the worst-case laboratory CC. These results suggest that sufficient amounts of calcium hydroxide and monosulfate hydrate were still available for sulfate attack. However, it should be noted that the exposure to 5 percent sulfate solution is very aggressive and not typical in actual MSE wall applications.

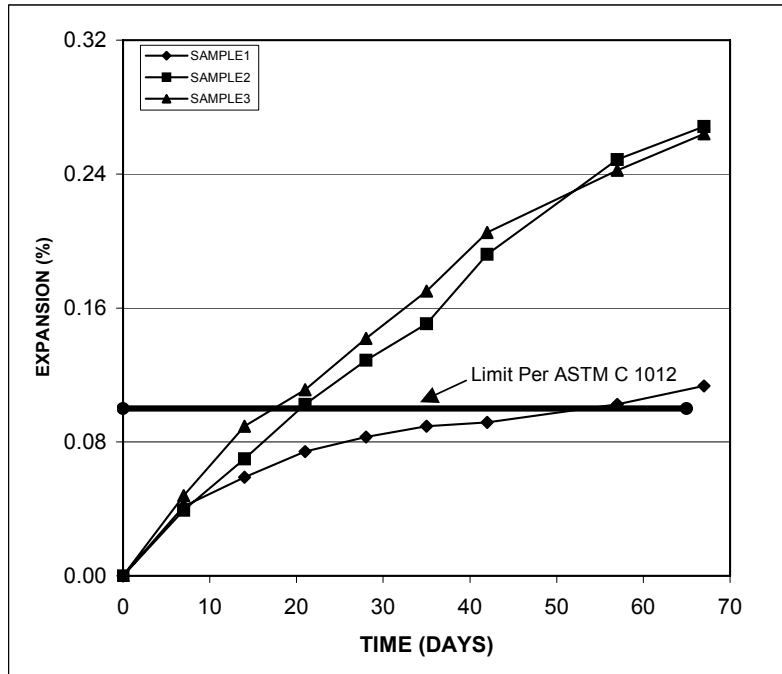


Figure 4.26 Commercial CC Sulfate Expansion Results. Samples placed in 5% Sulfate Solution.

## 4.8 Summary

This chapter presented results from a large series of tests aimed at characterizing the basic geotechnical properties of CC and RAP. Shear strength, hydraulic conductivity, collapse potential, field compaction, and durability were all assessed.

Strain-controlled, consolidated-drained triaxial tests and stress-controlled, large-scale direct shear tests were performed to assess the shear strength of CC and RAP over confining pressures from 5 to 100 psi. For CC, these tests indicate  $\phi' = 46^\circ$ ,  $c' = 8.7$  psi for this confining pressure range. These values are similar to those obtained for the CFM. The strain-controlled triaxial test results indicated  $\phi' = 37^\circ$ ,  $c' = 8$  psi for RAP, but the stress-controlled direct shear tests indicated significant creep deformations. Creep will be investigated in detail in Chapter 6.

The average measured hydraulic conductivity ( $k$ ) of RAP was  $10^{-3}$  cm/s, which is slightly larger than the value measured for the CFM. The measured  $k$  values of the CC were between  $10^{-5}$  cm/s and  $10^{-4}$  cm/s. These values indicate that CC is only marginally free-draining and additional drainage may be required behind an MSE wall.

The collapse potential of CC and RAP was minimal and this mechanism of deformation should not be a concern. Similarly, significant expansion of CC caused by alkali-silica reaction and sulfate attack should be minimal. Field compaction results indicated that the nuclear gauge may significantly overpredict the water content of RAP because of the additional hydrogen contained

in the bitumen coating. A slight overprediction was observed in CC because of the hydrogen contained in the cement paste.

Durability tests on CC indicated that significant expansion may occur if the original concrete had suffered sulfate attack. The laboratory produced CC that was exposed to sulfate attack experienced as much as 4 percent expansion when placed in a water solution. CC from commercial producers did not experience significant expansion. In general, it will be known if a concrete structure is taken out of service owing to sulfate attack. If this is the case, it is recommended that this concrete not be used for MSE backfill.



## **5. Evaluation of Pullout Resistance for CC and RAP**

### **5.1 Introduction**

Laboratory pullout experiments were conducted in a medium-sized (20 in. by 20 in. by 10.5 in. tall) pullout box, which is the same box that was used in the direct shear testing. Because this box is smaller than commonly used for pullout tests, it was necessary to ensure that the results from the box were reasonable. Hence, tests were performed on Ottawa Sand (OS) to compare the results with those obtained by Law Engineering and Environmental Services, Inc. (1998) using a large pullout box. After these validation tests, experiments were performed with metallic strip reinforcement embedded in CFM, CC, and RAP.

### **5.2 Experimental Materials and Test Equipment**

Pullout tests were performed using CFM, CC, RAP, and standard Ottawa Sand. The properties of CFM, CC and RAP were described earlier and each material was compacted for testing using the same input energy as Tex-113-E (2001). This is the same procedure that was used to construct the direct shear specimens. The Ottawa Sand (OS) conforms to ASTM C 778 ( $\phi' = 33^\circ$ ,  $G_s = 2.65$ ) and was used to permit direct comparisons with results obtained in a larger pullout test machine. The gradation of OS, with all particles between 0.15 mm and 1.18 mm (No. 100 to No. 16 sieve), is shown in Figure 5-1. The gradation curve shows that the sand is uniformly graded (SP). A target density of 103 pcf and a moisture content of about 3 percent were used for the tests for the OS because these soil conditions were used in the comparison study (Law Engineering and Environmental Services 1998). Compaction of OS specimens was performed by hand tamping using a square plate measuring 12 in. by 12 in. in cross-section.

Ribbed galvanized steel earth retaining strips were used as the reinforcement for pullout testing. Figure 5-2 shows a typical reinforcement specimen. Pullout tests were performed on 18-in. long strips, which was the maximum length that could fit in the medium-sized pullout box. Each strip used for testing included six sets of ribs, three on each side. The strip reinforcement was 2 in. wide, 18 in. long and about 0.16 in. (4 mm) thick. The ribs were about 0.12 in. (3 mm) high and spaced at about 7.5 inches (Figure 5-3).

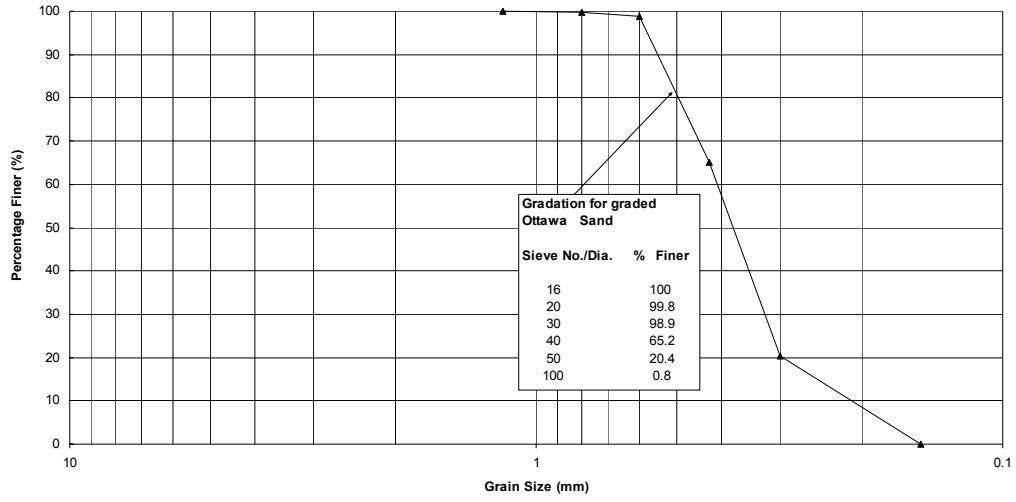


*Figure 5.1 Gradation of Ottawa Sand (OS)*



*Figure 5.2 Metallic ribbed strip reinforcement with sheathed telltales*

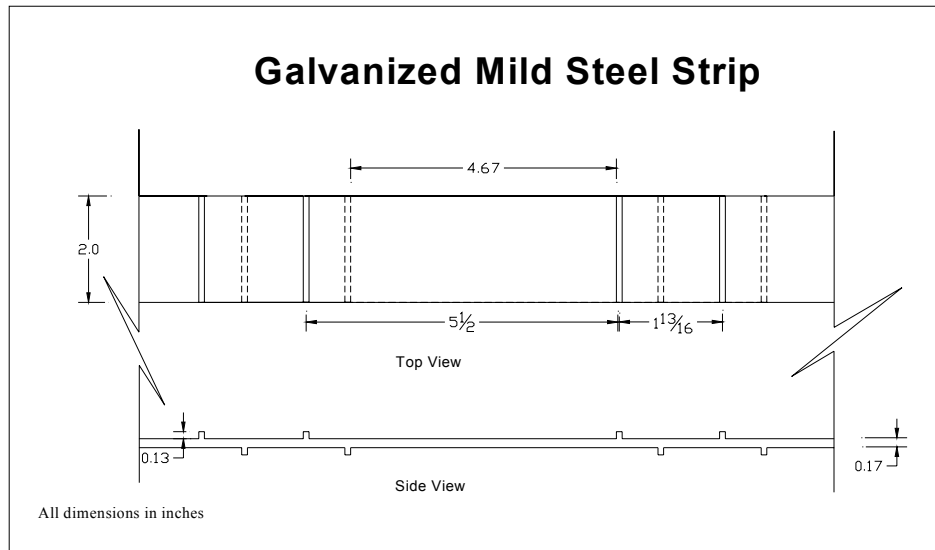
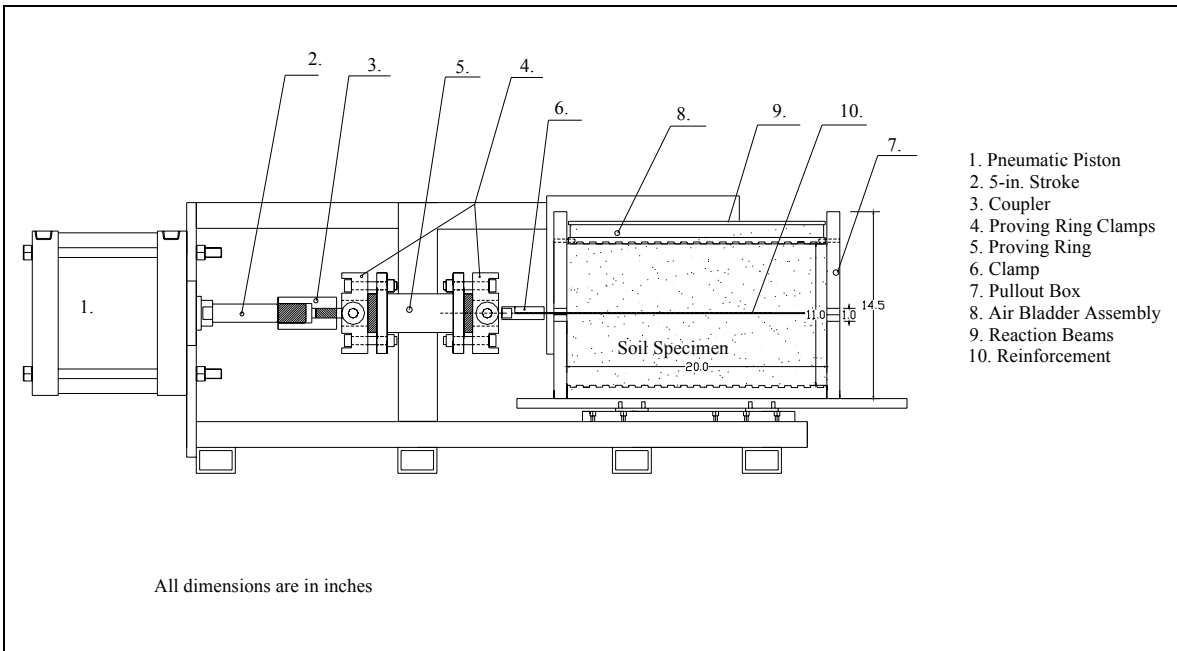


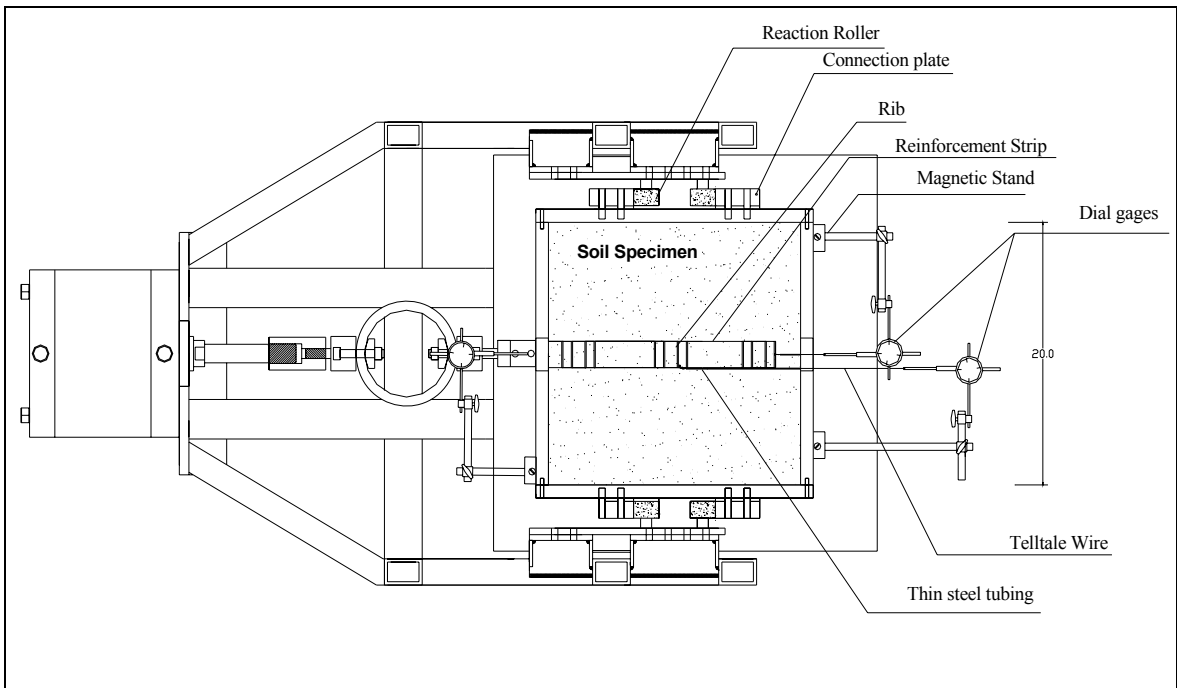
*Figure 5.3 Schematic of ribbed metallic strip reinforcement*

The pullout apparatus (Figures 5-4 and 5-5) consists of a pullout box (modified from the direct shear box), a clamp, an air bladder assembly, and a pneumatic piston. The pullout test box is a steel box, 20 in. by 20 in. in plan and 13.5 in. high. The box consists of two parts: a lower box that is 5 in. deep and a matching upper box that is 7.5 in. thick. Four 1-in. thick spacer bars separate the two boxes. The two halves of the box are rigidly connected to each other by means of four connection plates bolted to the sides of both boxes (Figure 5-4(b)). The spacer bar in the front of the box has a 2.5-in. wide by 0.5-in. high slot to allow the 2-in. wide metallic reinforcement to pass through. Telltales (thin wires) are connected to the reinforcement at different locations along the embedded length to measure the displacement during pullout. The spacer bar in the back end of the box has two small slots to allow the telltales to pass through.

The reinforcement is embedded at mid-height of the specimen and gripped by the clamp outside the pullout box. The air bladder assembly resting on top of the specimen applies normal pressure (up to 50 psi) to the specimen using air pressure. The normal pressure is applied uniformly through a top platen, while the reaction beams provide the required reaction. The pneumatic piston pulls the reinforcement out of the soil specimen through the clamp. A maximum pullout force of 20,000 lb can be applied with the piston at a pressure of 250 psi, delivered from a tank of bottled air. A regulator and a pressure gauge were installed in the air line to control and monitor the air pressure. A proving ring between the piston and clamp (Figure 5-4) was used to measure the pullout force.



(a)



(b)

Figure 5.4 (a) Vertical cross-sectional view of pullout apparatus, (b) Plan view of pullout apparatus

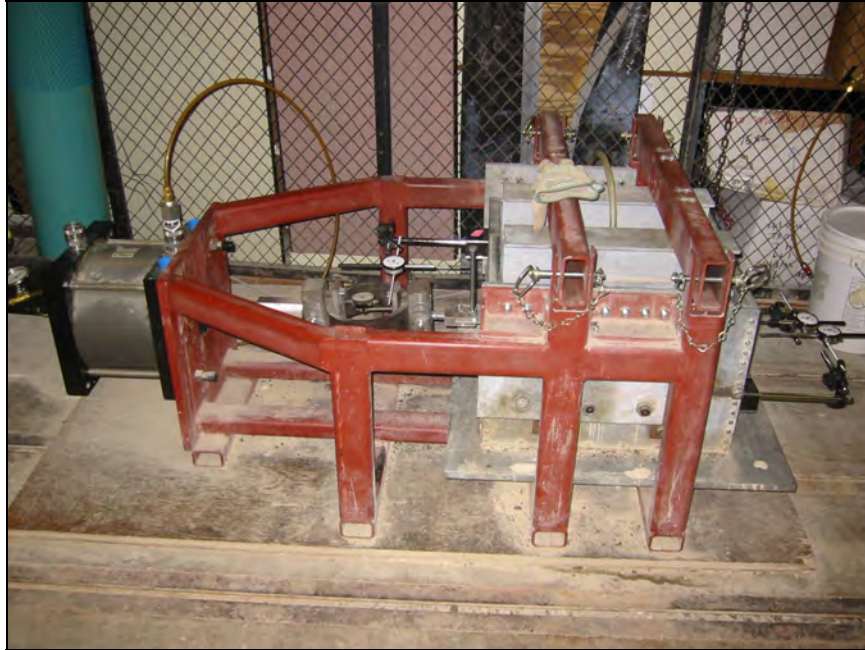


*Figure 5.5 Photographs of pullout apparatus*

Dial gauges with a 2-in. range were used to measure the horizontal displacement of the reinforcement. The displacement of the front of the strip was measured with a dial gauge attached to the pullout box, while the displacement of two points along the strip within the soil (middle and rear of the strip) were measured by dial gauges connected to thin stainless steel wires, 0.031 in. in diameter. The wires, called telltales, were connected to the strip, threaded through thin steel tubes having a 0.055 in. internal diameter, which isolated the telltales from the soil in which they were embedded, and connected to dial gauges outside the back of the box.

After compacting the full 10.5-in. thick soil specimen, with the reinforcement embedded at mid-height, pressure was applied to consolidate the soil under the desired normal stress (between 5 and 50 psi). Vertical strain during consolidation of between 1-2 percent was measured in the tests conducted.

After sample preparation and consolidation under the applied normal pressure, the reinforcement was pulled out with incremental increase in the pullout force. Failure was defined at a displacement of 0.75 in., a failure criterion recommended by Elias et al. (2001). Force increments between 60 and 100 lbs were used. The next increment of force was applied only when the displacement owing to the previous applied force had stopped.

### 5.3 Quantification of Pullout Resistance

Ultimate pullout resistance is generally defined as the force required to pull a reinforcement member out of soil at a particular confining pressure. The resistance is given per unit width of the reinforcement member. The general expression used to calculate pullout resistance (Christopher et al. 1990, Elias et al. 2001, FHWA MSE wall manual) is:

$$P_r = F^* \cdot \alpha \cdot \sigma'_v \cdot L_e \cdot C \quad (5.1)$$

where  $P_r$  is the ultimate pullout resistance per unit width of the reinforcement member (force/length),  $F^*$  is the pullout resistance factor or friction-bearing factor (dimensionless),  $\alpha$  is a correction factor that accounts for softening effects for extensible reinforcements (dimensionless),  $\sigma'_v$  is the effective vertical stress at the soil reinforcement interface (force/length<sup>2</sup>),  $L_e$  is the length of reinforcement in the resisting zone behind the failure surface (length), and  $C$  is the effective unit perimeter of the reinforcement (dimensionless). The ultimate pullout force can be calculated by multiplying the unit ultimate pullout resistance ( $P_r$ ) by the width of the reinforcement member.

To compute the pullout resistance,  $P_r$ , for use in design using Equation 5.1, the parameters  $F^*$ ,  $\alpha$ , and  $C$  must be evaluated for the given soil and reinforcement. For the geometry of a strip, shearing resistance develops on the top and bottom surfaces of the reinforcement and therefore  $C = 2$ . There is no softening effect for the metallic reinforcement, so  $\alpha = 1$ .  $F^*$  can be evaluated from semi-empirical equations (Elias et al. 2001) or can be measured during pullout tests. In this study, measurements of ultimate pullout force were converted to  $F^*$  and compared with those predicted by the equations from Elias et al. (2001).

Elias et al. (2001) recommends that  $F^*$  be taken as  $\mu^*$ , the apparent coefficient of friction, for metallic strips with no transverse elements.  $\mu^*$  incorporates the effects of the surface characteristics of the reinforcement (i.e., ribs versus smooth), the soil properties (specifically, the internal friction angle), and the overburden stress, which represents the tendency of the soil to dilate or contract. For smooth metallic strips, the apparent coefficient of friction ( $\mu^*$ ) is equal to  $\tan \rho$ , where  $\rho$  is the interface friction angle between the soil and the strip.  $\rho$  can be measured in the laboratory by performing interface shear tests. Generally,  $\tan \rho$  is less than  $\tan \phi'$ , where  $\phi'$  is the friction angle of the soil.

For ribbed reinforcement,  $\mu^*$  varies with depth. Figure 5-6 shows the variation of design  $\mu^*$  with depth for ribbed and smooth reinforcements (Christopher et al. 1990, Elias et al. 2001). The variation in  $\mu^*$  with depth for ribbed reinforcement is represented by the equation:

$$\mu^* = \mu_0^* - ((\mu_0^* - \tan \phi') / 20) \cdot z \quad (5.2)$$

where  $z$  is the depth of the reinforcement below ground level (ft),  $\phi'$  is the friction angle of the soil, and  $\mu_0^*$  is the apparent coefficient of friction at very low stresses. For granular soils,  $\mu_0^*$  can be approximated by the empirical relation (Christopher et al. 1990; Elias et al. 2001):

$$\mu_0^* = 1.2 + \log_{10} (C_u) \leq 2 \quad (5.3)$$

where  $C_u$  is the uniformity coefficient of the soil. The maximum value of  $\mu_0^*$  is 2, which represents an effective friction angle of  $63^\circ$ ; such a high value is because of the dilatancy effect observed at low overburden pressures near the soil surface. At depths below 20 ft,  $\mu^*$  is taken as  $\tan \phi'$  for ribbed metallic strips (Figure 5-6).

To measure  $F^*$  in this study, the pullout force ( $P_o$ ) was measured by the proving ring and was converted to  $F^*$  using:

$$F^* = (P_o/W) / (\alpha \cdot \sigma'_v \cdot L_e \cdot C) \quad (5.4)$$

For the test setup and reinforcement used in this study,  $W$  (reinforcement width) = 2 in.,  $\alpha = 1$ ,  $\sigma'_v$  is the vertical effective stress used during the test,  $L_e = 18$  in., and  $C = 2$ .

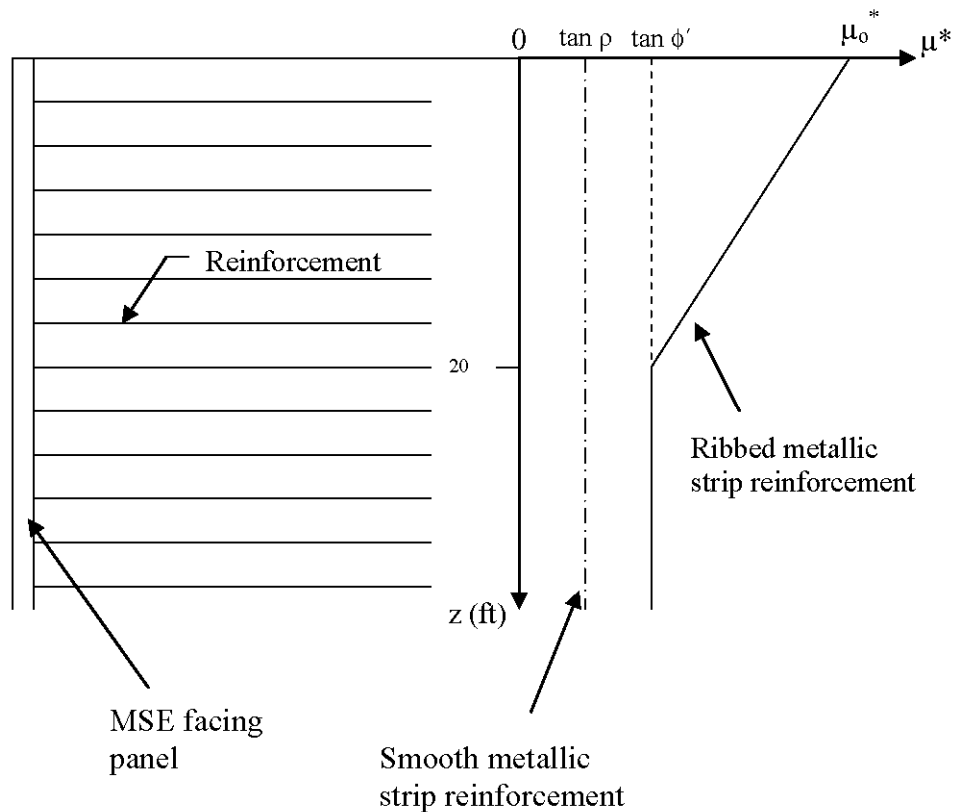


Figure 5.6 Reinforced earth design  $\mu^*$  values for smooth and ribbed metallic strips (from Christopher et al. 1990)

#### 5.4 Results from Pullout Testing

Testing was first performed on OS to validate the experimental equipment, followed by testing on CFM and CC. Initial tests of metallic strips in OS resulted in very low pullout resistance. It was observed that some sand was falling out from the front wall opening for the reinforcement during pullout. To prevent this loss of soil, blocking plates were placed over the front opening to reduce the size of the slot opening. The blocking plates prevented the OS from falling through the opening and the pullout resistance was increased. Because the CFM and CC were more well-graded than the OS, the blocking plate was not required for these other materials.

Table 5-1 summarizes the testing conditions for OS in this study and the comparison study by Law Engineering and Environmental Services, Inc. (1998). The soil conditions are very similar; the main differences are the size of the box and the control (displacement versus force) of the test. Tests at three overburden pressures were conducted and failure was defined at a displacement of 0.75 in., the failure criterion recommended by Elias et al. (2001). Figure 5-7 shows the values of friction factor ( $F^*$ ) at corresponding depths of normal pressure for tests in both types of boxes. It can be seen that the values of  $F^*$  obtained in this study using the medium-

sized box lie within the range of values obtained in tests in the much larger pullout box. This validates the results from the medium-sized pullout box in this study.

Table 5.1 Test conditions in different types of pullout boxes

	Medium Sized Pullout Box	Large Pullout Box
<b>Soil</b>	Graded Ottawa Sand ( $\phi' = 33^\circ$ )	Graded Ottawa Sand ( $\phi' = 33^\circ$ )
<b>Soil Density</b>	103 pcf	102.9 pcf
<b>Water Content</b>	3%	3.1%
<b>Reinforcement Type</b>	Ribbed metallic strip	Ribbed metallic strip
<b>Reinforcement Length</b>	18 in.	30 in.
<b>Method of Compaction</b>	Hand Tamping	Tamping
<b>Method of Pullout</b>	Force-control	Displacement-control

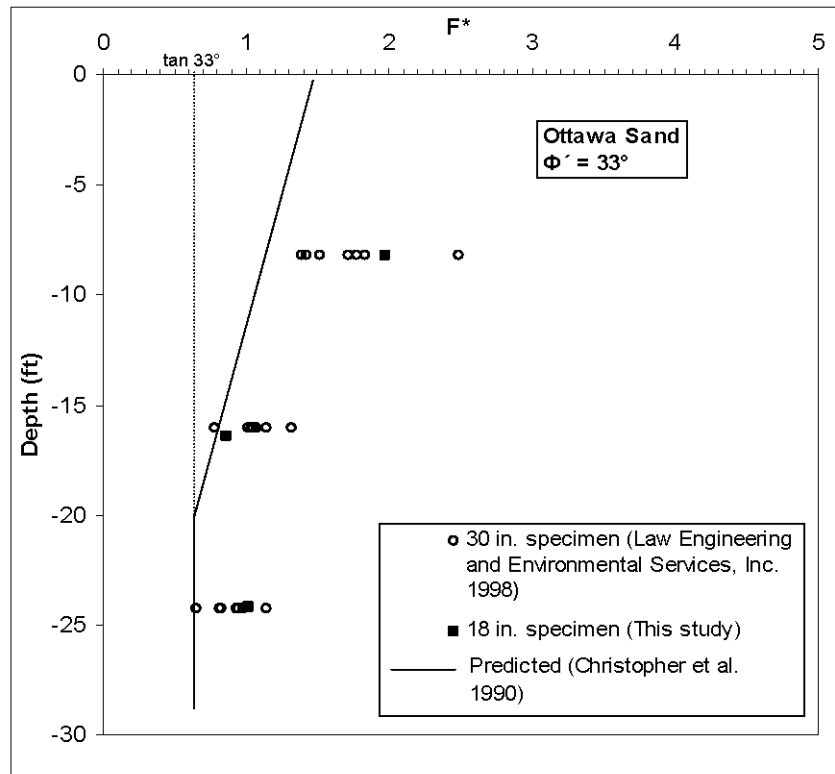


Figure 5.7 Pullout of ribbed metallic strips in Ottawa Sand

Tests were performed in CFM at three different normal pressures (10, 30, and 50 psi). A pressure of 50 psi represents the level of overburden pressure in a 50 to 60 ft high MSE wall. The test conditions and results are summarized in Table 5-2. The measured pullout force–displacement relationships at different normal pressures are shown in Figure 5-8, while the corresponding  $F^*$  obtained are compared with the predicted values in Figure 5-9. It can be seen from Figure 5-9 that  $F^*$  in CFM is larger than predicted by the theoretical expressions (FHWA 2001) and  $F^*$  increases dramatically at shallow depths (low confining stresses). This occurs because of the dilatancy of CFM at small overburden pressures, which gives rise to a curved failure envelope with higher friction angles at lower stress levels. For comparison, the lower bound  $F^*$  values for a friction angle of  $34^\circ$  are also shown. This friction angle represents the assumed friction angle represented on the TxDOT standard sheets for retaining walls (RW-MSE, RW-CB, RW-TEW). The data in Figure 5-9 reveal that the measured values of  $F^*$  are significantly larger than these lower bound values.

*Table 5.2 Pullout test results from medium-sized box on metallic ribbed strips in CFM*

Average unit weight = 135.5 pcf Average water content = 10.1% Effective Length = 18 in.					
<b>Test No.</b>	<b>Overburden Pressure (psi)</b>	<b>Equivalent Overburden Height (ft)</b>	<b>Ultimate Pullout Force (lbf)</b>	<b>Ultimate Pullout Resistance (lbf/inch)</b>	<b>Friction Factor <math>F^*</math></b>
<b>1</b>	10	11.2	3697	1848.5	4.87
<b>2</b>	30	32.5	4507	2253.5	2.05
<b>3</b>	50	53.7	5528	2764	1.52

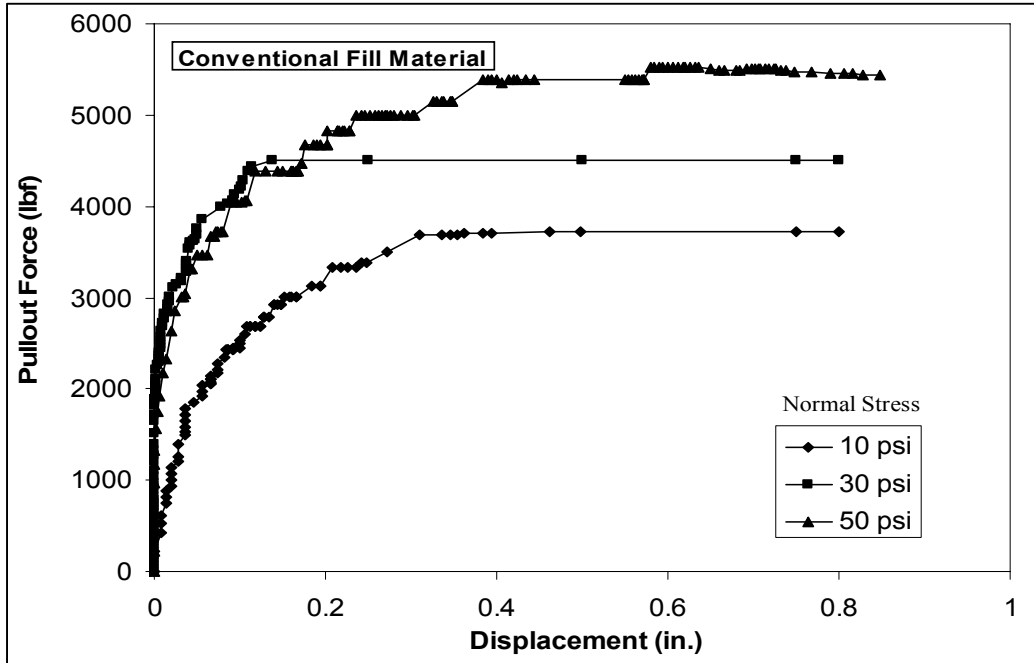


Figure 5.8 Results from three pullout tests on ribbed metallic strip in CFM

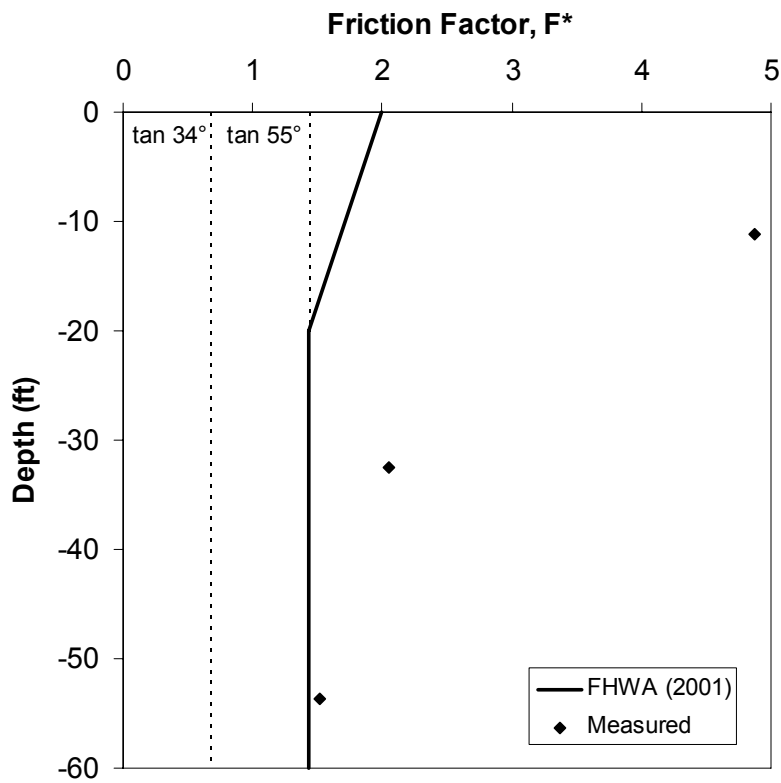


Figure 5.9 Theoretical and measured friction factors for Conventional Fill Material

Additionally, Figure 5.8 shows that failure occurred at displacements much smaller than the failure criterion of 0.75 in. for all three tests. This implies that both the bearing capacity of the ribs and the soil interface resistance are exceeded before a displacement of 0.75 in. in CFM.

For CC, tests were performed with the ribbed metallic strips at the same three normal pressures used in the testing of CFM (10, 30, and 50 psi). The test conditions and results are summarized in Table 5-3. The measured pullout force–displacement relationships for each test are plotted in Figure 5-10. The ultimate pullout resistance for CC was reached at displacements less than 0.75 in., but the failure at higher pressures occurred at displacements much greater than at lower pressures. The measured friction factors are compared with the predicted friction factors in Figure 5-11. The measured  $F^*$  values for CC increase at shallow depths, although not as dramatically as for CFM (Figure 5-9). The  $F^*$  values are also greater than the predicted values at all pressures. For comparison, the lower bound  $F^*$  values for the assumed friction angle of  $34^\circ$  are also shown. Again, this friction angle represents the assumed friction angle represented on the TxDOT standard sheets for retaining walls (RW-MSE, RW-CB, RW-TEW). The data in Figure 5-11 reveal that the measured values of  $F^*$  are significantly larger than these lower bound values. It can be concluded that CC, like CFM, has a high pullout capacity and the semi-empirical predictive equations for  $F^*$  can be used conservatively in the design of MSE walls with CC backfill.

*Table 5.3 Pullout test results from medium-sized box on ribbed metallic strips in CC*

Average unit weight = 132.6 pcf Average water content = 10% Effective Length = 18 in.					
Test No.	Overburden Pressure (psi)	Equivalent Overburden Height (ft)	Ultimate Pullout Force (lbf)	Ultimate Pullout Resistance (lbf/inch)	Friction Factor $F^*$
1	10	11.2	1588	794	2.09
2	30	33.2	4020	2010	1.83
3	50	54.9	6322	3161	1.74

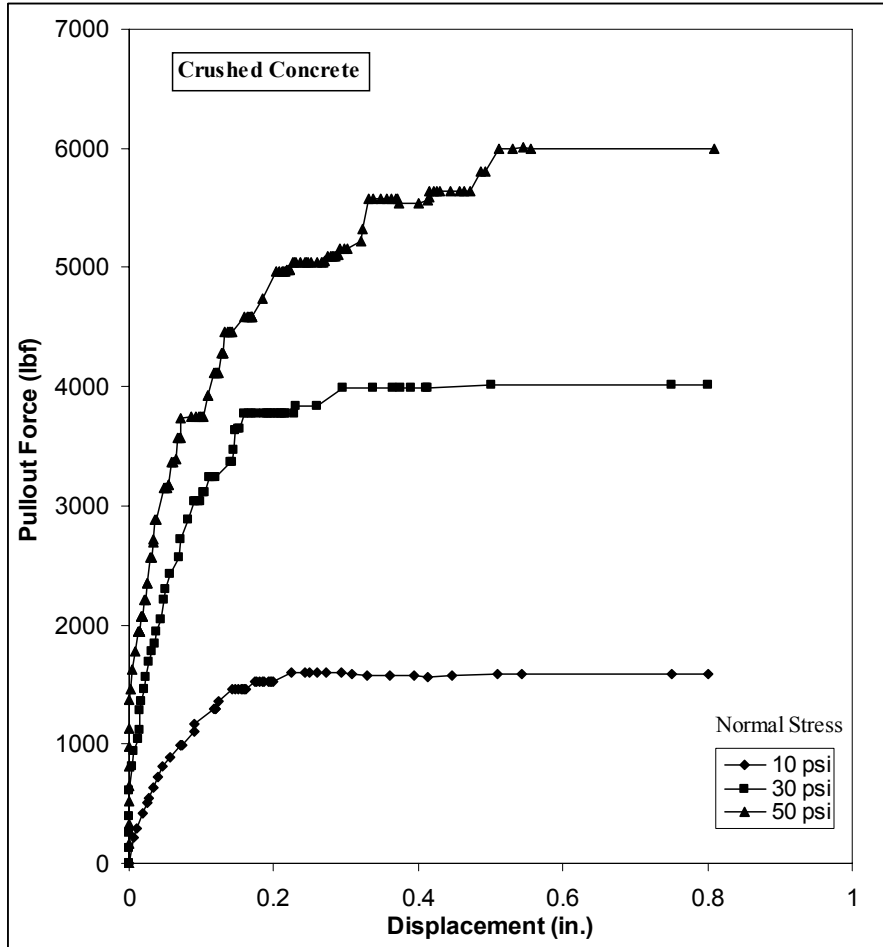


Figure 5.10 Results from three pullout tests on ribbed metallic strip in CC

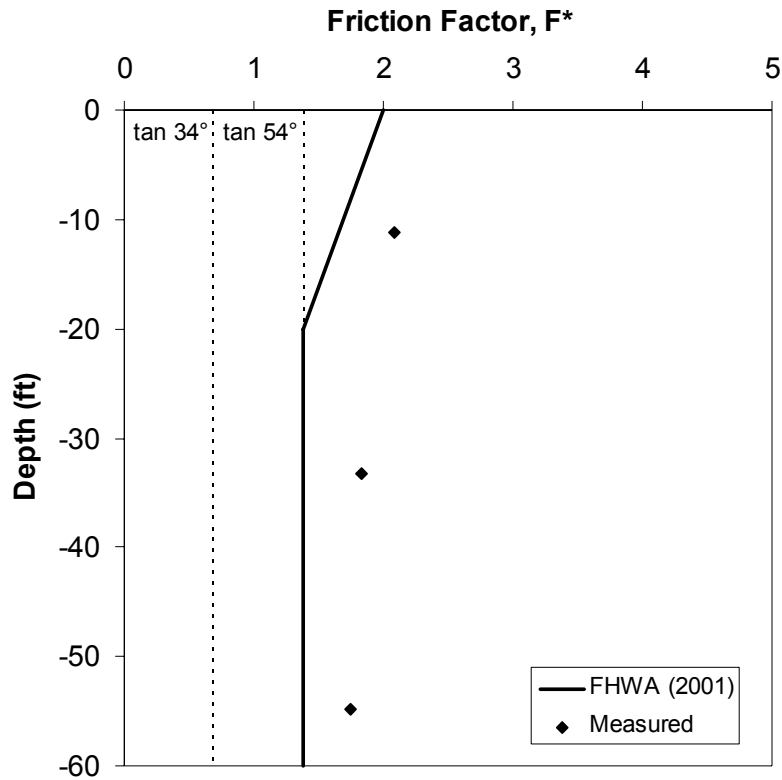


Figure 5.11 Theoretical and measured friction factors for Crushed Concrete

Tests were performed with the ribbed metallic strip in RAP at four different normal pressures (5, 10, 20, and 30 psi) according to the procedure described previously. Pressures larger than 30 psi were not used because RAP showed significant creeping behavior at high normal pressures, as discussed below. The tests' conditions and results are summarized in Table 5-4.

Pullout force versus displacement relationships are plotted in Figure 5-12, while the measured friction factors are compared with the predicted friction factors in Figure 5-13. At smaller confining pressures (smaller depths in Figure 5-13), the measured  $F^*$  values are slightly larger than predicted by FHWA (2001), but at larger depths the measured  $F^*$  values fall slightly below the predicted values and slightly above the lower bound values for a friction angle of  $34^\circ$ . This result is in stark contrast to the results for CFM and CC, where the friction factors generally were much larger than predicted by the semi-empirical relationships (Figures 5-9 and 5-11).

The lower friction values can be attributed to creep deformations during pullout, which caused significant deformation at each level of pullout force (Figure 5-12). The shapes of the pullout force versus displacement curves for RAP (Figure 5-12) are different than those observed for CFM and CC (Figures 5-8 and 5-10). The curves for CFM and CC are more hyperbolic, while the RAP curves show a stepping shape because of the large deformation that occurred over time at each load level. These time-dependent deformations became larger as the pullout force increased, and thus failure was defined when the test reached the 0.75-in. deformation limit.

Table 5.4 Pullout test results from medium-sized box on metallic ribbed strips in RAP

Average unit weight = 118.2 pcf Average water content = 3 % Effective Length = 18 in.					
Test No.	Overburden Pressure (psi)	Equivalent Overburden Height (ft)	Ultimate Pullout Force (lbf)	Ultimate Pullout Resistance (lbf/inch)	Friction Factor F*
1	5	6.7	778	389	1.95
2	10	12.8	1134	567	1.49
3	20	25	1297	648.5	0.87
4	30	37.2	1654	827	0.75
5	30	37.2	1524	762	0.69

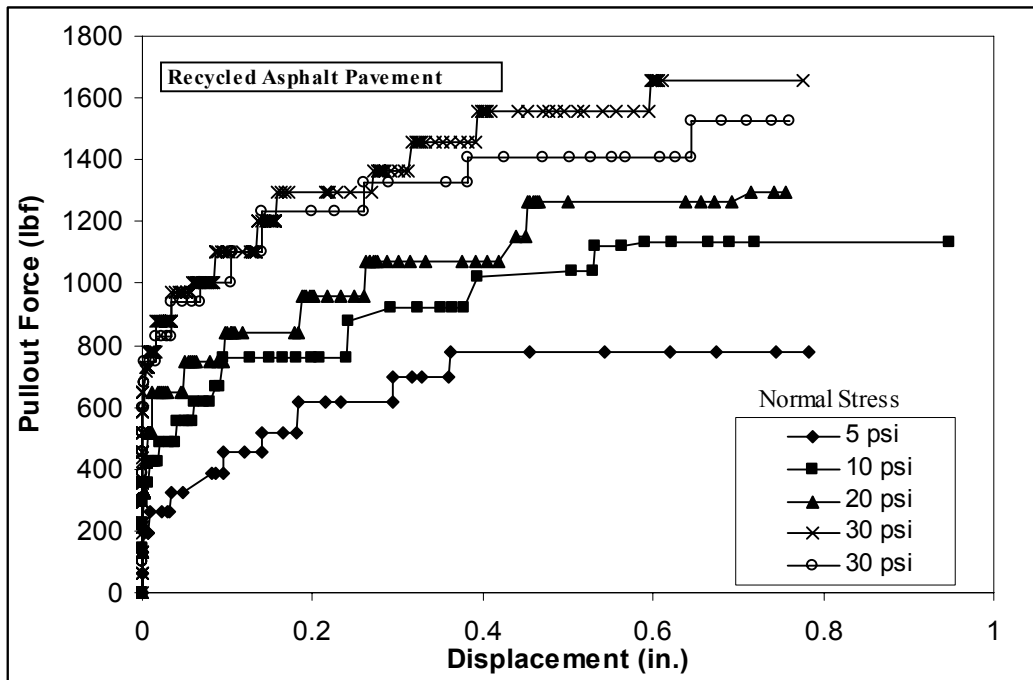


Figure 5.12 Results from five pullout tests on ribbed metallic strip in RAP

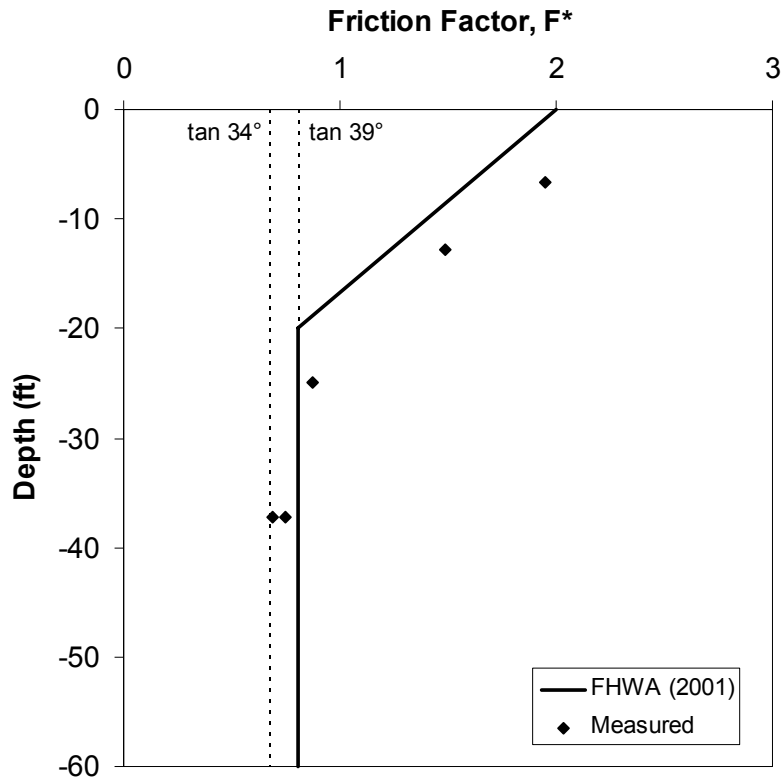


Figure 5.13 Comparison of friction factors in Recycled Asphalt Pavement

## 5.5 Summary

This chapter presents the pullout test results for ribbed metallic strips in CFM, CC, and RAP. Friction factor, ultimate pullout resistance, and creep were discussed and compared for each material. Based on the test results, ultimate pullout resistances of the ribbed metallic strips in the three fill materials can be assessed. At all pressures, CC and CFM have larger ultimate pullout resistances than RAP. The measured friction factors ( $F^*$ ) for CC and CFM were all larger than those predicted by current design procedures in FHWA (i.e., Elias et al. 2001), indicating that these current procedures can be conservatively used to predict the pullout resistance of reinforcement embedded in CC. The measured  $F^*$  values for RAP were slightly larger to slightly smaller than those predicted by current design procedures. The measured  $F^*$  values were smaller because the force-controlled tests performed allowed for creep deformations that caused the deformation limit of 0.75 in. to be reached before full shear failure along the reinforcement-soil interface. This result indicates that creep deformations between the RAP and reinforcement may cause excessive displacements in MSE walls constructed with RAP.

## 6. Evaluation of Creep Potential of RAP

### 6.1 Introduction

Backfill materials with any indication of creep potential have traditionally been avoided for use in MSE walls, primarily because of the difficulties involved in understanding the true interactive mechanism between the creeping backfill material and the reinforcement. Creep is a concern for RAP because of the viscoelastic behavior of the bitumen coating that surrounds the aggregate particles. The expectation for RAP to fail in creep rupture was observed during the large-scale direct shear tests discussed in Chapter 4 and the pullout tests discussed in Chapter 5. This chapter describes an experimental investigation initiated to study the creep behavior of RAP. A series of constant stress, drained triaxial tests was performed on compacted RAP specimens to assess its creep behavior.

### 6.2 Theoretical Background

Figure 6-1 is a plot of axial strain versus time for a constant stress level. The curve shows three distinct regions of creep behavior: primary creep, secondary creep, and tertiary creep followed by creep rupture. Primary creep occurs immediately after application of the stress in which the strain rate decreases with time. During secondary creep, the strain rate is at the minimum value ( $\dot{\epsilon}_{\min}$ ) and remains relatively constant throughout this secondary creep stage. At some point the strain may start to increase again, which is referred to as the initiation of the tertiary creep, which finally leads to complete creep rupture at the end of the tertiary creep.

In this study, Singh and Mitchell's creep model (1968), a widely accepted empirical model for soil creep, is used as the primary constitutive model to fit the observed experimental creep data. The Singh and Mitchell creep model is based on a simple three-parameter empirical relationship to predict the strain rate at a given time:

$$\dot{\epsilon} = Ae^{\bar{\alpha}\bar{D}} \left( \frac{t_1}{t} \right)^m \quad (6.1)$$

where:

$\dot{\epsilon}$	= strain rate
$t_1$	= reference time
$t$	= time
$\bar{D}$	= deviator stress level, $(\sigma'_1 - \sigma'_3)/(\sigma'_1 - \sigma'_3)_{\text{ult}}$
$A$	= strain rate at time $t_1$ and $\bar{D} = 0$
$m$	= absolute value of slope of a log(strain rate) versus log(time)
$\bar{\alpha}$	= slope of linear portion of plots between log(strain rate) versus deviator stress level, all points corresponding to the same time

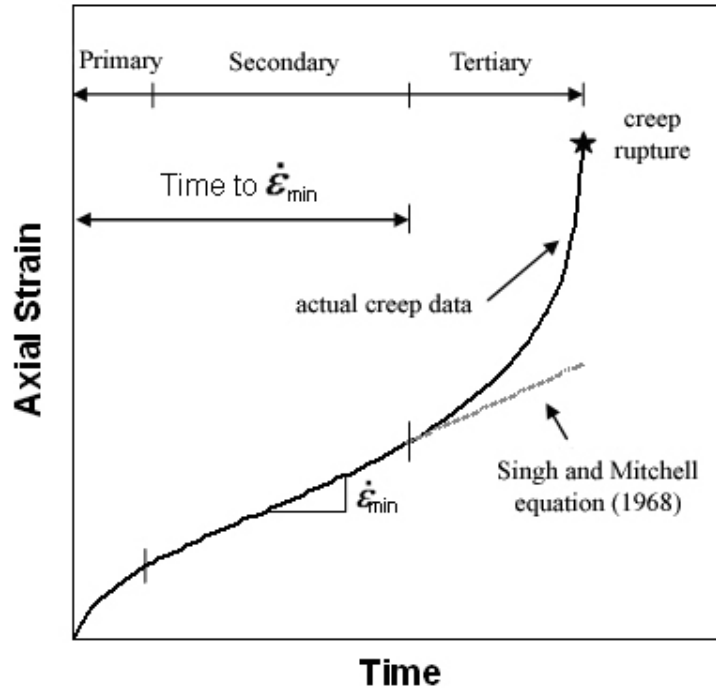


Figure 6.1 Time-dependent creep deformation under a constant stress level.

Equation (6.1) is suitable for soils that are subjected to deviator stress levels ( $\bar{D}$ ) within the range of 0.30 to 0.90 (or 30 percent to 90 percent of the soil failure stress determined in strength tests), a range considered within the region of engineering interest. More importantly, this equation only calculates the time-dependent creep deformation of a given soil up to the end of the secondary stage of creep. Thus, the Singh and Mitchell (1968) creep model can only predict creep strain rate from the beginning of deviator stress application to the end of secondary creep (Figure 6-1).

A minimum of two creep tests are required to obtain the three model parameters:  $A$ ,  $\bar{\alpha}$ , and  $m$ . The parameter  $A$  is related to the composition, structure, and stress history of the soil. The parameter  $\bar{\alpha}$  indicates the stress intensity effect on the creep rate. The parameter  $m$  controls the rate at which the strain rate decreases with time. By integration of equation (6.1), a general relationship between time and axial strain can be obtained. The integration provides two solutions depending on the  $m$  value:

$$\epsilon = Ae^{\alpha D} (t_1)^m \left( \frac{1}{1-m} \right) t^{1-m} + \text{constant} \quad (\text{for } m \neq 1) \quad (6.2)$$

$$\epsilon = Ae^{\alpha D} t_1 \ln t + \text{constant} \quad (\text{for } m = 1) \quad (6.3)$$

The constants of integration in these equations can be obtained from a known value of strain at some known value of time. It can be seen from equations (6.2) and (6.3) that creep axial strain is described by a power function in which a linear relationship is found between axial strain and logarithm of time for  $m = 1$ , while a non-linear relationship is observed for  $m \neq 1$ , as shown in Figure 6-2. Also in this figure an important physical significance of the  $m$  parameter is observed. Mathematically, the axial strain for a soil with an  $m$  value greater than 1.0 will approach an asymptotic value over time, while a soil with  $m$  less than 1.0 displays continuously increasing strains that eventually cause creep rupture.

Because of its important mathematical significance, the parameter  $m$  is considered the most meaningful parameter in the model because it is directly related to the creep potential. Typical values of  $m$  reported in the literature range from 0.7 to 1.3 (Mitchell 1993), with smaller values indicating a larger creep potential.

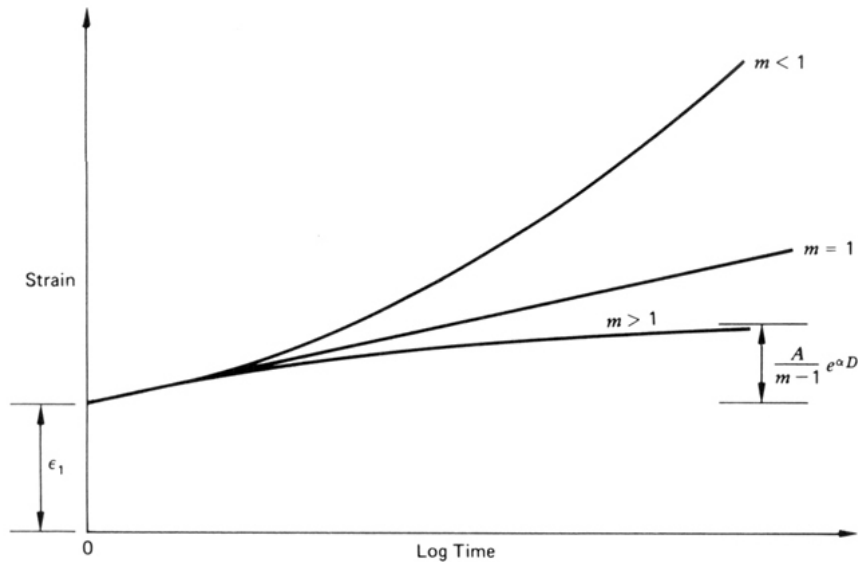


Figure 6.2 Effect of  $m$  values on predicted creep strains (Mitchell 1993)

### 6.3 Experimental Program

A series of constant-stress, drained triaxial creep tests were performed on a number of RAP specimens using the same apparatus for the triaxial tests used earlier for the shear strength measurements. Drained testing was selected over undrained testing because the RAP will respond drained in the field because of its large hydraulic conductivity.

Initial specimen preparation for the triaxial creep tests were the same as used for the triaxial shear strength tests described in Chapter 4. Each creep specimen was gradually loaded following the same loading path and rate of piston loading obtained earlier from the strain-controlled triaxial tests. After the target deviator stress level had been reached, mostly within 2 minutes after the initiation of the deviator stress application, the deviator stress was maintained constant at that stress level throughout the test duration, as shown in Figure 6-3. To maintain constant

deviator stress level on the test specimens, the deviator load was periodically adjusted as necessary to accommodate the change in area of the specimen owing to the volumetric strain experienced during the drained test.

Although asphalt behavior is temperature dependent, it is believed that the temperature variation of an enclosed backfill material behind a typical MSE wall will be relatively minimal. Therefore, all creep tests were performed at a constant room temperature of about 72°F. During testing, the axial deformation and deviator stress were recorded against time by an external Linear Variable Displacement Transducer (LVDT) and an external load cell. The creep test continued until complete creep rupture or until 10,000 minutes (~ 7 days) had elapsed.

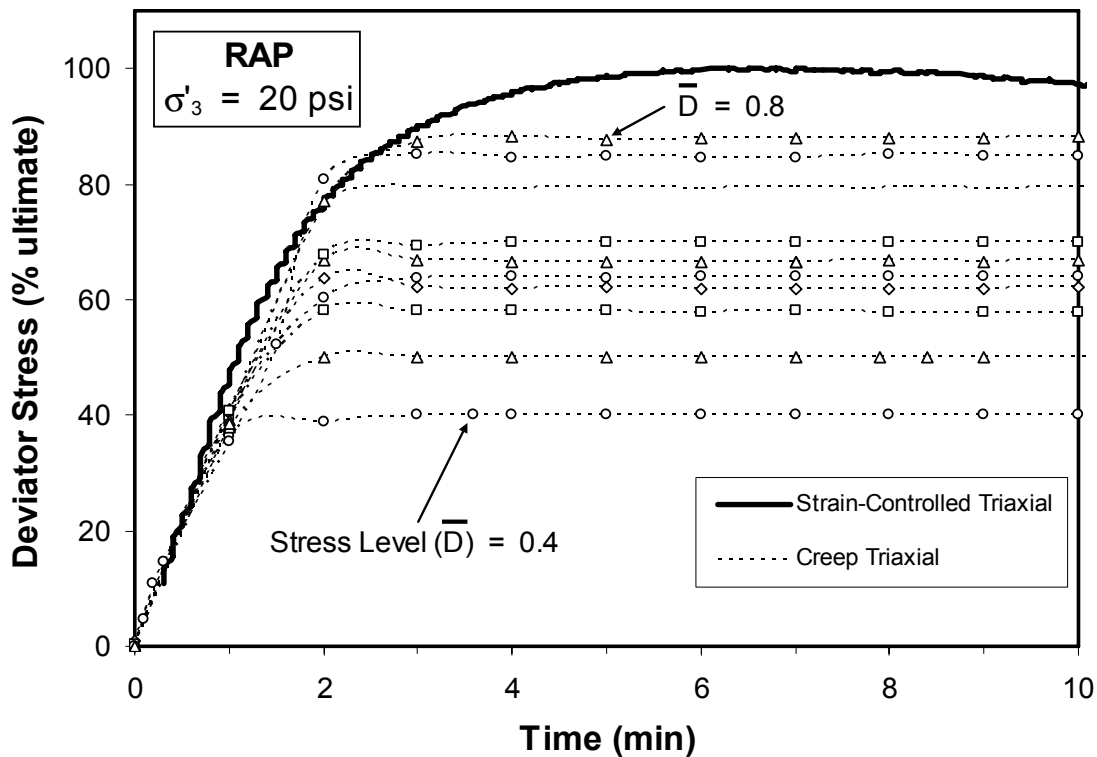


Figure 6.3 Deviator stress level versus time for creep test specimens at  $\sigma'_3 = 20$  psi

#### 6.4 Creep Test Results

A total of twenty-four, constant-stress, drained triaxial creep tests were performed on compacted RAP specimens. The entire testing program can be subdivided into three components: creep tests at an effective confining stress ( $\sigma'_3$ ) of 20 psi, creep tests at  $\sigma'_3 = 40$  psi, and creep tests at constant  $\bar{D}$  of 0.8 (80 percent of the ultimate strength) performed at  $\sigma'_3$  ranging between 5 psi and 50 psi. The following sections describe experimental results and the Singh and Mitchell creep parameters (i.e.  $A$ ,  $m$ , and  $\bar{\alpha}$ ) determined from the creep tests.

### 6.4.1 Creep Tests at $\sigma'_3 = 20$ psi

Ten creep tests were performed at  $\sigma'_3 = 20$  psi with stress levels ranging from 0.40 to 0.88 (40 percent to 88 percent of the ultimate strength). Figure 6-4 shows plots of axial strain ( $\epsilon$ ) versus  $\log(\text{time})$ . Six of the ten tests reached the tertiary creep stage within the 1 week of testing (i.e., 10,000 minutes). These tests all had  $\bar{D} \geq 0.64$ . This figure shows that, generally, larger axial strains were observed for tests performed at larger stress levels. Also, it appears that creep tests performed at  $\bar{D} < 0.64$  may have eventually reached creep rupture if the applied stress had been maintained long enough. However, it was very likely that these samples would take more than a month to reach a creep rupture, given the observed axial strain rates.

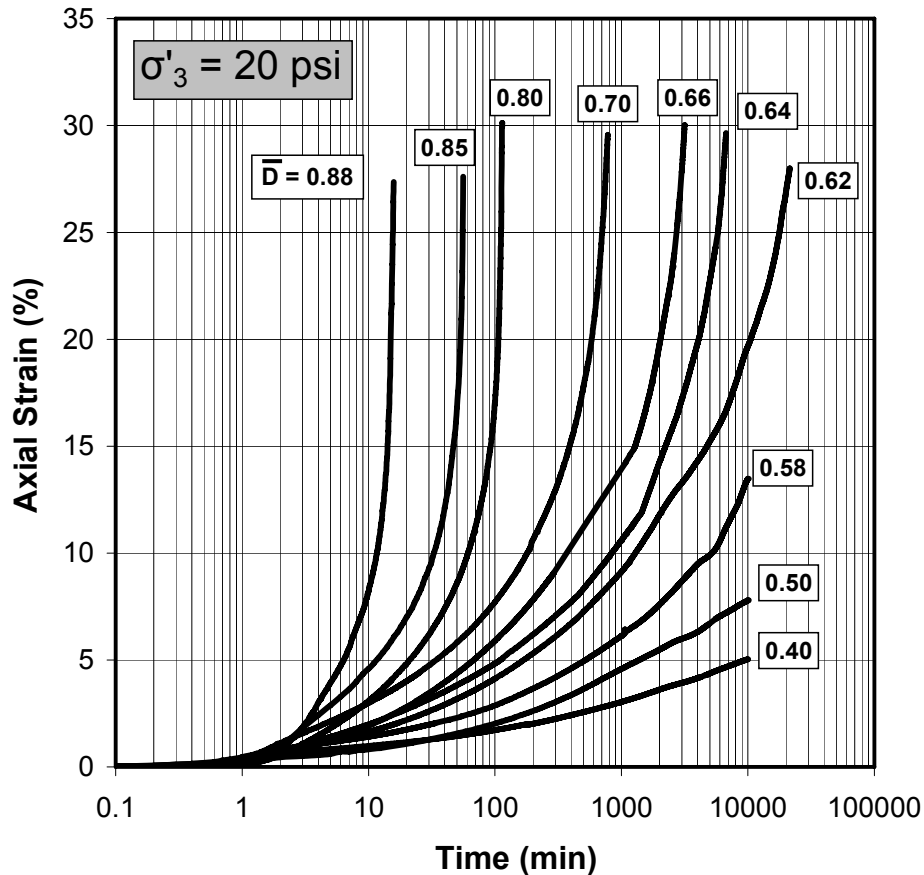


Figure 6.4 Axial strain versus time for RAP specimens tested at  $\sigma'_3 = 20$  psi

By differentiating the data in Figure 6-4 with respect to time, the axial strain rate ( $\dot{\epsilon}$ ) can be determined and plotted versus  $\log(\text{time})$ , as shown in Figure 6-5. The data indicate an increase in strain rate for larger values of  $\bar{D}$  at any given time, and large initial values of strain rate (0.1 to 1 percent/minute) are observed. Furthermore, a linear relationship between  $\log(\text{strain rate})$  and  $\log(\text{time})$  is clearly noticeable, particularly for  $\bar{D} \leq 0.70$ . At large stress levels,  $\bar{D} \geq 0.64$  for this case, the linear reduction in strain rate is followed by an increase in strain rate as creep rupture is approached. The slopes of the curves in Figure 6-5 provide the  $m$  parameter for the Singh and Mitchell (1968) creep equation. The best-fit  $m$  value for each stress level was determined

separately, and generally ranged from 0.69 to 0.76. The best-fit  $m$  value for all of the data at  $\sigma'_3 = 20$  psi is 0.70. This value is equal to the smallest  $m$  value for typical soils reported by Mitchell (1993) and indicates high creep potential.

The next step is to determine the appropriate  $A$  and  $\bar{\alpha}$  parameters. Using  $t_l = 5$  min, the resulting  $A$  and  $\bar{\alpha}$  values are  $2.8 \times 10^{-3}$  percent/min and 6.12, respectively. Kuhn and Mitchell (1993) reported that typical soils have  $A$  and  $\bar{\alpha}$  values ranging from  $2 \times 10^{-8}$  to  $4 \times 10^{-3}$  percent/min, and 1.0 to 7.0, respectively, for  $t_l = 1$  min.. The  $\bar{\alpha}$  parameter is theoretically independent to the value of  $t_l$  selected. Therefore, by direct comparison, this study indicates that RAP has an  $\bar{\alpha}$  value close to the high end of the range reported for typical soils. The  $A$  value, on the other hand, is strictly dependent on the selected  $t_l$  value, so it is difficult to compare the  $A$  value for RAP with those reported in the literature. Nonetheless, the small value of  $m$  and larger value of  $\bar{\alpha}$  suggest that RAP at  $\sigma'_3 = 20$  psi exhibits creep potential similar to that of a high creep potential clay.

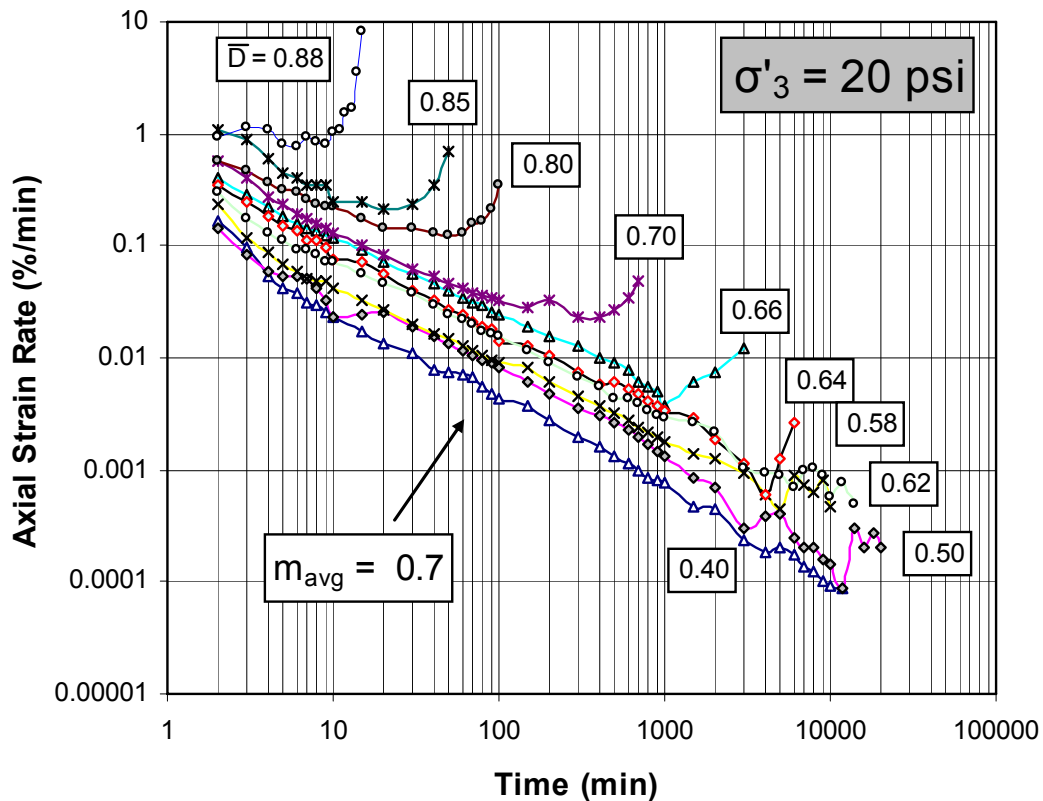


Figure 6.5 Axial strain rate versus time for RAP specimens tested at  $\sigma'_3 = 20$  psi

#### 6.4.2 Creep Tests at $\sigma'_3 = 40$ psi

A total of ten creep tests were performed at  $\sigma'_3 = 40$  psi with the applied stress level ( $\bar{D}$ ) ranging from 0.50 to 0.90. These tests were performed to investigate the influence of the effective confining stress on the creep behavior of RAP. Although some creep tests on clay have shown

that effective confining stress should not significantly affect creep behavior (e.g., Vaid and Campanella 1977), it was not clear that the same behavior would be observed in RAP.

Figure 6-6 graphically displays the observed creep axial strain versus log(time). Relationships similar to those obtained for  $\sigma'_3 = 20$  psi are observed. However, by direct comparison with Figure 6-4, it is evident that specimens performed at  $\sigma'_3 = 40$  psi required more time than specimens tested at  $\sigma'_3 = 20$  psi to reach the same creep deformation at the same stress level ( $\bar{D}$ ). Additionally, at  $\sigma'_3 = 20$  psi an applied  $\bar{D}$  greater than about 0.64 was required to reach creep rupture within 10,000 min, while a  $\bar{D}$  greater than about 0.8 is needed to reach creep rupture in 10,000 min at  $\sigma'_3 = 40$  psi (Figure 6.6). Therefore, it appears that confining stress has an impact on the creep behavior of RAP and that RAP is more stable with respect to creep at larger confining pressures.

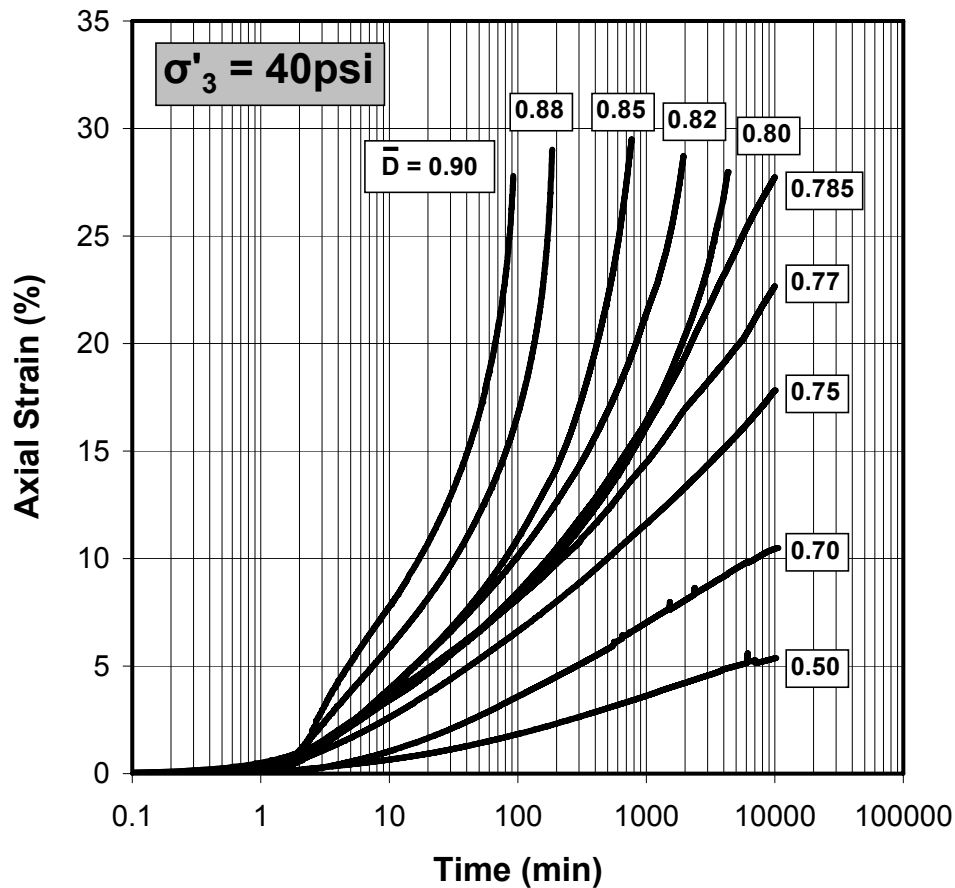


Figure 6.6 Axial strain versus time for RAP specimens tested at  $\sigma'_3 = 40$  psi

The test data shown Figure 6-6 were differentiated with respect to time to obtain the axial strain rate. Figure 6-7 shows the calculated strain rate versus log(time). Based on these data, specimens tested at  $\bar{D} \geq 0.80$  reached the tertiary creep stage within 1 week (10,000 min). Compared with the results shown in Figure 6-5 for  $\sigma'_3 = 20$  psi, the initial strain rates (at  $t \sim 2$  min) for  $\sigma'_3 = 40$

psi fall into the same range (i.e., 0.1 to 2 percent/min). However, the  $\sigma'_3 = 40$  psi data indicate a best-fit  $m$  value of 0.9, which is much larger than observed for  $\sigma'_3 = 20$  psi. The larger  $m$  value indicates that strain rate decreases more quickly with time, which represents a lower creep potential.

The appropriate  $A$  and  $\bar{\alpha}$  values were determined for  $\sigma'_3 = 40$  psi using  $t_l = 5$  min. The corresponding  $A$  and  $\bar{\alpha}$  values are  $2.1 \times 10^{-3}$  percent/min and 6.46, respectively. These values differ only slightly from the  $A$  and  $\bar{\alpha}$  values determined earlier for the tests at  $\sigma'_3 = 20$  psi (i.e.,  $A=2.8 \times 10^{-3}$  percent/min and  $\bar{\alpha}=6.12$ ). The similarity of the  $\bar{\alpha}$  values for tests at different  $\sigma'_3$  observed in this study is supported by previous findings reported by Singh and Mitchell (1968). They concluded that the  $\bar{\alpha}$  value (or slope of each plot) did not vary greatly with the consolidation pressure or the overconsolidation ratio.

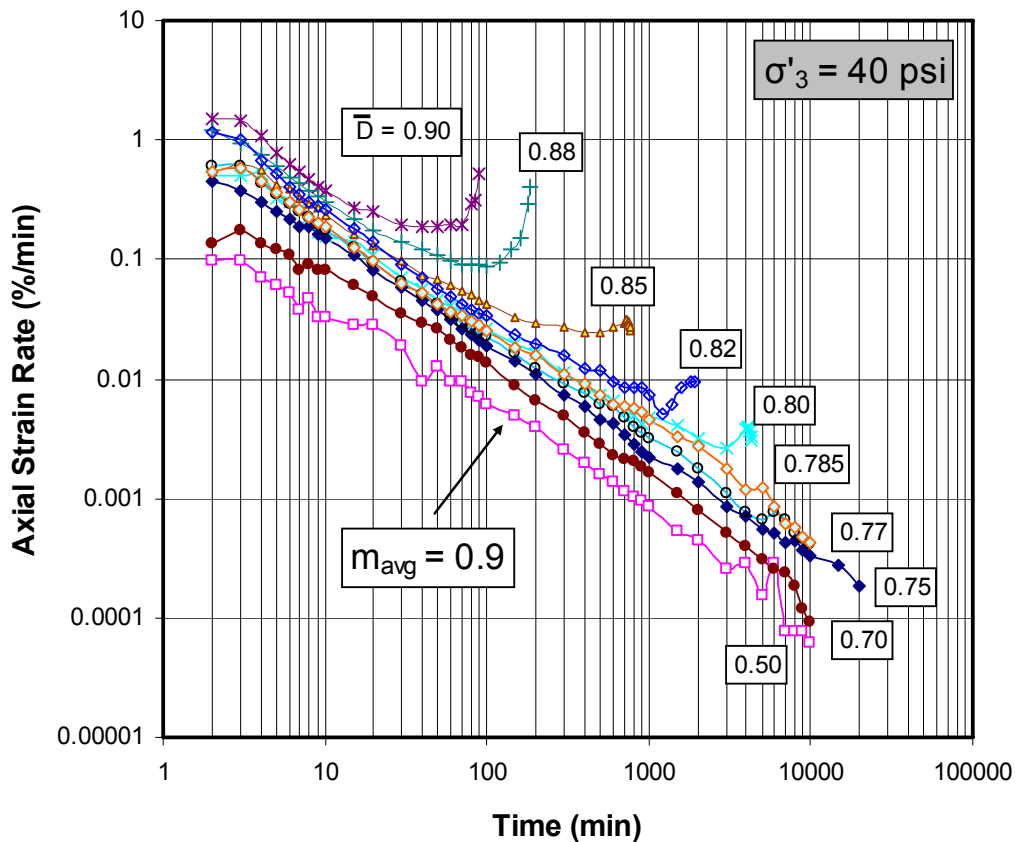


Figure 6.7 Axial strain rate versus time for RAP specimens tested at  $\sigma'_3 = 40$  psi

#### 6.4.3 Creep Tests at $\bar{D} = 0.80$

The influence of the consolidation pressure on the creep model parameters (i.e.,  $m$ ,  $A$ , and  $\bar{\alpha}$ ) was demonstrated in the previous section. The experimental findings showed that consolidation pressure has a greater effect on the  $m$  parameter than on  $A$  and  $\bar{\alpha}$ . This observation is significant

because the  $m$  parameter indicates whether the ongoing creep of a given soil will ultimately progress to complete rupture, while the  $A$  and  $\bar{\alpha}$  parameters are the amplification factors that only signify the shape of the creep curve. Therefore, additional tests were performed at a single  $\bar{D}$  but with different values of applied  $\sigma'_3$  to investigate the effect of confining pressure on the RAP creep behavior.

A large  $\bar{D}$  of 0.80 was chosen for this study to keep the test duration under an acceptable time constraint. A total of six creep tests were performed at six different confining pressures ( $\sigma'_3 = 5, 10, 20, 30, 40,$  and  $50$  psi). Plots of the observed axial strain versus  $\log(\text{time})$  and the corresponding axial strain rate plots are shown in Figures 6-8 and 6-9, respectively. The tests performed at smaller confining pressures (e.g., 5 and 10 psi) initially experienced the smallest strains (Figure 6-8), but these specimens experienced creep rupture in less than about 200 min. The test performed at 20 psi ruptured in even less time ( $\sim 100$  min), but the tests performed at confining pressures larger than 20 psi took considerably more time to reach creep rupture.

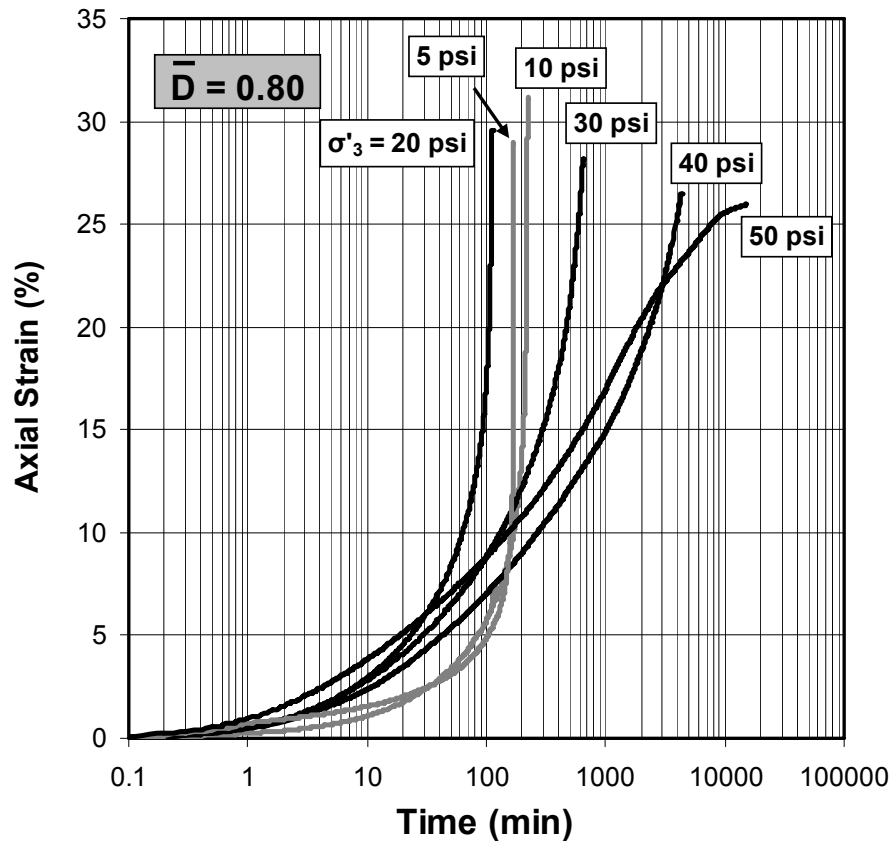


Figure 6.8 Figure 6-8 Axial strain versus  $\log(\text{time})$  for tests performed at different  $\sigma'_3$

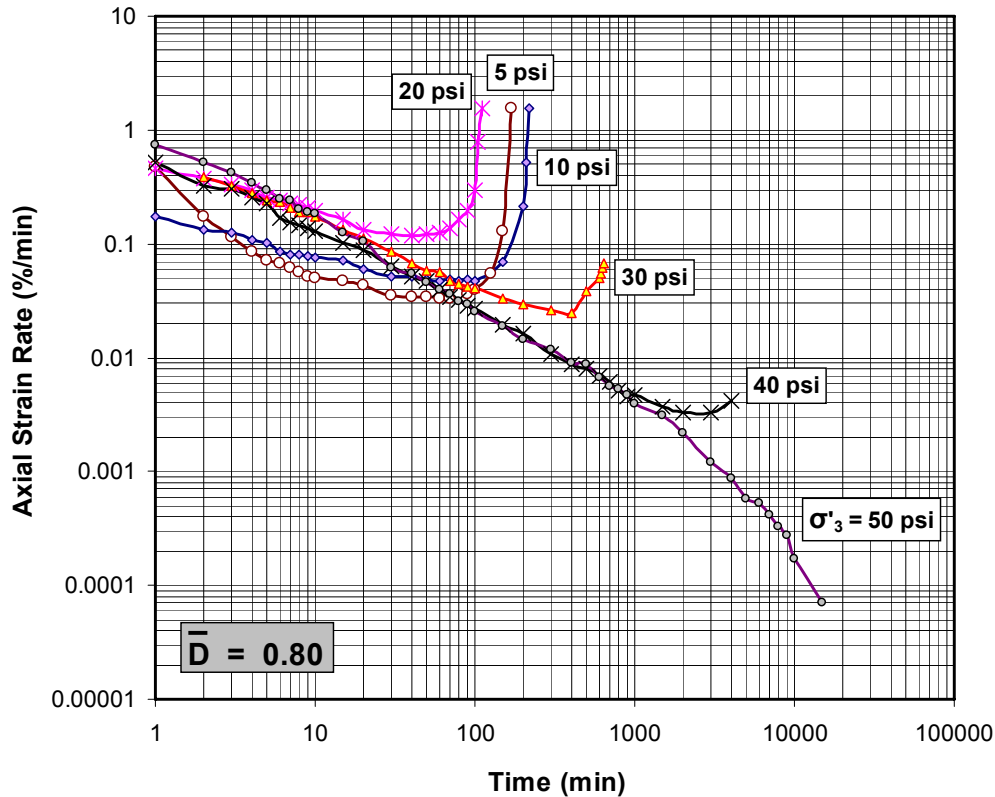


Figure 6.9 Axial strain rate versus time for tests performed at different  $\sigma'_3$

The axial strain rate data in Figure 6-9 reveal that the slope,  $m$ , of the log (axial strain rate) – log (time) curves varies with confining pressure. The values of  $m$  at lower confining pressures ( $\leq 20$  psi) are in the range of 0.4 to 0.5, indicating very flat curves and severe creep potential. At larger confining pressures the values of  $m$  are between 0.6 and 0.8, which still indicate significant creep potential, but the creep potential is less severe than at lower confining pressures.

#### 6.4.4 Creep Rupture

Creep failure can be defined as soil rupture at the end of tertiary creep. Alternatively, some researchers define creep failure as the time to reach the minimum strain rate at the end of secondary creep (Figure 6.1). Creep failure is critical for soils that display a value of  $m$  less than 1.0.

The time to creep rupture increases with decreasing stress level. Previous studies (Singh and Mitchell 1968, Campanella and Vaid 1974) have indicated a semi-logarithmic relationship between time to rupture ( $t_{rupture}$ ) and  $\bar{D}$ :

$$\log(t_{rupture}) = a - b \cdot \bar{D} \quad (6.4)$$

where  $a$  and  $b$  are experimentally determined parameters.

Seven of the creep tests performed at  $\sigma'_3 = 20$  psi and five of the tests performed at  $\sigma'_3 = 40$  psi experienced creep rupture within 1 week. These specimens initially exhibited a log-linear decrease in axial strain rate with time (Figures 6-5 and 6-7), followed by an acceleration in strain rate leading to creep rupture. The initiation of tertiary creep and imminent creep rupture can be identified as the point where the axial strain rate reaches a minimum ( $\dot{\epsilon}_{\min}$ ) and starts to increase. Creep rupture was defined by the vertical asymptote point in the axial strain versus log(time) plots (Figures 6-4 and 6-6).

The time required to reach creep rupture ( $t_{rupture}$ ) decreased at larger shear stress levels. For both sets of RAP tests, a linear relationship was observed between  $\log(t_{rupture})$  and shear stress level,  $\bar{D}$  (Figure 6-10). However, the values of  $t_{rupture}$  for tests performed at 40 psi were typically more than 10 times larger than the values of  $t_{rupture}$  at 20 psi. Fitting Equation (6.4) to the RAP data at 20 psi produces regression coefficients  $a = 10.9$  and  $b = 10.8$ . Coefficient  $b$  indicates that  $t_{rupture}$  increases by approximately one order of magnitude as the stress level decreases by 0.1. The regression coefficients for the 40 psi RAP data are  $a = 17.0$  and  $b = 16.7$ .

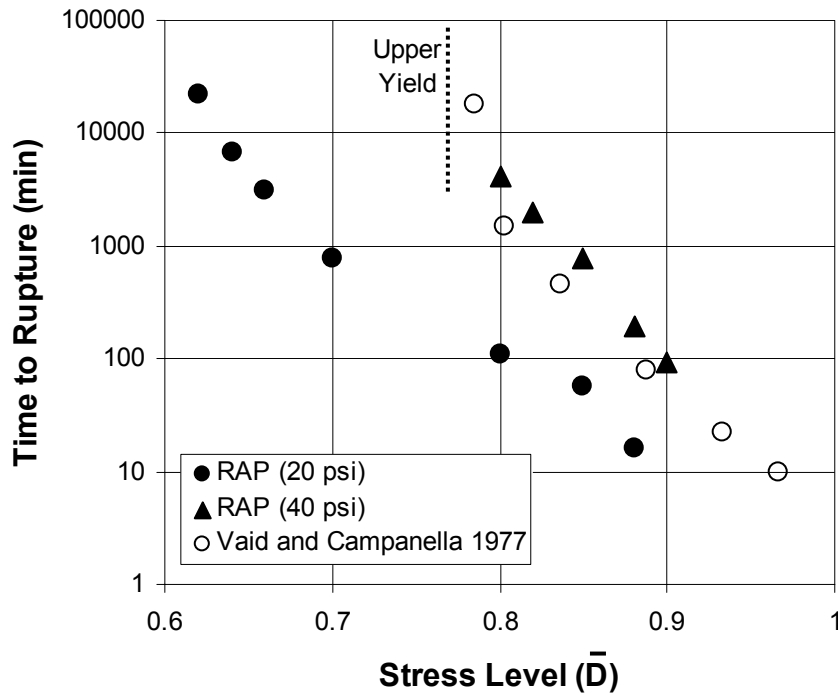


Figure 6.10 Time to creep rupture at different shear stress levels ( $\sigma_a / \sigma_{df}$ ) for RAP and Haney clay (Vaid and Campanella 1977)

For comparison, Figure 6-10 also shows rupture data from a series of undrained creep tests on Haney clay reported by Vaid and Campanella (1977). The stress levels for the Vaid and Campanella (1977) data were derived from the reported undrained shear strength, which was obtained from isotropically consolidated triaxial tests performed at a strain rate of 1 percent per minute. At a given shear stress level, the rupture life of Haney clay is longer than the rupture life

of RAP at 20 psi but similar to the rupture life of RAP at 40 psi. The Haney clay data in Figure 6-10 start to deviate from a linear relationship at stress levels below about 0.8. Based on this nonlinear trend in rupture time, Vaid and Campanella (1977) define an upper yield stress, below which creep rupture does not occur (Figure 6-10). For Haney clay, the upper yield stress represents a stress level of about 0.77. For RAP, the nonlinear trend was not apparent in the RAP data for either confining stress level; thus, an upper yield stress could not be determined for RAP.

#### 6.4.5 Discussion

For clays, most research on creep has focused on the behavior in an undrained condition. These studies have shown that the creep parameter  $m$  is generally less than 1.0 and creep rupture eventually occurs at larger stress levels because of increasing pore pressures generated by creep deformations. For the drained creep of clay, a creep parameter  $m$  less than 1.0 also has been reported (Bishop and Lovenbury 1969 and Tian et al. 1994 for normally consolidated clay, Tavenas et al. 1978 for overconsolidated clay). However, the observed creep strain rates for clays in the drained condition are smaller than those observed for clays in the undrained condition ( $\sim 10^{-2}$  to  $10^{-4}$  percent per minute at the initiation of drained creep,  $\sim 10^{-1}$  to  $10^0$  percent per minute at the initiation of undrained creep). Additionally, rupture during drained creep has only been observed in overconsolidated clays, where a dilative response leads to an increase in water content and softening over time.

The drained creep behavior of RAP observed in this study is similar to the undrained creep behavior of clays, in terms of the large strain rates at the initiation of creep ( $\sim 10^{-1}$  to  $10^0$  percent per minute) and the occurrence of creep rupture at larger stress levels. This behavior is unexpected for a gravel material but is caused by the presence of the residual bitumen coating the particles.

#### 6.5 Summary

This chapter presents results from a series of constant stress, drained creep tests performed on compacted RAP specimens. Tests were performed at varying shear stress levels and confining pressures, and deformations were monitored for up to 1 week.

Classical creep behavior was observed in all specimens, with strain rates decreasing log-linearly with time after the load was applied. The strain rate increased with increasing stress level. The creep behavior was observed to be confining pressure dependent, with more significant creep deformations and more rapid creep rupture occurring at smaller confining pressures. The creep parameter  $m$ , which is the slope of the  $\log(\text{axial strain rate}) - \log(\text{time})$  curve, was observed to vary between 0.4 and 0.9. Smaller values of  $m$  indicate more severe creep potential. Clays under undrained conditions typically display  $m$  values close to 0.7. Creep rupture occurred in many of the specimens within the 1 week of testing. The time required to reach creep rupture decreased with increasing shear stress level. When compared with creep rupture data for clays in the literature, RAP generally ruptured more quickly. It should be noted that the RAP tested in this study contained approximately 3.5% asphalt cement, which is on the low end of the expected range. Thus, RAP with a larger asphalt content may experience even more severe creep.

## **7. Corrosion Experimental Program**

### **7.1 Introduction**

Previous investigations on the corrosion performance of MSE reinforcement embedded in CC and RAP backfill materials are limited. Data are needed to provide state highway agencies with information so that decisions regarding the use of these materials can be better justified. The experimental program presented herein focused on the three backfill materials previously discussed: CFM, CC, and RAP.

The backfill materials were evaluated in reference to their effect on the corrosion of galvanized-steel and plain-steel earth reinforcing strips. Ribbed galvanized-steel and plain-steel earth reinforcing strips were selected for this study and are commonly used in Texas. For this program, the plain-steel strips embedded in CFM are assumed to be the control samples.

The experimental program can be subdivided into two main tasks: materials characterization and corrosion testing. The corrosion testing is subdivided into short-term testing (STT) and longer-term testing (LTT). The scope and justification of each task is briefly described next.

### **7.2 Research Objectives and Significance**

The objectives of this phase of the research are to generate data on the corrosion activity of metallic reinforcement embedded in CC, RAP, and CFM such that engineers can make more informed decisions regarding the use of these materials for MSE wall applications. The findings of this research are expected to be used as an aid in making decisions regarding the use of CC and RAP. If the corrosion performance of MSE reinforcement embedded in CC or RAP is similar to or better than the corrosion performance of MSE reinforcement embedded in CFM, recommendations can be made to use these recycled backfill materials. This could provide significant economic benefits as already discussed.

In addition to investigating the corrosion performance of MSE reinforcement embedded in these recycled materials, the research team investigated the possibility of using STT to assess the corrosion performance of MSE reinforcement embedded in different backfill materials. The results of the STT and LTT results will be presented and compared to determine if STT is a viable option for assessing the corrosivity of recycled backfill materials.

### **7.3 Experimental Program**

#### **7.3.1 Material Characterization**

In addition to the characterization data previously discussed, additional characterization information was needed for the corrosion of MSE strip reinforcement embedded in CFM, CC, and RAP. Material parameters believed to influence the corrosion activity of metallic materials embedded in backfill materials include the pH of the pore solution, resistivity, chloride content, sulfate content, sulfide content, oxidation-reduction potential, backfill texture and shape, and the presence of organics. Although all of these characteristics were evaluated as part of this research

program, it was found that several parameters did not show a direct influence on the corrosion activity of the samples in this test program. Also, some parameters could not be quantitatively assessed and correlations with these parameters could not be determined. In the cases where a parameter could not be directly correlated with corrosivity, only a brief overview of the testing and results are provided. If further information on these tests is desired, the reader is directed to Esfeller (2006).

### **7.3.2 Corrosion Testing**

Because limited studies have been performed on correlating STT results with LTT results and because STT is generally more cost-effective and more applicable for the construction industry, short-term corrosion tests were performed. These data were then compared with the LTT data obtained in this experimental program. STT was performed to assess the corrosivity of the CFM, CC, and RAP backfill materials. The STT required that a solution be decanted from each of the backfill materials and used as an electrolyte in corrosion cells to test the corrosion of galvanized-steel and plain-steel earth reinforcement strips. Three backfill materials, two reinforcement materials, and two environmental conditions were evaluated. Polarization resistance,  $R_p$ , (to measure the instantaneous corrosion rate), mass loss, resistivity, pH, chloride content, sulfate content, sulfide content, and oxidation-reduction (redox) potential were evaluated.

LTT is generally more desirable to assess the corrosivity of backfill materials because it allows for more realistic evaluation procedures. For the LTT performed in this research program, reinforcing strip samples were embedded in CFM, CC, and RAP. Plain-steel and galvanized-steel reinforcement samples were embedded in each backfill. For each combination (backfill type and reinforcement type), samples were exposed to two exposure conditions: chloride solution and distilled water solution applications. The solution was ponded on the samples every 7 days. Backfill material parameters were assessed to correlate corrosivity with resistivity, pH, chloride content, and sulfate content.  $R_p$  and open circuit potential (OCP) measurements were used to evaluate the corrosion performance of the embedded strip reinforcement samples. Mass loss testing (following ASTM G1 test procedure) was performed on the MSE reinforcing samples to also estimate the corrosion activity. The corrosion activity data were then used to assess the service life of each backfill and reinforcement material combination. The  $R_p$  and OCP data were used to determine if these procedures could reliably be used to predict corrosion activity of the reinforcements embedded in the backfill materials.

### **7.4 Materials Characterization**

As previously noted, three backfill materials were selected from suppliers in Texas. The materials used for the corrosion studies were obtained from the same batch of materials used for the geotechnical studies presented earlier. Galvanized- and plain-steel earth reinforcing strips were also obtained from the same manufacturer in Texas that provided the materials to the researchers at UT Austin. Although the backfill materials and earth reinforcement were selected as being representative of the industry, care should be taken when applying the results from these materials to other materials for MSE wall construction.

### 7.4.1 Backfill Materials

Several laboratory tests were performed to evaluate the engineering properties of the backfill materials. Morris and Delphia (1999) recommended that the following soil tests be required for backfill for MSE wall systems:

- Sampling
- Grain Size Distribution
- Atterberg Limits
- Classification
- pH
- Resistivity
- Relative Density
- In-Place Density

Morris and Delphia (1999) also recommended the following soil tests as being optional for identifying problem backfill soils for MSE walls:

- Shear Strength
- Permeability
- Collapse Potential
- Specific Gravity

Because salts are known to significantly influence the corrosion activity, other soil tests that should be required for MSE backfill materials include the determination of chloride, sulfate, and sulfide concentrations. Chloride, sulfate, and sulfide concentrations have been identified as promoting corrosion (Romanoff 1957) and could be important elements in determining backfill corrosivity (Elias 1990). Elias (1990) groups chlorides, sulfates, and sulfides under the term soluble salts with other salts such as carbonate. Carbonate forms a scale on most metals and can act as a corrosion inhibitor (Elias 1990). The soluble salts noted with the most significant impact on the corrosion of metallic reinforcement in soils are chloride, sulfate, and sulfide (Elias 1990). In this experimental program, of the soluble salts, only chloride content, sulfate content, and sulfide content were measured.

The oxidation-reduction (redox) potential of a soil can also provide information on the type of corrosion mechanism, i.e., aerobic or anaerobic (Elias 1990). Other countries such as the United Kingdom and Germany use the soil redox potential as one of the test criteria for the suitability of select backfill material used in conjunction with galvanized-steel earth reinforcement (Elias 1990). However, it is noted throughout the literature that correlating corrosion rate with redox potential has been unsuccessful.

The particle shape and surface characteristics of soil should also be investigated along with the grain size distribution, because this characteristic can provide an indication of aeration level in a backfill material. Aeration affects the corrosion mechanism by creating aerobic or anaerobic conditions. The defining particle shape and surface properties are form, angularity, and texture. Each of these defining shapes and surface characteristics can be classified on a scale proposed by Al-Rousan et al. (2004). Morris and Delphia (1999) obtained results that indicate that particle shape is a contributing factor in the compaction of cohesionless soils. Their results indicated that the maximum dry unit weight increases with increasing roundness, while the grading of soil was

shown to play a minor role in determining the compaction of cohesionless soils (Morris and Delphia 1999). The compaction of a soil is defined as the elimination of air voids between the soil particles. Compaction directly affects aeration. Therefore, it is important to measure the particle shapes and surface characteristics and not just the grain size distribution.

The proportion of organic materials should also be measured because microbes can produce organic acids that can cause pitting corrosion of the metallic earth reinforcement (Elias 1990). If the organic material is unevenly distributed throughout the backfill material, pockets of soil can become anaerobic because of sulfate-reducing bacteria, resulting in severe pitting corrosion (Elias 1990).

The CFM, CC, and RAP backfill materials used in this program were characterized with the following tests, in addition to the characterization tests presented earlier:

- Pore solution pH
- Resistivity
- Chloride content
- Sulfate content
- Sulfide content
- Redox potential
- Specific gravity
- Permeability (hydraulic conductivity)
- Shape and surface characteristics
- Presence of organics

The redox potential, shape and surface characteristics, permeability and presence of organics could not be correlated with corrosivity. For the redox potentials, more negative values indicate greater susceptibility to microbial attack. Results indicate that the redox potential values vary with backfill type and change little when solutions are drained through these materials. Although the CC showed negative values of redox potentials, the higher pH of this material makes the potential for microbial corrosion unlikely. Thus, the materials evaluated in this research are likely not susceptible to microbial attack.

A detailed assessment of the shape and texture of the three backfill materials was performed and the following was determined:

- backfill materials have similar angularity, texture, and form
- the CFM coarse aggregate has a higher percentage of rounded particles,
- the RAP fine aggregate is slightly more angular and elongated than the CFM and CC,
- the order of texture from higher roughness to lower roughness is CFM, RAP, and then CC, and
- higher percentages of circular coarse aggregate particles were found in the CC when compared with the CFM and RAP.

Specific gravity and permeability data were provided earlier and no further discussion on these parameters will be presented. MSE reinforcement type is also known to influence the rate of corrosion, and a discussion of the different reinforcement types will be presented later.

### **Pore Solution pH**

ASTM D 4972-95a, *Standard Test Method for pH of Soils*, was used to measure the pH of the pore solutions in the backfill materials. This method determines the solubility of soil minerals and the ion mobility. This method was selected for testing the backfill materials because it was deemed important that the pH be measured similar to the pH measurements required by the standard, *Method of Determining pH of Soil*, of the California Department of Transportation (Caltrans) California Test 643, *Method for Estimating the Service Life of Steel Culvert*. Caltrans has a service-life prediction equation that relies on pH data acquired by testing according to this test procedure. It was important that the collected data be compatible with the service-life prediction equation so that this existing method of service-life prediction can be compared to any new models that are proposed as a result of this experimental program. Note that the Caltrans service life model is for corrosion of galvanized steel culverts but is often used for other systems that contain galvanized steel products.

### **Resistivity**

Measurements of the minimum soil resistivity of each of the backfills were made according to the *Laboratory Method of Determining Minimum Resistivity* procedure outlined in Caltrans California Test 643. Resistivity was measured with a MC Miller Co., Miller Soil Box and Nilsson Soil Resistance Meter Model 400. The inside dimensions of the soil box was 1.5 in. (39.37 mm) wide by 8.75 in. (222.3 mm) long by 1.25 in. (31.90 mm) deep. The soil box test setup is similar to that found in ASTM G57-95a, *Standard Test Method for Field Measurement of Soil Resistivity Using the Wenner Four-Electrode Method*.

### **Soluble Salts**

The soluble salts that can promote corrosion are chlorides, sulfates, and sulfides (Elias 1990). There are several methods for measuring the concentration of each of these ions in water. However, ASTM D4327, *Chemically Suppressed Ion Chromatography*, was used to assess the concentrations of chlorides and sulfates because it is reliable and can quantify these concentrations in one test. The ion chromatography testing was done using a Dionex<sup>®</sup> DX-80 Ion Analyzer. The ion chromatograph sample loop size was 0.000338 oz (10  $\mu$ L). The analytical column used in the ion chromatograph was the Dionex<sup>®</sup> IonPac<sup>®</sup> AS14A. To analyze a sample, 0.0338 oz (1 ml) of the sample was injected into the ion chromatograph using a 0.0338 oz (1 ml) sterile, single use syringe. The sample was injected through a 0.000007874-in. (0.20  $\mu$ m) Corning<sup>®</sup> sterile syringe filter. The filter is required to avoid clogging the resin of the columns (ASTM D4327).

There are many methods available to measure the sulfide ( $S^{2-}$ ) concentration. Methods listed in the Standard Methods for Examining Water include the: methylene blue, gas dialysis (automated methylene blue), iodometric, and ion-selective electrode methods. The standard test method published as ASTM D4658, *Procedure for Sulfide Ion in Water*, requires the use of an ion-selective electrode to determine the sulfide ion concentration in water. The ion-selective electrode method is less complex than the other methods, but still requires extensive preparation to mix reagents and calibrate the ion-selective electrode. ASTM D4658 was used to measure the concentration of sulfide ion.

Samples for chloride, sulfate, and sulfide analysis were collected and stored in a refrigerator at approximately 40°F (4.4°C) prior to testing. The samples collected for sulfide analysis were stored in a separate container because chemicals were added to preserve the sample. ASTM D4658 required that 2 molar zinc acetate and 6 molar sodium hydroxide be added to the samples collected for sulfide analysis. ASTM D4658 specifies that for a 3.38 oz (100 ml) bottle, 4 drops of 2 molar zinc acetate be added and 1 drop of 6 molar sodium hydroxide be added after the bottle is filled three-fourths full. The samples collected for characterization were 4.22 oz (125 ml), therefore 5 drops of 2 molar zinc acetate were added along with 2 drops of 6 molar sodium hydroxide after the bottle was filled three-fourths full with the sample. ASTM D4658 requires that the bottle used to collect the sample be stoppered and that no air bubbles be trapped beneath the stopper. This is required because trapped air can oxidize the sulfide and convert it to sulfate. The 125 ml (4.2 fl oz) Nalgene bottles were completely filled and capped off, and an effort was made to trap no air beneath the cap. The ion selective electrode used to find the sulfide concentration was an Orion<sup>®</sup> Silver/Sulfide Electrode Model 9616. A Denver<sup>®</sup> model 250 pH/ISE/conductivity meter was used to display the readings.

The solutions collected from the first drainage of distilled water through the backfills during the STT were used to characterize the backfills. The concentration of chloride and sulfate ions was determined following ASTM D4327.

#### **7.4.2 MSE Reinforcement**

Ribbed galvanized-steel and plain-steel earth reinforcing strips were characterized and used in the experimental program. The earth reinforcing strips were acquired from the Reinforced Earth Company. The earth reinforcing strips were characterized by size, shape, and composition.

##### **Size**

ASTM G162, *Standard Practice for Conducting and Evaluating Laboratory Corrosion Tests in Soils*, recommends that certain details of exposed specimen be reported. The items that should be reported are alloy and temper, metallurgical history, chemical composition, processing parameters for formed parts, coating chemistry, weight, and thickness. The plain-steel earth reinforcement used in this program had approximate dimensions of 1-15/16 in. wide (49 mm) by 78 in. (1980 mm) long by 0.16 in. (4 mm) thick. The galvanized-steel earth reinforcement strips were slightly wider and thicker, 2 in. (51 mm) wide and 0.19 in. (5 mm) thick. The strips also have a 9/16 in. (14 mm) diameter hole. The center of the hole is located 1-1/2 in. (38 mm) from the end of the strip.

The ribs on the plain-steel earth reinforcing strips were located on the top and bottom sides, and in a staggered configuration as shown in Figure 7.1. Two ribs, spaced 1-11/16 in. (43 mm) apart, were located approximately every 7 in. (178 mm) along the length of the plain-steel strips. Two ribs, spaced 1-13/16 in. (46 mm) apart were located approximately every 7-5/16 in. (186 mm) along the length of the galvanized-steel strips. The ribs in the earth reinforcing strips were approximately 0.04 in. (1mm) wide at the top, 0.2 in. (5 mm) wide at the base, and 0.08 in. (2 mm) tall.

These earth reinforcing strips were cut into smaller pieces so that they could be embedded in the backfill materials for the short- and longer-term corrosion testing. Samples were also cut from

the MSE reinforcement strips to determine composition and galvanized coating thickness. The chemical composition of the steel, and the composition and coating weight of the galvanization was found through testing performed by Atlas Testing Laboratories, Los Angeles, California.

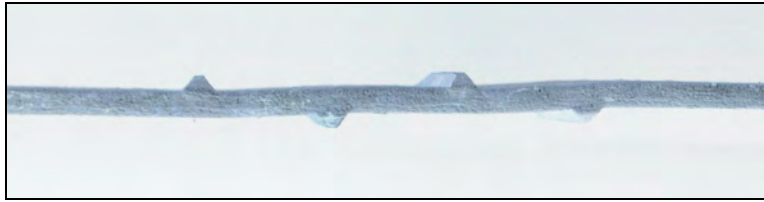


Figure 7.1 Side view of a galvanized earth reinforcing strip showing ribs.

### Chemical Composition

A plain-steel specimen 2 in. (50.8 mm) wide by 2 in. (50.8 mm) long was tested according to ASTM E415, *Standard Test Method for Optical Emission Vacuum Spectrometric Analysis of Carbon and Steel*. The material was identified as a Society of Automotive Engineers - American Iron and Steel Institute (SAE-AISI) 1513 steel or Unified Numbering System for Metals and Alloys (UNS) G15130. The chemical composition limits for SAE-AISI 1513 are: 0.10 to 0.16 percent carbon, 1.10 to 1.40 percent manganese, 0.040 percent maximum phosphorus, and 0.050 percent maximum sulfur. The chemical analysis results used to identify the plain-steel material type are shown in Table 7.1.

Table 7.1 Chemical Analysis of Plain-steel Earth Reinforcing Strip Specimen.

Elements	Percent
Carbon	0.15
Chromium	0.10
Copper	0.42
Manganese	1.22
Molybendum	0.05
Nickel	0.27
Phosphorus	0.013
Silicon	0.16
Sulfur	0.021
Iron	Remainder

The steel is categorized as a Group II SAE-AISI plain carbon steel because it contains 0.15 to less than 0.30 percent carbon. This plain-steel is not considered a mild steel because it contains greater than 0.75 percent manganese. Group II steels with less than approximately 0.75 percent manganese are commonly referred to as mild steels (Davis 1996). In general, carbon steels are best suited for galvanizing when alloying/impurities are less than the following levels: 0.25 percent carbon, 1.3 percent manganese, 0.05 percent phosphorus, and 0.05 percent silicon (Davis 1996). All compositional limits were met with the exception of the silicon.

Approximately 0.07 oz (2 grams) of galvanization were used to perform the wet chemical analysis to determine the chemical composition of this layer. Test method ASTM E1097, *Standard Guide for Direct Current Plasma Emission Spectrometry Analysis*, was performed and yielded the results shown in Table 7.2. These results show that the galvanized coating is composed of greater than 98 percent zinc.

Table 7.2 Chemical composition of the galvanized coating on reinforcing strips.

Elements	Percent
Aluminum	<0.01
Boron	<0.01
Cadmium	0.03
Chromium	<0.01
Cobalt	<0.01
Copper	0.04
Iron	0.59
Lead	1.1
Magnesium	<0.01
Manganese	<0.01
Nickel	<0.01
Silicon	<0.01
Tin	0.04
Titanium	<0.01
Zinc	Remainder

### Galvanization Coating Weight

A galvanized-steel specimen 2 in. (50.8 mm) wide by 3 in. (76.2 mm) long by 3/16 in. (4.75 mm) thick was tested to find the galvanization coating weight. ASTM A90, *Standard Test Method for Weight [Mass] of Coating on Iron and Steel Articles with Zinc Coatings*, was performed. The coating weight for the specimen was 3.31 oz/ft<sup>2</sup> (1.01 kg/m<sup>2</sup>) of sheet. This coating weight corresponds to an average galvanized coating thickness of 5.5 mils (140 µm), which surpasses the minimum sacrificial galvanized coating thickness for earth reinforcement required by the Federal Highway Administration (FHWA), which is 3.4 mils (86 µm) corresponding to a coating weight of 2 oz/ft<sup>2</sup> (0.61 kg/m<sup>2</sup>).

The thickness of the galvanized-steel earth reinforcement was confirmed using an optical microscope. Two samples were selected at random and prepared for microscopic measurement of the galvanized coating thickness. Three microscopic measurements were randomly made of the galvanized coating on each sample. The average galvanized coating thickness determined by microscopic examination was approximately 6 mils (150 µm). Figure 7-2 shows a micrograph of the galvanized coating. These measurements confirmed the average coating weight found by using test method ASTM A90. ASTM A90 is considered the more accurate method for determining the coating thickness.

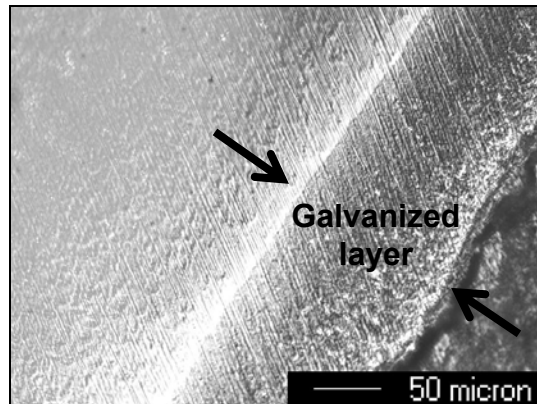


Figure 7.2 Micrograph of the galvanized coating on a galvanized-steel strip.

## 7.5 Corrosion Testing Methods

### 7.5.1 Short-term Corrosion Testing Program

A description of the experimental design, test setup, and testing program for the STT is provided in this subsection. The methods and materials used for performing the STT are also described. The STT consisted of placing samples in corrosion cells with a decanted solution from the backfill materials to monitor the corrosion with respect to time.

#### Experimental Design

Backfill material corrosivity should be examined with regard to backfill type, reinforcement type, and exposure condition. Because backfill materials for MSE walls are repeatedly exposed to drainage cycles, the pore solution of the backfill materials could change with time. Therefore, the number of drainages through the backfill was an additional variable examined. Water was passed through the backfill materials and the resulting pore solution was evaluated after different numbers of drainage cycles. This was performed because the pore solution is expected to have a significant impact on corrosion performance and the pore solution could change with each drainage. STT was performed using decanted pore solutions from the 1<sup>st</sup> and 100<sup>th</sup> drainage.

For the STT, the backfill, reinforcement, chloride concentration, and pore solution drainage cycle were variables evaluated for influence on backfill corrosivity. These variables were controlled in the experiment. The three backfill materials (CFM, CC, and RAP), two reinforcement types (galvanized-steel [G] and plain-steel [S]), two chloride concentrations (high chlorides [CL] and low chlorides [NCL]), and two pore solutions (1st drainage [1] and 100th drainage [100]) were evaluated. Thus, there are 24 levels to the experiment. The level identifications were determined by the controlled variables in the STT experiment as shown in Table 7-3. Three replicates were evaluated for each level.

The testing program consisted of performing characterization tests on the decanted backfill solution, electrochemical tests, and mass loss testing when the samples were removed from the corrosion cells (at the end of the test period). The characterization test program for the decanted backfill solutions is shown in Table 7-4. The objective of this test program was to determine if there were significant changes in the decanted solution because of the number of drainages. The testing program for the STT is summarized in Table 7-5.

*Table 7.3 Sample identifications based on the controlled variables for STT.*

Backfill Type	Reinforcement Type	Chloride Concentration	Drainage Number	Level Name
CFM	G	CL	1	CFM_G_CL_1
			100	CFM_G_CL_100
		NCL	1	CFM_G_NCL_1
			100	CFM_G_NCL_100
	S	CL	1	CFM_S_CL_1
			100	CFM_S_CL_100
		NCL	1	CFM_S_NCL_1
			100	CFM_S_NCL_100
CC	G	CL	1	CC_G_CL_1
			100	CC_G_CL_100
		NCL	1	CC_G_NCL_1
			100	CC_G_NCL_100
	S	CL	1	CC_S_CL_1
			100	CC_S_CL_100
		NCL	1	CC_S_NCL_1
			100	CC_S_NCL_100
RAP	G	CL	1	RAP_G_CL_1
			100	RAP_G_CL_100
		NCL	1	RAP_G_NCL_1
			100	RAP_G_NCL_100
	S	CL	1	RAP_S_CL_1
			100	RAP_S_CL_100
		NCL	1	RAP_S_NCL_1
			100	RAP_S_NCL_100

Table 7.4 Testing program for decanted backfill material pore solutions.

Characterization Test	ASTM Designation	Performed on Drainages
Resistivity	G57	1, 10, 20, 50, 100
pH	D4972	1, 10, 20, 50, 100
Redox potential	none	1, 10, 50, 100
Sulfate	D4327	1, 10, 100
Chloride	D4327	1, 10, 100
Sulfide	D4658	1, 10, 100

Table 7.5 Testing program for the samples while in the corrosion cells.

Test Type	Target Test Time <sup>a</sup> (Days)	Target Test Time <sup>a</sup> (Hours)
$R_p$	1	24
$R_p$	2	48
$R_p$	4	96
$R_p$	7	168
$R_p$	14	336
$R_p$	21	504
$R_p$	28	672
Cyclic Polarization	29	696

<sup>a</sup>Target test times measured from the time the samples were placed in the cells and oxygen purging began.

$R_p$  and cyclic polarization testing were used to evaluate the corrosion activity of the samples in the corrosion cells. More frequent  $R_p$  testing was performed at the beginning of the test because the rate of change of the corrosion rate was expected to vary more during this time period. Cyclic polarization testing was performed only at the end of the testing period because of the destructive nature of this test.

The final test performed on the reinforcement samples was mass loss testing. The mass loss testing was performed according to ASTM G1, *Standard Practice for Preparing, Cleaning, and Evaluating Corrosion Test Specimens*.

## Experimental Setup

### *Preparation of Reinforcing Samples*

The earth reinforcing strips were prepared to minimize localized corrosion. Epoxy was applied to the samples to expose an area of approximately 11/16 in. (17.5 mm) square. Counter electrodes for the corrosion measurements were 1 in. (25 mm) by 1 in. (25 mm) 52 mesh pure platinum wire gauze tack welded to an American Wire Gauge (AWG) 20 (0.81 mm) diameter 99.95

percent platinum wire 6 in. (152 mm) long. A counter electrode with a geometric area of at least twice the surface area of the working electrode is recommended for electrochemical testing (Tait 1994). The total area of the wire mesh was determined to be 1.08 in<sup>2</sup> (0.0007 m<sup>2</sup>), over twice the area of the working electrode.

After the samples were epoxied, the samples were cleaned again in denatured ethyl alcohol in the ultrasonic cleaner. Figure 7.3 shows a photograph of a typical sample. After cleaning, the samples were weighed to the nearest 0.0000035 oz (0.0001 gram). The weight was recorded as "weight after epoxing." The samples were weighed twice (i.e., before and after epoxy application) because if underfilm corrosion occurs during the testing and the epoxy flakes off, the weight with no epoxy would be needed to calculate the mass loss. After weighing the samples, photographs of the front and back of each sample were obtained. The samples were then stored in a desiccator until the day of testing.



Figure 7.3 Typical steel sample following preparation for STT.

#### ***Preparation of Backfill Materials for Obtaining Pore Solution***

The backfill materials were prepared by sieving, mixing, and adjusting the moisture content as described earlier. The backfill materials were placed in 14.5 gal (55 L) Nalgene<sup>®</sup> carboys with a piece of woven silt fabric placed over the outlet on the inside of the container. This was done to limit the loss of fine particles through the outlet. Approximately 11.9 gal (45 L) of backfill material was placed in each container and 2.9 gallons (10 L) of solution was poured on top of this backfill to collect at least 1.85 gal (7 L). This amount was needed to perform the tests in the corrosion cells. The backfill materials were not compacted in the containers according to the recommended dry density because of the inability of the containers to support the stress.

#### ***Corrosion Cells***

The corrosion cells used in the research were manufactured by EG&G Instruments, Inc., Princeton Applied Research. Model K47 corrosion cells were used in this research. This corrosion cell system consists of a corrosion flask, a specimen holder, a counter electrode holder with counter electrode, a reference electrode, a bridge tube, a purge and vent tube, and a ball and socket clamp. Figure 7.4 shows the corrosion cell system and components. Non-standard

components of the model K47 used in the experiment were platinum counter electrodes and size 24/40 rubber septum stoppers. The reference electrode, specimen holder, and in general, the corrosion cell met the specifications under the apparatus section of ASTM G5, *Standard Reference Test Method for Making Potentiostatic and Potentiodynamic Anodic Polarization Measurements*. The only difference between the polarization cell described in ASTM G5 and the corrosion cell used in this research is that the corrosion cell did not have a thermometer inserted into the solution chamber. All testing was performed at laboratory temperatures ranging from ~ 65° to 75 °F. All cell components were properly cleaned prior to use.

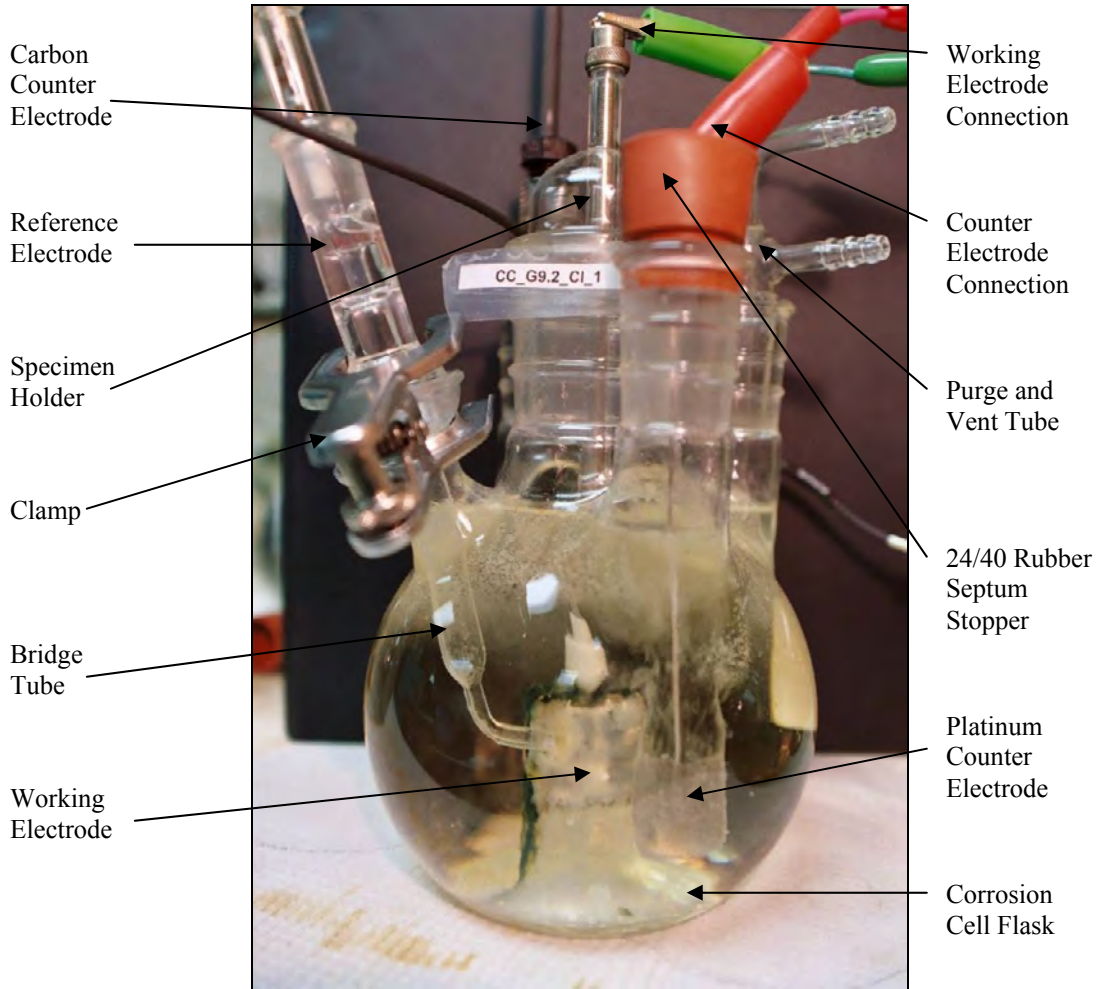


Figure 7.4 Corrosion cell system and components used for the STT.

Figure 7.5 shows the system for collecting the pore solution from the backfill materials. The same procedure was used to collect solution samples for characterization and for the STT testing. Before collecting the pore solution for analysis, the solution was allowed to remain in the carboy for at least 24 hours. The solutions were analyzed after the 1<sup>st</sup>, 10<sup>th</sup>, and 100<sup>th</sup> drainages. Additional pH, resistivity, and redox potential readings were obtained at the 20<sup>th</sup> and 50<sup>th</sup> drainages. All drainages between those being analyzed were allowed to remain in the container for at least 45 minutes. After 45 minutes, the containers were drained and then refilled for the

next drainage. The solution was not left in the containers for more than 24 hours unless the drainage was to be analyzed. While performing the drainages, there was a considerable difference between the drainage times for the CFM and RAP compared to the CC. It took the solution approximately 30 minutes to drain through the CC, whereas it took approximately 15 minutes for the CFM and RAP. This behavior is in accordance with the permeability study that was performed to characterize the backfill materials referred to earlier. The filtered solutions were collected and then transferred into the corrosion cells (or used for characterization).

To ensure similar initial conditions, all cells were purged with oxygen. The backfill solutions in the cells were purged with 99.99 percent pure oxygen for 12 hours at the regulated rate of 0.2 SCFH (standard cubic feet per hour) ( $0.00566 \text{ m}^3/\text{h}$ ) after placing metallic samples in the cells. The corrosion cells are shown in Figure 7.6.

### ***Potentiostat Settings for STT***

The potentiostat used for the STT program was a Verstat<sup>TM</sup> II manufactured by Perkin Elmer<sup>®</sup> Instruments. The potentiostat was controlled by the SoftCorr<sup>TM</sup> III user interface. A scan rate of 0.167 mV/sec was used for the STT studies. IR compensation was not used.



*Figure 7.5 Drainage collection from the backfill materials for the STT.*



Figure 7.6 Purging of corrosion cells with oxygen during the STT.

## 7.5.2 Long-term Corrosion Testing Program

### Experimental Design

The LTT consists of monitoring the corrosion of plain-steel and galvanized-steel samples embedded in the three backfills. Similar to the STT, the factor of interest was the backfill corrosivity. This factor was examined with regard to backfill material type, reinforcement type, and exposure types. Table 7.6 shows the experimental program and sample identification system for the LTT samples. Eight replications were made at each level for the measurement of potential readings and mass loss. Two replications were made at each level for the  $R_p$  and cyclic polarization testing.

Table 7.6 Sample identifications based on the controlled variables for LTT samples.

Backfill Type	Reinforcement Type	Chloride Concentration	Level Name
CFM	G	CL	CFM_G_CL
		NCL	CFM_G_NCL
	S	CL	CFM_S_CL
		NCL	CFM_S_NCL
CC	G	CL	CC_G_CL
		NCL	CC_G_NCL
	S	CL	CC_S_CL
		NCL	CC_S_NCL
RAP	G	CL	RAP_G_CL
		NCL	RAP_G_NCL
	S	CL	RAP_S_CL
		NCL	RAP_S_NCL

Data were collected during the LTT period using different measurements. OCP measurements were taken at predetermined intervals on all the samples to provide an indication of when the

reinforcement began to actively corrode. These readings were taken before and after solution application because it was found that dryness of the backfill materials had a significant impact on the corrosion potential readings. The corrosion potential readings could also be useful in monitoring the degradation of the galvanized layer. An assessment of the galvanized layer degradation can be made by monitoring the OCP over time of the galvanized-steel samples and by comparing these readings to the OCP readings of steel samples under the same conditions. Elias (1990) recommended the use of OCP measurements with  $R_p$  measurements to provide an effective monitoring scheme of the composition of the exposed surface. Thus, some samples were equipped for measuring the  $R_p$ , which can provide information on the instantaneous corrosion activity.  $R_p$  measurements were often made both before and after solution application.

At the end of 336 days, the metallic reinforcement was removed from each of the cells and mass loss testing following ASTM G1 was performed. At the end of the LTT, measurements were also made on samples of the backfill materials to determine pH, resistivity, chloride, sulfate, sulfide, and redox potential.

## **Experimental Setup**

### ***Preparation of Reinforcing Samples***

Steel reinforcing strips were cut into lengths of approximately 7 in. (178 mm). The reinforcing strip edges were ground to round off the cut edges. A hole was drilled and tapped in the samples to accommodate insertion of a 4-in. (102 mm) long 5-40 threaded stainless-steel connection rod. The insertion of the threaded rod into each sample was necessary so that connection to the working electrode could be made for potential readings. The threaded rod protruded to the outside of the form so that a potential meter could be easily connected to obtain the OCP readings. After drilling and tapping, the samples were cleaned in an ultrasonic cleaner with denatured ethyl alcohol.

Sikadur<sup>®</sup> 35 epoxy was applied to all sides of the sample, except for the exposed area (~2 in. wide [51 mm] by 4 in. [102 mm] long). The epoxy was also applied to the stainless steel rod except for the last 1-1/2 in. (38 mm) of the rod.

### **Preparation of the Backfill Forms**

The dimensions of the backfill forms were determined by the maximum size aggregate (MSA). Because the MSA used in this research was 1-1/2 in. (38 mm), a form that could accommodate this backfill material was designed. It was determined that the inside dimensions of the backfill form should be 6 in. (152 mm) wide by 10 in. (254 mm) long by 6 in. (152 mm) deep. A perspective view of a form with a plexi-glass dam on the top for ponding is shown in Figure 7.7.

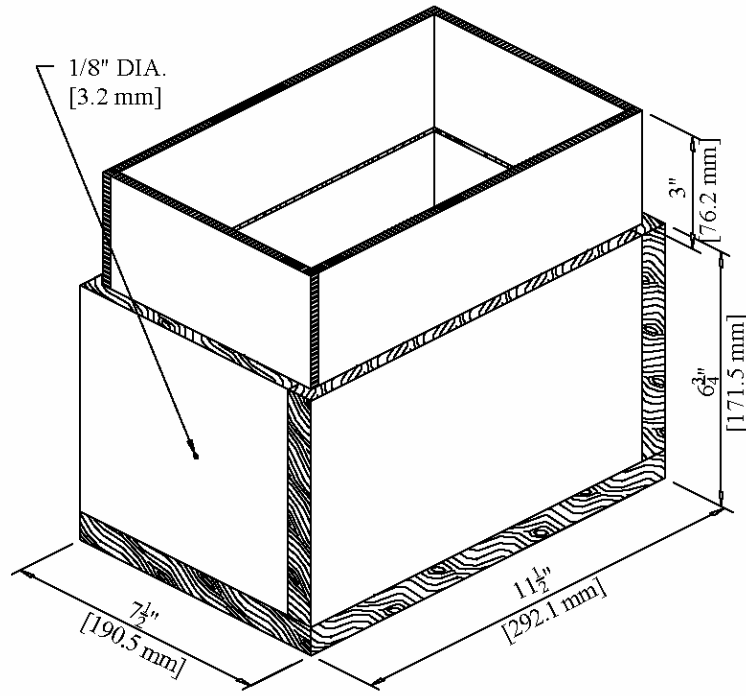


Figure 7.7 Perspective view of form for backfill materials used during LTT.

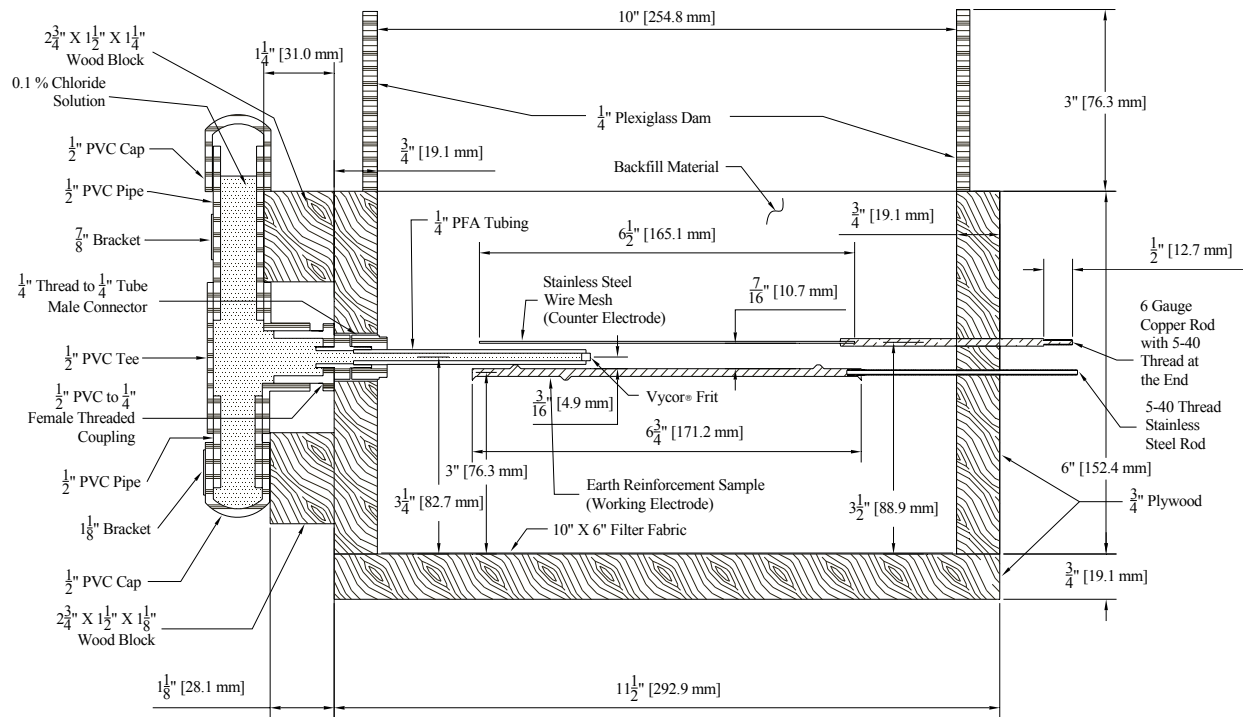


Figure 7.8 Section View of LTT Sample for Performing Corrosion Testing.

Before placing the backfill material in the backfill form, a piece of woven silt fabric was placed in the bottom to cover drainage holes drilled in the bottom of the form. This was necessary to prevent the loss of fine aggregate particles from the backfill form. The samples to be tested by  $R_p$  required slight modification of the forms. A detailed section view of the LTT setup for performing these corrosion measurements is shown in Figure 7.8. Special Luggin probes (Figure 7.8) were fabricated to perform the  $R_p$  and cyclic polarization tests. The counter electrode was made from a 3 in. (76 mm) by 6 in. (152 mm) stainless-steel wire gauze connected to an AWG 8 (3.26 mm) copper wire.

### ***Corrosion Testing Sample Assembly***

After the backfill forms were prepared and the woven silt fabric was placed in the bottom of the form, two layers of backfill material were compacted in the forms. The reinforcement sample was then inserted into the form, and two additional layers of backfill material were placed and compacted in the forms. For the LTT samples requiring  $R_p$  testing, special care was taken to not damage the probes. Approximately ½ in. (13 mm) of fines from the respective backfill materials was placed between the counter electrode and reinforcing sample (working electrode). The materials in the forms were compacted following Tex-113E and were at the target moisture contents described earlier.

Dams were added after the backfill material was compacted in the backfill forms. Dams were needed at the top of each backfill form to allow ponding of solution. The dams were constructed of four pieces of plexiglass.

### ***Backfill Sample Collection and Assessment (Post Test)***

At the end of the LTT, samples of the backfill materials were collected for analysis. Approximately 1.1 lb (500 grams) of backfill materials just above the surface of the reinforcement was evaluated for pH, resistivity, chloride ion concentration, sulfate ion concentration, sulfide concentration, and redox potential analysis. Pore solution pH, sulfide, and redox potential testing were performed on these samples as described earlier.

### ***Potentiostat Settings for LTT***

The potentiostat used for the LTT program was a Solartron™ 1287 and was controlled by the Corrware™ software interface. This potentiostat was used for all LTT  $R_p$  measurements. The Verstat™ II potentiostat by Perkin Elmer® Instruments was used for all LTT cyclic polarization measurements and was controlled by the SoftCorr™ III user interface. The potentiostat settings for the  $R_p$  testing were the same as the STT investigation (1.67 mV/sec and no IR compensation). The cyclic polarization scan was from -225 mV to +1000 mV and back to -225 mV and was performed at a scan rate of 1 mV/sec.

## **7.6 Summary**

Materials and methods used to characterize the corrosivity of CC, RAP, and CFM backfill materials were presented. These methods were implemented to characterize the corrosivity of these materials and to provide data so that the corrosion activity and service life of MSE wall systems could be estimated. The following chapters will present the results of this testing program, analysis of the test results, and predictions of the service life for MSE wall systems.

## 8. Results from Corrosion Testing

### 8.1 Introduction

The results of the STT and LTT programs are presented in this section. The results of each program are presented separately and then compared to determine if STT represents results from the generally more reliable LTT results. If no correlation can be identified, service life predictions will be performed using the data from the LTT experiments. Based on the results from these tests, a general assessment of corrosivity will be made for the backfill materials.

### 8.2 Short-term Testing Results

The STT results consist of measurements made on the metal (G or S) interactions between the solution environment (CL or NCL) decanted through the backfill materials (CFM, CC, or RAP). As indicated, this decanted solution is referred to as *pore solution*. Changes in the pore solution chemistry as a function of the number of drainages through the backfill materials were investigated and are presented in this section. STT results from mass loss and electrochemical testing are also presented in this section. The STT was performed so results could be compared with LTT results. If it is determined that the STT can provide adequate insight into the corrosivity of the backfill materials, then the STT could be more economical for assessing the corrosivity of backfill materials.

#### 8.2.1 Pore Solution

Pore solution characteristics such as pH, resistivity, oxidation-reduction potential, chloride concentration, and sulfate concentration were measured as a function of the number of drainages through the backfill materials. These characteristics were measured for solutions obtained from the 1<sup>st</sup>, 10<sup>th</sup>, and 100<sup>th</sup> drainages. Additional measurements on the 20<sup>th</sup> and 50<sup>th</sup> drainages were made for pH and resistivity. The measurements provide insight into the characteristics of the pore solution that influence the corrosivity of these materials.

Figure 8.1 compares the change in pH with the number of drainages for each material-environment combination. For each material-environment grouping, it was found that the CC has the highest pH, followed by CFM and then RAP. The change of the pH with the number of drainages differs depending on the environment. The NCL solution (distilled water) tended to decrease the pH of each of the extracted pore solutions as the number of drainages increased. Between the 1<sup>st</sup> and 100<sup>th</sup> drainage, the pH of CC dropped from approximately 11.9 to 10.9, CFM decreased from approximately 8.5 to 7.8, and the pH of the solution from the RAP stayed nearly the same. Thus, for the NCL drainages, only small to moderate changes in pH were observed.

For the CL solution drainages, Figure 8.1 shows that the pH of the CC decreased slightly from approximately 12.1 to 11.8, while the pH of CFM increased from 8 to 9.7 and RAP increased

from 7 to 9. It is unclear what caused the increases in pH for the CFM and RAP CL drainages. However, these small changes are likely insignificant.

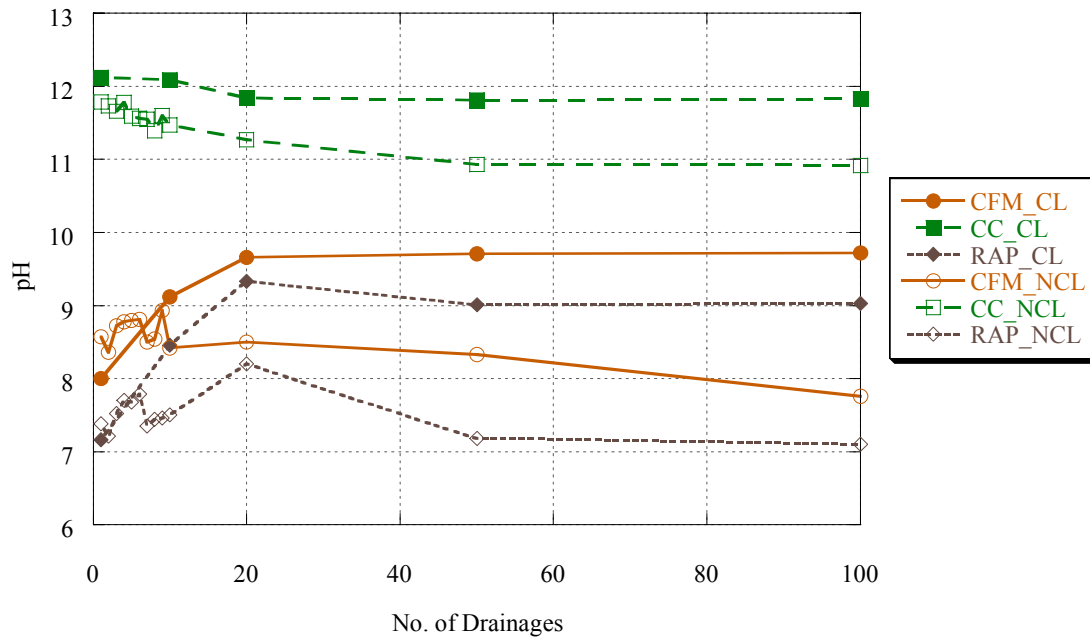


Figure 8.1 Pore solution pH versus the number of drainages through the backfill materials.

Figure 8-2 shows resistivity versus the number of NCL drainages through each backfill material. Resistivity readings were taken for the 1<sup>st</sup> through 10<sup>th</sup>, 20<sup>th</sup>, 50<sup>th</sup>, and 100<sup>th</sup> NCL drainages. CFM had the highest resistivity followed by RAP and CC. However, the CFM pore solution had the most variability in the resistivity readings. The resistivity of the first CFM drainage was approximately 4,900  $\Omega$ -cm, increased to 22,000  $\Omega$ -cm for the 10<sup>th</sup> NCL drainage and then increased further to 31,000  $\Omega$ -cm for the 50<sup>th</sup> NCL drainage. The resistivity of the CFM NCL drainages then decreased to approximately 15,000  $\Omega$ -cm for the 100th NCL drainage. The resistivity of the NCL pore solution passed through the RAP increased from 1,700  $\Omega$ -cm for the 1<sup>st</sup> drainage to 4,800  $\Omega$ -cm for the 10<sup>th</sup> NCL drainage and then remained fairly constant for the remaining readings. The pore solution resistivity readings for CC NCL drainages displayed less variability than the CFM and RAP readings and stabilized at approximately 1,200  $\Omega$ -cm. The resistivity of the distilled water applied to the backfills was 5,400  $\Omega$ -cm. The resistivity values for the CFM and RAP exceed the minimum requirement of 3000  $\Omega$ -cm; the CC does not.

The resistivity values of the pore solution for drainages using CL solution are shown in Figure 8-3. Resistivity readings were taken for the 1<sup>st</sup>, 10<sup>th</sup>, 20<sup>th</sup>, 50<sup>th</sup>, and 100<sup>th</sup> drainages. The resistivity of the solution from the first CL drainage differs for each backfill material. CC has the highest resistivity at approximately 360  $\Omega$ -cm, followed by CFM at 280  $\Omega$ -cm and RAP at 210  $\Omega$ -cm. After 100 drainages, the resistivity had stabilized at approximately 190  $\Omega$ -cm for all three backfill materials.

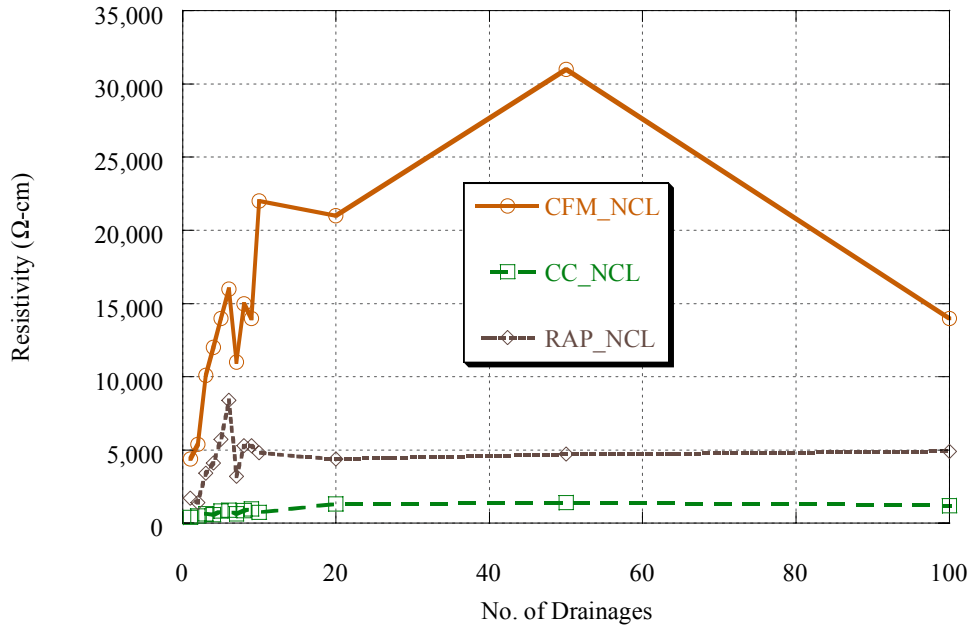


Figure 8.2 Pore solution resistivity for NCL drainages versus the number of drainages through the backfill materials.

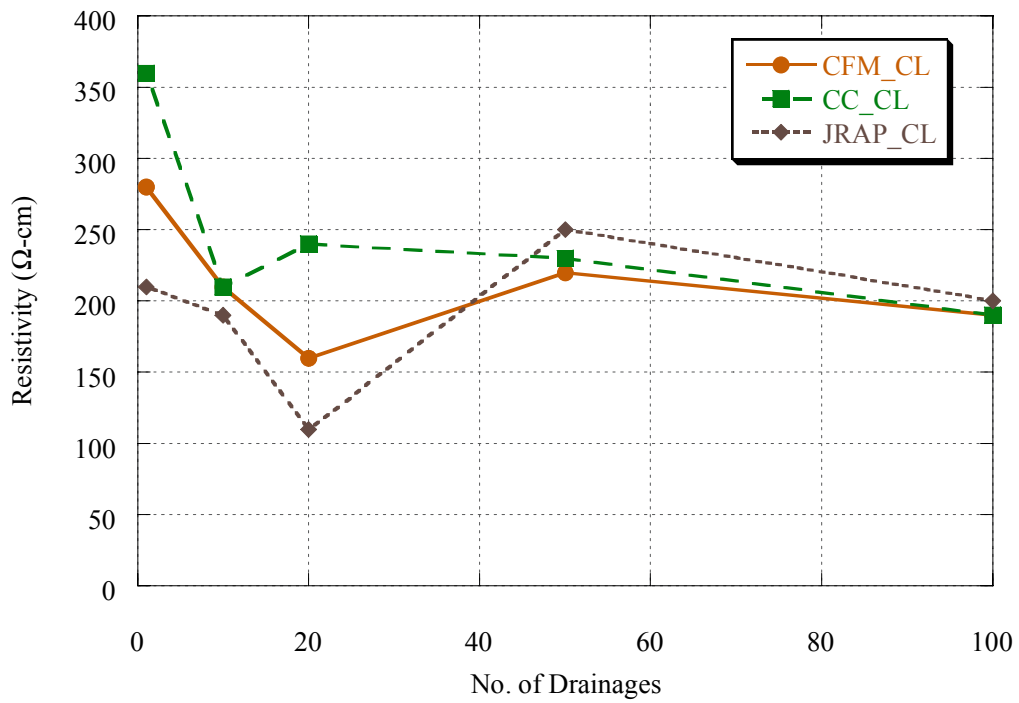


Figure 8.3 Pore solution resistivity for CL drainages versus the number of drainages through the backfill materials.

The pore solution chloride ion concentration of the backfill materials was evaluated after 1, 10, and 100 drainages were passed through each of the different backfill materials. Figure 8.4 shows the pore solution chloride concentration for the CL drainages. As expected, each of the backfill materials' pore solution significantly increased in chloride concentration from the 1<sup>st</sup> to 10<sup>th</sup> drainage, followed by a slight increase from the 10<sup>th</sup> to 100<sup>th</sup> drainage, approaching the chloride concentration of the applied 3 percent CL solution.

Figure 8.5 shows the pore solution chloride ion concentration of the NCL drainages from the backfill materials. The pore solution chloride concentration decreased rapidly for all backfill types, followed by a slight decrease. These results indicate that the chloride ions can be washed from the backfill materials. Although this can be advantageous, this should not be construed as allowing the use of chloride ion contaminated materials for backfill applications. If metallic materials are buried in chloride ion contaminated materials, the chloride ions can react with the metallic materials. If localized pitting occurs, the chloride ions may be difficult to remove, continuing the corrosion process. Although the work has shown that chloride ions can be removed from the backfill materials, the work has not shown that they can be removed from the steel interface where localized corrosion reactions occur, and these ions should be limited.

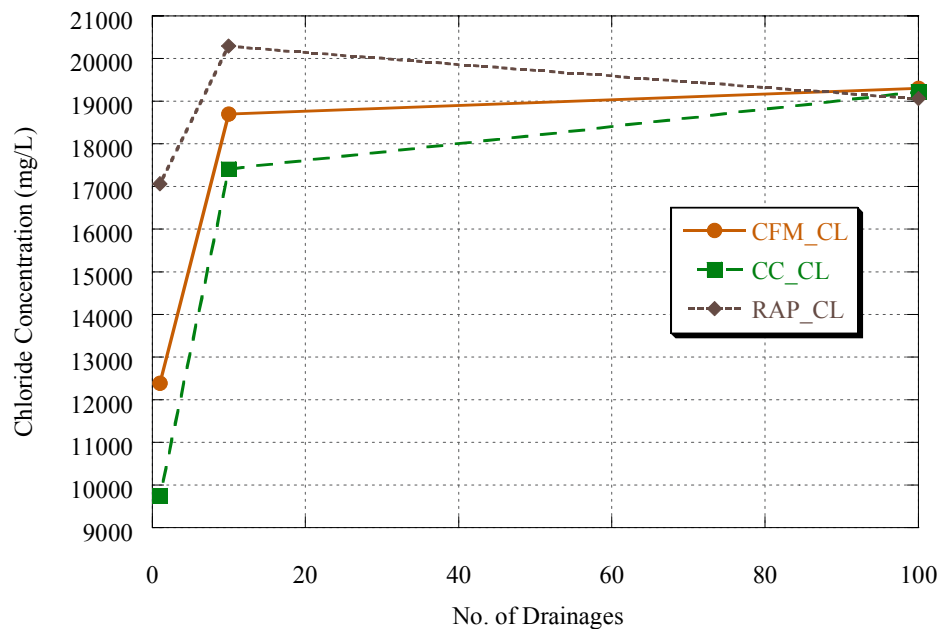
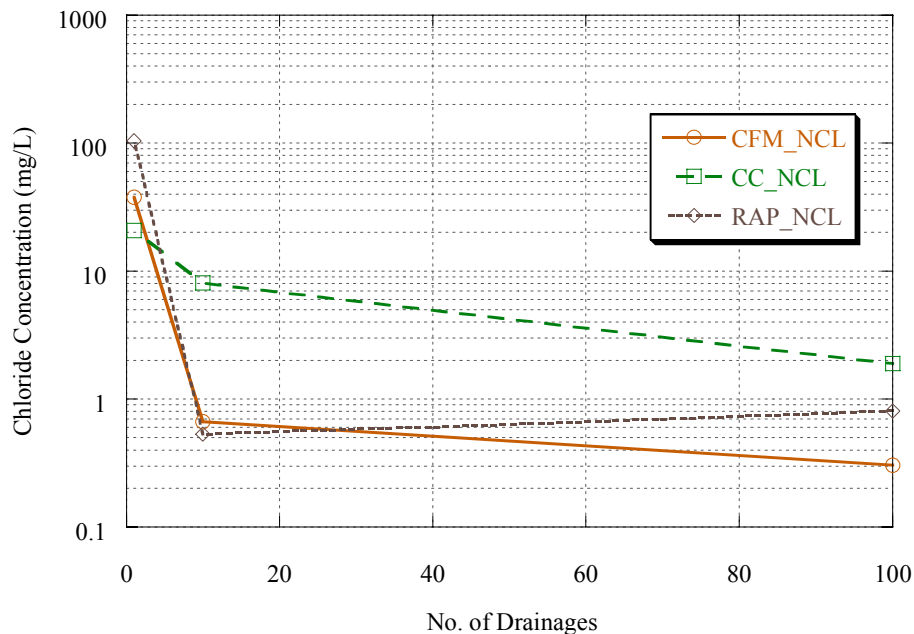


Figure 8.4 Pore solution chloride concentration for CL drainages versus the number of drainages through the backfill materials.



*Figure 8.5 Pore solution chloride concentration for NCL drainages versus the number of drainages through the backfill materials.*

The pore solution sulfate concentrations of the CL drainages from the backfill materials are shown in Figure 8.6. The pore solution sulfate concentration for the backfill materials was highest for CC, followed by RAP and then CFM. For all cases when the chloride solution was drained through the materials, the sulfate concentration stayed relatively constant. This indicates that the sulfate ions are less likely to be washed from the backfill materials.

Figure 8.7 shows the pore solution sulfate concentration of the NCL drainages from the backfill materials. The pore solution sulfate concentration of the backfill materials for the first NCL drainage was approximately 150 mg/L for RAP, 50 mg/L for CFM, and 25 mg/L for CC. Unlike the CL drainages, the pore solution sulfate concentration quickly decreased for each of the backfill materials. This indicates that drainages in the field may easily wash away sulfates, assuming sulfates or chlorides are not in the source solution. However, as with chloride ions, care should be taken to minimize sulfate concentrations of backfill materials.

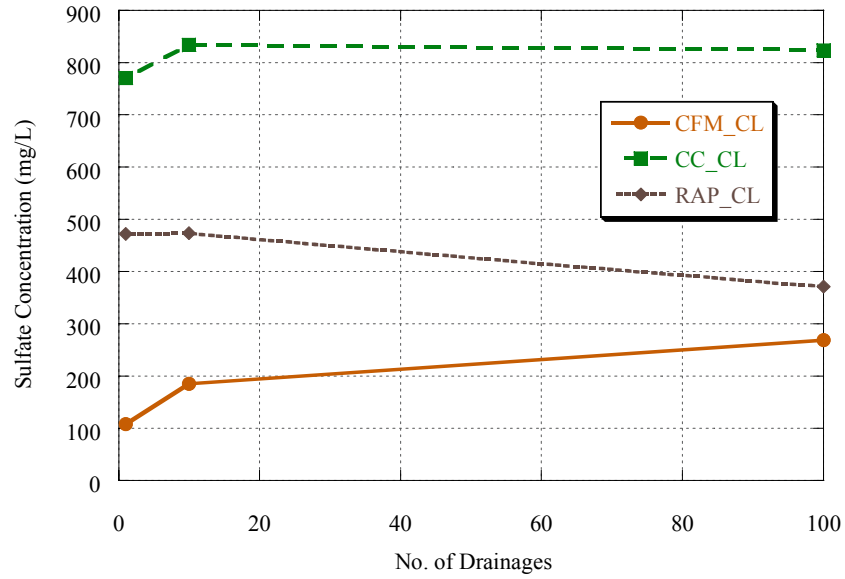


Figure 8.6 Pore solution sulfate concentration for CL drainages versus the number of drainages through the backfill materials.

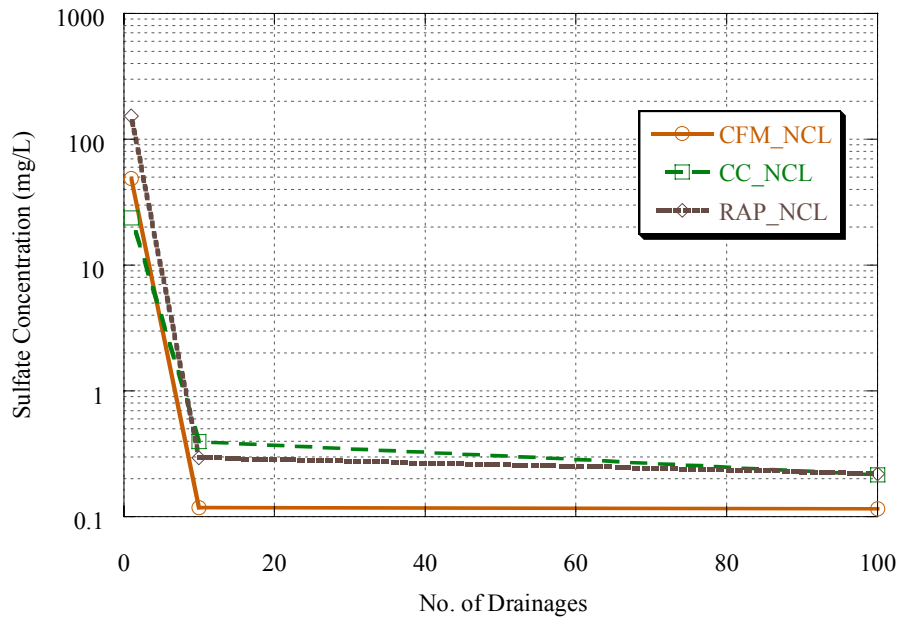


Figure 8.7 Pore solution sulfate concentration for NCL drainages versus the number of drainages through the backfill materials.

### 8.2.2 Mass Loss and Corrosion Rates

Metallic samples were weighed before and after exposure to the different solutions (drainages) collected from the backfill materials. The difference in weight is referred to as the mass loss. The mass loss was determined for each STT sample following ASTM G1. The mass loss was used to determine the average corrosion rates ( $r$ ) using the following equation:

$$r = \frac{m}{tA} \quad (8.1)$$

where  $m$  is the mass loss,  $t$  is the time of exposure, and  $A$  is the exposed area of the sample. Figure 8.8 shows the average corrosion rates determined from the mass loss results for all STT CL groups. In general, the average corrosion rates for the galvanized samples decreased with an increasing number of drainages. The zinc galvanization is typically susceptible to corrosion when the chloride ion concentration exceeds 50 mg/L. All values were higher than this threshold value. The decrease in corrosion activity could be a result of the very high chloride ion concentration. It has been reported that when high concentrations of chloride ions are present, the solubility of oxygen decreases. As the solubility of oxygen decreases, less oxygen is available for the cathodic corrosion reactions, thus limiting the corrosion rate. Higher corrosion rates could have depleted the oxygen available for the reactions, especially with the high uniform corrosion observed on these samples. It appears that the very high chloride ion concentrations and the high early uniform corrosion activity limited the overall average corrosion rate of the galvanized samples exposed to solutions from the 100<sup>th</sup> CL drainage.

The steel samples exposed to the solutions from the CL drainages showed different trends than the galvanized samples exposed to the same solution. The average corrosion rates for the plain-steel MSE strip reinforcement increased when exposed to 100<sup>th</sup> drainage solution. This increase is likely because of the lower initial corrosion activity where the oxygen was not depleted. In general, very high corrosion rates were observed for all samples exposed to solutions containing chloride ions. This work shows that although the initial physiochemical parameters of the backfill materials can influence the corrosion activity of the MSE reinforcement, exposure conditions can significantly alter the corrosivity of the backfill materials.

Figure 8.9 shows the corrosion rate results from the STT for all NCL groups. The boxplots show slight decreases in the corrosion rates. However, there are no significant differences between backfill materials within any of the groups. For the NCL samples, the testing period for the STT appears to be too short. More time is likely required to allow for more corrosion and the possibility of greater differences between the results.

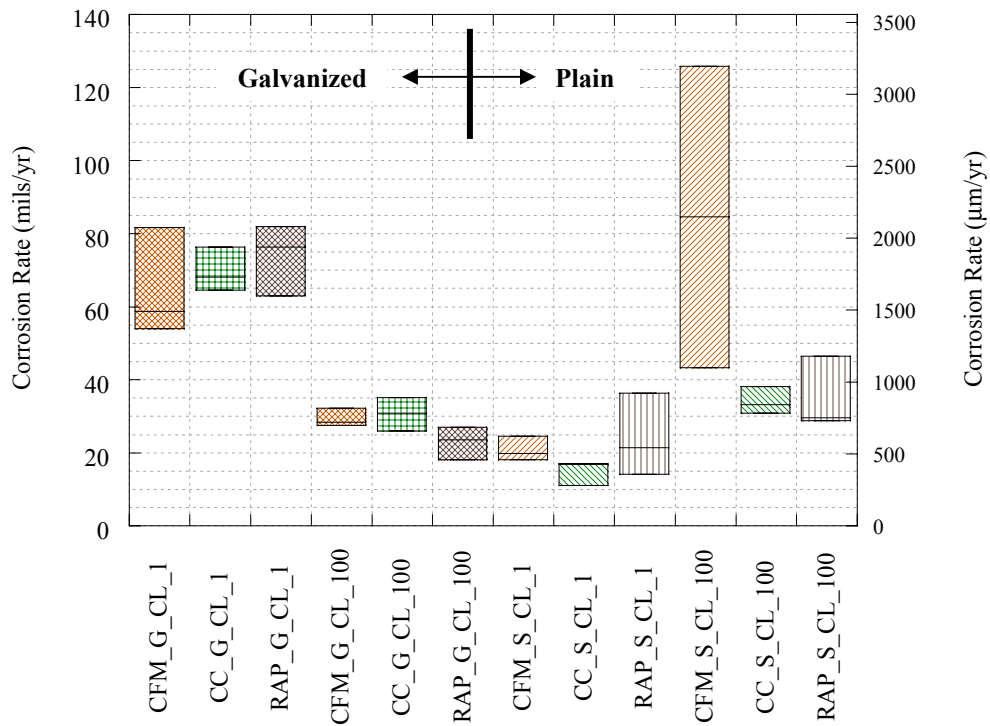


Figure 8.8 Boxplots of corrosion rates calculated from mass loss data for all STT CL groups.

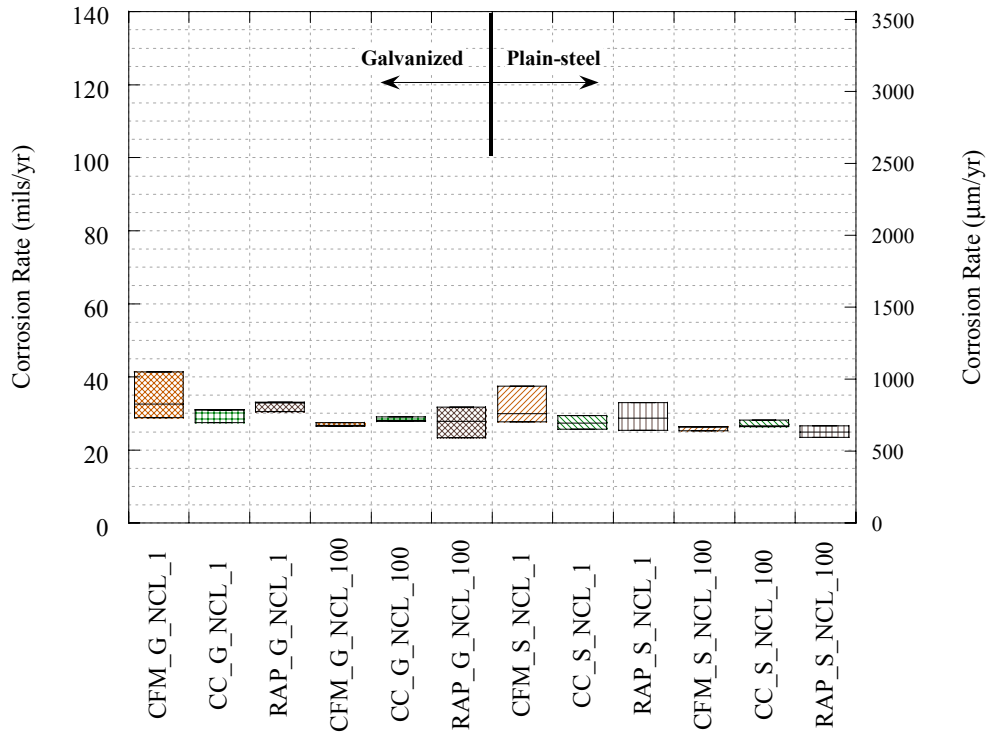


Figure 8.9 Boxplots of corrosion rates calculated from mass loss data for all STT NCL groups.

The corrosion rates for all STT G groups are shown in Figure 8.10. The only significant difference between G\_CL and G\_NCL groups is between the G\_CL\_1 and all other groups. Although this comparison is with the G\_CL\_100 group, the possible reason for the lower corrosion rates of the G\_CL\_100 group was explained previously. There is no significant difference between G\_CL\_100 and G\_NCL\_100. The lack in differences of corrosion rates for the plain steel samples indicate that the STT period was likely too short to provide reliable comparative corrosion performance data.

Figure 8-11 illustrates the corrosion rate results for all STT plain-steel groups. Interestingly, samples exposed to the solution from the first chloride drainage exhibited lower corrosion activity than those exposed to the solution from the last drainage, even though chloride ion concentrations were very high (See Figure 8.4). The lower corrosion rates were unexpected and can not be explained at this time.

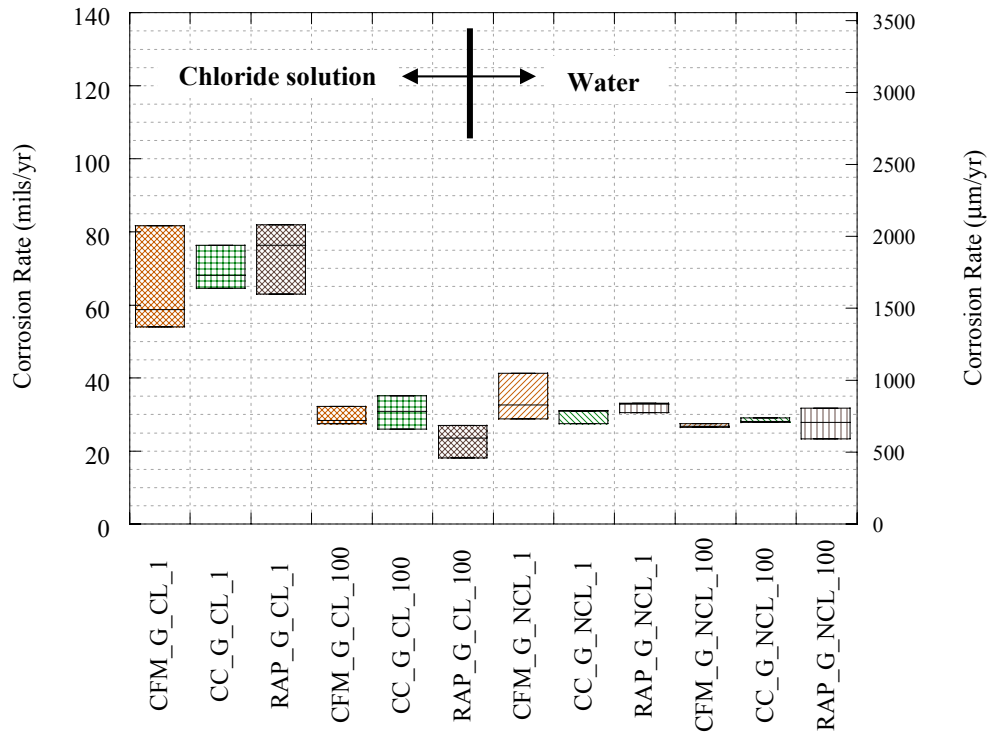


Figure 8.10 Boxplots of corrosion rates calculated from mass loss data for all STT G groups.

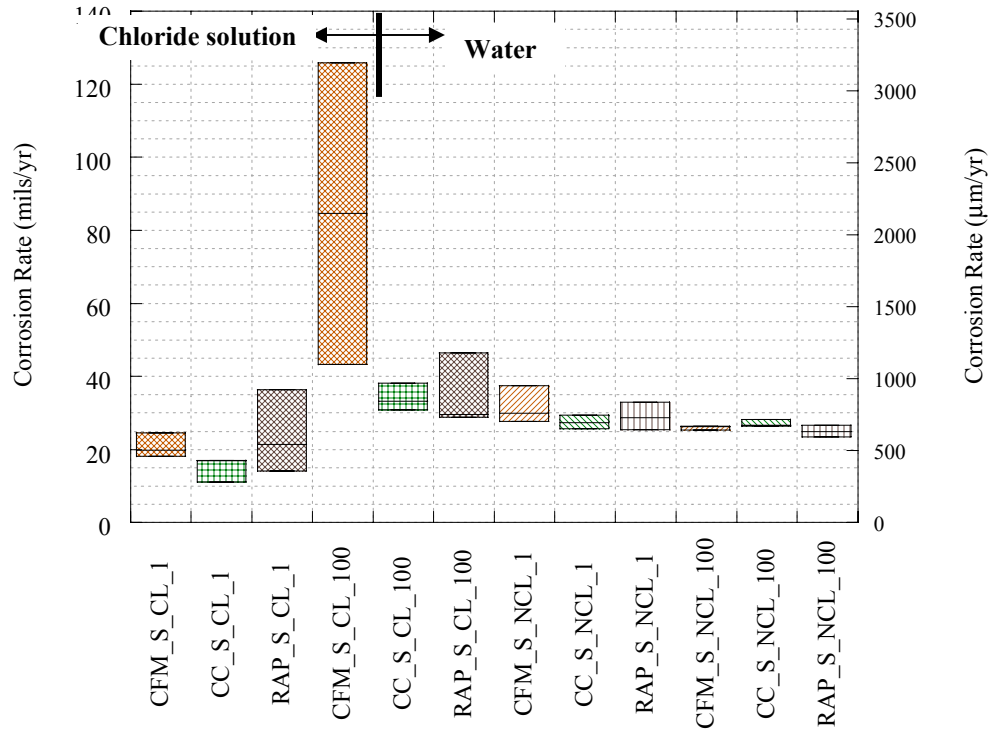


Figure 8.11 Boxplots of corrosion rates calculated from mass loss data for all STT S groups.

### 8.2.3 Electrochemical Test Results

Electrochemical testing was performed on all STT samples. Non-destructive  $R_p$  testing was performed on these samples on a periodic basis. Destructive, cyclic polarization testing was performed on these samples at the end of the STT.

Data collected from  $R_p$  and cyclic polarization testing were used to estimate corrosion rates. These tests were performed on all the STT samples.  $R_p$  testing consisted of measuring the current versus applied voltage across a specified potential range in relation to the OCP to determine the  $R_p$ . The inverse  $R_p$  value is directly related to the corrosion rate as follows:

$$r = \frac{B}{R_p} \quad (8.2)$$

Here,  $B$  is the Stern-Geary coefficient. Because this coefficient has not been evaluated for metallic materials embedded in backfill materials, especially the recycled backfill materials, the researchers performed cyclic polarization testing to estimate these coefficients for the different MSE reinforcement types and exposure conditions. Figures 8-12 and 8-13 show the ranges of Stern-Geary coefficients for the different reinforcement types. In general, these values are typical of values reported in the literature for other systems.

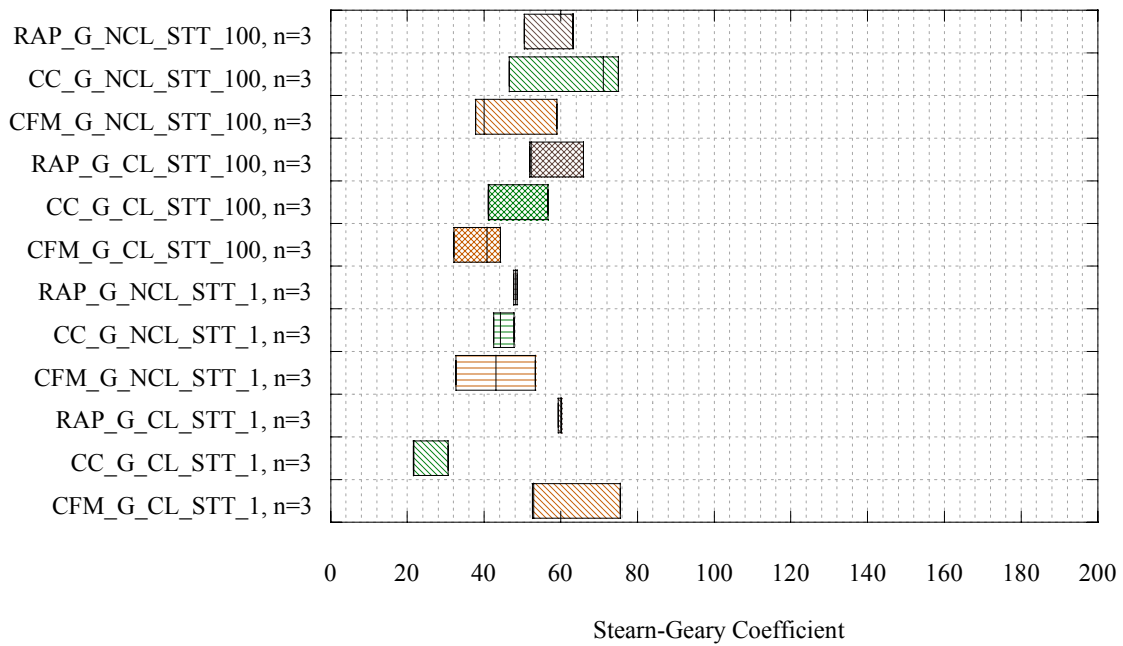


Figure 8.12 Box-plot of Stern-Geary coefficients derived from cyclic polarization testing plots for all the STT G samples.

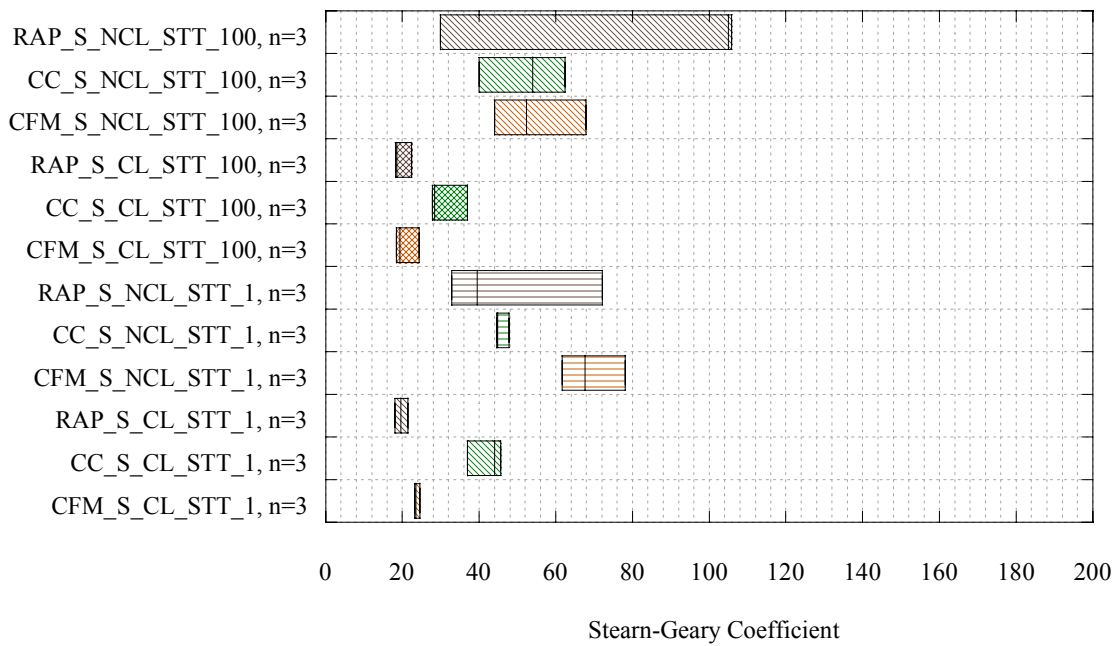


Figure 8.13 Box-plot of Stern-Geary coefficients derived from cyclic polarization testing plots for all the STT S Samples.

Figure 8.14 shows a typical comparison of actual corrosion rates determined from mass loss testing and average corrosion rates obtained from the  $R_p$  testing program for the STT. All comparisons showed little to no correlation. For the complete comparison of all conditions, the reader is directed to Esfeller (2006). It is clear that the  $R_p$  results show little or no correlation with the actual corrosion rates determined from mass loss testing. This indicates that the electrochemical testing used in the STT program is not appropriate to measure the corrosivity of backfill materials.

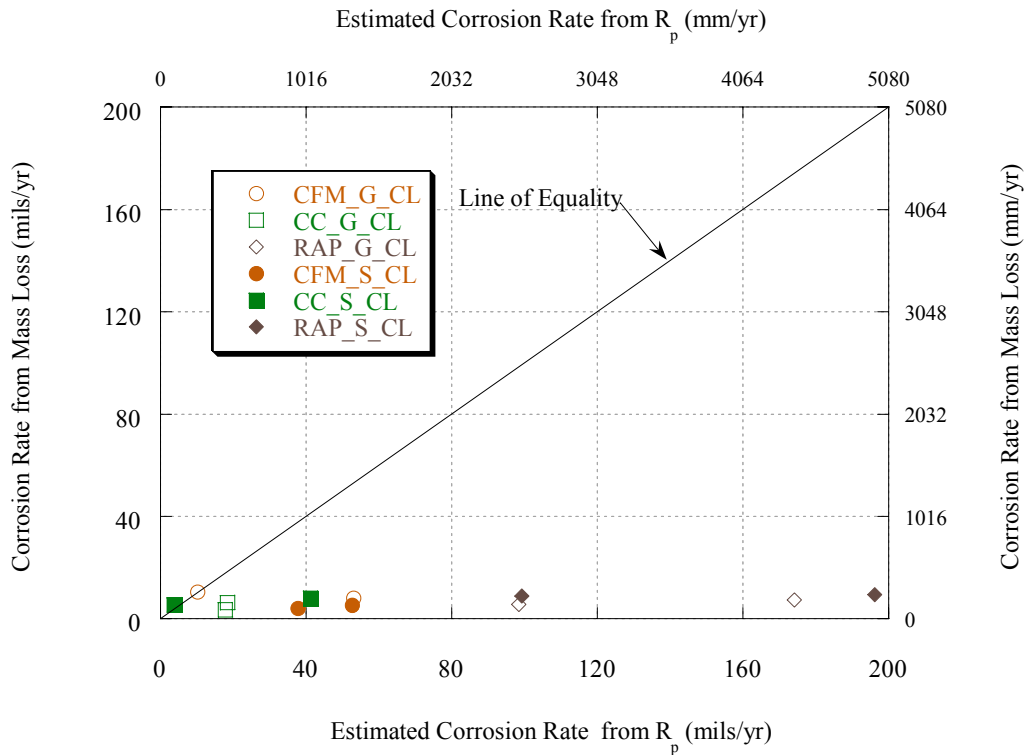


Figure 8.14 Corrosion rates calculated from mass loss (ordinate) versus the  $R_p$  corrosion rates for the CL LTT samples.

### 8.2.4 Summary

The number of drainages through the backfill materials influences the solution characteristics. This indicates that the exposure conditions in the field could change depending on the local environment, changing the corrosion rate of the MSE strip reinforcement. This research showed that there is little difference in corrosion rates when water was drained through the different backfill materials. However, exposure to chloride containing solutions did increase the corrosion rates in most cases. Results indicate that the STT duration was not sufficiently long to adequately distinguish differences in corrosion rates between different backfill materials. The cyclic polarization testing resulted in reasonable Stern-Geary coefficients for use in determining corrosion activity of metallic materials embedded in recycled backfill materials.

### 8.3 Long-term Testing Results

The LTT results consisted of measurements made on the backfill material, metal, or material-metal environment. General backfill material characteristics were described earlier. The results shown here include measurements on the backfill materials after exposure to the particular environment, which may influence the characteristics of the backfill. Results from the corrosion tests are also presented.

#### 8.3.1 Potential Readings

Potential readings were measured versus Cu-Cu<sub>2</sub>SO<sub>4</sub> (Copper-Copper Sulfate). Two plot types were used to examine the potential readings: distribution of potential and potential versus time. The first plot type shows the distribution of the potential readings (percent of potential readings versus potential). These plots were made for each LTT sample type and grouped by each material-metal-environment combination group. The average distributions for each group were plotted for comparison. The average distributions for the LTT galvanized-steel samples shown in Figure 8-15 indicate that the RAP exhibits the most negative potential values and CC exhibits the most positive potentials. In general, more negative potentials indicate higher likelihood of corrosion activity.

The average distributions for the LTT steel samples shown in Figure 8.16 indicate that the average potential values are the most negative for the CFM and most positive for the CC in chloride environments. The RAP exhibits the most negative potential value for the non-chloride environment, while CC exhibits the most positive potential in this environment.

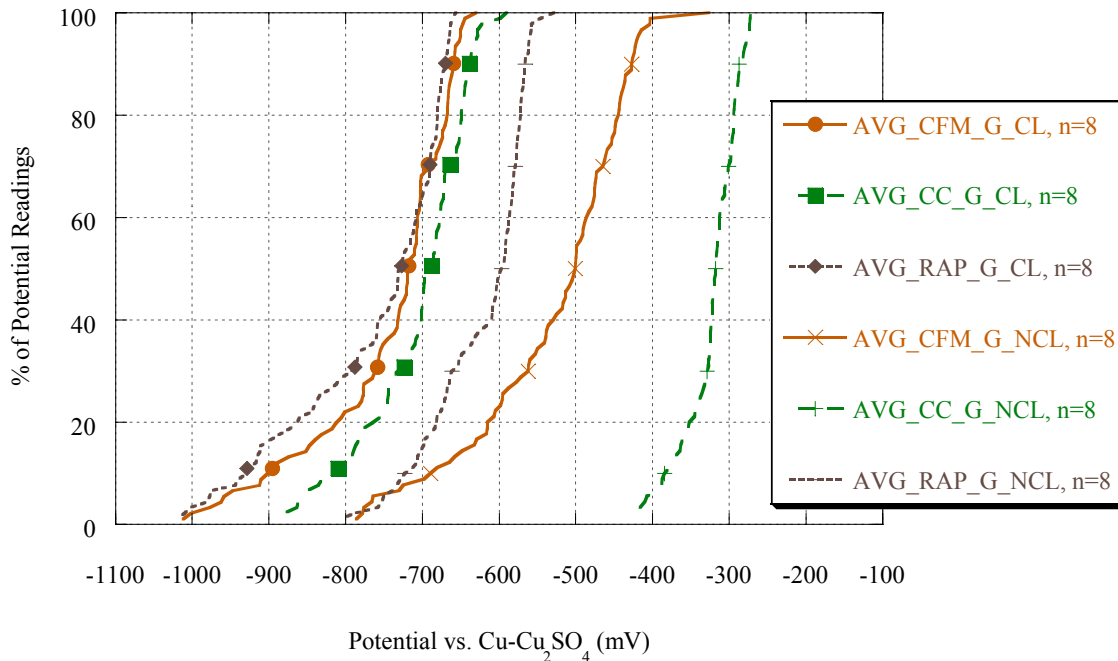


Figure 8.15 Distribution Plot of Average Cu-Cu<sub>2</sub>SO<sub>4</sub> Potential Readings for LTT G Samples.

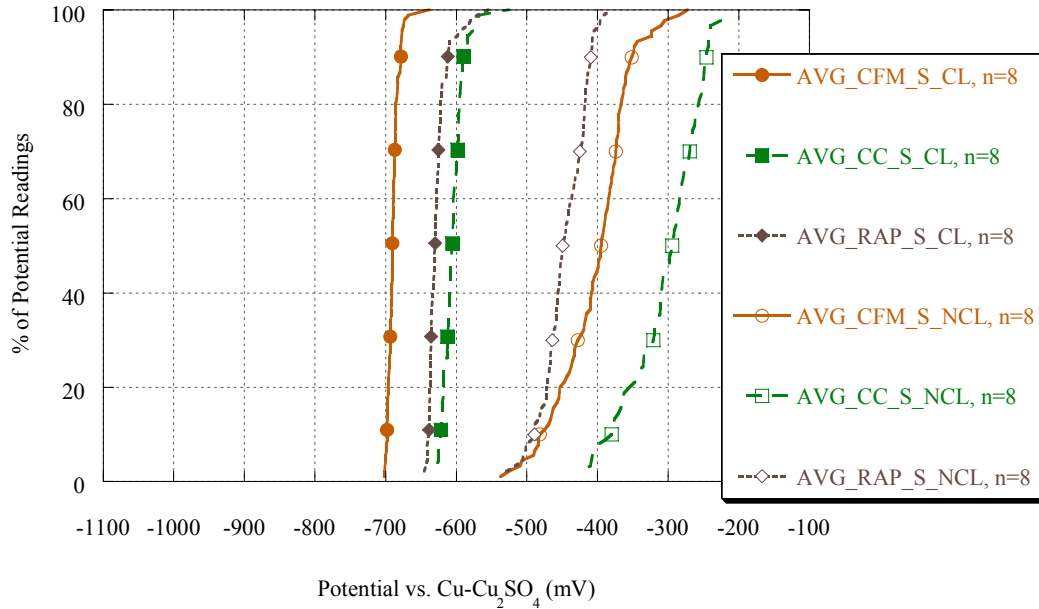


Figure 8.16 Distribution plot of average potential readings for LTT S samples.

Using the ranges proposed by Applegate (1960) for probable corrosiveness of steel, CC\_S\_NCL is mild to very mild, RAP\_S\_NCL and CFM\_S\_NCL are moderate to mild, and all CL groups have severe probable corrosiveness based on their potential readings. These findings contradict the fact that high pH values are detrimental to corrosivity of soils and backfill materials.

The potential versus time from first solution application plots display how the potential readings change with time. All the potential versus time plots started at 14 or 15 days (which was when the first potential reading measurements were made following the first solution application to the samples) and ended at 336 or 337 days. Frequent variations are observed in the plots because before-solution-application and after-solution-application potential readings were measured. The average potential versus time plots for the LTT galvanized-steel samples are shown in Figure 8.17.

The potential versus time plots for all galvanized material-environment combinations shown in Figure 8.17 exhibit similar behavior, with the data becoming more positive over time. However, in general, as a sample converts from passive to active corrosion, the potential typically becomes more negative. It is likely that the samples transferred from a passive to active state within the first 14 days (i.e., the potential became more negative during the first 14 days of testing). At 336 days, the G\_CL samples had the same average potential reading of approximately -675 mV for each backfill. All G\_CL samples tended to have the same degree of variation between the before and after solution application measurements.

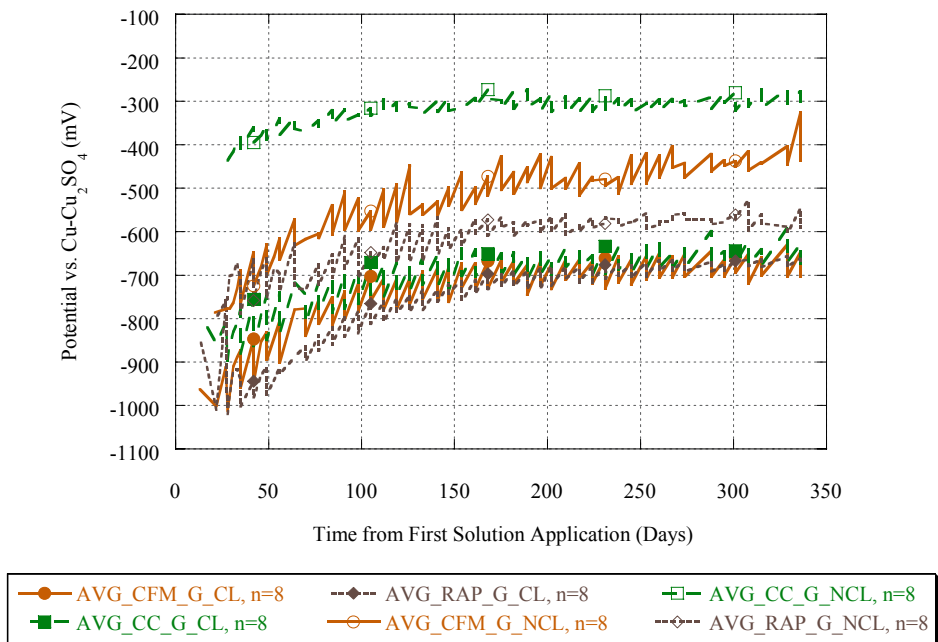


Figure 8.17 Average potential readings versus time plot for LTT G samples.

The average potential versus time S<sub>CL</sub> plots in Figure 8.18 show the potential values becoming more negative during the first 20 days of readings. The S<sub>CL</sub> potential readings were fairly constant for the entire test period for CFM and RAP. The CC<sub>S<sub>CL</sub></sub> readings showed a linear, slightly decreasing trend. At the end of the test period, the S<sub>CL</sub> readings for CC and RAP were about the same, while the CFM<sub>S<sub>CL</sub></sub> readings were about 60 mV more negative. The potential versus time plots for the S<sub>CL</sub> samples displayed less variation because of differences between the before-solution-application and the after-solution-application potential readings when compared to the S<sub>NCL</sub> samples.

Several general observations can be made regarding the potential readings. The galvanized-steel samples showed more variation in the potential readings compared to steel samples. This could indicate regular transitions between passive and active corrosion. For the steel samples, the NCL potential readings showed more variation compared to the CL readings. The potential readings from the plain-steel samples exposed to chloride ions exhibited a narrow distribution compared to the other metal-environment combinations. Potential reading distributions from samples exposed to water (no added chloride ions) are more positive than the samples exposed to chlorides for all backfill-metal combinations. This indicates that all backfill materials containing moderate to high levels of chloride ions actively corrode. CC backfill had more positive potential readings than the other backfills for each metal-environment combination indicating less corrosion activity. This indicates that this backfill may be less corrosive even though it exhibits the highest pH.

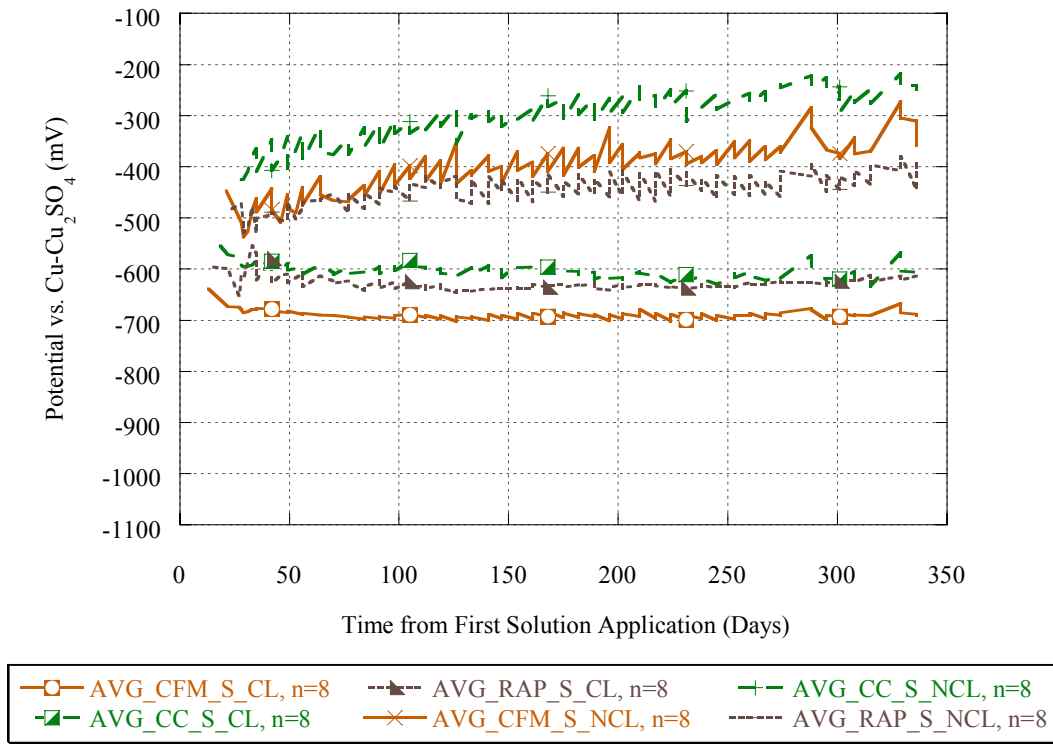


Figure 8.18 Average  $\text{Cu-Cu}_2\text{SO}_4$  potential readings versus time plot for LTT S samples.

### 8.3.2 Backfill Material Characteristics

The pore solution pH, resistivity, and soluble salts were measured for all LTT samples to confirm that the study evaluating the influence of number of drainages represented the conditions in the LTT program. The density was also evaluated to ensure that the samples exhibited similar compaction levels.

The densities of the LTT samples are shown in Figure 8.19. The results show no significant difference in sample densities between the groups except for CFM\_G\_CL. The target dry densities in  $\text{lb/ft}^3$  ( $\text{kg/m}^3$ ) for the samples are 125 (2002), 119 (1906), and 117 (1874) for CFM, CC, and RAP, respectively. Density could change the aeration of the backfill which in turn could influence the corrosion activity of the samples. All densities were similar to the maximum dry density, indicating similar conditions for all samples.

Figure 8-20 shows the boxplots of the pore solution pH values taken from the LTT samples after testing was complete. The CC has the highest pH, followed by CFM, then the RAP. The pore solution pH values obtained from the drainage study are also shown in Figure 8-20. In general,

the pH values of the pore solutions from the LTT studies were higher than the pore solution pH values obtained in the drainage study. However, in most cases the differences were minimal.

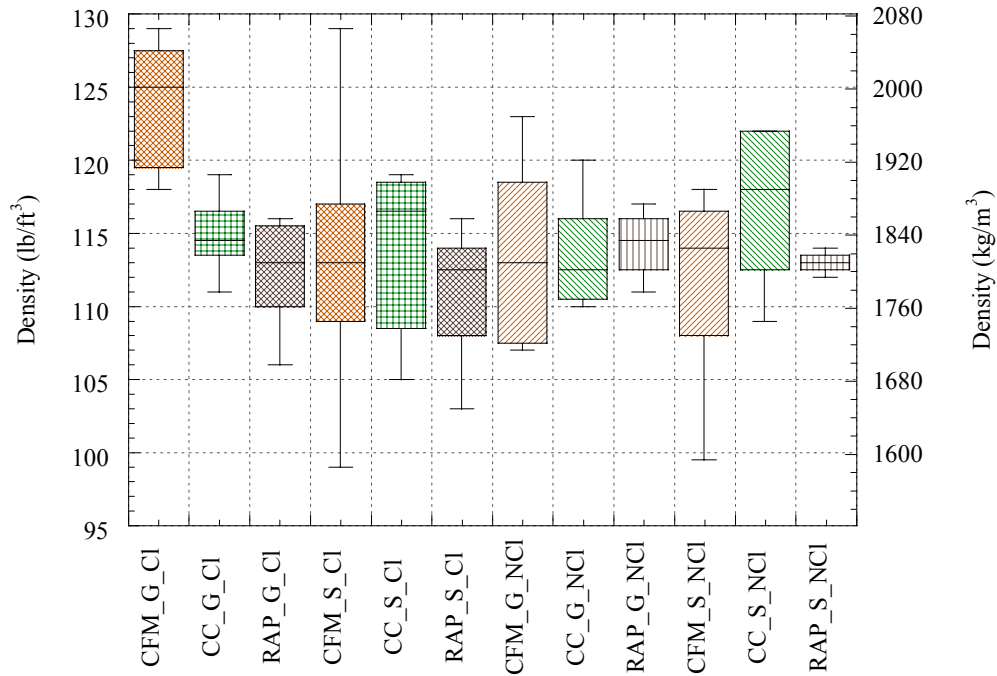


Figure 8.19 Boxplots of LTT sample densities.

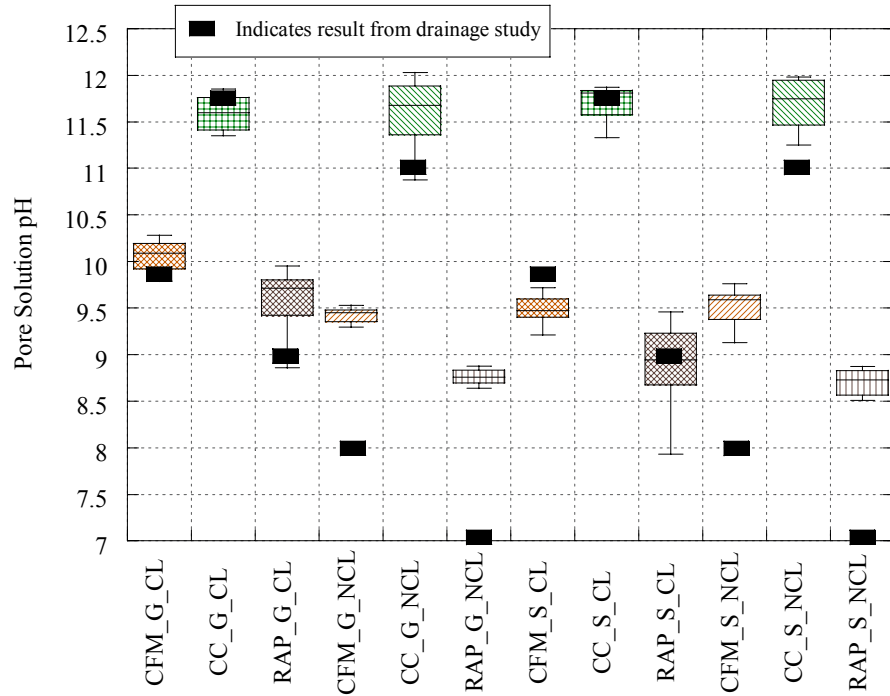


Figure 8.20 Boxplots of LTT pH values.

As already noted, resistivity can directly influence the corrosion activity. Figure 8.21 shows the resistivity values of the LTT NCL samples. This figure also shows the resistivity values obtained from the drainage studies. With the exception of the NCL RAP samples, the results show good correlation between the drainage study results and the LTT results.

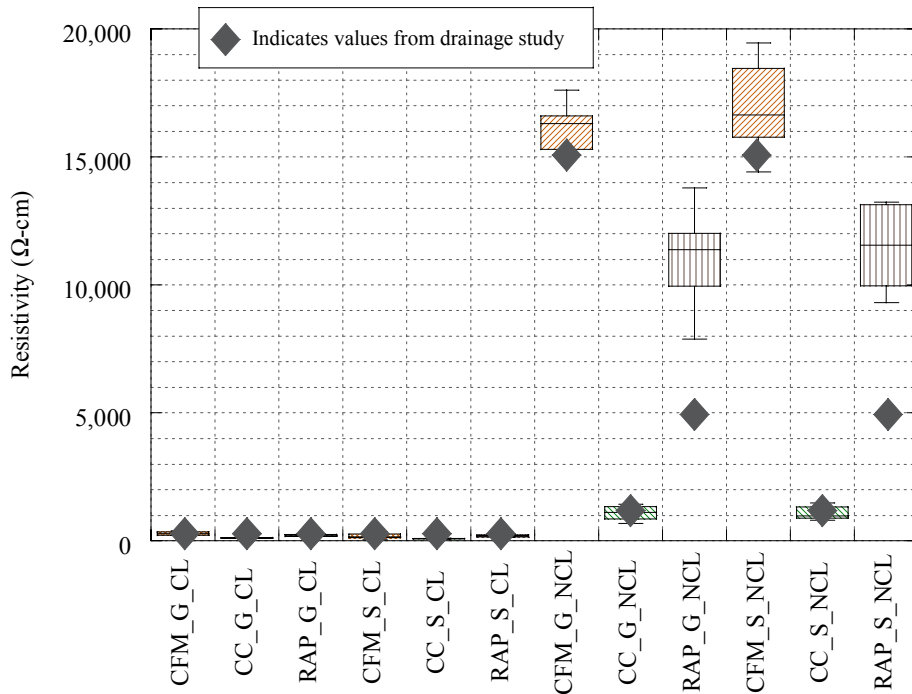


Figure 8.21 Boxplots of resistivity values from the LTT Samples.

The LTT samples were evaluated for chloride and sulfate concentrations after the corrosion testing was complete. The concentration of chloride for the NCL samples was mostly below 30 mg/L as shown in Figure 8.22. The chloride concentration for the CL samples ranged between 750 and 4,000 mg/L. The CC samples have significantly higher chloride concentrations than the CFM and RAP. There is no significant difference between CFM and RAP chloride concentrations. Correlations with the values obtained from the drainage study indicate that when chloride solutions are passed through the samples, the results from the drainage study significantly overestimate the amount of chloride ions in the LTT samples. For the non-chloride solutions (NCL), relatively good correlations were observed. It should be noted that the CC samples retained more chlorides than the RAP and CFM. This indicates that the CC samples may absorb chloride ions more readily than the CFM and RAP samples.

The sulfate concentrations of the LTT samples are shown in Figure 8.23. CC exhibits a significantly higher sulfate concentration than CFM and RAP in both the CL and NCL solution environments. The sulfate concentrations of CFM and RAP were lower than 50 mg/L, whereas the sulfate concentration of CC samples ranged between 50 to 500 mg/L. There is more variability in the sulfate concentrations of CC than the CFM and RAP. It is likely that the CC backfill materials have higher sulfate concentrations because of past exposure or possible from the gypsum present in cement. However, it is clear that the chloride solution increased the sulfate concentration for all backfill types. Although no sulfate was intentionally added to the chloride solution, residual sulfates may have been present.

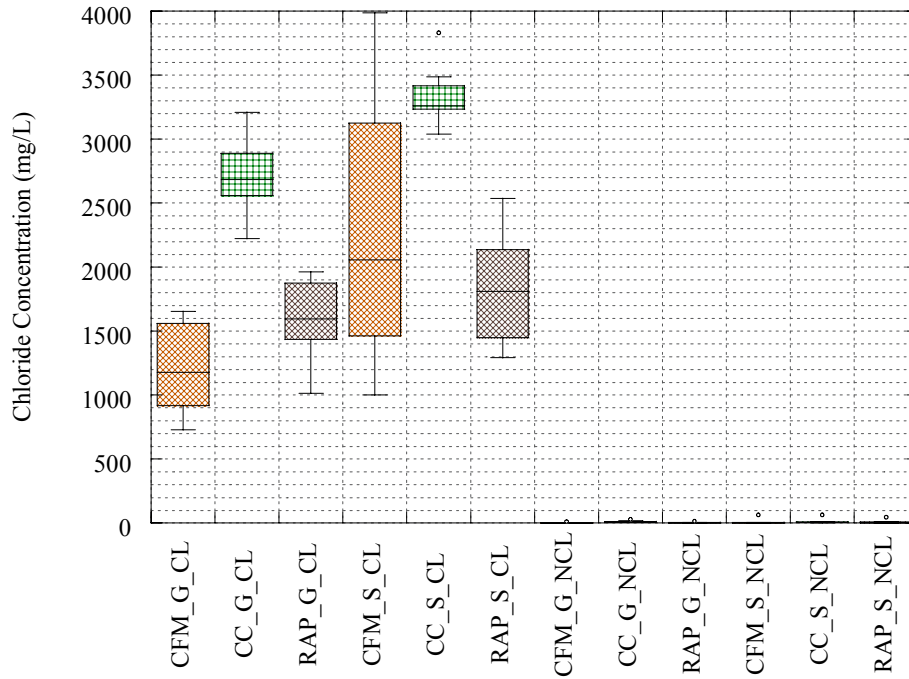


Figure 8.22 Boxplots of chloride concentration for each LTT group.

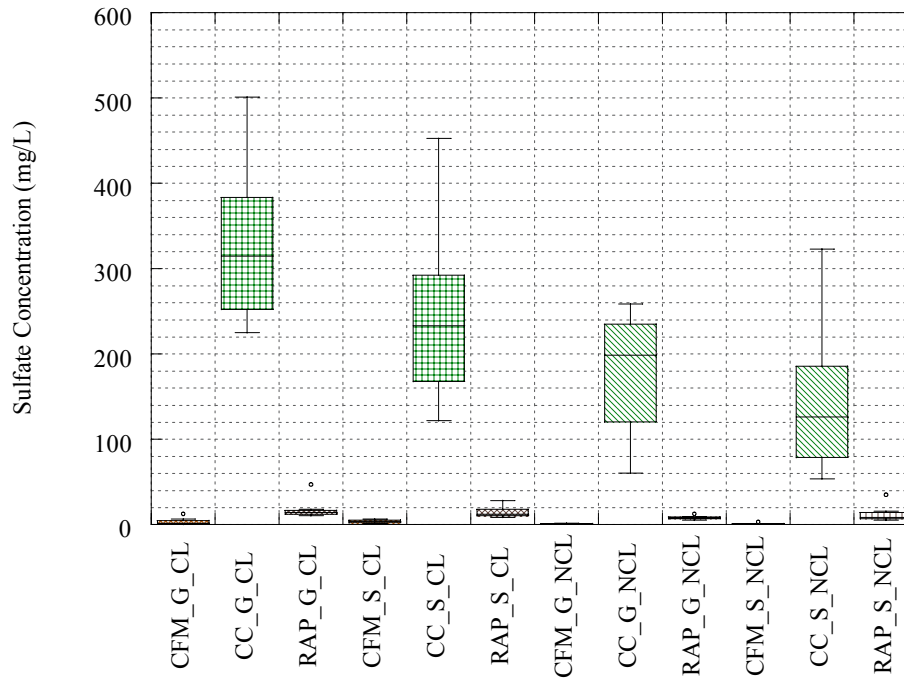


Figure 8.23 Boxplots of sulfate concentrations for each LTT group.

### 8.3.3 Mass Loss and Corrosion Rates

The mass loss of the LTT samples was the most significant measurement made toward assessing the corrosivity of the backfill materials. The mass loss measurements were used to calculate the corrosion rates for each sample group. The LTT samples were exposed to weekly applications of solution (water or chloride solution) for a period of approximately one year. Figure 8.24 shows that there is a significant difference in corrosion rates between a CL and NCL environment. There was no significant difference in the corrosion rates between galvanized-steel and plain-steel reinforcement except for RAP in the NCL environment. The average corrosion rate for galvanized reinforcement in CFM and RAP was lower than plain-steel reinforcement in CFM and RAP.

The average corrosion rate for all NCL sample groups was below 1.5 mpy (38  $\mu\text{m}/\text{yr}$ ). The average corrosion rate for samples exposed to the chloride solution exceeded 6 mpy (152  $\mu\text{m}/\text{yr}$ ). In general, the average corrosion rate was lowest for CC. There was more variability in the galvanized-steel mass loss measurements compared to the plain-steel samples. During the mass loss testing, it was observed that the epoxy coating was more likely to flake off the galvanized-steel samples. This could be due to underfilm corrosion. This was likely the largest contributing factor in increasing the variability. Another factor that could have caused the increase in variability is that the galvanized samples were only cleaned with an ammonium hydroxide based acid (i.e., to determine mass loss), while the steel samples were cleaned with a much stronger hydrochloric based acid according to ASTM G1 specification. Some of the galvanization on the galvanized-steel samples was completely consumed at the end of the test period, indicating that the galvanized coating likely only extends the service life of the MSE reinforcement for a short period.

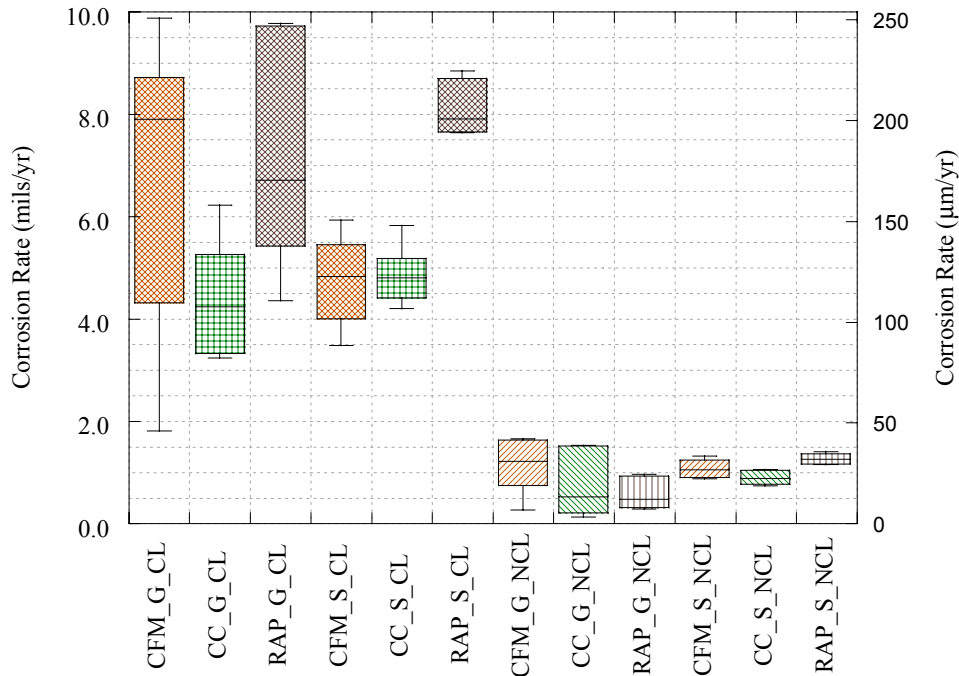


Figure 8.24 Boxplot of corrosion rates calculated from mass loss data for all LTT samples.

### 8.3.4 LTT Electrochemical Test Results

Electrochemical testing was performed on 24 of the 96 LTT samples. Non-destructive  $R_p$  testing was performed on these samples on a weekly basis. Destructive, cyclic polarization testing was performed on these samples at the end of the LTT period. The remaining samples were used for mass loss testing.

Similar to the STT samples,  $R_p$  testing was performed for the LTT samples. However, this testing was only performed on 24 of the LTT samples, whereas it was performed on all the STT samples. The incremental corrosion currents for the LTT were summed and averaged over the 337-day testing period.

Figure 8.25 shows a scatter plot of actual measured corrosion rate from mass loss testing versus the estimated average corrosion rate from the  $R_p$  testing for all LTT CL test samples that were equipped with polarization resistance apparatus. The figure shows that the corrosion rates from the  $R_p$  testing overestimated the actual corrosion rate determined from mass loss testing for all samples except one galvanized sample embedded in CFM and exposed to chlorides and one steel sample embedded in CC and exposed to chlorides. The cause of the large discrepancy between the actual corrosion rate and estimated corrosion rates for the LTT CL samples is unknown.

The corrosion rates determined from mass loss testing versus the estimated average corrosion rates determined from  $R_p$  testing for all LTT NCL samples are shown in Figure 8.26. This plot shows that approximately half of the corrosion rates determined from  $R_p$  testing approximated

the corrosion rates from mass loss testing, while the other half were significantly overestimated. The largest overestimates were for plain-steel samples embedded in CFM and exposed to water (NCL solution).

Other researchers have found an approximate 20 percent difference between measured mass loss and mass loss calculated by the  $R_p$  method when corrosion testing in soils was performed in identical conditions (Serra and Mannheimer 1979). Samples exposed to chloride solutions can exhibit very high corrosion activity over short durations.

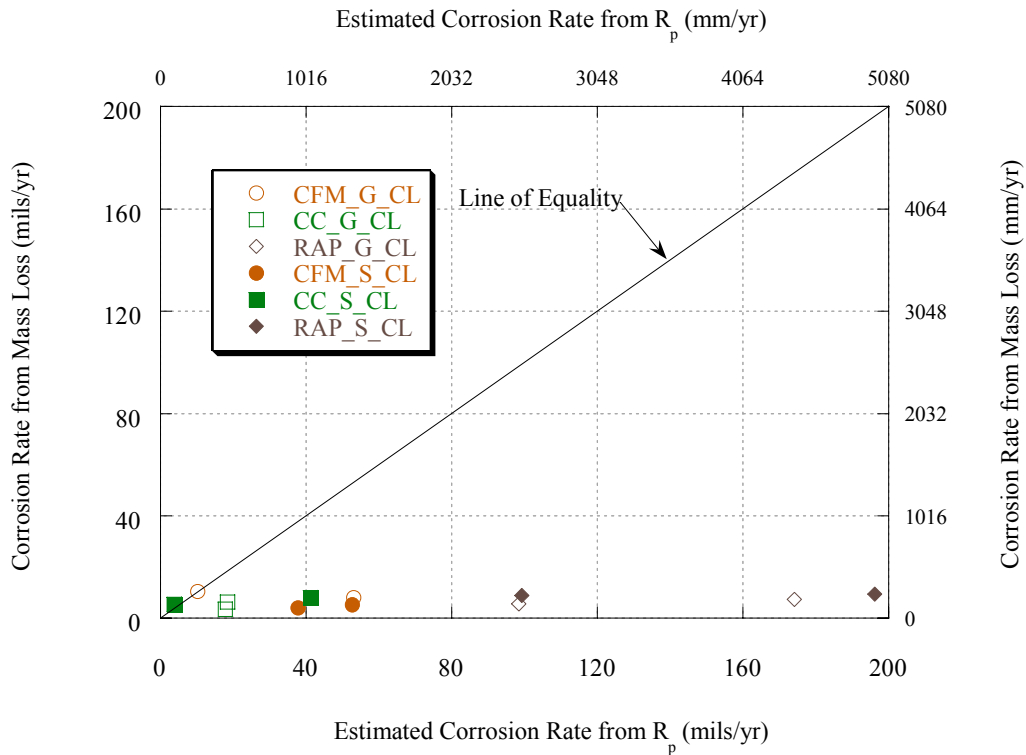


Figure 8.25 Corrosion rates calculated from mass loss versus the estimated corrosion rate calculated from  $R_p$  measurements for the LTT samples exposed to chloride solution.

The Stern-Geary coefficients do not remain constant over the length of the testing period. The electrochemical testing required to determine the Stern-Geary coefficients has the potential to alter the corrosion process, which could jeopardize the reliability of the experiment if testing were performed at the beginning of the experiment. As such, the Stern-Geary coefficients were only determined at the end of the experiment. The coefficients that were estimated were assumed to be accurate for the entire duration of the LTT in order to estimate mass loss. Although the applied assumption likely introduces some error, the mass loss values could not have been estimated to any reasonable degree of accuracy without the application of a fair approximation for the Stern-Geary coefficients.

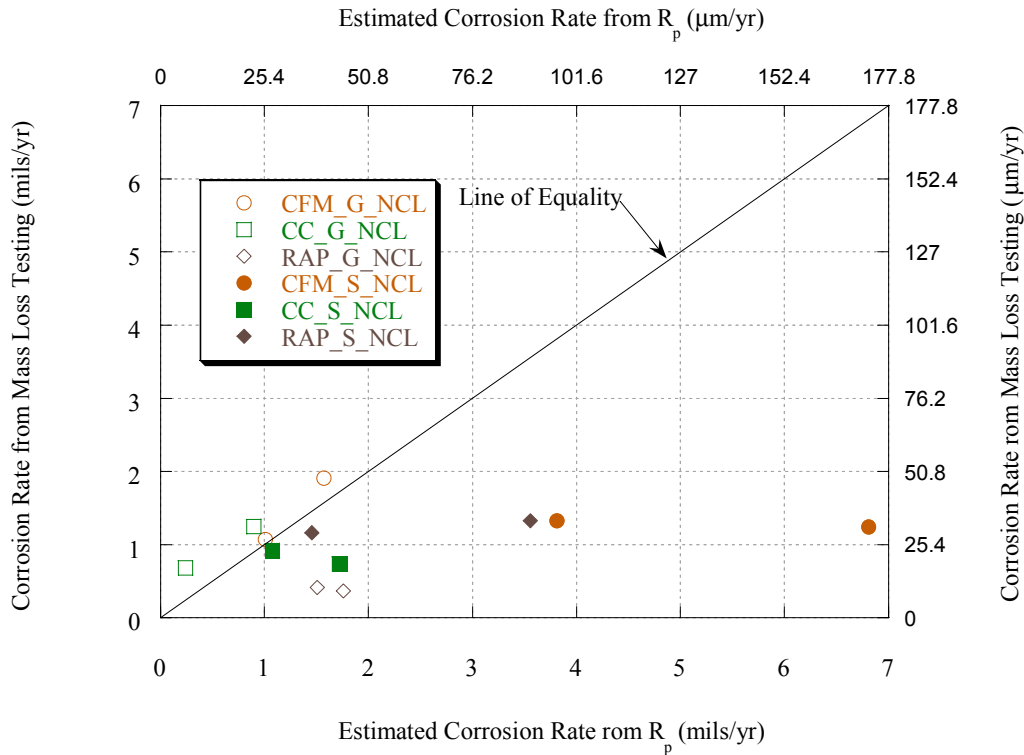


Figure 8.26 Corrosion rates calculated from mass loss versus the corrosion rate determined from average  $R_p$  measurements for the NCL LTT samples.

Figure 8-27 shows the Stern-Geary coefficients determined from the STT and the cyclic polarization testing of the galvanized reinforcement LTT samples. Several significant differences in the Stern-Geary coefficients from the LTT between the groups are shown. For each backfill material, the G\_CL group is significantly different from the G\_NCL group with the exception of CC. The CC\_G\_NCL group has an average Stern-Geary coefficient of approximately 52, while the CC\_G\_CL group has an average coefficient of approximately 56. These values match documented values of the Stern-Geary coefficient for steel embedded in concrete (52 for active conditions). Only moderate correlation between the STT and LTT coefficients was determined.

The Stern-Geary coefficients determined from the cyclic polarization testing of the S\_LTT samples are shown in Figure 8.28. There are no significant differences within the S\_CL or the S\_NCL groups except for the CFM\_S group. In this instance, CFM\_S\_CL exhibits a Stern-Geary coefficient of approximately 55, compared with CFM\_S\_NCL at approximately 95. There is a larger amount of variation in the RAP\_S groups. The Stern-Geary coefficients determined from the STT tended to provide lower values than did the coefficients from the LTT testing. This could be a result of the LTT samples being actively corroding, which results in higher coefficient values.

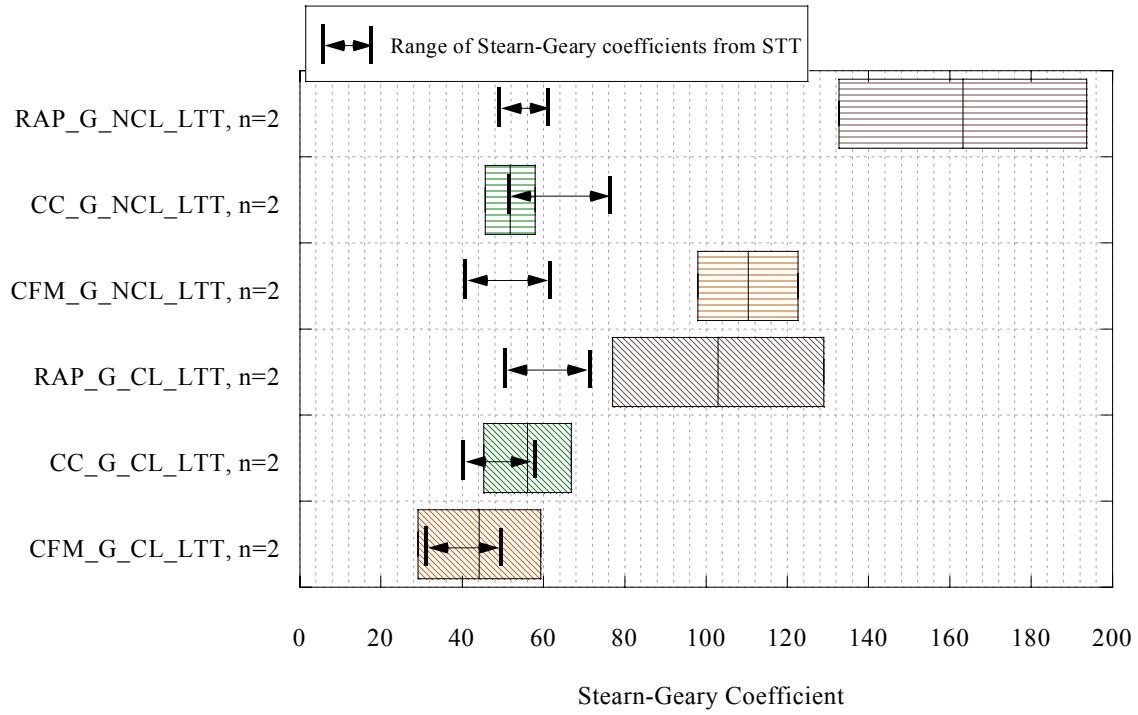


Figure 8.27 Box-plot of Stern-Geary constants derived from cyclic polarization testing plots for all the LTT G samples.

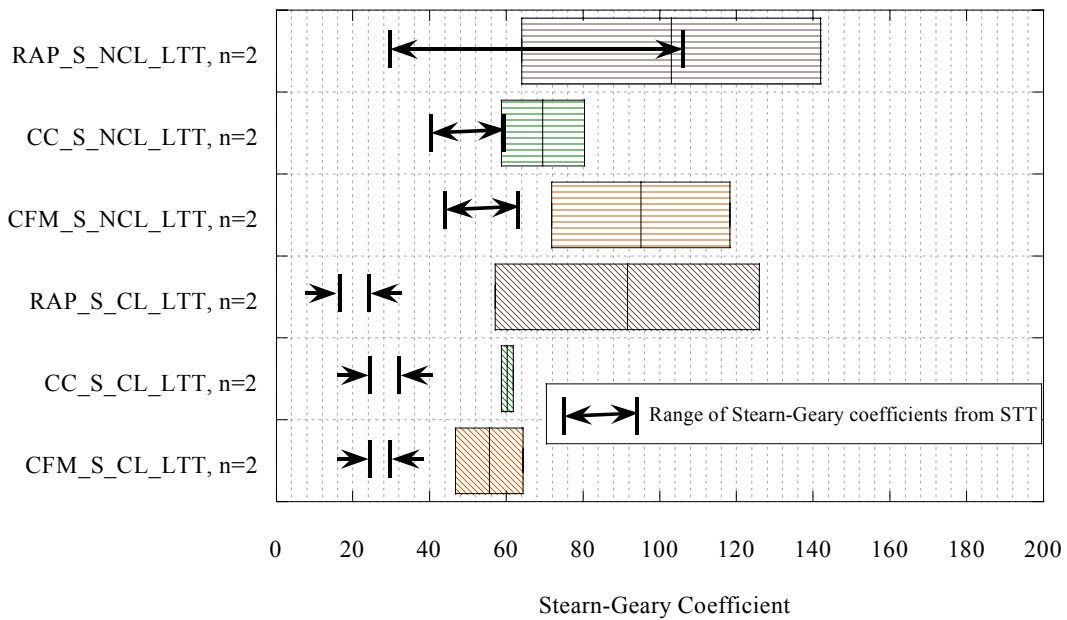


Figure 8.28 Box-plot of Stern-Geary coefficients derived from cyclic polarization testing plots for all the LTT S samples.

## 8.4 Comparison of Short-term and Longer-term Test Results

As mentioned, one purpose of the STT was to determine if a shorter testing period could provide adequate insight into the corrosivity of the backfill materials. The STT also eliminates several variables that could be factors in the LTT such as backfill material density, frequency of solution application, and backfill material gradation. In general, measurements of the pore solution properties were similar between the STT and the LTT. With regard to the prediction of mass loss and corrosion rates, Figure 8-29 displays the corrosion rates determined from mass loss testing of the STT samples from the 1<sup>st</sup> and 100<sup>th</sup> compared to the corrosion rates determined from the mass loss testing of the LTT samples. Clearly, no correlation between the STT the LTT can be determined from the data. Therefore, the STT is determined to not be representative of the LTT results, which provide reasonable corrosion rates for MSE wall structures.

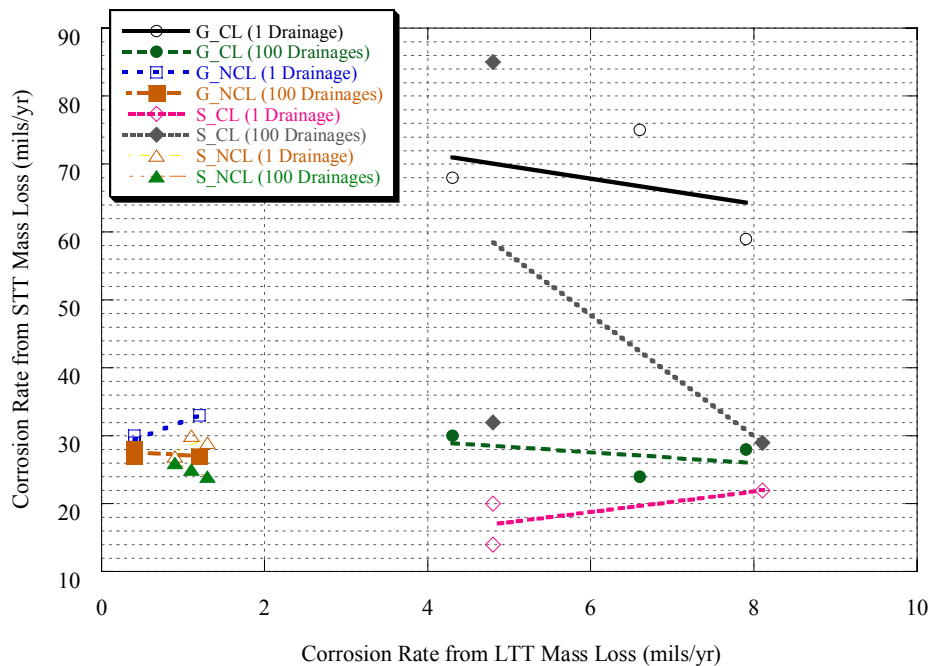


Figure 8.29 Comparison of corrosion rates from STT and LTT.

## 8.5 Summary

The longer-term testing provided valuable insight into the corrosion performance and applicability of short-term testing for predicting longer-term performance. The corrosion rates determined from mass loss testing provided reasonable values likely found in the field. Measuring the OCP can provide information on the state of the MSE reinforcement, but threshold values that indicate active corrosion (i.e., when the potential exceeds some certain value it is assumed to be actively corroding) could not be determined from this research. The pore solution pH and resistivity values from the STT samples show relatively good correlation with the LTT samples. Thus, values determined from early testing of samples taken from the field may be representative of future values. However, the general exposure conditions must be known (i.e., chloride exposure, no chloride exposure, etc.). Estimating chloride ion

concentrations from STT does not produce representative estimates of the longer-term chloride concentrations.

Mass loss testing of MSE reinforcement embedded in the LTT sample setup is likely representative of field conditions and can provide representative corrosion rates likely found in the field. The electrochemical testing does not seem to correlate well with the mass loss results. To better represent the longer-term test results,  $R_p$  testing may have to be performed at shorter intervals. However, this testing is time consuming and may not be applicable for most state highway agencies, including TxDOT. Stern-Geary coefficients were determined for all conditions. The coefficients from both the STT and LTT can be used to estimate corrosion rates of MSE reinforcement. Coefficients determined from the STT are likely more representative of passive conditions and results from the LTT are likely more representative of active corrosion conditions. The STT is not a reliable test for predicting actual corrosion rates.

## **9. Corrosion Service Life Model**

### **9.1 Introduction**

Corrosion of MSE wall reinforcement strips can result in failure of these systems. This research evaluated the corrosion performance of galvanized- and plain-reinforcement embedded in a conventional fill, in crushed concrete, and in recycled asphalt pavement materials in two different exposure conditions – plain water and chloride solution. The value of this work is in determining how these materials, under different exposure conditions, influence the service life of MSE walls reinforced with galvanized- or plain-steel reinforcement. This section will use data obtained from the experimental program to estimate the service life of MSE walls in cases when the failure is associated with corrosion of the reinforcement.

### **9.2 Methodology and Assumptions**

The end of the service life of a MSE wall can be estimated by determining the point in time when the corrosion of the strip reinforcement results in a reduced cross-section such that the stress on the reinforcement exceeds the capacity of the reduced cross-section. In general, MSE reinforcement strips are typically designed for  $0.55(f_y)$ , where  $f_y$  is the yield strength of the steel. MSE wall reinforcement generally must meet the requirements of ASTM A82, which requires a 65 ksi yield strength. However, it is common to use 60 ksi in design, and this value will be used herein. For the purpose of service life analysis, the ultimate strength of the reinforcement will also be assumed to be 60 ksi. It will also be assumed here that when 45 percent of the steel reinforcement (not including the galvanized coating) cross-section is corroded, the stress on the strip will exceed the strip capacity and will fail. The thickness of the strips in this analysis was 0.16 in. for the plain-steel strip and 0.19 in. for the galvanized strip. It should be noted that uniform corrosion will be assumed for all service life predictions. A galvanized coating thickness of 0.0034 in. was assumed. Corrosion caused by chlorides and/or sulfates can result in localized corrosion and earlier failures.

To estimate the cross-sectional loss, average corrosion rates determined in Chapter 8 from the LTT will be used. However, these samples were exposed to wet-dry cycles every two weeks. Because it was determined that the corrosion activity increased significantly during the wet cycles, these corrosion rates likely overestimate the corrosion rate in the field, especially in drier areas throughout the state. A better estimate would be to assume that the MSE reinforcement is exposed to “wet” conditions for a shorter duration of the year than the “drier” conditions for the same year. This would reduce the annual average corrosion rate from that determined in this research. To better estimate the corrosion rates for these “field” conditions, the corrosion rates determined in this study will be reduced by 33 percent.

### **9.3 Service Life Prediction of MSE Walls in Environments with No Chlorides**

This research determined that solution constituents have a significant impact on the corrosion performance of MSE wall reinforcing strips. Other factors contributing to the corrosion rate and

resulting service life of MSE walls include reinforcement type and backfill type. This section will present results using the data reported in Chapter 8 and the assumptions presented in the previous section. As discussed, the MSE wall reinforcement exposed to water (NCL) exhibited lower corrosion activity than MSE wall reinforcement samples exposed to solution containing chloride ions (CL).

Figure 9.1 shows the predicted service life of MSE walls exhibiting corrosion of the reinforcement for galvanized reinforcement in CFM, CC, and RAP. Note that the average corrosion rates (with modifications as presented earlier) were used in this analysis. Using average modified corrosion rates will result in half of the MSE walls failing earlier than the values shown in the figure and half of the MSE walls failing later than the values. Note that the corrosion rates of the galvanized samples were used for determining cross-sectional area loss until the time when this galvanized coating layer would have been completely consumed. The galvanized layer was consumed in 4.5, 6.8, and 3.9 years for the CFM, CC, and RAP backfill materials, respectively. After the galvanized layer was consumed, corrosion rates of the plain-steel samples were used to determine the time to yielding (i.e., the end of the service life). Yielding of the wall strip reinforcement was estimated to be 53, 62, and 77 years for the CFM, CC, and RAP, respectively. Clearly, CC had no detrimental affects on the corrosion of MSE wall reinforcement strips in these environments. Note that the estimated service life of the MSE walls backfilled with CC exceeded the estimated service life of the wall backfilled with CFM when exposed to solutions with no (or low) chloride ion concentrations. MSE walls backfilled with RAP exhibited shorter service life periods. This condition would likely represent MSE wall structures in TxDOT districts away from the coast and in the hatched areas shown in Figure 9.2. The hatched area of the map in Figure 9.2 show TxDOT districts that use limited amounts of de-icing or anti-icing chemicals.

One concern with using the average corrosion rate values is that half of the MSE walls will fail before these service life times. To provide higher reliability in estimating the service life of MSE wall structures experiencing corrosion of the reinforcing strips, 70 and 90 percentile calculations were performed. Figures 9.3 and 9.4 illustrate the estimated service life of MSE walls exhibiting corrosion of the reinforcing strips. Figure 9.3 shows the estimate assuming the 90<sup>th</sup> percentile of the corrosion rates determined in the LTT study. This indicates that only 10 percent of the MSE walls will fail before these times. Figure 9.4 shows the estimated service life using the 70<sup>th</sup> percentile of the corrosion data (30 percent of the walls are estimated to reach the end of their service life before these times). Corrosion studies often indicate that corrosion rates typically exhibit lognormal distributions. As such, logarithmic transformations were applied to the data prior to determining the 70<sup>th</sup> and 90<sup>th</sup> percentiles.

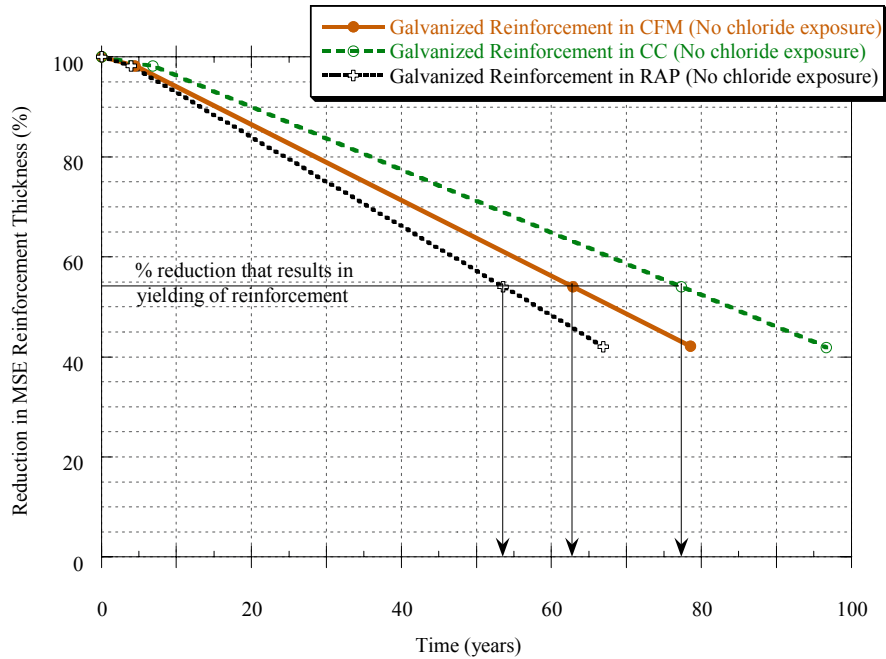


Figure 9.1 Estimated service life times for galvanized MSE strips embedded in CFM, CC, and RAP using average corrosion rates.

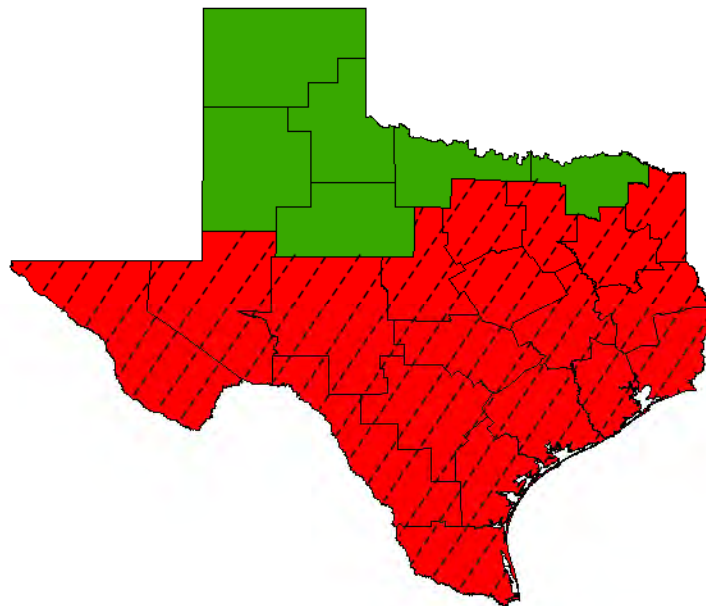


Figure 9.2 Texas locations where deicing/anti-icing chemicals are used (non-hatched area).

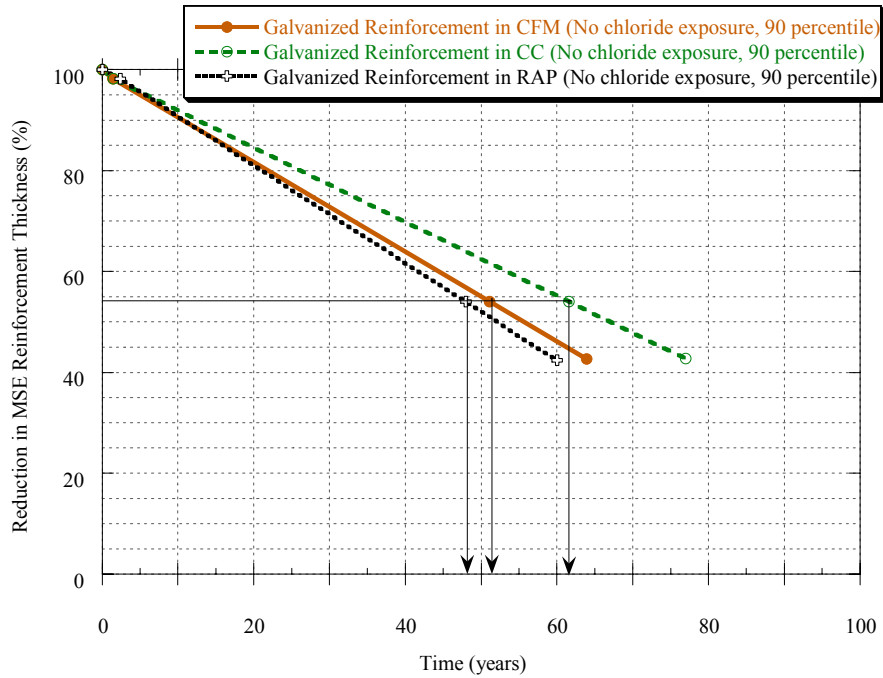


Figure 9.3 Estimated service life times for galvanized MSE strips embedded in CFM, CC, and RAP using the 90<sup>th</sup> percentile of the corrosion rates.

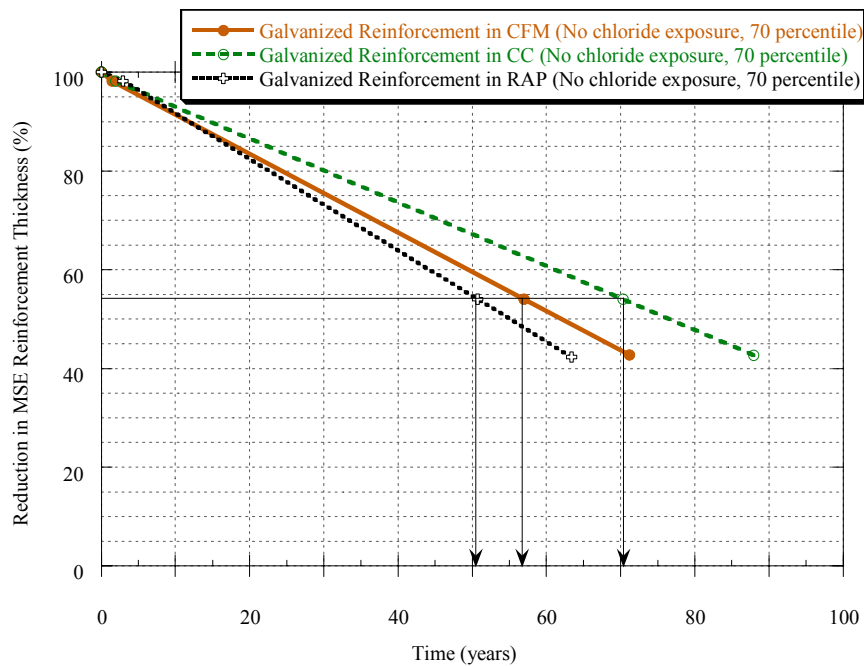


Figure 9.4 Estimated service life times for galvanized MSE reinforcing strips embedded in CFM, CC, and RAP using the 70<sup>th</sup> percentile of the corrosion rates.

The service life of MSE walls containing plain-steel strip reinforcement can be determined in the same manner as the galvanized-strip reinforcement with the exception of using the corrosion rate of the galvanized coating. Figures 9-5 through 9-7 show the time to strip yielding (i.e., the end of the service life) for MSE walls containing corroding plain-steel strip reinforcement. Figure 9-5 shows the service life using the mean corrosion rates, Figure 9-6 shows the service life times using the 70<sup>th</sup> percentile of the corrosion data, and Figure 9-7 shows the service life times using the 90<sup>th</sup> percentile of the data. Table 9.1 shows the service life times for each condition in table format.

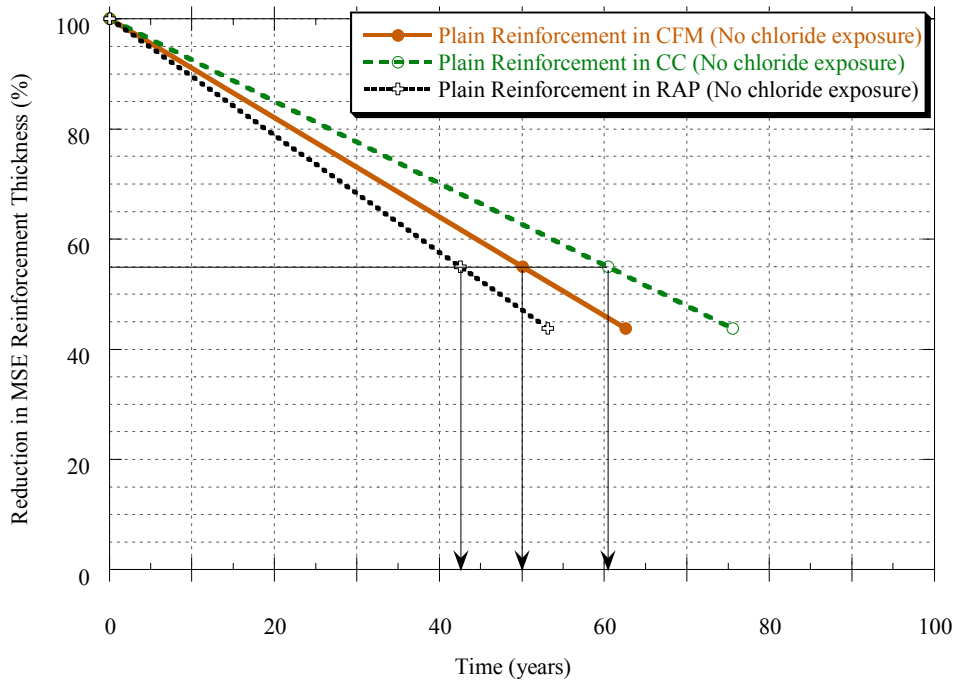


Figure 9.5 Estimated service life times for plain-steel MSE reinforcing strips embedded in CFM, CC, and RAP using the average corrosion rates.

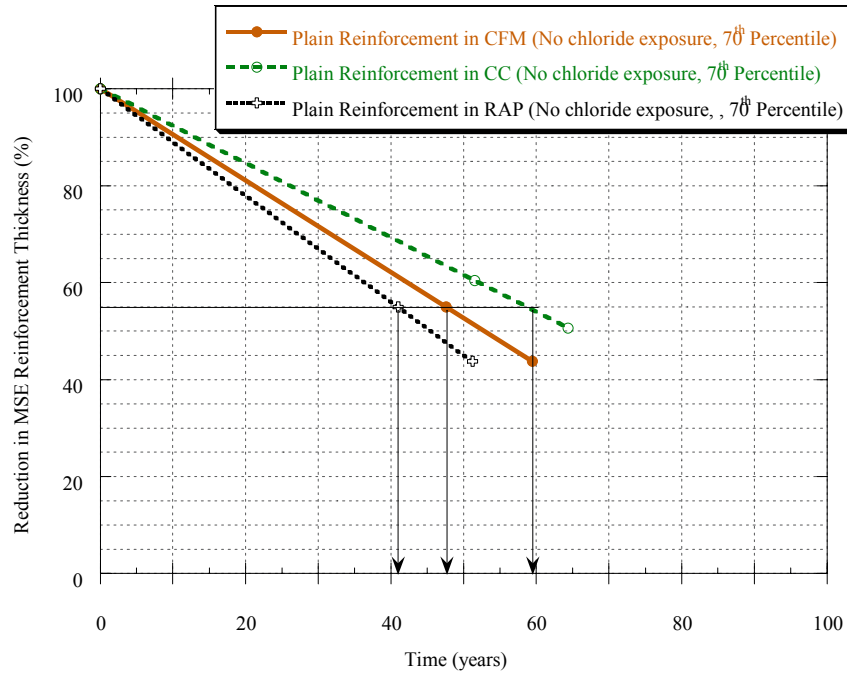


Figure 9.6 Estimated service life times for plain-steel MSE reinforcing strips embedded in CFM, CC, and RAP using the 70<sup>th</sup> percentile of the corrosion rates.

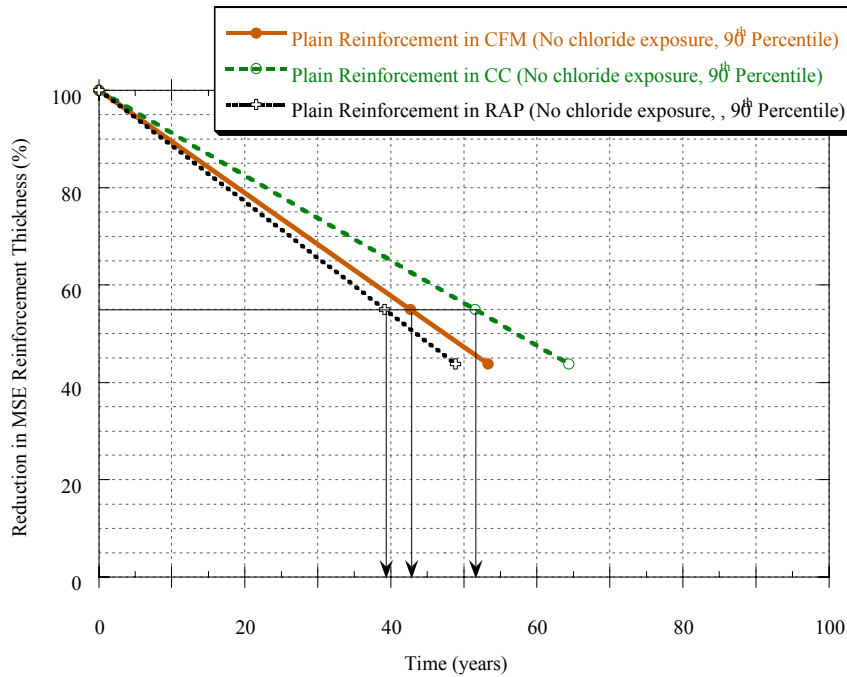


Figure 9.7 Estimated service life times for plain-steel MSE reinforcing strips embedded in CFM, CC, and RAP using the 90<sup>th</sup> percentile of the corrosion rates.

*Table 9.1 Estimated service life (years) of MSE walls in the various backfill materials with plain-steel and galvanized strips exposed to solutions without chloride ions.*

Percentile	MSE Walls with Galvanized Strip			MSE Walls with Plain-steel Strip		
	RAP	CFM	CC	RAP	CFM	CC
Average	54	62	77	43	50	60
70 <sup>th</sup>	50	57	70	41	47	59
90 <sup>th</sup>	48	51	62	39	43	52

#### **9.4 Service Life Prediction of MSE Walls in Environments Containing Chloride Ions**

The corrosion of MSE wall strips exposed to environments containing chloride ions was much more aggressive than environments containing no or low chloride ion concentrations. The methodology to estimate the service life for strips embedded in the different backfill materials exposed to solutions with chloride ion is the same as the method presented in Section 9.3. Table 9.2 shows all the results for the different samples exposed to solutions containing chloride ions. Note the significant reductions in service life when compared with the data in Table 9-1.

*Table 9.2 Estimated service life (years) of MSE walls in the various backfill materials with plain-steel and galvanized strips exposed to solutions containing chloride ions.*

Percentile	MSE Walls with Galvanized Strip			MSE Walls with Plain-steel Strip		
	RAP	CFM	CC	RAP	CFM	CC
Average	8	13	13	7	11	11
70 <sup>th</sup>	8	12	13	7	10	11
90 <sup>th</sup>	7	12	12	6	10	10

#### **9.5 Service Life Model Comparison**

One objective of this research was to evaluate the service life of MSE walls. One existing method sometimes used to estimate the service life of MSE walls (whether correctly or incorrectly) is the California Test 643, *Method for Estimating the Service Life of Steel Culvert*.

The method uses the chart shown in Figure 9-8 to estimate the service life of culverts. Figure 9-9 shows a comparison of the results from the CalTrans method and results from this research. The mean pore solution pH and the resistivity values from the LTT samples were used to estimate the service life with the CalTrans method.

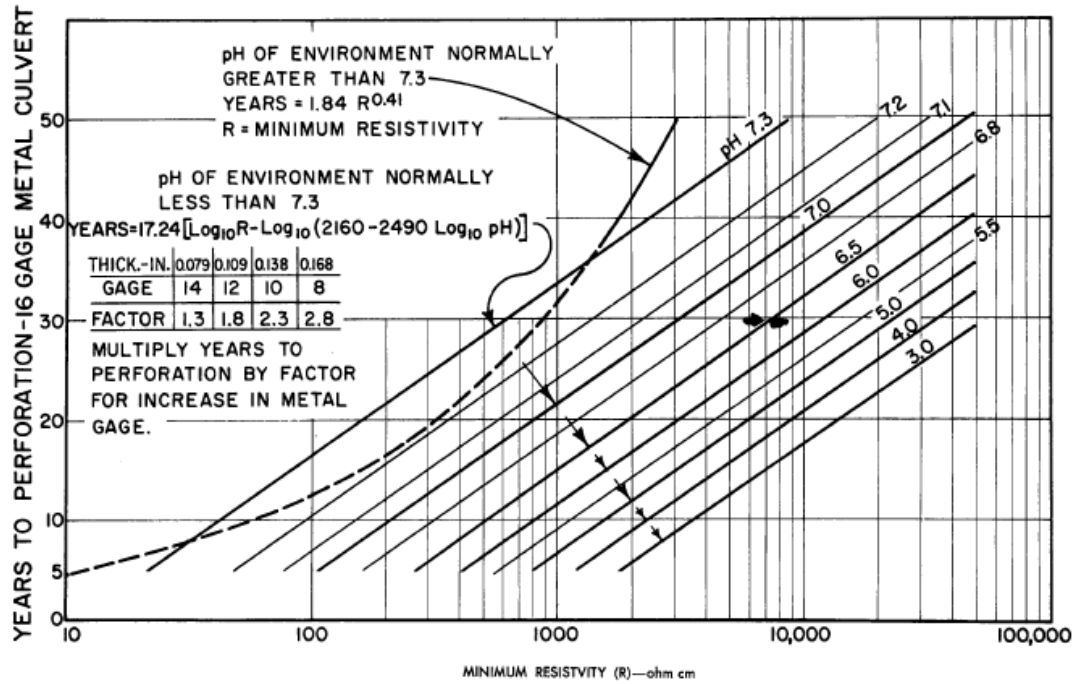


Figure 9.8 Estimated service life times for plain-steel MSE reinforcing strips embedded in CFM, CC, and RAP using the 90<sup>th</sup> percentile of the corrosion rates.

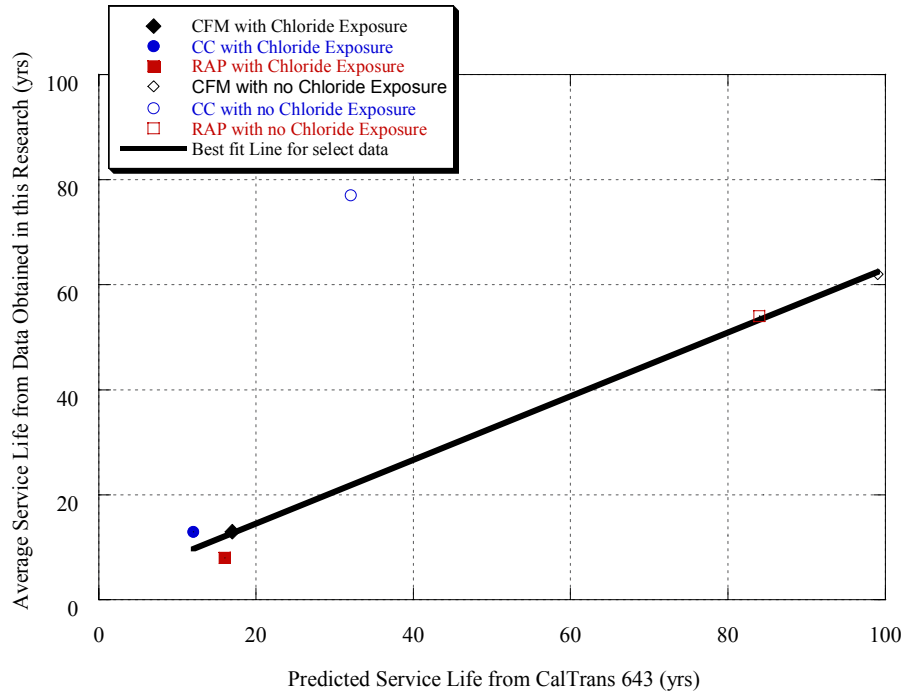


Figure 9.9 Correlation between CalTrans 643 and mean results determined in this research.

With the exception of the service life of the CC in chloride environments, the CalTrans methods provide similar service life predictions. However, care must be taken when using the CalTrans method. For CC with exposure to no chloride ions, the CalTrans method significantly underestimates the service life time determined in this research. These samples clearly showed improved performance in the test performed in this study. Excluding the CC backfill material exposed to no or low chloride concentrations and containing galvanized MSE wall strips, the following equation can be used to estimate the service life using resistivity data:

$$\text{Service Life of MSE Wall} = 2.32 + 1.12 \cdot (\text{resistivity})^{0.41} \quad (9.1)$$

Note that this assumes average corrosion rates. This equation also assumes that the pH of the pore solution is greater than 8.8 (the lowest mean pH value evaluated in this research). The service life of an MSE wall with galvanized strips and CC backfill exposed to an environment that likely contains no or low chloride ion concentrations should use the corrosion rates shown in Chapter 8.

## 9.6 Comparison of Service Life Times of MSE Walls Backfilled with CFM, CC and RAP

One of the major objectives of this research was to evaluate the potential corrosivity of CC and RAP backfill materials and to compare the service life times of MSE walls using these backfill materials. Table 9-3 shows the change in service life of RAP and CC backfill materials compared to CFM. In all cases where the MSE wall backfill material was RAP, shorter service life spans

were observed when compared the CFM backfill material. For non-chloride ion exposure conditions the percent change in service life varied between approximately 6 and 14 percent. For exposure conditions that included chloride ions the percent reduction ranged from approximately 30 to 42 percent. However, these service life spans ranged from 10 to 13 years for this exposure, and small changes resulted in large percentages. For all cases where CC was used as the backfill, the service life of the MSE wall increased. The percent increase for the non-chloride application ranged from approximately 17 to 20 percent. The percent increase for the exposure conditions containing chloride ions ranged from 0 to 10 percent for the CC backfill materials.

*Table 9.3 Percent change in service life when compared with CFM in same backfill and exposure condition.*

Percentile	Water				Solution with Chloride Ions			
	Galvanized		Plain-steel		Galvanized		Plain-steel	
	RAP	CC	RAP	CC	RAP	CC	RAP	CC
Average	-12.9	19.5	-14.0	16.7	-38.5	0.0	-36.4	0.0
70 <sup>th</sup>	-12.3	18.6	-12.8	20.3	-33.3	8.3	-30.0	10.0
90 <sup>th</sup>	-5.9	17.7	-9.3	17.3	-41.7	0.0	-40.0	0.0

## 9.7 Summary

This research shows that MSE walls backfilled with CC exhibit longer service life spans than MSE walls constructed with the CFM used in this study. Results also indicate that MSE walls backfilled with RAP will exhibit shorter service life spans than similar MSE walls constructed with CFM. Chloride ions clearly have a significant negative impact on the service life, and care must be taken when designing MSE walls in environments where chloride ions may permeate to the reinforcement.

## 10. Conclusions and Recommendations

### 10.1 Introduction

This report describes the results from an experimental program aimed at evaluating crushed concrete (CC) and recycled asphalt pavement (RAP) for use as backfill for mechanically stabilized earth (MSE) walls. Both the mechanical properties and corrosivity of CC and RAP were considered. The conclusions and findings related to the Geotechnical Evaluation and the Corrosion Evaluation of CC and RAP are given below, separately. Additionally, recommendations are summarized with respect to new test methods, material specifications, and construction specifications required for these materials.

### 10.2 Geotechnical Evaluation

#### 10.2.1 Crushed Concrete (CC)

Generally, CC displays adequate gradation, compaction, shear strength, and pullout properties, but it displays a low hydraulic conductivity. Thus, it is recommended that MSE walls with crushed concrete backfill include adequate drains and high permittivity filter fabrics behind MSE walls to avoid drainage problems. Additional recommendations for CC based on its potential for corrosion of metallic reinforcement are given in Section 10.3. A summary of the various geotechnical test results for CC evaluated in this study is provided below.

Gradation: The gradation of crushed concrete provided by commercial producers in Texas meets the TxDOT Item 423 Type B backfill gradation specification, which is the gradation generally designated for permanent MSE walls.

Drainage properties: Falling-head, rising-tail hydraulic conductivity tests were performed on CC specimens in a triaxial apparatus. The hydraulic conductivity of CC ranged from  $10^{-4}$  to  $10^{-5}$  cm/s over confining pressures of 5 to 50 psi. The hydraulic conductivity of the conventional crushed limestone was close to  $10^{-3}$  cm/s. The low hydraulic conductivity of CC is a concern; therefore, it is recommended that MSE walls with crushed concrete backfill include adequate drains and high permittivity filter fabrics behind the wall to avoid drainage problems.

Strength: The results from consolidated-drained shear strength tests indicate that crushed concrete has strength characteristics comparable to conventional fill materials. Using 4-in. diameter triaxial tests and large-scale (20 in. by 20 in.) direct shear tests, the derived effective shear strength parameters for CC were:  $c'=9$  psi,  $\phi'=46^\circ$ . A conventional crushed limestone backfill, which also met the TxDOT backfill gradation specifications, displayed very similar shear strength parameters ( $c'=10$  psi,  $\phi'=46^\circ$ ).

Pullout testing: Pullout tests were performed in the 20 in. by 20 in. shear box using steel, ribbed reinforcement embedded in crushed concrete. Measured values of pullout force were used to evaluate  $F^*$ , the pullout resistance factor or friction-bearing factor, which is used to predict the

ultimate pullout resistance of reinforcement for MSE wall design. The measured  $F^*$  values at different confining pressures were all greater than those predicted by the design procedures from FHWA, indicating that the traditional predictive equations for  $F^*$  can be used for CC.

Durability testing: Crushed concrete derived from concrete that had suffered sulfate attack experienced significant expansion upon wetting, and this deformation could damage an MSE wall. Thus, it is recommended that concrete structures that have experienced sulfate attack not be crushed and used as backfill.

*Based on the results discussed above, CC is recommended for use as select backfill for MSE walls.*

### **10.2.2 Recycled Asphalt Pavement (RAP)**

Although RAP displays adequate gradation, strength, and hydraulic conductivity properties, it displays a significant potential for creep deformations. These creep deformations may lead to excessive deformation in an MSE wall, making this material unacceptable for use as select backfill. Additional recommendations for RAP based on its potential for corrosion of metallic reinforcement are given in Section 10.3. A summary of the various geotechnical test results for RAP evaluated in this study is provided below.

Gradation: The gradation of RAP in Texas stockpiles meets the TxDOT Item 423 Type B backfill gradation specification, which is the gradation generally designated for permanent MSE walls.

Drainage properties: Falling-head, rising-tail hydraulic conductivity tests were performed on RAP specimens in a triaxial apparatus. The hydraulic conductivity of RAP ranged from  $0.5 \times 10^{-3}$  to  $4 \times 10^{-3}$  cm/s over confining pressures of 5 to 50 psi. These values indicate that RAP is a free-draining material that does not require additional drainage measures.

Strength: The results from strain-controlled consolidated-drained triaxial tests indicate that RAP has acceptable, although somewhat marginal, strength characteristics comparable to conventional fill materials. The derived effective shear strength parameters for RAP were:  $c' = 8$  psi,  $\phi' = 37^\circ$ . Because these tests were strain-controlled, they do not include the effects of creep. The large-scale direct shear tests, which are force controlled, could not be successfully performed on RAP because of the creep deformations.

Pullout testing: Pullout tests were performed in the 20 in. by 20 in. shear box using steel, ribbed reinforcement embedded in RAP. The force-controlled pullout tests experienced significant creep deformations, with the deformation limit of 0.75 in. reached before shear failure along the reinforcement-soil interface. Nonetheless, derived  $F^*$  values at the deformation limit were similar to those predicted by design procedures, except at larger confining pressures.

Creep testing: A series of deviatoric creep tests were performed under drained conditions in a triaxial apparatus. These tests indicated that the creep potential in RAP is significant, and its creep behavior is similar to that of clays under undrained conditions. Additionally, creep rupture

is a concern and the creep potential of creep appears to most severe at smaller confining pressures.

It should be noted that the creep properties of RAP, as well as its other properties, will be influenced by the properties of the parent hot mix asphalt. Most importantly, the asphalt content and asphalt cement performance grade will affect the creep response of RAP, with ageing and aggregate type also having an impact. The RAP tested in this study contained approximately 3.5 percent asphalt cement, which is on the low end of the expected values. RAP with more asphalt cement may experience more creep than was observed in this study.

Finally, although TxDOT has built several MSE walls with RAP and these walls have performed well, our research concludes that the creep potential of RAP may influence the long-term performance of MSE walls that use RAP as select backfill. Based on our research findings and observations, until a better understanding of the stress levels that exists in the reinforced backfill, *it is our recommendation that RAP not be used as select backfill for permanent MSE walls.* However, it may be possible to use RAP as backfill for temporary walls that will not be in service for more than a few years.

### 10.3 Corrosion Evaluation

This research included a comprehensive investigation of the corrosivity of RAP, CC, and CFM. In addition to the corrosivity investigations, the researchers attempted to develop a short-term test for evaluating this corrosivity of backfill materials. Results from this work indicate that chloride ion concentration was a significant factor in the corrosivity of backfill materials. In many cases, the resistivity provided an indication of the corrosivity. However, reports and specifications indicating that higher pore solution pH values lead to higher corrosivity of the backfill materials is likely not valid for recycled materials. This research indicates that CC backfill materials for MSE walls, which have elevated pore solution pH values, exhibited lower corrosivity and resulted in longer estimated service life times for MSE walls.

The longer-term testing provided reasonable corrosion rates for MSE wall strips and could be used for evaluating the corrosivity of various backfill materials. Also, with the exception of MSE walls exposed to environments where no or low chlorides are expected to be in the vicinity of the galvanized strip reinforcement, a modified version of the CalTrans equation that requires only the resistivity of the backfill solution can be used. Note that this equation is for galvanized strips with the backfill material having a pore solution pH greater than 8.8.

It is recommended that only mass loss information be determined from the LTT, as electrochemical tests in general did not provide a good estimate of the average corrosion rate and/or service life. Short-term testing using decanted pore solution is not recommended as limited correlations with the longer-term tests were observed.

The corrosion investigations determined that the corrosivity of RAP was greater than CFM, which was greater than CC. The percent increase in the estimated service life values for the CC ranged from 0 to 20 percent. Percent reductions in the service life times for RAP ranged from 6 to 42 percent. *As such, from a corrosion perspective, it is recommended that CC be approved for use as a MSE wall backfill material.* However, special care must be taken to ensure that the permeability of this material remains sufficiently high. Short-term test results in the laboratory

indicated that the permeability of CC is lower than the RAP and CFM evaluated in this program. Because chloride ions can be detrimental to the service life of MSE walls, it is recommended that the CC be evaluated for chloride ion concentrations prior to using these materials as backfill for MSE wall. Also, if MSE walls are placed in areas that could contaminate the backfill material, special attention should be paid to protecting the reinforcing strips from this corrosive environment. *At this time, from a corrosion perspective, it is recommended that RAP not be used as a backfill material* for MSE walls unless the material is evaluated using the longer-term test procedure described herein or significant cost savings and minimum service life requirements can be met.

## **10.4 Specification Recommendations**

The results of this research have indicated that CC is a suitable backfill material for MSE walls, while RAP is not suitable because of its significant potential for creep deformations. Nonetheless, the recommendation that CC can be used as MSE backfill necessitates some potential changes to material and construction specifications. However, new material test methods are not required. The recommended changes to material and construction specifications are:

1. pH and Resistivity specifications for MSE wall backfill materials should be waived for crushed concrete.
2. Concrete structures that have suffered sulfate attack cannot be crushed and used as backfill in MSE walls.
3. MSE walls with crushed concrete backfill should include adequate drains and high permittivity filter fabrics behind the wall to avoid drainage problems.

## References

AASHTO (2004). "Standard Specification for Performance-Graded Asphalt Binder (AASHTO MP1a-04)," *Standard Specifications for Transportation Materials and Methods of Sampling and Testing*, Washington, DC.

AASHTO (2004). "Standard Method of Test for the Moisture-Density Relations of Soils Using a 2.5-kg (5.5-lb) Rammer and a 305-mm (12-in.) Drop (AASHTO T-99)," *Standard Specifications for Transportation Materials and Methods of Sampling and Testing*, Washington, DC.

AASHTO (2005). "Standard Method of Test for Direct Shear Test of Soils under Consolidated Drained Conditions (AASHTO T-236)," *Standard Specifications for Transportation Materials and Methods of Sampling and Testing*, Washington, DC.

Al-Rousan, T., Masad, E., Myers, L., and Speigelman, C. (2005). "New Methodology for Shape Classification of Aggregates." *Transportation Research Record: Journal of the Transportation Research Board*, Issue 1913, 11-23.

Applegate, L. M. (1960). *Cathodic Protection*, McGraw-Hill Book Co, Inc., New York, N. Y.

ASTM (2001). "Standard Test Method for Density, Relative Density (Specific Gravity), and Absorption of Coarse Aggregate (ASTM C127)." *Annual Book of ASTM Standards*, American Society for Testing and Materials, West Conshohocken, PA.

ASTM (2002). "Standard Specification for Standard Sand (ASTM C 778)." *Annual Book of ASTM Standards*, American Society for Testing and Materials, West Conshohocken, PA.

ASTM (2001). "Standard Test Method for Determination of Length Change of Concrete Due to Alkali Silica Reaction (ASTM C1293)." *Annual Book of ASTM Standards*, American Society for Testing and Materials, West Conshohocken, PA.

ASTM (2001). "Standard Test Method for Particle-Size Analysis of Soils (ASTM D422)." *Annual Book of ASTM Standards*, American Society for Testing and Materials, West Conshohocken, PA.

ASTM (2001). "Standard Test Method for Specific Gravity of Soils (ASTM D854)." *Annual Book of ASTM Standards*, American Society for Testing and Materials, West Conshohocken, PA.

ASTM (2001). "Standard Test Methods for Density and Unit Weight of Soil in Place by the Sand-Cone Method (ASTM D1556)." *Annual Book of ASTM Standards*, American Society for Testing and Materials, West Conshohocken, PA.

ASTM (2001). "Standard Test Methods for Density and Unit Weight of Soil in Place by the Rubber Balloon Method (ASTM D2167)." *Annual Book of ASTM Standards*, American Society for Testing and Materials, West Conshohocken, PA.

ASTM (2001). "Standard Test Method for Permeability of Granular Soils (Constant Head) (ASTM D2434)." *Annual Book of ASTM Standards*, American Society for Testing and Materials, West Conshohocken, PA.

ASTM (2001). "Standard Test Methods for Density of Soil and Soil-Aggregate in Place by Nuclear Methods (Shallow Depth) (ASTM D2922)." *Annual Book of ASTM Standards*, American Society for Testing and Materials, West Conshohocken, PA.

ASTM (2001). "Standard Test Methods for Density of Bituminous Concrete in Place by Nuclear Methods (ASTM D2950)." *Annual Book of ASTM Standards*, American Society for Testing and Materials, West Conshohocken, PA.

ASTM (2001). "Standard Test Method for Direct Shear Test of Soils under Consolidated Drained Conditions (ASTM D3080)." *Annual Book of ASTM Standards*, American Society for Testing and Materials, West Conshohocken, PA.

ASTM (2005). "Standard Test Methods for Asphalt Content of Bituminous Mixtures by the Nuclear Method (ASTM 4125-05)," *Annual Book of ASTM Standards*, American Society for Testing and Materials, West Conshohocken, PA

ASTM (2001). "Standard Test Method for Consolidated Undrained Triaxial Compression Test for Cohesive Soils (ASTM D4767)." *Annual Book of ASTM Standards*, American Society for Testing and Materials, West Conshohocken, PA.

ASTM (2001). "Standard Test Methods for Density of Soil and Rock in Place by the Water Replacement Method in a Test Pit (ASTM D5030)." *Annual Book of ASTM Standards*, American Society for Testing and Materials, West Conshohocken, PA.

ASTM (2001). "Standard Test Methods for Measurement of Hydraulic Conductivity of Saturated Porous Materials Using a Flexible Wall Permeameter (ASTM D5084)." *Annual Book of ASTM Standards*, American Society for Testing and Materials, West Conshohocken, PA.

ASTM (2001). "Standard Test Method for Measurement of Collapse Potential of Soils (ASTM D5333)." *Annual Book of ASTM Standards*, American Society for Testing and Materials, West Conshohocken, PA.

Anderson, L.R., Nelson, K.J., and Sampaco, C.L. (1995) "Mechanically Stabilized Earth Walls." *Transportation Research Circular*, Vol. 444, 17 pp.

Barksdale, R. D., Itani, S. Y., and Swor, T. E. (1992) "Evaluation of Recycled Concrete, Opened-graded Aggregate, and Large Top-size Aggregate Bases." *Transportation Research Record*, Vol. 1345, Transportation Research Board, National Research Council, Washington, D.C., pp.92-105.

Bishop, A.W., and Lovenbury, H.T. (1969) "Creep Characteristics of Two Undisturbed Clays," *Proceedings, 7<sup>th</sup> International Conference on Soil Mechanics and Foundation Engineering*, Mexico, 1, 29-37.

Black, K. N. (1995). "The Nuclear Asphalt Content Gauge." *Public Roads*, Winter, Vol. 58, No. 3, pp. 8-13.

Campanella, R.G. and Vaid, Y.P. (1974) "Triaxial and Plane Strain Creep Rupture of an Undisturbed Clay," *Canadian Geotechnical Journal*, 11(1), pp. 1-10.

Casagrande, A. and Fadum, R.E. (1940) "Notes on Soil Testing for Engineering Purposes," *Harvard Univ. Grad. School of Engineering Publ. 268*, 74 pp.

Christopher, B.R., Gill, S.A., Giroud, J.P., Juran, I., Mitchell, J.K., Schlosser, F. and Dunnicliff, J. (1990), "Reinforced Soil Structures – Volume 1, Design and Construction Guidelines – Volume 2, Summary of research and systems information," U.S. Department of Transportation Federal Highway Administration Report No. FHWA RD 89-043.

Cuttell, G. D., Snyder, M. B., Vandenbossche, J. M., and Wade, M. J. (1997) "Performance of Rigid Pavements Containing Recycled Concrete Aggregates." *Transportation Research Record*, Vol. 1574, Transportation Research Board, National Research Council, Washington, D.C., pp. 89-98.

Davis, J.R. (1996). Carbon and Alloy Steels: ASM Specialty Handbook. ASM International, Materials Park, OH.

Elias, V. (1990). Durability/Corrosion of Soil Reinforced Structures, Federal Highway Administration Report No. FHWA-RD-89-186.

Elias, V., Christopher, B.R. and Berg, R. (2001), "Mechanically Stabilized Earth Walls and Reinforced Soil Slopes Design and Construction Guidelines," NHI FHWA Report No. FHWA-NHI-00-043, U.S. Department of Transportation, Washington, D.C.

Elias, V., and Christopher, B. (1996). "Mechanically Stabilized Earth Walls and Reinforced Soil Slopes Design and Construction Guidelines." FHWA Demonstration Project 82, *FHWA SA-96-071*.

Esfeller, M. (2006). "Electrochemical Assessment and Service-life Prediction of Mechanically Stabilized Earth Walls Backfilled with Crushed Concrete and Recycled Asphalt Pavement," M.S. Thesis, Texas A&M University, May 2006.

Estakhri, C.K. and Button, J.W. (1992) "Routine Maintenance Uses for Milled Reclaimed Asphalt Pavement (RAP)," *TTI Report 1272-1*, Texas Transportation Institute, College Station, Texas.

Federal Highway Administration (FHWA) (2000). "User Guidelines: Reclaimed Asphalt Pavement, Reclaimed Concrete Material." <http://www.tfhrc.gov/////hnr20/recycle/waste/>, accessed October 1, 2000.

Federal Highway Administration (FHWA) (2004) "Transportation Applications of Recycled Concrete Aggregate," *FHWA State of the Practice National Review*, September, 2004, Washington, DC, 47 pp.

- Guilloux, A., Schlosser, F., and Long, N.T. (1979) "Etude du frottement sable – armature en laboratoire," *Proc. Int. Conf. Soil Reinforcement*, Paris, Vol. 1, pp. 35-40.
- Halm, H. J. (1980). "Concrete Recycling." *Transportation Research News*, Issue 89, Transportation Research Board, National Research Council, Washington, D.C, pp.6-10.
- Herrin, M. and Jones, G., (1963) "Behavior of Bituminous Materials from the Viewpoint of Absolute Rate Theory," *Proceedings of the Association of Asphalt Paving Technologists*, Vol. 32, pp. 82-105.
- Houston, W.N., Mahmoud, H.H., and Houston, S.L. (1993) "A Laboratory Procedure for Partial-Wetting Collapse Determination," *Geotechnical Special Publication No. 39*, ASCE, pp. 54-63.
- Kelly, T. (1998). "Crushed Cement Concrete Substitution for Construction Aggregates – A Materials Flow Analysis," U.S. Geological Survey Circular.
- Kennedy, T. W., Tahmoressi, M., and Solaimanian, M. (1989). "Evaluation of a Thin-Lift Nuclear Gauge." *Transportation Research Record*, Vol. 1217, Transportation Research Board, National Research Council, Washington, D.C., pp. 9-19.
- Kuhn, M.R. and Mitchell, J.K. (1993) "New Perspectives on Soil Creep," *Journal of Geotechnical Engineering*, ASCE, Vol. 119, No. 3, pp. 507-524.
- Lambe, T. W. and Whitman, R.V. (1979) "Soil Mechanics," John Wiley & Sons, New York, NY.
- Law Engineering and Environmental Services (1998), "Pullout Testing of Narrow Ladder Strip (NLRS)," Report, presented to Reinforced Earth Company.
- Lawton, E.C., Fragaszy, R.J., and Hetherington, M.D. (1992) "Review of Wetting-Induced Collapse in Compacted Soil," *Journal of Geotechnical Engineering*, Vol. 118, No. 9, pp. 1376-1394.
- Lutenegger, A.J., Saber, R.T. (1988) "Determination of Collapse Potential of Soils," *Geotechnical Testing Journal*, American Society of Testing and Materials, Vol. 11, No. 3, pp. 173-178.
- Mack, J. W., Solberg, C.E., and Voight, G.F. (1993) "Recycling Concrete Pavements," *Concrete Construction*, Vol. 38, No. 7, pp. 470-473.
- Mamlouk, M. S. (1988). "Nuclear Density Testing of Granular Materials: State of the Art." *Research Report No. FHWA-AZ88-839*, Federal Highway Administration.
- Marx, E. (2001) "Influence of Compaction Conditions on the Settlement Due to Wetting of Fine Uniform Sands," M.S. Thesis, The University of Texas at Austin, 126 pp.
- Mitchell, J.K. 1993 *Fundamentals of Soil Behavior*. John Wiley and Sons, New York.

- Mitchell, J.K., Campanella, R.G., and Singh, A. (1968) "Soil Creep as a Rate Process," *Journal of Soil Mechanics and Foundations Division*, ASCE, Vol. 94, No. SM1, pp. 231-253.
- Mitchell, J.K. and Christopher, B. (1990). "North American Practice in Reinforced Soil Systems," *Geotechnical Special Publication No. 25, Design and Performance of Earth Retaining Structures*, June 18-21, Ithaca, NY, pp. 322-346.
- Morris, D. V., and Delphia, J. G. (1999). "Specifications for Backfill of Reinforced-Earth Retaining Walls." *Texas Transportation Institute, FHWA/TX-99/1431-S*.
- Nagi, M., and Whiting, D. (1999). "Evaluation of Precision of a Nuclear Gauge for Measurement of Water and Cement Content of Fresh Concrete." *Cement, Concrete, and Aggregates*, CCAGDP, Vol. 21, No. 1, June 1999, pp. 1-11.
- Ogolla, M.A. (2002) "Durability of Recycled Crushed Concrete and Recycled Asphalt Pavements in Mechanically Stabilized Earth Retaining Walls," Master's Thesis, The University of Texas at Austin, 130 pp.
- O'Mahony, M. M., and Milligan, G. W. E. (1991) "Use of Recycled Materials in Subbase Layers." *Transportation Research Record*, Vol. 1310, Transportation Research Board, National Research Council, Washington, D.C., pp. 73-80.
- Palossy, L., Scharle, P., and Szalatkay, I. (1993) "Earth Walls," Ellis Horwood, West Sussex, England, 246 pp.
- Petrarca, R. W., and Galdiero, V. A. (1984) "Summary of Testing of Recycled Crushed Concrete." *Transportation Research Record*, Vol. 989, Transportation Research Board, National Research Council, Washington, D.C, pp.19-26.
- Popova, S. N., Popov, B. N., White, R. E., Petrou, M. F., and Morris, D. (1998) "Corrosion Effects of Stabilized Backfill on Steel Reinforcement." *ACI Structural Journal*, Vol. 95, No. 5, pp. 570-577.
- Regimand, A., and Gilbert, A. B. (1999). "Apparatus and Method for Field Calibration of Nuclear Surface Density Gauges." *Field Instrumentation for Soil and Rock*, ASTM STP 1358, Eds., G. N. Durham and W. A. Marr, American Society for Testing and Materials, West Conshohocken, PA, pp. 135-147.
- Roberts, Kandhal, P., Brown, E.R., Lee, D.-Y., and Kennedy, T. (1996). *Hot Mix Asphalt Materials, Mixture Design, and Construction*. NAPA Research and Education Foundation, Lanham, MD.
- Romanoff, M. (1957). "Underground Corrosion", NBS Circular 579, U.S. Department of Commerce.
- Sanders, S. R., Rath, D., and Parker Jr., F. (1994). "Comparison of Nuclear and Core Pavement Density Measurements." *Journal of Transportation Engineering*, Vol. 120, Issue 6, pp. 953-966.

Sawicki, A. (1999) "Creep of Geosynthetic Reinforced Soil Retaining Walls." *Geotextiles and Geomembranes*, Vol.17, pp. 51-65.

Senior, S. A., Szoke, S. I., and Rogers, C. A. (1994) "Ontario's Experience with Reclaimed Materials for Use in Aggregates." *International Road Federation Conference*, Calgary, Alberta.

Serra, E. T. and Mannheimer, W. A. (1981) "On the Estimation of the Corrosion Rates of Metals in Soils by Electrochemical Measurements." *Underground Corrosion*, ASTM STP, Edward Escalante, Ed., American Society for Testing and Materials, pp. 111-122.

Singh, A., and Mitchell, J.K. (1968) "General Stress-Strain-Time Function for Soils," *Journal of Soil Mechanics and Foundations Division*, Proceedings of the ASCE, Vol. 94, No. SM1, pp. 21-46.

Tait, W.S. (1994). *An Introduction to Electrochemical Corrosion Testing for Practicing Engineers and Scientists*. Pair O Docs Publications, Racine, WI.

Tavenas, F., Leroueil, S., La Rochelle, P., and Roy, M. (1978). "Creep Behavior of an Undisturbed Lightly Overconsolidated Clay," *Canadian Geotechnical Journal*, Vol. 15, No. 3, pp. 402-423

Texas Department of Transportation (TxDOT) (1999a) "Year of the Recycled Roadway Materials - January: Crushed Concrete." <http://www.dot.state.tx.us/insdtdot/orgchart/gsd/recycle/mat.htm>, accessed October 1, 2000, 17 pp.

Texas Department of Transportation (TxDOT) (1999b) "Year of the Recycled Roadway Materials - June: Reclaimed Asphalt Pavement." <http://www.dot.state.tx.us/insdtdot/orgchart/gsd/recycle/mat.htm>, accessed October 1, 2000, 23 pp.

TxDOT (2004) "Standard Specifications for Construction and Maintenance of Highways, Streets, and Bridges," *Texas Department of Transportation*, Austin, Texas, 1028 pp.

Texas Department of Transportation, Tex-113-E (2001). *Laboratory Compaction Characteristics and Moisture-Density Relationship of Base Materials*.

Texas Department of Transportation, Tex-114-E (2001) *Laboratory Compaction Characteristics and Moisture-Density Relationship of Subgrade and Embankment Soils*.

Texas Department of Transportation, Tex-117-E (2001) *Triaxial Compression Tests for Disturbed Soils and Base Materials*.

Tian, W.-M., Silva, A.J., Veyera, G.E., and Sadd, M.H. (1994), "Drained Creep of Undisturbed Cohesive Marine Sediments," *Canadian Geotechnical Journal*, Vol. 31, No. 6, pp. 841-855.

Troxler Electronics, Inc. (2001). "Manual of Operation and Instruction: Model 3440 Surface Moisture-Density Gauge." Troxler Laboratories, Research Triangle Park, North Carolina, 220 pp.

Vaid, Y.P. and Campanella, R.G. (1977) "Time-Dependent Behavior of Undisturbed Clay," Journal of the Geotechnical Engineering Division, ASCE, Vol. 103, No. 7, pp. 693-709.